

AD-A279 903



14



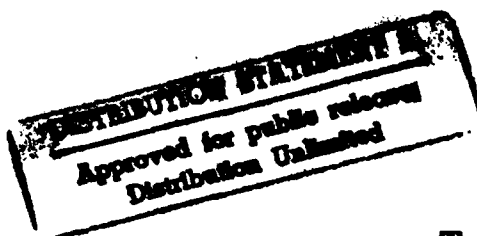
COLLEGE PARK CAMPUS

**7% SUPERCONVERGENCE OF FINITE ELEMENT APPROXIMATIONS
IN THE INTERIOR OF GENERAL MESHES OF TRIANGLES**

by

I. Babuška
T. Strouboulis
C. S. Upadhyay

DTIC
ELECTE
JUN 02 1994
S B D



Technical Note BN-1160

and

CMC Report No. 93-08
Texas Engineering Experiment Station
The Texas A&M University System

December 1993



INSTITUTE FOR PHYSICAL SCIENCE
AND TECHNOLOGY

94-16397



19396

94 6 1 123

REPORT DOCUMENTATION PAGE		READ INSTRUCTIONS BEFORE COMPLETING FORM
1. REPORT NUMBER Technical Note BN-1160 & CMC Report No. 93-08	2. GOVT ACCESSION NO.	3. RECIPIENT'S CATALOG NUMBER
4. TITLE (and Subtitle) η %-Superconvergence of Finite Element Approximations in the Interior of General Meshes of Triangles		5. TYPE OF REPORT & PERIOD COVERED Final Life of Contract
7. AUTHOR(s) I. Babuska ¹ - T. Strouboulis ² - C. S. Upadhyay ²		6. PERFORMING ORG. REPORT NUMBER
9. PERFORMING ORGANIZATION NAME AND ADDRESS Institute for Physical Science and Technology University of Maryland College Park, MD 20742-2431		8. CONTRACT OR GRANT NUMBER(s) 1 ONR N00014-90-J-1040 NSF CCR-88-20279 2 USARO DAAL03-G-028; NSF MSS- 9025110; TARP-71071
11. CONTROLLING OFFICE NAME AND ADDRESS Department of the Navy Office of Naval Research Arlington, VA 22217		10. PROGRAM ELEMENT, PROJECT, TASK AREA & WORK UNIT NUMBERS
14. MONITORING AGENCY NAME & ADDRESS (if different from Controlling Office)		12. REPORT DATE December 1993
		13. NUMBER OF PAGES 48 + Figures
		15. SECURITY CLASS. (of this report)
		15a. DECLASSIFICATION/DOWNGRADING SCHEDULE
16. DISTRIBUTION STATEMENT (of this Report) Approved for public release: distribution unlimited		
17. DISTRIBUTION STATEMENT (of the abstract entered in Block 20, if different from Report)		
18. SUPPLEMENTARY NOTES		
19. KEY WORDS (Continue on reverse side if necessary and identify by block number) DTIC QUALITY INSPECTED 2		
20. ABSTRACT In this paper we introduce a new definition of superconvergence - the η %-superconvergence, which generalizes the classical idea of superconvergence to general meshes. We show that this new definition can be employed to determine the regions of least-error in any element in the interior of any grid by using a computer-based approach. We present numerical results for the standard displacement finite element method for the scalar equation of orthotropic heat-conduction, for meshes of conforming triangles of degree p , $1 \leq p \leq 5$, and elements in the interior of the mesh. The results demonstrate that, unlike classical superconvergence, η %-superconvergence is applicable to the complex grids which are employed in practical engineering computations.		

$\eta\%$ -Superconvergence of Finite Element Approximations in the Interior of General Meshes of Triangles

I. Babuška*

**Institute for Physical Science and Technology and Department of Mathematics,
University of Maryland, College Park, MD 20742, U.S.A.**

T. Strouboulis[†] and C.S. Upadhyay[†]

**Department of Aerospace Engineering, Texas A&M University,
College Station, TX 77843, U.S.A.**

December 1993

***The work of this author was supported by the U.S. Office of Naval Research under Contract N00014-90-J-1030 and by the National Science Foundation under Grant CCR-88-20279.**

[†]The work of these authors was supported by the U.S. Army Research Office under Grant DAAL03-G-028, by the National Science Foundation under Grant MSS-9025110 and by the Texas Advanced Research Program under Grant TARP-71071.

Abstract:

In this paper we introduce a new definition of superconvergence - the $\eta\%$ -superconvergence, which generalizes the classical idea of superconvergence to general meshes. We show that this new definition can be employed to determine the regions of least-error in any element in the interior of any grid by using a *computer-based approach*. We present numerical results for the standard displacement finite element method for the scalar equation of orthotropic heat-conduction, for meshes of conforming triangles of degree p , $1 \leq p \leq 5$, and elements in the interior of the mesh. The results demonstrate that, unlike classical superconvergence, $\eta\%$ -superconvergence is applicable to the complex grids which are employed in practical engineering computations.

Accession For	
NTIS GRA&I	<input checked="checked" type="checkbox"/>
DTIC TAB	<input type="checkbox"/>
Unannounced	<input type="checkbox"/>
Justification	
By _____	
Distribution/	
Availability Codes	
Dist	Avail and/or Special
A-1	

1 Introduction.

Let $\{u_h\}$ be a one parameter sequence of finite element solutions of a problem which are computed using a sequence of meshes $\mathcal{T} = \{T_h\}$ and let u denote the exact solution. Let us assume that we are interested in the values of the solution or its derivatives or linear combinations of these quantities i.e. in the linear functional $F(u)(\bar{x})$. Let us assume that for every element τ of the mesh T_h a special point \bar{x} , which depends on the geometry (but not the size) of the element, is given. Then denoting

$$(1.1) \quad \Psi(u - u_h) := \max_{\bar{x} \in \tau} |F(u - u_h)(\bar{x})|$$

we are interested in the values of *relative error* in $F(u)$ at \bar{x} ,

$$(1.2) \quad \Theta(\bar{x}; F; u, u_h, h, \tau) := \begin{cases} \frac{|F(u - u_h)(\bar{x})|}{\Psi(u - u_h)} & , \text{ if } \Psi(u - u_h) \neq 0 ; \\ 0 & , \text{ if } \Psi(u - u_h) = 0 . \end{cases}$$

If the point \bar{x} is such that

$$(1.3) \quad \Theta(\bar{x}; F; u, u_h, h, \tau) \leq \frac{\eta}{100} \quad \text{as} \quad h \rightarrow 0$$

then \bar{x} will be called a u - $\eta\%$ -superconvergence point relative to the exact solution u and the family of meshes \mathcal{T} . Consider now a family \mathcal{U} of solutions; the point \bar{x} will be a \mathcal{U} - $\eta\%$ -superconvergence point relative to the family of meshes \mathcal{T} if it is u - $\eta\%$ -superconvergence point for every $u \in \mathcal{U}$. Obviously $\Theta(\bar{x}; F; u, u_h, h, \tau) \leq 1$ and thus all points in every element τ are 100%-superconvergence points. Note that if there exists a point \bar{x} in the element τ for which $\eta = 0$ in (1.3), i.e.

$$(1.4) \quad \Theta(\bar{x}; F; u, u_h, h, \tau) \rightarrow 0 \quad \text{as} \quad h \rightarrow 0$$

for a particular u (resp. for every $u \in \mathcal{U}$) then \bar{x} is a u -superconvergence (resp. \mathcal{U} -superconvergence) point in the classical sense. The superconvergence of this type was studied by many investigators; see for example [1-28] and the citations in these papers. It should be noted that the $\eta\%$ -superconvergence has not been analyzed in the literature. In this paper we will study the $\eta\%$ -superconvergence, when $F(u)$ is a linear combination of derivatives of u , for the model-problem of orthotropic heat-conduction for meshes of triangles of degree p , $1 \leq p \leq 5$. In

[29] we will address $\eta\%$ -superconvergence for meshes of quadrilaterals with local refinements.

In [28] we studied classical superconvergence by a computer-based approach. We observed that *the superconvergence points are very sensitive to the geometry of the mesh, the solution-type and the coefficients of the differential operator*. Hence the superconvergence points may not exist (in the classical sense) for the complex grids employed in practical computations. In contrast, the $\eta\%$ -superconvergence points will always exist for a sufficiently high η and can be defined for entire classes of grid geometries, solution-types and coefficients of the differential operator. Thus *the $\eta\%$ -superconvergence points are robust and can be used to sample the solution in practical engineering computations*.

Following this Introduction we outline the model problem of orthotropic heat-conduction and we define various quantities associated with the geometry of the error. We outline the theoretical setting of this study and give a computer-based approach to obtain the $\eta\%$ -superconvergence points. We then give various examples of the $\eta\%$ -superconvergence points for various grid geometries, solution-types and coefficients of orthotropy and demonstrate how to obtain robust sampling points for the practical grids.

2 Preliminaries.

2.1 The model problem

Let us consider the model problem of heat-conduction in orthotropic medium with mixed boundary conditions. Let $\Omega \subseteq \mathbb{R}^2$ be a bounded polygonal domain and let its boundary $\partial\Omega$ be split into two parts Γ_D and Γ_N (Γ_D has positive length). Let u be the solution of the problem

$$(2.1a) \quad \mathcal{L}(u) := - \sum_{k,\ell=1}^2 \frac{\partial}{\partial x_k} \left(K_{k\ell} \frac{\partial u}{\partial x_\ell} \right) = \bar{f}, \quad \text{in } \Omega,$$

$$(2.1b) \quad u = 0, \quad \text{on } \Gamma_D,$$

$$(2.1c) \quad \sum_{k=1}^2 q_k(u) n_k = \bar{g}, \quad \text{on } \Gamma_N.$$

Here $K_{k\ell}$, $k, \ell = 1, 2$ are the entries of the *thermal-conductivity* matrix which satisfy the conditions

$$(2.2a) \quad K_{kl} = K_{lk}, \quad k, l = 1, 2,$$

$$(2.2b) \quad 0 < K_{\min}(\xi_1^2 + \xi_2^2) \leq \sum_{k,l=1}^2 K_{kl} \xi_k \xi_l \leq K_{\max}(\xi_1^2 + \xi_2^2) \quad \forall \xi = (\xi_1, \xi_2) \in \mathbb{R}^2,$$

where K_{\min}, K_{\max} are the principal thermal conductivities;

$$(2.3) \quad q_k(u) := \sum_{l=1}^2 K_{kl} \frac{\partial u}{\partial x_l}, \quad k = 1, 2,$$

are the components of the flux (*heat-flux*); $n_k, k = 1, 2$ are the components of the unit outer normal of $\partial\Omega$; $\bar{f} \in L^2(\Omega), \bar{g} \in L^2(\Gamma_N)$ are given data.

Let $H_{\Gamma_D}^1(\Omega) := \{u \in H^1(\Omega) \mid u = 0 \text{ on } \Gamma_D\}$. Then the above problem may be put in the variational form: Find $u \in H_{\Gamma_D}^1(\Omega)$ such that

$$(2.4) \quad B_{\Omega}(u, v) = L_{\Omega}(v) \quad \forall v \in H_{\Gamma_D}^1(\Omega)$$

where

$$(2.5) \quad B_{\Omega}(u, v) := \int_{\Omega} \sum_{k,l=1}^2 K_{kl} \frac{\partial u}{\partial x_l} \frac{\partial v}{\partial x_k}, \quad L_{\Omega}(v) := \int_{\Omega} \bar{f}v + \int_{\Gamma_N} \bar{g}v.$$

Let $\mathcal{T} := \{T_h\}$ be a *regular-family* of meshes of triangles with straight edges. (It is assumed that for any triangles $\tau_i, \tau_j \in T_h$, the intersection $\tau_i \cap \tau_j$ is either empty, a vertex or a common edge, and that the minimal angle of all the triangles is bounded below by a positive constant, the same for all meshes.) The meshes T_h are not assumed to be quasiuniform. We introduce the conforming finite-element spaces

$$(2.6) \quad S_h^p := \left\{ u \in C^0(\Omega) \mid u|_{\tau_k} \in \mathcal{P}_p(\tau_k), \quad k = 1, \dots, M(T_h) \right\},$$

where $\mathcal{P}_p(\tau)$ denotes the space of polynomials of degree p over the triangle τ ; $M(T_h)$ is the number of elements in T_h . The finite element solution u_h of the model problem satisfies: Find $u_h \in S_{h,\Gamma_D}^p := S_h^p \cap H_{\Gamma_D}^1(\Omega)$ such that

$$(2.7) \quad B_{\Omega}(u_h, v_h) = L_{\Omega}(v_h) \quad \forall v_h \in S_{h,\Gamma_D}^p$$

We let $e_h := u - u_h$ denote the error in the finite element solution.

2.2 Definition of $\eta\%$ -superconvergence quantities

Let $T_h \in \mathcal{T}$ be a finite element grid, $\tau \in T_h$ be any element and K be the thermal-conductivity matrix expressed in a given fixed coordinate system. Let $F(u)$ be the solution-quantity of interest, for example we may have $F(u) = \frac{\partial u}{\partial x_1}$ or $\frac{\partial u}{\partial x_2}$ or $q_1(u) = K_{11} \frac{\partial u}{\partial x_1} + K_{12} \frac{\partial u}{\partial x_2}$ or $q_2(u) = K_{21} \frac{\partial u}{\partial x_1} + K_{22} \frac{\partial u}{\partial x_2}$, etc. We now define several geometrical quantities associated with the error in the finite element solution in the element τ .

Given η , $0 \leq \eta \leq 100$ we define the following:

1. $\eta\%$ -contour of $F(u)$ in the element $\tau \in T_h$ for the exact solution u and for material-orthotropy K :

$$(2.8) \quad C_{F(u)}^{\eta\%}(u; K; \tau, T_h) := \left\{ \tau \in T_h \mid \Theta(\tau; F; K; u, u_h, h, \tau) = \frac{\eta}{100} \right\},$$

Here $\Theta(\tau; F; K; u, u_h, h, \tau)$ is the relative error as defined in (1.2); note that K was added to the list of arguments to indicate the dependence of the relative error on the orthotropy.

2. $\eta\%$ -band of $F(u)$ in the element $\tau \in T_h$ for the exact solution u and for material-orthotropy K :

$$(2.9) \quad B_{F(u)}^{\eta\%}(u; K; \tau, T_h) := \left\{ \tau \in T_h \mid \Theta(\tau; F; K; u, u_h, h, \tau) < \frac{\eta}{100} \right\}$$

3. Superconvergence points of $F(u)$ in the element $\tau \in T_h$ for the class of exact solutions \mathcal{U} and for material-orthotropy K :

$$(2.10) \quad \mathcal{X}_{F(u)}^{\eta\%}(\mathcal{U}; K; \tau, T_h) := \bigcap_{u \in \mathcal{U}} C_{F(u)}^{\eta\%}(u; K; \tau, T_h)$$

4. $\eta\%$ -superconvergence regions of $F(u)$ in the element $\tau \in T_h$ for the class of exact solutions \mathcal{U} and for material-orthotropy K :

$$(2.11) \quad \mathcal{R}_{F(u)}^{\eta\%}(\mathcal{U}; K; \tau, T_h) := \bigcap_{u \in \mathcal{U}} B_{F(u)}^{\eta\%}(u; K; \tau, T_h)$$

5. Common $\eta\%$ -superconvergence region of $F(u)$ in the element $\tau \in T_h$ for the class of exact solutions \mathcal{U} , the class of materials \mathcal{M} and the class of meshes \mathcal{T} :

$$(2.12) \quad \bar{\mathcal{R}}_{F(u)}^{\eta\%}(\mathcal{U}; \mathcal{M}; \tau, T) = \bigcap_{T_h \in T} \bigcap_{K \in \mathcal{M}} \mathcal{R}_{F(u)}^{\eta\%}(\mathcal{U}; K; \tau, T_h)$$

Here \mathcal{M} is a class of thermal conductivity matrices referred to a given fixed coordinate system and τ is understood to be an element of *fixed geometry* (but not fixed size) embedded in all the meshes in the family T .

Remark 2.1. In some cases the sets defined above may be empty.

Remark 2.2. The function u is a solution (resp. \mathcal{U} is a class of solutions) of (2.1) for a given set of data (resp. for given classes of data). When $\bar{f} \equiv 0$ we say that exact solution u is "harmonic" (resp. \mathcal{U} is the class of "harmonic" solutions). (When u satisfies Laplace's equation, $-\Delta u = 0$ (i.e. when $K = I$), the solution is harmonic in the classical sense.) The majority of steady-state computations in engineering are done to approximate "harmonic" solutions; thus it is important to study superconvergence for this class of solutions.

One is interested to know a-priori the $\eta\%$ -superconvergence regions for the smallest possible values of $\eta\%$, for which they exist, for classes of solutions of interest (In practical computations in plane elasticity and heat-conduction the class of solutions of interest is the subclass of "harmonic" solutions with a finite number of algebraic point singularities of the type r^α). In general, if T_h is any grid, it is impossible to predict the locations of the $\eta\%$ -superconvergence regions. Here we will make additional assumptions about the approximation which will enable us to determine a-priori the $\eta\%$ -superconvergence regions for the meshes which occur in engineering computations. We will consider that the problem was solved using a sequence of meshes $\{T_h\}$ (not necessarily uniform meshes) which are constructed by a mesh-generator or an adaptive process. We will address the superconvergence as $h \rightarrow 0$ i.e. we are interested in the asymptotic locations of the $\eta\%$ -superconvergence regions in the limit as the mesh-parameter h tends to zero.

In this paper we will determine the asymptotic $\eta\%$ -superconvergence regions for elements in the interior of the mesh and smooth solutions. (The solutions can have isolated point-singularities at the boundaries but they are analytic in the interior of the domain.) The theoretical results will be given for a special class of *locally periodic meshes*. However through numerical examples we will demonstrate that the conclusions of the theoretical study hold, for all practical purposes, for the complex grids which are used in the practical engineering computations (for example the grid shown in Fig. 1).

2.3 The class of locally periodic meshes

We now present the definition of a special class of locally periodic meshes. Let us consider a locally periodic meshes (or grid) defined as follows. Let $0 < H < H^0$,

$$\mathfrak{x}^0 = (x_1^0, x_2^0) \in \Omega,$$

$$(2.13) \quad S(\mathfrak{x}^0, H) := \left\{ \mathfrak{x} = (x_1, x_2) \mid |x_i - x_i^0| < H, \quad i = 1, 2 \right\}$$

and assume H^0 is sufficiently small such that $\bar{S}(\mathfrak{x}^0, H^0) \subset \Omega$. Further, let γ be a set of multi-indices (i, j) , $\mathfrak{x}^{(i,j)} = (x_1^{(i,j)}, x_2^{(i,j)}) \in \Omega$ and

$$(2.14) \quad c(\mathfrak{x}^{(i,j)}, h) := S(\mathfrak{x}^{(i,j)}, h) \subset S(\mathfrak{x}^0, H), \quad (i, j) \in \gamma$$

be the set of the h -cells (or cells) which cover exactly $S(\mathfrak{x}^0, H)$ i.e.

$$(2.15a) \quad \bigcup_{(i,j) \in \gamma} \bar{c}(\mathfrak{x}^{(i,j)}, h) = \bar{S}(\mathfrak{x}^0, H)$$

$$(2.15b) \quad c(\mathfrak{x}^{(i_1, j_1)}, h) \cap c(\mathfrak{x}^{(i_2, j_2)}, h) = \emptyset \quad \text{for } (i_1, j_1) \neq (i_2, j_2)$$

We will refer to $S(\mathfrak{x}^0, H)$ as the *subdomain of periodicity of the mesh centered at \mathfrak{x}^0* . Denoting by

$$(2.16) \quad \bar{c} := S(0, 1) := \left\{ (\bar{x}_1, \bar{x}_2) \mid |\bar{x}_1| < 1, |\bar{x}_2| < 1 \right\}$$

the *unit- (master-) cell \bar{c}* , the h -cell is an h -scaled and translated master-cell.

Let \tilde{T} be a triangular mesh on the master-cell (the master-mesh) and $\tilde{T}_h^{(i,j)}$ be the mesh on $c(\mathfrak{x}^{(i,j)}, h)$ which is the scaled and translated image of \tilde{T} . We will consider the family \mathcal{T} of locally periodic meshes. Let $T_h \in \mathcal{T}$ and $T_h(\mathfrak{x}^0, H)$ be the restriction of T_h on $S(\mathfrak{x}^0, H)$ and $T_h^{(i,j)}$ the restriction of $T_h(\mathfrak{x}^0, H)$ on $c(\mathfrak{x}^{(i,j)}, h)$. We assume that $T_h^{(i,j)} = \tilde{T}_h^{(i,j)}$, $(i, j) \in \gamma$ i.e. $T_h(\mathfrak{x}^0, H)$ is made by the periodic repetition of the h -scaled master mesh.

The type of meshes under consideration is depicted in Fig. 2a, where the subdomains $S(\mathfrak{x}^0, H) \supset S(\mathfrak{x}^0, H_1)$ are covered by a periodic array of cells. An example is shown in Fig. 2b (where the master-mesh in the master-cell is shown in Fig. 2c). Here we are interested in the superconvergence regions in the elements belonging to the patch shown in the Figs. 2b, 2c. Outside the square $S(\mathfrak{x}^0, H)$ the mesh is arbitrary; it could have curved elements, etc. The values of H_1 depend on h i.e. $H_1 = H_1(h)$. More precisely we will assume that there exist C_1 and C_2 independent of h such that

$$(2.17) \quad C_1 H_1^\alpha \leq h \leq C_2 H_1^\alpha, \quad \alpha > 1$$

3 The theoretical setting

We will here for simplicity address only the case of Poisson's equation ($K = I$ in (2.1)). Nevertheless, the results could be easily generalized to the general setting for orthotropic medium.

Given a function u and the multi-index $\alpha := (\alpha_1, \alpha_2)$ we define

$$(3.1a) \quad D^\alpha u := \frac{\partial^{|\alpha|} u}{\partial x_1^{\alpha_1} \partial x_2^{\alpha_2}}, \quad |\alpha| := \alpha_1 + \alpha_2$$

$$(3.1b) \quad (\mathcal{D}^k u)(\mathfrak{s}) := \left[\left(\sum_{|\alpha|=k} |D^\alpha u|^2 \right)(\mathfrak{s}) \right]^{\frac{1}{2}}, \quad k \geq 0, \text{ integer}$$

and let us denote

$$(3.2a) \quad \|u\|_{S(\mathfrak{s}^0, H_i)} := \|u\|_{L^2(S(\mathfrak{s}^0, H_i))}$$

$$(3.2b) \quad |u|_{S(\mathfrak{s}^0, H_i)} := \|u\|_{L^\infty(S(\mathfrak{s}^0, H_i))}$$

$$(3.2c) \quad \|u\|_{S(\mathfrak{s}^0, H_i)} := \sum_{|\alpha|=1} |D^\alpha u|$$

Let Q be a polynomial of degree $p + 1$ on the master-cell \tilde{c} and let \tilde{T} be the master-mesh. Then denote

$$(3.3) \quad \rho := Q - Q_1^{\text{INT}}$$

where Q_1^{INT} is the interpolant of degree p of the function Q defined over the master-mesh \tilde{T} (for which $h = 1$). Then we have

$$(3.4) \quad \begin{cases} \rho(1, \tilde{x}_2) = \rho(-1, \tilde{x}_2), & |\tilde{x}_2| < 1 \\ \rho(\tilde{x}_1, 1) = \rho(\tilde{x}_1, -1), & |\tilde{x}_1| < 1 \end{cases}$$

because $S_1^p(\tilde{c})$ includes all polynomials of degree p on \tilde{c} . Further let

$$(3.5) \quad H_{\text{PER}}^1(\tilde{c}) := \left\{ u \in H^1(\tilde{c}) \mid u \text{ satisfies (3.4)} \right\}$$

and

$$(3.6) \quad S_{1,\text{PER}}^p(\tilde{c}) := \left\{ u \in H_{\text{PER}}^1(\tilde{c}) \mid u \in \mathcal{P}_p(\tilde{\tau}) \quad \forall \tilde{\tau} \in \tilde{T} \right\}$$

Further let $\tilde{z}^p \in S_{1,\text{PER}}^p(\tilde{c})$ such

$$(3.7a) \quad B_{\tilde{c}}(\tilde{z}^p, \tilde{v}) = (\rho, \tilde{v}) \quad \forall \tilde{v} \in S_{1,\text{PER}}^p(\tilde{c})$$

and

$$(3.7b) \quad \int_{\tilde{c}} (\rho - \tilde{z}^p) = 0$$

Note that the function \tilde{z}^p exists and is uniquely determined (we will compute it numerically in the examples). Let us also define $\psi \in H^1(\tilde{c})$ by

$$(3.8) \quad \psi := \rho - \tilde{z}^p = Q - Q_1^{\text{INT}} - \tilde{z}^p.$$

Below we outline the main theorem of the paper.

We will make the following assumptions about the exact solution u :

Assumption I

On $\tilde{S}(\mathfrak{s}^0, H)$

$$(3.9) \quad |D^\alpha u| \leq K < \infty, \quad 0 \leq |\alpha| \leq p+2$$

Remark 3.1. Assumption I states that the solution is locally smooth in the subdomain $\tilde{S}(\mathfrak{s}^0, H)$ i.e. the subdomain should be sufficiently far from boundaries, material-interfaces and points where the data are rough.

Assumption II

If $a_\alpha := (D^\alpha u)(\mathfrak{s}^0)$, $\alpha = (\alpha_1, \alpha_2)$, $|\alpha| \leq p+1$ then

$$(3.10) \quad R^2 = \sum_{|\alpha|=p+1} a_\alpha^2 > 0$$

Further, we assume that the mesh $T(\Omega, h)$ is such that:

Assumption III

On $S(\mathfrak{x}^0, H_1)$, $H_1 < H < H^0$

$$(3.11) \quad \|e_h\|_{S(\mathfrak{x}^0, H_1)} \leq Ch^\beta H_1$$

with $\beta \geq (p+1) - \epsilon$, where ϵ is specified in the theorem below and where C is independent of $T(\Omega, h)$, H_1 , but it depends on K and R .

Remark 3.2. We do not assume that u is smooth in Ω outside of $S(\mathfrak{x}^0, H)$. For example, Ω can have a boundary with reentrant corners (as in Fig. 2(a)) and hence u can be unsmooth in the neighborhood of these corners. Nevertheless assumption III makes an implicit requirement on the (refinement of the) mesh in the neighborhood of these corners. If u is smooth in a convex Ω and the mesh is quasi-uniform then

$$(3.12) \quad \|e_h\|_\Omega \leq Ch^{p+1} |\ln h|^r \|D^{p+1}u\|_\Omega, \quad r \geq 0$$

and hence in assumption III we can take $\beta < p+1$ arbitrary. Assumption III is related to the pollution problem which is analyzed in [38].

Remark 3.3. Assumptions II, III imply that the principal part of the error in $S(\mathfrak{x}^0, H_2)$ is related to the non-zero $(p+1)$ -derivatives of the exact solution at \mathfrak{x}^0 .

Let $\psi_h \in H_{\text{PER}}^1(c(\mathfrak{x}^{(i,j)}, h))$ be the function ψ , defined above, scaled and translated onto the cell $c(\mathfrak{x}^{(i,j)}, h)$ of the mesh in $S(\mathfrak{x}^0, H)$ i.e.

$$(3.13) \quad \psi_h(\mathfrak{x}) := h^{p+1} \psi(\tilde{\mathfrak{x}}), \quad \frac{\partial \psi_h}{\partial x_i}(\mathfrak{x}) = h^p \frac{\partial \psi}{\partial \tilde{x}_i}(\tilde{\mathfrak{x}}), \quad i = 1, 2,$$

where $\mathfrak{x} \in c(\mathfrak{x}^{(i,j)}, h)$, $\tilde{\mathfrak{x}} = \frac{1}{h}(\mathfrak{x} - \mathfrak{x}^{(i,j)})$.

It is easy to see that ψ_h can be periodically extended over $S(\mathfrak{x}^0, H_1)$. In [28] we have proven the following theorem using the theory of interior estimates (see [31]-[37]):

Theorem 1. Let $H_2 < H_1 < H < H^0$ and the assumptions I-III and (2.17)-(2.18) hold with

$$(3.14) \quad \alpha = \frac{6p+1}{6p}, \quad \nu = \frac{1}{6(6p+1)} \quad \beta = p+1-\epsilon, \quad \epsilon = \nu$$

Then for any $\mathfrak{x} \in S(\mathfrak{x}^0, H_2)$

$$(3.15) \quad \left| \frac{\partial e_h}{\partial x_i}(\mathfrak{x}) \right| = \left| \frac{\partial \psi_h}{\partial x_i}(\mathfrak{x}) \right| + |\lambda| C h^{p+\nu}$$

with $|\lambda| \leq 1$ and C independent of h .

Remark 3.4. Note that ψ (and thus ψ_h) depends on the polynomial Q which approximates well the solution in $S(\mathfrak{x}^0, H)$. Theorem 1 states that for small h (and hence H_1) we have on $S(\mathfrak{x}^0, H_2)$

$$(3.16) \quad \frac{\partial e_h}{\partial x_i}(\mathfrak{x}) \approx \frac{\partial \psi_h}{\partial x_i}(\mathfrak{x})$$

or more precisely

$$(3.17) \quad \left| \frac{\partial e_h}{\partial x_i}(\mathfrak{x}) \right| = \left| h^p \frac{\partial \psi}{\partial \tilde{x}_i}(\tilde{\mathfrak{x}}) \right| + |\lambda| C h^{p+\nu}.$$

On the other hand it is easy to see that

$$(3.18) \quad \max \left(\left| \frac{\partial e_h}{\partial x_1} \right|_{\alpha(\mathfrak{x}^{(i,j)}, h)}, \left| \frac{\partial e_h}{\partial x_2} \right|_{\alpha(\mathfrak{x}^{(i,j)}, h)} \right) \geq C h^p$$

where C depends on the constant R defined in (3.10). Nevertheless this does not mean that

$$(3.19) \quad \left| \frac{\partial e_h}{\partial x_i} \right|_{\tau} \geq C h^p, \quad i = 1, 2$$

The case that

$$(3.20) \quad \left| \frac{\partial e_h}{\partial x_i} \right|_{\tau} \leq C h^{p+\sigma_0}, \quad \sigma_0 > 0 \quad \text{for either } i = 1 \text{ or } 2$$

is very exceptional. Hence we will assume that (3.20) does not happen i.e. we will assume that there exists a constant $\bar{c} > 0$ independent of h such that

$$(3.21) \quad \left| \frac{\partial e_h}{\partial x_i} \right|_{\tau} \geq \bar{c} \|e_h\|_{\tau}$$

This assumption could formally be achieved by imposing additional assumptions on the a_{α} 's (defined in assumption II). Note also that assumption (3.21) is always assumed in the classical superconvergence theories.

Remark 3.9. Under assumption (3.21) Theorem 1 states that: A point $\bar{\omega}$ in the element $\bar{\tau}$ is asymptotically $\eta\%$ -superconvergence point for $F(u) = \frac{\partial u}{\partial x_i}$ if and only if

$$(3.22a) \quad \bar{\Theta}(\bar{\omega}; F; I; Q, z^p, 1, \bar{\tau}) \leq \frac{\eta}{100}$$

where

$$(3.22b) \quad \bar{\Theta}(\bar{\omega}; F; I; Q, z^p, 1, \bar{\tau}) := \frac{|\bar{F}(\psi)(\bar{\omega})|}{\bar{\Psi}(\psi)}, \quad \bar{\Psi}(\psi) := |\psi|_{\tau}$$

Remark 3.10. The term $\eta\%$ -superconvergence is not precisely descriptive. We have used it because we wanted that $\eta\%$ -superconvergence points for $\eta = 0$ be superconvergence points in the common terminology.

Theorem 1 shows that the $\eta\%$ -superconvergence can be analyzed by a local analysis in the neighborhood of the elements under consideration. By this we mean that the $\eta\%$ -superconvergence regions of the finite element solution are very close to the ones determined from the local analysis provided that the mesh is sufficiently fine.

4 The methodology for determining the $\eta\%$ -superconvergence quantities

In this paper superconvergence is treated as local behavior and is based on assumptions about the local behavior of the solution in the interior of the domain. We will consider the class of solutions which are locally smooth in $S(\omega^0, H)$, namely,

$$(4.1) \quad \mathcal{U}^G := \left\{ u \in H^1(\Omega) \mid |D^{\alpha} u|_{S(\omega^0, H)} < K, \quad 0 \leq |\alpha| \leq p+2 \right\}$$

where $S(\mathfrak{x}^0, H)$ denotes an interior subdomain of interest in which the mesh is locally periodic as described above (the subdomain must be a finite distance away from the boundary and points of roughness of the source term; see Fig. 2a). In many instances we are only interested in the subclass of solutions in \mathcal{U}^G which are "harmonic" (we say that u is "harmonic" if it satisfies the homogeneous differential equation), namely,

$$(4.2) \quad \mathcal{U}^{H^*} := \left\{ u \in \mathcal{U}^G \mid \mathcal{L}(u) = 0 \text{ in } \Omega \right\}$$

We may also assume that the functions are "harmonic" in a subdomain which is slightly bigger than $S(\mathfrak{x}^0, H)$ and which includes $S(\mathfrak{x}^0, H)$ in its interior.

In the previous Section we outlined Theorem 1 which states that we can obtain the asymptotic values of the error ψ_h for any smooth solution u in the interior of a periodic mesh-subdomain by solving the periodic boundary-value problem (3.7), using the master-mesh \tilde{T} over the master-cell \tilde{c} , with data obtained from the local $(p+1)$ -degree Taylor-series expansion of the exact solution (which approximates well the function u in $S(\mathfrak{x}^0, H)$). Based on this result we will construct a numerical procedure to determine the $\eta\%$ -superconvergence quantities for a given class of smooth solutions by employing the corresponding class of $(p+1)$ -degree monomials.

a. The classes of $(p+1)$ -degree monomial solutions.

Let us assume that for a given locally periodic grid with corresponding periodic master-mesh \tilde{T} , given material orthotropy and given class of smooth solutions \mathcal{U} we consider

$$(4.3) \quad \mathcal{Q} := \left\{ Q \mid Q(x_1, x_2) = \sum_{k=1}^{nd} \alpha_k Q_k(x_1, x_2), \quad Q_k(x_1, x_2) = \sum_{\ell=0}^{p+1} \beta_{\ell} x_1^{\ell} x_2^{p+1-\ell} \right\}$$

the class of $(p+1)$ -degree monomials which occur in all $(p+1)$ -degree Taylor-series expansions of functions from \mathcal{U} . Here Q_k , $k = 1, \dots, nd$ denotes a set of linearly independent monomials which span \mathcal{Q} . For example let us assume that \mathcal{U} is the class of smooth solutions \mathcal{U}^G given in (4.1); in this case we may choose

$$(4.4) \quad Q_k(x_1, x_2) := x_1^{p+2-k} x_2^{k-1}, \quad 1 \leq k \leq nd = p+2$$

and we obtain the class of all $(p+1)$ -degree monomials \mathcal{Q}^G .

In many practical applications we are interested only in the class of "harmonic" solutions \mathcal{U}^{H^*} given in (4.2). Then \mathcal{Q} is the two-dimensional linear space of "harmonic" monomials of degree $(p+1)$ and will be denoted by \mathcal{Q}^{H^*} . For example in the case of Laplace's equation ($K = I$) we have

$$(4.5a) \quad Q^H := \left\{ Q^H \mid Q^H(x_1, x_2) = \sum_{k=1}^2 \alpha_k Q_k^H(x_1, x_2) \right\},$$

$$(4.5b) \quad Q_1^H(x_1, x_2) = \operatorname{Re}(z^{p+1}), \quad Q_2^H(x_1, x_2) = \operatorname{Im}(z^{p+1}), \quad z = x_1 + ix_2.$$

Note that in this case we do not use the quotes since the functions are harmonic in the classical sense (i.e. they satisfy Laplace's equation).

b. Freezing the periodicity for general meshes.

In the previous Section the theoretical results for the asymptotic values of the error in the interior of periodic mesh-subdomains in locally periodic grids were outlined. In particular, it was stated that the asymptotic error-function ψ_h in any element τ in the h -cell in the interior of any periodic mesh-subdomain can be obtained by solving a periodic boundary-value problem (3.7), using the master-mesh \bar{T} over the master-cell \bar{c} , with data obtained from the local $(p+1)$ -degree Taylor-series expansion of the exact solution. In order to apply the results of the theoretical study to the practical meshes, for which the mesh is not locally periodic, the following technique of *freezing the periodicity* will be employed:

1. Let X be a vertex of the mesh. We will be interested in the $\eta\%$ -superconvergence regions in the elements in the mesh-cell ω_0^h (see for example Figs. 3a, 41) in a neighborhood of elements around the vertex X . Define an s -layered mesh-cell of elements ω_s^h surrounding the mesh-cell ω_0^h (see Figs. 3a and 41 where ω_s^h is shown with a thick black perimeter; this cell is enclosed in the general mesh given in Fig. 1) by

$$(4.6) \quad \omega_s^h := \bigcup_{\substack{X \in N(\tau') \\ \tau' \subseteq \omega_{s-1}^h}} \omega_X, \quad \omega_h^0 := \omega_X \supset \tau; \quad \omega_X := \bigcup_{X \in N(\tau')} \tau';$$

where $N(\tau')$ denotes the set of the three vertices of element τ' and ω_X is a mesh-cell of elements connected to vertex X which includes the element τ .

2. Complete the mesh-cell ω_s^h (shown in Fig. 3b) to a periodic-grid over a slightly larger square periodic-cell which encloses ω_s^h , as shown in Fig. 3c. The periodic-cell is then scaled and translated to the unit master-cell \bar{c} .

3. Assume that the mesh in the neighborhood of element τ is made from the periodic repetition of h -cells obtained from the master-cell, as shown in Fig. 2b (where the master-cell is given in Fig. 2c), and let h tend to zero. Then the theoretical-setting of the previous Section applies and the asymptotic error-function ψ_h in the element τ can be obtained from the interpolation-error and the solution of the periodic boundary-value problem (3.7) over the master-cell \tilde{c} .

In the numerical examples it will be demonstrated that the results of $\eta\%$ -superconvergence obtained from the above methodology hold, for all practical purposes, for the complex grids used in engineering computations (provided that the pollution-error is controlled, the approximation is in the asymptotic range and that sufficient number of mesh-layers are included in the mesh-cell ω_i^h).

c. Determination of the $\eta\%$ -superconvergence quantities.

Based on the results of the theoretical study, outlined in Section 3, the asymptotic locations of the $\eta\%$ -superconvergence quantities in the element τ for a solution u (resp. class of solutions \mathcal{U}) can be obtained from the corresponding quantities, defined on the master-cell \tilde{c} , for the local $(p+1)$ -degree Taylor expansion Q of u (resp. the class \mathcal{Q} of the local $(p+1)$ -degree Taylor series expansions of functions $u \in \mathcal{U}$), namely:

$$(4.7a) \quad \lim_{h \rightarrow 0} C_{F(u)}^{\eta\%}(u; K; \tau, T_h) = \tilde{C}_{F(u)}^{\eta\%}(Q; K; \tilde{\tau}, \tilde{T})$$

$$(4.7b) \quad \lim_{h \rightarrow 0} B_{F(u)}^{\eta\%}(u; K; \tau, T_h) = \tilde{B}_{F(u)}^{\eta\%}(Q; K; \tilde{\tau}, \tilde{T})$$

$$(4.7c) \quad \lim_{h \rightarrow 0} \chi_{F(u)}^{\sup}(\mathcal{U}; K; \tau, T_h) = \tilde{\chi}_{F(u)}^{\sup}(\mathcal{Q}; K; \tilde{\tau}, \tilde{T})$$

$$(4.7d) \quad \lim_{h \rightarrow 0} \mathcal{R}_{F(u)}^{\eta\%}(\mathcal{U}; K; \tau, T_h) = \tilde{\mathcal{R}}_{F(u)}^{\eta\%}(\mathcal{Q}; K; \tilde{\tau}, \tilde{T})$$

where the superconvergence quantities over $\tilde{\tau} \in \tilde{T}$ are defined as the corresponding quantities in (2.2) by employing the relative error function given by (3.22b). The above equalities are understood through the transformation which maps the master-cell into the h -cells.

Remark 4.1. The above limits hold for the locally periodic meshes under the assumptions of the theoretical analysis of Section 3. Hence for the general grids

the limit should be understood for the mesh which is constructed by freezing the periodicity (see also Figs. 2 and 3).

The asymptotic $\eta\%$ -contours for a given solution u can be obtained by contouring the function ψ , defined in (3.8), corresponding to the local Taylor-series expansion Q of u . The superconvergence points \bar{x} for a given class of solutions \mathcal{U} should satisfy

$$(4.8) \quad F(\psi_i)(\bar{x}) = 0 \quad \text{for} \quad 1 \leq i \leq nd$$

Here $\psi_i := \rho_i - z_i^p$, where z_i^p is the solution of (3.7) for $\rho_i = Q_i - (Q_i)_1^{\text{INT}}$ where Q_i is the i -th basis monomial of the nd -dimensional monomial space \mathcal{Q} corresponding to the class \mathcal{U} , as discussed in (4.3), (4.4). When (4.8) holds, the zero-contours of $F(\psi_i)$ intersect at \bar{x} for $1 \leq i \leq nd$.

Remark 4.2. For the class of general solutions \mathcal{U}^G , $nd = p + 2$, and as p increases (for $p \geq 3$) the likelihood of zero-contours for each one of the ψ_i 's crossing simultaneously at one point is very small. Thus a few or no superconvergence points exist for the class \mathcal{U}^G and $p \geq 3$. On the other hand for the class of "harmonic" solutions \mathcal{U}^H , $nd = 2$ independent of p , and many superconvergence exist and their number increases with p . For details see [28].

The asymptotic $\eta\%$ -superconvergence bands for a solution u can be determined from the function $F(\psi)$ by using piecewise linear interpolation of $F(\psi)$ on a sufficiently fine uniform mesh obtained by subdividing the triangle τ .

The asymptotic $\eta\%$ -superconvergence regions for a class of solutions \mathcal{U} can be determined by using numerical optimization. In particular, consider the uniform subdivision of the element τ into subtriangles with vertices at the set of points $\Xi := \{\xi_k\}_{k=1}^{np}$. Define the relative-error function at the point ξ_k

$$(4.9) \quad \bar{\Theta}_{F(u)}^{\Xi}(\xi_k; F; K; Q, \{z_i^p\}_{i=1}^{nd}, 1, \bar{\tau}) := \max_{\alpha_i} \frac{\left| \sum_{i=1}^{nd} \alpha_i F(\psi_i)(\xi_k) \right|}{\max_{j=1, \dots, np} \left| \sum_{i=1}^{nd} \alpha_i F(\psi_i)(\xi_j) \right|} \cdot 100,$$

Then the function $\bar{\Theta}_{F(u)}^{\Xi}(\bar{w}; F; K; Q, \{z_i^p\}_{i=1}^{nd}, 1, \bar{\tau})$ can be defined for any point $\bar{w} \in \bar{\tau}$ by using linear interpolation in the subtriangles. The asymptotic $\eta\%$ -superconvergence regions in the element τ can be approximated using the level-sets of the functions $\bar{\Theta}_{F(u)}^{\Xi}(\bar{w}; F; K; Q, \{z_i^p\}_{i=1}^{nd}, 1, \bar{\tau})$ i.e.

$$(4.10) \quad \bar{\mathcal{R}}_{F(u)}^{\eta\%}(Q; K; \bar{\tau}, \bar{T}) \approx \left\{ \bar{w} \in \bar{\tau} \mid \bar{\Theta}_{F(u)}^{\Xi}(\bar{w}; F; K; Q, \{z_i^p\}_{i=1}^{nd}, 1, \bar{\tau}) < \eta\% \right\}$$

We will call this approach the *direct approach*. It is also possible to use a *simplified approach* which avoids the use of numerical optimisation at every point. First observe that

$$\begin{aligned}
 (4.11) \quad & \max_{\alpha_i} \frac{\left| \sum_{i=1}^{nd} \alpha_i F(\psi_i)(\tilde{s}) \right|}{\max_{j=1, \dots, np} \left| \sum_{i=1}^{nd} \alpha_i F(\psi_i)(\xi_j) \right|} = \max_{\alpha_i} \left(\frac{\left(\sum_{i=1}^{nd} \alpha_i^2 \right)^{\frac{1}{2}}}{\max_{j=1, \dots, np} \left| \sum_{i=1}^{nd} \alpha_i F(\psi_i)(\xi_j) \right|} \frac{\left| \sum_{i=1}^{nd} \alpha_i F(\psi_i)(\tilde{s}) \right|}{\left(\sum_{i=1}^{nd} \alpha_i^2 \right)^{\frac{1}{2}}} \right) \leq \\
 & \leq \max_{\alpha_i} \frac{\left(\sum_{i=1}^{nd} \alpha_i^2 \right)^{\frac{1}{2}}}{\max_{j=1, \dots, np} \left| \sum_{i=1}^{nd} \alpha_i F(\psi_i)(\xi_j) \right|} \left(\sum_{i=1}^{nd} (F(\psi_i)(\tilde{s}))^2 \right)^{\frac{1}{2}} \leq \\
 & \leq \left[\min_{\alpha_i} \frac{\max_{j=1, \dots, np} \left| \sum_{i=1}^{nd} \alpha_i F(\psi_i)(\xi_j) \right|}{\left(\sum_{i=1}^{nd} \alpha_i^2 \right)^{\frac{1}{2}}} \right]^{-1} \left(\sum_{i=1}^{nd} (F(\psi_i)(\tilde{s}))^2 \right)^{\frac{1}{2}}
 \end{aligned}$$

Hence we can define the function

$$(4.12) \quad \hat{\Theta}_{F(u)}^{\tilde{s}}(\tilde{s}; F; K; Q, \{x_i^j\}_{i=1}^{nd}, 1, \tilde{\tau}) := \frac{1}{Z_{\tilde{s}}} \sqrt{\sum_{i=1}^{nd} (F(\psi_i)(\tilde{s}))^2},$$

where

$$(4.13) \quad Z_{\tilde{s}} := \min_{\alpha_i} \frac{\max_{j=1, \dots, np} \left| \sum_{i=1}^{nd} \alpha_i F(\psi_i)(\xi_j) \right|}{\left(\sum_{i=1}^{nd} \alpha_i^2 \right)^{\frac{1}{2}}}$$

The quantity $Z_{\tilde{s}}$ can be computed using numerical optimization. Let

$$(4.14) \quad \widehat{\mathcal{R}}_{F(u)}^{\eta\%}(Q; K; \tau, \tilde{T}) := \left\{ \tilde{s} \in \tau \mid \hat{\Theta}_{F(u)}^{\tilde{s}}(\tilde{s}; F; K; Q, \{x_i^j\}_{i=1}^{nd}, 1, \tilde{\tau}) < \frac{\eta}{100} \right\}$$

denote the approximate regions of $\eta\%$ -superconvergence for the class of solutions Q obtained by the simplified approach.

The common $\eta\%$ -superconvergence region in an element τ for a given class of meshes and materials can be determined by using either the direct or the simplified approach.

Remark 4.3. Note that we have

$$(4.15) \quad \widehat{\mathcal{R}}_{F(u)}^{\eta\%}(Q; K; \bar{\tau}, \bar{T}) \subseteq \bar{\mathcal{R}}_{F(u)}^{\eta\%}(Q; K; \bar{\tau}, \bar{T})$$

and we get a conservative estimate for the $\eta\%$ -superconvergence regions when the simplified approach is used. For the class of harmonic functions \mathcal{U}^H we observed that the regions obtained by the two approaches are very close. However for the class of general solutions \mathcal{U}^G the simplified approach is too pessimistic and the more expensive direct approach must be employed.

Remark 4.4. The functions defined in (4.9), (4.12) depend on the set of points Ξ . To ensure good accuracy in the approximation of the $\eta\%$ -superconvergence regions a sufficient number of points must be employed.

5 Numerical studies of superconvergence

We will now present a model study of the $\eta\%$ -superconvergence properties of finite element solutions in the interior of any grid, for any smooth solution and material-orthotropy. We will address the following questions:

1. Given an element τ in the interior of a periodic subdomain of a locally periodic mesh T_h , where are the points of superconvergence and what is their sensitivity with respect to:
 - (i) The class of solutions (harmonic or general);
 - (ii) The material orthotropy;
 - (iii) The geometry of the mesh and the number of mesh-layer in the mesh-cells ω_i^h ?
2. Given $\eta\%$ (between 0%-100%) where are the regions in which the derivatives of the error, or the components of the flux are within $\eta\%$ of the maximum error in the respective quantities in the element τ ? In particular:
 - a. For the periodic meshes shown in Fig. 4 where are the $\eta\%$ -superconvergence regions for the x_1 -derivative and how do these regions vary with the degree p of the elements:
 - (i) For the class of harmonic solutions \mathcal{U}^H ;

- (ii) For the class of general solutions \mathcal{U}^G ?
- b. For periodic meshes what is the effect of the mesh-distortion, the material-orthotropy and the surrounding mesh on the location of the $\eta\%$ -superconvergence regions in a typical element?
- c. For a general mesh, like the ones used in practical engineering computations, how different are the regions which are determined by freezing the periodicity from the regions determined from the actual mesh?

We will answer the above mentioned questions by employing the computer-based approach outlined in Section 4.

5.1 Robustness of the superconvergence points with respect to the class of solutions and distortions of the mesh for the Laplace equation ($K = I$)

We considered the four periodic patterns shown in Fig. 4. In [28] we determined the points of superconvergence for the periodic meshes shown in Fig. 4 for the classes \mathcal{U}^H and \mathcal{U}^G . The points are listed in Tables 1 for $1 \leq p \leq 5$ for the class of harmonic solutions. Table 2 indicates which points in each pattern are also superconvergence points for the class of general solutions. In order to investigate the robustness of these points with respect to the class of solutions we computed (Table 3) the maximum $\eta\%$ -error in the x_1 -derivative of the solution for the class of general solutions \mathcal{U}^G at the superconvergence points for the class \mathcal{U}^H for quadratic elements i.e. the value

$$(5.1) \quad \bar{\eta}^*(\bar{\omega}) := \max_{Q \in \mathcal{Q}^G} \Theta\left(\bar{\omega}; \frac{\partial u}{\partial x_1}; I; Q, z^p, 1, \bar{\tau}\right), \quad \bar{\omega} \in \mathcal{X}_{\frac{\partial u}{\partial x_1}}^{\text{sup}}(Q^H; I; \bar{\tau}, \bar{T})$$

From the numerical results we observe that the relative error at the superconvergence points for the class of harmonic solutions may be large for solutions which are not harmonic.

5.2 Determination of the $\eta\%$ -superconvergence regions for the periodic meshes ($K = I$)

From the previous example it is clear that the superconvergence points are very sensitive to class of solutions and the geometry of the mesh. Moreover, the points may not exist at all; for example there are no superconvergence points for the x_1 -derivative of the solution in the Union-Jack pattern for the class of general solutions. We will now report the $\eta\%$ -superconvergence regions for the periodic

meshes shown in Fig. 4. We will show that, unlike the superconvergence points, these regions always exist (in any element in any pattern) for sufficiently high $\eta\%$.

We determined the $\eta\%$ -superconvergence regions for the classes of harmonic and general solutions, for the elements $\bar{\tau}$ in the periodic-cell which consists of: two elements for the Regular pattern; four elements for the Chevron and Criss-Cross patterns; eight elements for the Union-Jack pattern. The levels of $\eta\%$ in the Figures were chosen to be 10%, 20%, 30%. In Figs. 5-8 the regions $\bar{\mathcal{R}}_{\frac{\partial u}{\partial x_1}}^{\eta\%}(Q^H; I; \bar{\tau}, \bar{T})$ and the contours of zero-error in the x_1 -derivative of the solution for the basis harmonic-monomials are given for $p = 1, 2, 3, 4, 5$. It should be noted that for the class of harmonic solutions the results were obtained using the "simplified approach" (these results are very close to corresponding results obtained using the direct approach). The regions $\bar{\mathcal{R}}_{\frac{\partial u}{\partial x_1}}^{\eta\%}(Q^G; I; \bar{\tau}, \bar{T})$ for $p = 1, 2, 3$, are given in Figs. 9-12. It should be noted that for the class of general solutions the direct approach must be used in the determination of the $\eta\%$ -superconvergence regions, as the simplified approach is too pessimistic (it results in regions which are much smaller than the actual ones).

We observe that:

1. For the class of harmonic solutions, the $\eta\%$ -superconvergence regions for the error in the x_1 -derivative grow with the degree p of the elements.
2. For the class of general solutions, the $\eta\%$ -superconvergence regions for the x_1 -derivative are small (except for the Regular pattern for $p = 1, 2$) and they diminish in size as p grows, i.e. for higher p 's ($p \geq 3$) the regions may not exist at all for small η 's, for example for $\eta \leq 30$.

5.3 Robustness of $\eta\%$ -superconvergence regions: Effect of mesh-distortion ($K = I$)

To study the robustness of the superconvergence points with respect to distortions of the mesh we considered the Regular pattern with the central node displaced (see Fig. 13) and computed the maximum $\eta\%$ -error in the x_1 -derivative of the solution at the points with the same master-element coordinates as the superconvergence points in the undistorted mesh (given in Table 1a) i.e.

(5.2)

$$\bar{\eta}^{\%}(\bar{\tilde{\omega}}') := \max_{Q \in Q^H} \Theta\left(\bar{\tilde{\omega}}'; \frac{\partial u}{\partial x_1}; I; Q, x^p, 1, \bar{\tau}'\right), \quad \bar{\tilde{\omega}}' = \mathcal{F}(\bar{\tilde{\omega}}), \quad \bar{\tilde{\omega}} \in \mathcal{X}_{\frac{\partial u}{\partial x_1}}^{\text{sup}}(Q^H; I; \bar{\tau}, \bar{T})$$

where $\bar{\tau}' = \mathcal{F}(\bar{\tau})$ and $\mathcal{F} : \bar{T} \rightarrow \bar{T}'$ denotes the transformation from the undistorted master-mesh \bar{T} to the distorted master-mesh \bar{T}' and $\mathcal{X}_{\frac{\partial u}{\partial x_1}}^{\text{sup}}(Q^H; I; \bar{\tau}, \bar{T})$ denotes the

set of superconvergence points in the undistorted pattern. The value of $\bar{\eta}\%$ was computed for both the class of harmonic and class of general solutions (Table 4), for quadratic elements.

In order to study the robustness of the $\eta\%$ -superconvergence regions with respect to distortions of the mesh, the regions $\tilde{\mathcal{R}}_{\frac{\partial u}{\partial x_1}}^{\eta\%}(Q^H; I; \bar{\tau}, \bar{T})$ were determined as a function of the mesh-distortion for periodic grids of quadratic elements in the Regular and Union-Jack patterns. In both patterns the central node was moved to (0.4, 0.4), (0.6, 0.6), (0.8, 0.9) from its position (0.5, 0.5) in the undistorted pattern, as shown in Fig. 13. The regions $\tilde{\mathcal{R}}_{\frac{\partial u}{\partial x_1}}^{\eta\%}(Q^H; I; \bar{\tau}, \bar{T})$ ($\eta = 10, 20, 30$) are given in Figs. 14, 15 (Fig. 14 for the Regular pattern, and Fig. 15 for the Union-Jack pattern).

We make the following observations:

1. For both the classes of harmonic and general solutions, the $\eta\%$ -error at the points with master-coordinates corresponding to the superconvergence points in the undistorted pattern can vary from 2.5% to 100% when the pattern is distorted.
2. For small distortions of the pattern, i.e. when the central node is located at (0.4, 0.4) or at (0.6, 0.6) the regions for $\eta\%$ -error ($\eta = 10, 20, 30$) do not differ much from the regions in the undistorted pattern and there are big common regions for all the distorted meshes and the values of $\eta\%$ considered.
3. For large distortions of the pattern, i.e., when the central node is located at (0.8, 0.9) the common regions for all the distorted meshes exist only for large values of $\eta\%$ ($\eta \geq 30$).

5.4 Robustness of $\eta\%$ -superconvergence regions: Effect of grid-material orientation ($K \neq I$)

Given a mesh and an orthotropic material, we would like to find the $\eta\%$ -superconvergence region $\tilde{\mathcal{R}}_{F(u)}^{\eta\%}(Q^{H''}; \mathcal{M}; \bar{\tau}, \bar{T})$ for $F(u) = \frac{\partial u}{\partial x_1}$ or $q_1(u)$ which is common to a given class of orthotropic materials \mathcal{M} . We considered the Union-Jack pattern and quadratic elements and let $\eta\% = 25\%$. We assumed that $\frac{K_{\max}}{K_{\min}} = 2$ or 4 and we let angle θ of orientation of the principal plane of orthotropy with respect to the mesh vary from 0° to 90° . We use the notation

$$(5.3) \quad \mathcal{M}_r := \left\{ K = K(\theta) \mid \frac{K_{\max}}{K_{\min}} = r \text{ and } \theta \in [0, 90^\circ] \right\}$$

We determined the common regions $\tilde{\mathcal{R}}_{\frac{\partial x}{\partial x_1}}^{25\%}(Q^H; \mathcal{M}_2; \bar{\tau}, \bar{T})$ (shown in Fig. 16) and $\tilde{\mathcal{R}}_{\frac{\partial x}{\partial x_1}}^{25\%}(Q^H; \mathcal{M}_3; \bar{\tau}, \bar{T})$ (shown in Fig. 17). The common 25%-superconvergence regions were approximated by finding the intersections of the 25%-superconvergence regions for $\theta = 0^\circ, 15^\circ, 30^\circ, 45^\circ, 60^\circ, 75^\circ, 90^\circ$ as shown in Figs. 16, 17, 18. In Fig. 18 we give the common region $\tilde{\mathcal{R}}_{\frac{\partial x}{\partial x_1}}^{25\%}(Q^H; \mathcal{M}_4; \bar{\tau}, \bar{T})$. It can be seen that for $\frac{K_{\max}}{K_{\min}} = 2$ the common regions of 25% error, for the x_1 -derivative or the x_1 -components of the flux for all $\theta \in [0, 90^\circ]$, are of significant size with respect to the size of element. However, for $\frac{K_{\max}}{K_{\min}} = 4$ the common regions of 25% error, for the x_1 -derivative for all $\theta \in [0, 90^\circ]$, are small. It is clear that the 25%-common region will disappear for higher values of the ratio $\frac{K_{\max}}{K_{\min}}$.

5.5 Robustness of the $\eta\%$ -superconvergence regions: Effect of the surrounding mesh

Here we shall demonstrate that the $\eta\%$ -superconvergence regions and contours in an element τ are affected only by one or two surrounding layers of elements. We considered five 3×3 -cell periodic meshes $T_1 - T_5$, as shown in Fig. 19. We determined the regions $\tilde{\mathcal{R}}_{\frac{\partial x}{\partial x_1}}^{\eta\%}(Q^H; I; \bar{\tau}, \bar{T}_i)$ $i = 1, \dots, 5$, where $\eta = 10, 20, 30$ and for the elements of degree $p = 2, 3, 4$. The $\eta\%$ -superconvergence regions and the 0% contours are shown in Figs. 20-22. Fig. 23 displays the common region $\tilde{\mathcal{R}}_{\frac{\partial x}{\partial x_1}}^{25\%}(Q^H; I; \bar{\tau}, T)$, where $T = \{T_i\}_{i=1}^5$, (shaded gray) for the five 3×3 -cell meshes for $p = 2, 3$. Next, we added one layer of elements around the five 3×3 -cell meshes, to get the five 5×5 -cell meshes T'_i , $i = 1, \dots, 5$, as shown in Fig. 24. Figs. 25-27 display the regions $\tilde{\mathcal{R}}_{\frac{\partial x}{\partial x_1}}^{\eta\%}(Q^H; I; \bar{\tau}, T'_i)$, $i = 1, \dots, 5$, for $p = 2, 3, 4$. In Fig. 28 we show the common region $\tilde{\mathcal{R}}_{\frac{\partial x}{\partial x_1}}^{25\%}(Q^H; I; \bar{\tau}, T')$, where $T' = \{T'_i\}_{i=1}^5$, for the five 5×5 -cell meshes for $p = 2, 3$.

From the results we observe that:

1. The regions $\tilde{\mathcal{R}}_{\frac{\partial x}{\partial x_1}}^{\eta\%}(Q^H; I; \bar{\tau}, T_i)$, are essentially identical with the corresponding regions $\tilde{\mathcal{R}}_{\frac{\partial x}{\partial x_1}}^{\eta\%}(Q^H; I; \bar{\tau}, T'_i)$. However, the zero-contours for the x_1 -derivative of the error for the harmonic monomials are different for the corresponding grids T_i, T'_i , $i = 1, \dots, 5$.
2. The common regions $\tilde{\mathcal{R}}_{\frac{\partial x}{\partial x_1}}^{25\%}(Q^H; I; \bar{\tau}, T)$ and $\tilde{\mathcal{R}}_{\frac{\partial x}{\partial x_1}}^{25\%}(Q^H; I; \bar{\tau}, T')$ are, for all practical purposes, identical.

To see whether the mesh beyond two mesh-layers of elements affects the common $\eta\%$ -superconvergence region in element $\bar{\tau}$ and the zero-contours for the x_1 -derivative of the error for the basis monomials, we surrounded the 5×5 -cell mesh of Fig. 24e by 5 more layers of uniform elements to get the mesh T_s'' shown in Fig. 29. From Fig. 30 we can see that the $\eta\%$ -superconvergence regions $\tilde{\mathcal{R}}_{\frac{\partial x}{\partial x_1}}^{\eta\%}(Q^H; I; \bar{\tau}, T_s'')$ for the element $\bar{\tau}$ are identical to the corresponding contours and $\eta\%$ -superconvergence regions for the 5×5 -cell mesh T_s' . We also surrounded the 5×5 -cell mesh of Fig. 24e by 5 layers of distorted elements to obtain the mesh T_s''' , as shown in Fig. 31. From Fig. 32 we can observe that the regions $\tilde{\mathcal{R}}_{\frac{\partial x}{\partial x_1}}^{\eta\%}(Q^H; I; \bar{\tau}, T_s''')$ for the element $\bar{\tau}$ are practically identical to those for the 5×5 -mesh T_s' .

From the above examples we can conclude that: *The $\eta\%$ -superconvergence regions in element $\bar{\tau}$ are not affected, for all practical purposes, by the mesh outside the immediate 2 layers of elements surrounding the element.*

5.6 $\eta\%$ -superconvergence for general meshes

In order to demonstrate that the method of freezing the periodicity gives accurate prediction of the $\eta\%$ -superconvergence for general meshes we considered the following examples:

1. *An example which shows how the conclusions from the periodic grid translate to grids in finite domains.*

We considered a 5×5 mesh of Union-Jack cells surrounded by an arbitrary quasiuniform mesh generated by a remeshing algorithm. For the mesh and the mesh-cells shown in Figs. 33a-33c, we determined the $\eta\%$ -superconvergence regions for the x_1 -derivative of the error for cubic elements and the class of quartic harmonic polynomial solutions. In Figs. 34a-34c we give the $\eta\%$ -superconvergence regions for the x_1 -derivative for the mesh-cells shown (shaded gray) in Figs. 33a-33c, respectively. These regions were determined from the approximate solutions of Dirichlet boundary-value problems over the finite-domain using data obtained from the basis harmonic-monomials. Comparing Figs. 34a-34c (for the Union-Jack cells in the mesh which covers the finite-domain) with Fig. 7c which gives the $\eta\%$ -superconvergence regions for the periodic Union-Jack cell, we can observe only a slight-difference between the corresponding regions shown in Fig. 7c and Fig. 34c. This example indicates that the results on the $\eta\%$ -superconvergence regions obtained from the periodic cell hold, for all practical purposes, even for cells very close to the boundary of the periodic submesh.

2. *An example which demonstrates that the results obtained using the method of freezing the periodicity hold for arbitrary meshes and solutions which are not polynomials.*

We considered the mesh shown in Fig. 1 in the square domain $\Omega = (0, 1)^2$ and identified several elements in small mesh-cells enclosed in the interior of the mesh. The mesh-cells ω_0^h are shown in Figs. 35a-35c; in these Figures the mesh-cells are shaded gray. For each mesh-cell we isolated a corresponding submesh ω_3^h of the original grid which includes the mesh-cell ω_0^h and three mesh-layers around it; the submeshes ω_3^h are shown within the thick-line perigram in Figs. 35a-35c. Each one of the submeshes was scaled and completed to a square periodic-cell \tilde{c} , as shown in Figs. 36a-36c. We considered the class of the following four harmonic solutions:

$$(5.4a) \quad u_i(r_i, \theta_i) = r_i^{\alpha_i} \sin(\alpha_i \theta_i), \quad i = 1, \dots, 4,$$

$$(5.4b) \quad r_i^2 = (x_1 - x_1^i)^2 + (x_2 - x_2^i)^2, \quad \theta_i = \tan^{-1} \left(\frac{x_2 - x_2^i}{x_1 - x_1^i} \right).$$

The solutions are specified by the following parameters:

$$(5.5) \quad \begin{cases} (x_1^1, x_2^1) = (2., 0.), & \alpha_1 = \frac{3}{4}, & (x_1^2, x_2^2) = (1.5, 0.5), & \alpha_2 = \frac{2}{3}, \\ (x_1^3, x_2^3) = (0.5, 2.), & \alpha_3 = \frac{1}{2}, & (x_1^4, x_2^4) = (-3., 0.), & \alpha_4 = \frac{3}{5}. \end{cases}$$

We determined the common region $\tilde{\mathcal{R}}_{\frac{\partial \omega}{\partial \sigma_1}}^{25\%}(\mathcal{U}; I; \tau, T_h)$ from the actual mesh and $\tilde{\mathcal{R}}_{\frac{\partial \omega}{\partial \sigma_1}}^{25\%}(\mathcal{U}; I; \tilde{\tau}, \tilde{T})$ from the periodic meshes \tilde{T} obtained by freezing the periodicity locally, $\mathcal{U} = \{u_i\}_{i=1}^4$ for linear and quadratic elements. The regions $\tilde{\mathcal{R}}_{\frac{\partial \omega}{\partial \sigma_1}}^{25\%}(\mathcal{U}; I; \tilde{\tau}, \tilde{T})$ were obtained by solving Neumann boundary-value problems, using data from the exact solutions, over the entire domain Ω and using the mesh T_h of Fig. 1. The regions $\tilde{\mathcal{R}}_{\frac{\partial \omega}{\partial \sigma_1}}^{25\%}(\mathcal{U}; I; \tilde{\tau}, \tilde{T})$ were obtained by solving periodic boundary-value problems, using data obtained from the local Taylor-series expansion, over the periodic-cell and the periodic meshes of Fig. 36a-36c. In Figs. 37a-37c we give the region $\tilde{\mathcal{R}}_{\frac{\partial \omega}{\partial \sigma_1}}^{25\%}(\mathcal{U}; I; \tau, T_h)$ for linear elements while Figs. 38a-38c we show the corresponding regions $\tilde{\mathcal{R}}_{\frac{\partial \omega}{\partial \sigma_1}}^{25\%}(\mathcal{U}; I; \tilde{\tau}, \tilde{T})$ obtained from the solutions of the periodic boundary-value problems. In Figs. 39a-39c (resp. Figs. 40a-40b) we give the region $\tilde{\mathcal{R}}_{\frac{\partial \omega}{\partial \sigma_1}}^{25\%}(\mathcal{U}; I; \tau, T_h)$ (resp. $\tilde{\mathcal{R}}_{\frac{\partial \omega}{\partial \sigma_1}}^{25\%}(\mathcal{U}; I; \tilde{\tau}, \tilde{T})$) for quadratic elements.

We observe that the regions $\tilde{\mathcal{R}}_{\frac{\eta}{100}}^{25\%}(\mathcal{U}; I; \tau, T_h)$ obtained by using the solutions of the Neumann boundary-value problems over the entire grid practically coincide with the regions $\tilde{\mathcal{R}}_{\frac{\eta}{100}}^{25\%}(\mathcal{U}; I; \bar{\tau}, \bar{T})$ determined from the periodic boundary-value problems over the periodic meshes. Hence the method of freezing the periodicity gives results which hold for the practical grids.

5.7 Robustness of the $\eta\%$ -superconvergence points in practical computations.

Here we give an example which shows that $\eta\%$ -superconvergence points are robust and can be used to sample the solution in the interior of any grid used in practical computations. For the mesh-cell ω_0^h , shown shaded gray in Fig. 41, we determined the $\tilde{\mathcal{R}}_{\frac{\eta}{100}}^{\eta\%}(Q^H; I; \bar{\tau}, T_h)$ for $\eta = 10, 20, 30$, for $p = 1, 2, 3$. The $\eta\%$ -regions are shown in Fig. 42a, 42b, 42c for $p = 1, 2, 3$, respectively. We extracted some random sampling points within the 10%-regions for the x_1 -derivative of the solution for the class of harmonic solutions (as shown in Fig. 43) and we solved a Neumann boundary value problem over the mesh shown in Fig. 1, with the exact solution u_i and domain Ω^i given as:

$$(5.6a) \quad u_1(x_1, x_2) = \frac{1}{1.5^2 - (z + z_0)^2} + \frac{1}{1.5^2 + (z + z_0)^2} - \frac{1}{1.5^2 - 1.0} + \frac{1}{1.5^2 + 1.0}$$

where $z_0 = 0.5(1 + i)$, $\Omega^1 = (-0.5, 0.5)^2$, and

$$(5.6b) \quad u_2(x_1, x_2) = \operatorname{Re}((z - z_0)^{\frac{1}{2}})$$

where $z_0 = 0.5 + 2.0i$, $\Omega^2 = (0, 1)^2$.

For the two solutions given above we determined the relative error in the x_1 -derivative of the solution at the sampling points for $p = 1, 2$, as shown in Table 5a, 5b. From the results we observe that:

- (1) As p increases, the $\eta\%$ regions for the x_1 -derivative of the solution increase in size relative to the elements.
- (2) From the results shown in Table 5a, 5b, we can see that the relative error at the sampling points is less than 15% for the two solutions considered.

Thus, this example shows that from the $\eta\%$ -regions obtained from the computer-based approach of this paper we can extract *robust sampling points*, which can be used for any solution in the given class.

6 Summary of conclusions

1. The new concept of $\eta\%$ -superconvergence was introduced and the $\eta\%$ -superconvergence regions for various flux-quantities and for various classes of solutions and materials were defined.
2. The $\eta\%$ -superconvergence regions can be found for any mesh using a computer based-approach.
3. The $\eta\%$ -superconvergence regions for the x_1 -derivative were determined for four periodic patterns and it was observed that:
 - a. The regions always exist for sufficiently high η .
 - b. For fixed value of η the regions
 - (i) always exist for the class of harmonic solutions and grow in size relative to the element as the degree p of the elements is increased;
 - (ii) may not exist for the class of general solutions and shrink in size as the degree p of the elements is increased.

These observations can be expected to hold for periodic grids made by the repetition of any periodic pattern.

4. The $\eta\%$ -superconvergence regions can, for all practical purposes, be determined for any general finite element grid, like for example, the grids employed in practical engineering computations by using the technique of freezing the periodicity. Thus the new concept of $\eta\%$ -superconvergence can be employed to identify optimal sampling points for the flux-quantities in the interior of any practical grid.
5. We defined the common $\eta\%$ -superconvergence regions for entire classes of grids and materials. These regions can be determined numerically and can be used to identify robust sampling points for the flux-quantities of interest for entire classes of grids, solutions and materials.

References

1. L.A. OGANESYAN AND L.A. RUKHOVETS, *Study of the rate of convergence of variational difference schemes for second-order elliptic equations in a two-dimensional field with a smooth boundary*, U.S.S.R. Comput. Math. Math. Phys., 9 (1968), pp. 153-183.
2. J. DOUGLAS, JR., AND T. DUPONT, *Superconvergence for Galerkin methods for the two point boundary problem via local projections*, Numer. Math., 21 (1973), pp. 270-278.

3. J. DOUGLAS, JR., AND T. DUPONT, *Galerkin approximations for the two point boundary problem using continuous piecewise polynomial spaces*, Numer. Math., 22 (1974), pp. 99-109.
4. J. DOUGLAS, JR., T. DUPONT AND M.F. WHEELER, *An L^∞ estimate and a superconvergence result for a Galerkin method for elliptic equations based on tensor products of piecewise polynomials*, RAIRO Anal. Numér., 8 (1974), pp. 61-66.
5. T. DUPONT, *A unified theory of superconvergence for Galerkin methods for two-point boundary problems*, SIAM J. Numer. Anal., 13 (1976), pp. 362-368.
6. J.H. BRAMBLE AND A.H. SCHATZ, *Higher order local accuracy by averaging in the finite element method*, Math. Comp., 31 (1977), pp. 94-111.
7. V. THOMÉE *High order local approximations to derivatives in the finite element method*, Math. Comp. 31 (1977), pp. 652-660.
8. M. ZLÁMAL, *Superconvergence and reduced integration in the finite element method*, Math. Comp., 32 (1978), pp. 663-685.
9. P. LESAINTE AND M. ZLÁMAL, *Superconvergence of the gradient of finite element solutions*, RAIRO Anal. Numér., 13 (1979), pp. 139-166.
10. R.Z. DAUTOV, A.V. LAPIN AND A.D. LYASHKO, *Some mesh schemes for quasi-linear elliptic equations*, U.S.S.R. Comput. Math. Math. Phys., 20 (1980), pp. 62-78.
11. M. KŘÍŽEK AND P. NEITTAANMÄKI, *Superconvergence phenomenon in the finite element method arising from averaging gradients*, Numer. Math., 45 (1984), pp. 105-116.
12. N. LEVINE, *Superconvergent recovery of the gradient from piecewise linear finite-element approximations*, IMA J. Numer. Anal., 5 (1985), pp. 407-427.
13. M.F. WHEELER AND J.R. WHITEMAN, *Superconvergent recovery of gradients on subdomains from piecewise linear finite-element approximations*, Numer. Methods for PDEs, 3 (1987), pp. 65-82.
14. M.T. NAKAO, *Superconvergence of the gradient of Galerkin approximations for elliptic problems*, RAIRO Math. Model. Numer. Anal., 21 (1987), pp. 679-695.
15. M. KŘÍŽEK AND P. NEITTAANMÄKI, *On superconvergence techniques*, Acta Applic. Math., 9 (1987), pp. 175-198.
16. M. KŘÍŽEK AND P. NEITTAANMÄKI, *On a global superconvergence of the gradient of linear triangular elements*, J. Comput. Appl. Math., 18 (1987), pp. 221-233.
17. I. HLAVÁČEK AND M. KŘÍŽEK, *On a superconvergent finite element scheme for elliptic systems. I. Dirichlet boundary condition*, Aplik. Mat., 32 (1987), pp. 131-154.

18. I. HLAVÁČEK AND M. KŘÍŽEK, *On a superconvergent finite element scheme for elliptic systems. II. Boundary conditions of Newton's or Neumann's type*, Aplik. Mat., 32 (1987), pp. 200-213.
19. I. HLAVÁČEK AND M. KŘÍŽEK, *On a superconvergent finite element scheme for elliptic systems. III. Optimal interior estimates*, Aplik. Mat., 32 (1987), pp. 276-289.
20. A.B. ANDREEV AND R.D. LAZAROV, *Superconvergence of the gradient for quadratic triangular finite elements*, Numer. Methods for PDEs, 4 (1988), pp. 15-32.
21. Q.D. ZHU AND Q. LIN, *Superconvergence Theory of FEM*, Hunan Science Press, 1989.
22. G. GOODSSELL AND J.R. WHITEMAN, *A unified treatment of superconvergent recovered gradient functions for piecewise linear finite element approximations*, Internat. J. Numer. Methods Engrg., 27 (1989), pp. 469-481.
23. G. GOODSSELL AND J.R. WHITEMAN, *Pointwise superconvergence of recovered gradients for piecewise linear finite element approximations to problems of planar linear elasticity*, Numer. Methods for PDEs, 6 (1990), pp. 59-74.
24. G. GOODSSELL AND J.R. WHITEMAN, *Superconvergence of recovered gradients of piecewise quadratic finite element approximations. Part I: L_2 -error estimates*, Numer. Methods for PDEs, 7 (1991), pp. 61-83.
25. G. GOODSSELL AND J.R. WHITEMAN, *Superconvergence of recovered gradients of piecewise quadratic finite element approximations. Part II: L_∞ -error estimates*, Numer. Methods for PDEs, 7 (1991), pp. 85-99.
26. R. DURÁN, M.A. MUSCHIETTI AND R. RODRÍGUEZ, *On the asymptotic exactness of error estimators for linear triangular finite elements*, Numer. Math., 59 (1991), pp. 107-127.
27. R. DURÁN, M.A. MUSCHIETTI AND R. RODRÍGUEZ, *Asymptotically exact error estimators for rectangular finite elements*, SIAM J. Numer. Anal., 29 (1992), pp. 78-88.
28. I. BABUŠKA, T. STROUBOULIS, C.S. UPADHYAY AND S.K. GANGARAJ, *Study of superconvergence by numerical approach. Superconvergence of the gradient in finite element solutions of Laplace's and Poisson's equation*, in preparation.
29. I. BABUŠKA, T. STROUBOULIS, S.K. GANGARAJ AND C.S. UPADHYAY, *$\eta\%$ -superconvergence in the interior of locally refined meshes of quadrilaterals. Superconvergence of the gradient in finite element solutions of Laplace's and Poisson's equations*, in preparation.
30. B.A. SZABÓ AND I. BABUŠKA, *Finite Element Analysis*, John Wiley & Sons, Inc., New York, 1991.

31. J.A. NITSCHKE AND A.H. SCHATZ, *Interior estimates for Ritz-Galerkin methods*, Math. Comp. 28 (1974), pp. 937-958.
32. J.H. BRAMBLE, J.A. NITSCHKE AND A.H. SCHATZ, *Maximum-norm estimates for Ritz-Galerkin methods*, Math. Comp. 29 (1975), pp. 677-688.
33. A.H. SCHATZ AND L.B. WAHLBIN, *Interior maximum norm estimates for finite element methods*, Math. Comp. 31 (1977), pp. 414-442.
34. A.H. SCHATZ AND L.B. WAHLBIN, *Maximum norm estimates in the finite element method on plane polygonal domains. Part 1*, Math. Comp. 32 (1978), pp. 73-109.
35. A.H. SCHATZ AND L.B. WAHLBIN, *Maximum norm estimates in the finite element method on plane polygonal domains. Part 2, refinements*, Math. Comp. 33 (1979), pp. 465-492.
36. L.B. WAHLBIN, *Local behavior in finite element methods*, in: P.G. Ciarlet and J.L. Lions, eds., Handbook of Numerical Analysis, Vol. II (North-Holland, Amsterdam, 1991), pp. 357-522.
37. A.H. SCHATZ AND L.B. WAHLBIN, *Interior maximum norm estimates for finite element methods, Part II*, unpublished manuscript.
38. I. BABUŠKA, T. STROUBOULIS, A. MATHUR AND C.S. UPADHYAY, *Pollution error in the h -version of the finite-element method and the local quality of a-posteriori error estimators*, in preparation.

List of Figures

Fig. 1. Typical example of a general finite-element grid used in practical engineering computations. This grid was generated using a commercial mesh-generator for a problem with a material interface.

Fig. 2. (a) An example of a domain with a locally periodic subdomain in its interior which is covered exactly by a periodic array of h -cells; (b) A detailed depiction of the mesh $T_h(\mathfrak{s}^0, H)$ in the interior of the periodic mesh-subdomain $S(\mathfrak{s}^0, H)$. This grid is made by the periodic repetition of the h -scaled master mesh \tilde{T} ; (c) The master mesh \tilde{T} in the master-cell \tilde{c} .

Fig. 3. Extraction of a mesh cell ω_i^h and completion to a periodic mesh \tilde{T} in the periodic cell \tilde{c} (a) The grid (of Fig. 1) with the mesh-cell ω_i^h (with its perimeter shown in thick black line) and the mesh-cell ω_0^h (shaded gray); (b) The mesh-cell ω_i^h with the mesh-cell ω_0^h (shaded gray) in its interior; (c) The scaled mesh-cell ω_i^h embedded in a periodic mesh \tilde{T} .

Fig. 4. Periodic meshes of triangles with the elements τ shaded gray: (a) Regular pattern; (b) Chevron pattern; (c) Union-Jack pattern; (d) Criss-Cross pattern.

Fig. 5. $\eta\%$ -superconvergence regions for periodic meshes: The regions $\tilde{\mathcal{R}}_{\frac{\eta}{2},1}^{\eta\%}(Q^H; I; \tilde{\tau}, \tilde{T})$ for the levels $\eta = 10, 20, 30$, and the zero-contours $\tilde{\mathcal{C}}_{\frac{\eta}{2},1}^{0\%}(Q_i^H; I; \tilde{\tau}, \tilde{T})$, $i = 1, 2$, for the Regular pattern. (a) $p = 1$; (b) $p = 2$; (c) $p = 3$; (d) $p = 4$; (e) $p = 5$. The regions were determined using the simplified approach.

Fig. 6. $\eta\%$ -superconvergence regions for periodic meshes: The regions $\tilde{\mathcal{R}}_{\frac{\eta}{2},1}^{\eta\%}(Q^H; I; \tilde{\tau}, \tilde{T})$ for the levels $\eta = 10, 20, 30$, and the zero-contours $\tilde{\mathcal{C}}_{\frac{\eta}{2},1}^{0\%}(Q_i^H; I; \tilde{\tau}, \tilde{T})$, $i = 1, 2$, for the Chevron pattern. (a) $p = 1$; (b) $p = 2$; (c) $p = 3$; (d) $p = 4$; (e) $p = 5$. The regions were determined using the simplified approach.

Fig. 7. $\eta\%$ -superconvergence regions for periodic meshes: The regions $\tilde{\mathcal{R}}_{\frac{\eta}{2},1}^{\eta\%}(Q^H; I; \tilde{\tau}, \tilde{T})$ for the levels $\eta = 10, 20, 30$, and the zero-contours $\tilde{\mathcal{C}}_{\frac{\eta}{2},1}^{0\%}(Q_i^H; I; \tilde{\tau}, \tilde{T})$, $i = 1, 2$, for the Union-Jack pattern. (a) $p = 1$; (b) $p = 2$; (c) $p = 3$; (d) $p = 4$; (e) $p = 5$. The regions were determined using the simplified approach.

Fig. 8. $\eta\%$ -superconvergence regions for periodic meshes: The regions $\tilde{\mathcal{R}}_{\frac{\eta}{2},1}^{\eta\%}(Q^H; I; \tilde{\tau}, \tilde{T})$, for the levels $\eta = 10, 20, 30$, and the zero-contours

$\bar{\mathcal{R}}_{\frac{\eta\%}{20}}^{\eta\%}(Q_i^H; I; \bar{\tau}, \bar{T})$, $i = 1, 2$, for the Criss-Cross pattern. (a) $p = 1$; (b) $p = 2$; (c) $p = 3$; (d) $p = 4$; (e) $p = 5$. The regions were determined using the simplified approach.

Fig. 9. $\eta\%$ -superconvergence regions for periodic meshes: The regions $\bar{\mathcal{R}}_{\frac{\eta\%}{20}}^{\eta\%}(Q^G; I; \bar{\tau}, \bar{T})$, for the levels $\eta = 10, 20, 30$, for the Regular pattern. (a) $p = 1$; (b) $p = 2$; (c) $p = 3$. The regions were determined using the direct approach.

Fig. 10. $\eta\%$ -superconvergence regions for periodic meshes: The regions $\bar{\mathcal{R}}_{\frac{\eta\%}{20}}^{\eta\%}(Q^G; I; \bar{\tau}, \bar{T})$, for the levels $\eta = 10, 20, 30$, for the Chevron pattern. (a) $p = 1$; (b) $p = 3$. It should be noted that for $p = 2$ there is no region for $\eta\% \leq 30\%$. The regions were determined using the direct approach.

Fig. 11. $\eta\%$ -superconvergence regions for periodic meshes: The regions $\bar{\mathcal{R}}_{\frac{\eta\%}{20}}^{\eta\%}(Q^G; I; \bar{\tau}, \bar{T})$, for the levels $\eta = 10, 20, 30$, for the Union-Jack pattern. (a) $p = 2$; (b) $p = 3$. Note that for $p = 1$ there is no region $\eta\% \leq 30\%$.

Fig. 12. $\eta\%$ -superconvergence regions for periodic meshes: The regions $\bar{\mathcal{R}}_{\frac{\eta\%}{20}}^{\eta\%}(Q^G; I; \bar{\tau}, \bar{T})$, for the levels $\eta = 10, 20, 30$, for the Criss-Cross pattern. (a) $p = 1$; (b) $p = 2$; (c) $p = 3$. The regions were determined using the direct approach.

Fig. 13. Robustness of $\eta\%$ -superconvergence regions: Effect of mesh distortion. The undistorted patterns are given in the domain $(0, 1) \times (0, 1)$ with the central node located at $(0.5, 0.5)$. (a) Regular pattern with the central node at $(0.4, 0.4)$; (b) Regular pattern with the central node at $(0.5, 0.5)$; (c) Regular pattern with the central node at $(0.6, 0.6)$; (d) Regular pattern with the central node at $(0.8, 0.9)$; (e) Union-Jack pattern with the central node at $(0.4, 0.4)$; (f) Union-Jack pattern with central node at $(0.5, 0.5)$; (g) Union-Jack pattern with the central node at $(0.6, 0.6)$; (h) Union-Jack pattern with the central node at $(0.8, 0.9)$.

Fig. 14. Robustness of $\eta\%$ -superconvergence regions: Effect of mesh-distortion. Distorted Regular pattern, quadratic elements and cubic harmonic polynomial solutions. The regions $\bar{\mathcal{R}}_{\frac{\eta\%}{20}}^{\eta\%}(Q^H; I; \bar{\tau}, \bar{T})$ when the central node is at: (a) $(0.4, 0.4)$; (b) $(0.5, 0.5)$; (c) $(0.6, 0.6)$; (d) $(0.8, 0.9)$. The regions were determined using the direct approach.

Fig. 15. Robustness of $\eta\%$ -superconvergence regions: Effect of mesh-distortion; Distorted Union-Jack pattern, quadratic elements and cubic harmonic polynomial solutions. The regions $\bar{\mathcal{R}}_{\frac{\eta\%}{20}}^{\eta\%}(Q^H; I; \bar{\tau}, \bar{T})$ when the central node is at: (a) $(0.4, 0.4)$; (b) $(0.5, 0.5)$; (c) $(0.6, 0.6)$; (d) $(0.8, 0.9)$. The regions were determined using the direct approach.

Fig. 16. Robustness of $\eta\%$ -superconvergence regions: Effect of the grid-material orientation; Union-Jack pattern, quadratic elements and cubic "harmonic" polynomial solutions. The common region $\tilde{\mathcal{R}}_{\frac{\mathcal{Q}}{\mathcal{Q}_1}}^{25\%}(Q^H; \mathcal{M}_2; \bar{\tau}, \bar{T})$ for $\frac{K_{\max}}{K_{\min}} = 2$ and all grid-material orientations $\theta \in [0^\circ, 90^\circ]$.

Fig. 17. Robustness of $\eta\%$ -superconvergence regions: Effect of the grid-material orientation; Union-Jack pattern, quadratic elements and cubic "harmonic" polynomial solutions. The common region $\tilde{\mathcal{R}}_{\frac{\mathcal{Q}}{\mathcal{Q}_1(u)}}^{25\%}(Q^H; \mathcal{M}_2; \bar{\tau}, \bar{T})$ for $\frac{K_{\max}}{K_{\min}} = 2$ and all grid-material orientations $\theta \in [0^\circ, 90^\circ]$.

Fig. 18. Robustness of $\eta\%$ -superconvergence regions: Effect of the grid-material orientation; Union-Jack pattern, quadratic elements and cubic "harmonic" polynomial solutions. The common region $\tilde{\mathcal{R}}_{\frac{\mathcal{Q}}{\mathcal{Q}_1}}^{25\%}(Q^H; \mathcal{M}_4; \bar{\tau}, \bar{T})$ for $\frac{K_{\max}}{K_{\min}} = 4$ and all grid-material orientations $\theta \in [0^\circ, 90^\circ]$.

Fig. 19. Robustness of the $\eta\%$ -superconvergence regions: Effect of the surrounding mesh; The five 3×3 -cell meshes used with the element $\bar{\tau}$ subdomain shaded gray. (a) Mesh T_1 ; (b) Mesh T_2 ; (c) Mesh T_3 ; (d) Mesh T_4 ; (e) Mesh T_5 .

Fig. 20. Robustness of the $\eta\%$ -superconvergence regions: Effect of the surrounding mesh; Quadratic elements, cubic harmonic polynomial solutions. The regions $\tilde{\mathcal{R}}_{\frac{\mathcal{Q}}{\mathcal{Q}_1}}^{\eta\%}(Q^H; I; \bar{\tau}, \bar{T}_k)$ and the zero-contours $C_{\frac{\mathcal{Q}}{\mathcal{Q}_1}}^{0\%}(Q_i^H; I; \bar{\tau}, \bar{T}_k)$, $i = 1, 2$, for $k = 1, \dots, 5$, in the element $\bar{\tau}$ for the five 3×3 -cell meshes of Fig. 19. (a) Mesh T_1 ; (b) Mesh T_2 ; (c) Mesh T_3 ; (d) Mesh T_4 ; (e) Mesh T_5 .

Fig. 21. Robustness of the $\eta\%$ -superconvergence regions: Effect of the surrounding mesh; Cubic elements, quartic harmonic polynomial solutions. The regions $\tilde{\mathcal{R}}_{\frac{\mathcal{Q}}{\mathcal{Q}_1}}^{\eta\%}(Q^H; I; \bar{\tau}, \bar{T}_k)$ and the zero-contours $C_{\frac{\mathcal{Q}}{\mathcal{Q}_1}}^{0\%}(Q_i^H; I; \bar{\tau}, \bar{T}_k)$, $i = 1, 2$, for $k = 1, \dots, 5$, in the element $\bar{\tau}$ for the five 3×3 -cell meshes of Fig. 19. (a) Mesh T_1 ; (b) Mesh T_2 ; (c) Mesh T_3 ; (d) Mesh T_4 ; (e) Mesh T_5 .

Fig. 22. Robustness of the $\eta\%$ -superconvergence regions: Effect of the surrounding mesh; Quartic elements, quintic harmonic polynomial solutions. The regions $\tilde{\mathcal{R}}_{\frac{\mathcal{Q}}{\mathcal{Q}_1}}^{\eta\%}(Q^H; I; \bar{\tau}, \bar{T}_k)$ and the zero-contours $C_{\frac{\mathcal{Q}}{\mathcal{Q}_1}}^{0\%}(Q_i^H; I; \bar{\tau}, \bar{T}_k)$, $i = 1, 2$, for $k = 1, \dots, 5$, in the element $\bar{\tau}$ for the five 3×3 -cell meshes of Fig. 19. (a) Mesh T_1 ; (b) Mesh T_2 ; (c) Mesh T_3 ; (d) Mesh T_4 ; (e) Mesh T_5 .

Fig. 23. Robustness of the $\eta\%$ -superconvergence regions: Effect of the surrounding mesh; Elements of order p , harmonic polynomial solutions of degree $(p + 1)$.

The common region $\tilde{\mathcal{R}}_{\frac{\partial \Omega}{\partial x_1}}^{25\%}(Q^H; I; \bar{\tau}, \{\tilde{T}_i\}_{i=1}^5)$ from the various 3×3 -cell meshes for elements of degree p ; (a) $p = 2$; (b) $p = 3$.

Fig. 24. Robustness of the $\eta\%$ -superconvergence regions: Effect of the surrounding mesh; The five 5×5 -cell meshes (with the element $\bar{\tau}$ shaded gray) formed by surrounding the corresponding 3×3 -cell meshes of Fig. 19 by one layer of elements. (a) Mesh T'_1 ; (b) Mesh T'_2 ; (c) Mesh T'_3 ; (d) Mesh T'_4 ; (e) Mesh T'_5 .

Fig. 25. Robustness of the $\eta\%$ -superconvergence regions: Effect of the surrounding mesh; Quadratic elements, cubic harmonic solutions. The regions $\tilde{\mathcal{R}}_{\frac{\partial \Omega}{\partial x_1}}^{7\%}(Q^H; I; \bar{\tau}, \tilde{T}'_k)$ and the zero-contours $C_{\frac{\partial \Omega}{\partial x_1}}^{0\%}(Q^H_i; I; \bar{\tau}, \tilde{T}'_k)$, $i = 1, 2$, for $k = 1, \dots, 5$, in the element $\bar{\tau}$ for the five 5×5 -cell meshes of Fig. 24. (a) Mesh T'_1 ; (b) Mesh T'_2 ; (c) Mesh T'_3 ; (d) Mesh T'_4 ; (e) Mesh T'_5 .

Fig. 26. Robustness of the $\eta\%$ -superconvergence regions: Effect of the surrounding mesh; Cubic elements, quartic harmonic solutions. The regions $\tilde{\mathcal{R}}_{\frac{\partial \Omega}{\partial x_1}}^{7\%}(Q^H; I; \bar{\tau}, \tilde{T}'_k)$ and the zero-contours $C_{\frac{\partial \Omega}{\partial x_1}}^{0\%}(Q^H_i; I; \bar{\tau}, \tilde{T}'_k)$, $i = 1, 2$, for $k = 1, \dots, 5$, in the element $\bar{\tau}$ for the five 5×5 -cell meshes of Fig. 24. (a) Mesh T'_1 ; (b) Mesh T'_2 ; (c) Mesh T'_3 ; (d) Mesh T'_4 ; (e) Mesh T'_5 .

Fig. 27. Robustness of the $\eta\%$ -superconvergence regions: Effect of the surrounding mesh; Quartic elements, quintic harmonic solutions. The regions $\tilde{\mathcal{R}}_{\frac{\partial \Omega}{\partial x_1}}^{7\%}(Q^H; I; \bar{\tau}, \tilde{T}'_k)$ and the zero-contours $C_{\frac{\partial \Omega}{\partial x_1}}^{0\%}(Q^H_i; I; \bar{\tau}, \tilde{T}'_k)$, $i = 1, 2$, for $k = 1, \dots, 5$, in the element $\bar{\tau}$ for the five 5×5 -cell meshes of Fig. 24. (a) Mesh T'_1 ; (b) Mesh T'_2 ; (c) Mesh T'_3 ; (d) Mesh T'_4 ; (e) Mesh T'_5 .

Fig. 28. Robustness of the $\eta\%$ -superconvergence regions: Effect of the surrounding mesh; Elements of degree p , harmonic polynomial solutions of degree $(p + 1)$. The common region $\tilde{\mathcal{R}}_{\frac{\partial \Omega}{\partial x_1}}^{25\%}(Q; I; \bar{\tau}, \{\tilde{T}'_i\}_{i=1}^5)$ from the various 5×5 -cell meshes for elements of degree p ; (a) $p = 2$; (b) $p = 3$.

Fig. 29. Robustness of the $\eta\%$ -superconvergence regions: Effect of the surrounding mesh; Mesh \tilde{T}''_5 formed by surrounding the 5×5 -cell mesh \tilde{T}'_5 of Fig. 24e with 5 more layers of uniform elements. The element $\bar{\tau}$ is shown shaded gray.

Fig. 30. Robustness of the $\eta\%$ -superconvergence regions: Effect of the surrounding mesh; Elements of degree p , harmonic polynomial solutions of degree $(p + 1)$. The regions $\tilde{\mathcal{R}}_{\frac{\partial \Omega}{\partial x_1}}^{7\%}(Q^H; I; \bar{\tau}, \tilde{T}''_5)$ and the zero-contours $C_{\frac{\partial \Omega}{\partial x_1}}^{0\%}(Q^H_i; I; \bar{\tau}, \tilde{T}''_5)$, $i = 1, 2$, for the mesh shown in Fig. 29. (a) $p = 2$; (b) $p = 3$; (c) $p = 4$.

Fig. 31. Robustness of the $\eta\%$ -superconvergence regions: Effect of the surrounding mesh; Mesh formed \tilde{T}_5^m by surrounding the 5×5 -cell mesh \tilde{T}_5^l of Fig. 24c with 5 more layers of distorted elements. The element $\tilde{\tau}$ is shown shaded gray.

Fig. 32. Robustness of the $\eta\%$ -superconvergence regions: Effect of the surrounding mesh; Elements of degree p , harmonic polynomial solutions of degree $(p + 1)$. The regions $\tilde{\mathcal{R}}_{\frac{\partial}{\partial x_1}}^{\eta\%}(Q^H; I; \tilde{\tau}, \tilde{T}_5^m)$ and the zero-contours $C_{\frac{\partial}{\partial x_1}}^{0\%}(Q_i^H; I; \tilde{\tau}, \tilde{T}_5^m)$, $i = 1, 2$, for the mesh shown in Fig. 31. (a) $p = 2$; (b) $p = 3$; (c) $p = 4$.

Fig. 33. $\eta\%$ -superconvergence for general solutions and meshes: An arbitrary mesh T_h with a 5×5 -cell mesh of Union-Jack pattern embedded in it.
 (a) Union-Jack cell (shaded gray) in the center of the 5×5 periodic submesh;
 (b) Union-Jack cell (shaded gray) off-center of the 5×5 periodic submesh;
 (c) Union-Jack cell (shaded gray) at the boundary of the 5×5 periodic submesh.

Fig. 34. $\eta\%$ -superconvergence for general solutions and meshes; Cubic elements, quartic harmonic solution. The regions $\tilde{\mathcal{R}}_{\frac{\partial}{\partial x_1}}^{\eta\%}(Q^H; I; \tau, T_h)$ and the zero-contours $C_{\frac{\partial}{\partial x_1}}^{0\%}(Q_i^H; I; \tau, T_h)$, $i = 1, 2$. (a) Union-Jack cell shown in Fig. 33a; (b) Union-Jack cell shown in Fig. 33b; (c) Union-Jack cell shown in Fig. 33c.

Fig. 35. $\eta\%$ -superconvergence for general solutions and meshes: The grid of Fig. 2 with the elements τ (shaded gray) and the mesh-cell ω_j^h . (a) Mesh-cell 1; (b) Mesh-cell 2; (c) Mesh-cell 3.

Fig. 36. $\eta\%$ -superconvergence for general solutions and meshes: Periodic cells enclosing the mesh-cells of Fig. 35. (a) Periodic cell enclosing mesh-cell 1; (b) Periodic cell enclosing mesh-cell 2; (c) Periodic cell enclosing mesh-cell 3.

Fig. 37. $\eta\%$ -superconvergence for general solutions and meshes: Neumann boundary value problem over the domain and the actual mesh of Fig. 1; linear elements, harmonic solutions with point singularities outside the domain (see Section 5.6). The region $\tilde{\mathcal{R}}_{\frac{\partial}{\partial x_1}}^{25\%}(\mathcal{U}; I; \tau, T_h)$ for the x_1 -derivative of the solution for (a) Elements τ in mesh-cell 1 (Fig. 35a); (b) Elements τ in mesh-cell 2 (Fig. 35b); (c) Elements τ in mesh-cell 3 (Fig. 35c).

Fig. 38. $\eta\%$ -superconvergence for general solutions and meshes: Periodic boundary value problem over the periodic cells of Fig. 36; linear elements, quadratic harmonic polynomial solutions obtained from a local Taylor-series expansion of the solutions with point singularities outside the domain (see Section 5.6). The region $\tilde{\mathcal{R}}_{\frac{\partial}{\partial x_1}}^{25\%}(Q^H; I; \tilde{\tau}, \tilde{T})$ for: (a) Elements τ in periodic-cell of Fig. 36a; (b) Elements τ in the periodic-cell of Fig. 36b; (c) Elements τ in the periodic-cell of Fig. 36c.

Fig. 39. $\eta\%$ -superconvergence for general solutions and meshes: Neumann boundary value problem over the actual mesh of Fig. 1; quadratic elements, harmonic solutions with point singularities outside the domain (see Section 5.6). The region $\tilde{\mathcal{R}}_{\frac{\eta}{2n+1}}^{25\%}(U; I; \tau, T_h)$ for: (a) Elements τ in mesh cell 1 (Fig. 35a); (b) Elements τ in mesh cell 2 (Fig. 35b); (c) Elements τ in mesh cell 3 (Fig. 35c).

Fig. 40. $\eta\%$ -superconvergence for general solutions and meshes: Periodic boundary value problem over the periodic cells of Fig. 36; quadratic elements, cubic harmonic polynomial solutions obtained from a local Taylor-series expansion of the solutions with point singularities outside the domain (see Section 5.6). The region $\tilde{\mathcal{R}}_{\frac{\eta}{2n+1}}^{25\%}(Q^H; I; \tilde{\tau}, \tilde{T})$ for: (a) Elements τ in periodic cell of Fig. 36a; (b) Elements τ in the periodic cell of Fig. 36b; (c) Elements τ in the periodic cell of Fig. 36c.

Fig. 41. Robustness of the $\eta\%$ -superconvergence points in practical computations: The mesh of Figure 1 with a mesh-cell ω_0^h (shown shaded gray) and the corresponding mesh-cell ω_s^h (enclosed by the thick-line perigram).

Fig. 42. Robustness of the $\eta\%$ -superconvergence points in practical computations: The mesh-cell ω_0^h with the regions $\tilde{\mathcal{R}}_{\frac{\eta}{2n+1}}^{\eta\%}(Q^H; I; \tau \tilde{T})$, for the levels $\eta = 10, 20, 30$, for elements of degree p . (a) $p = 1$; (b) $p = 2$; (c) $p = 3$.

Fig. 43. Robustness of the $\eta\%$ -superconvergence points in practical computations: Random sets of 10%-superconvergence points. The mesh-cell ω_0^h with the regions $\tilde{\mathcal{R}}_{\frac{\eta}{2n+1}}^{10\%}(Q^H; I; \tau \tilde{T})$ and the sampling points for elements of degree p . (a) $p = 1$; (b) $p = 2$.

Regular, Chevron, Union-Jack patterns					
Superconvergence points for the class of harmonic solutions					
The vertices of the triangle are at (0.0,0.0), (1.0,0.0), (1.0, 1.0)					
Points	$p = 1$	$p = 2$	$p = 3$	$p = 4$	$p = 5$
1	0.5000000000, 0.0000000000	0.2113248654, 0.0000000000	0.0000000000, 0.0000000000	0.0118976218, 0.0000000000	0.0000000000, 0.0000000000
2		0.7886751346, 0.0000000000	0.3752181980, 0.0858825088	0.2821230756, 0.0000000000	0.1726731646, 0.0000000000
3		0.7500000000, 0.0458758546	0.5000000000, 0.0000000000	0.7178769244, 0.0000000000	0.5000000000, 0.0000000000
4		0.7500000000, 0.4541241452	0.4715185566, 0.3241733208	0.9881023782, 0.0000000000	0.8273268354, 0.0000000000
5			1.0000000000, 0.0000000000	0.1195044522, 0.0224992688	1.0000000000, 0.0000000000
6			0.8638176260, 0.6824066036	0.7053452590, 0.0071869378	0.4640525316, 0.0103019842
7				0.3095295948, 0.2201118672	0.2328766474, 0.15749286240
8				0.6402277154, 0.5196142358	0.4734766188, 0.3874100850
9				0.9063362308, 0.7871241952	0.7356302926, 0.6425966766
10					0.9343659198, 0.7080184052

Table 1a. Classical superconvergence points for periodic meshes: Elements of degree p , class of harmonic solutions. The superconvergence points for the x_1 -derivative of the error and the class of harmonic solutions for $p = 1, 2, 3, 4, 5$ for the element τ (shaded gray in Fig. 4) for the Regular, Chevron, Union-Jack patterns.

Criss-Cross pattern					
Superconvergence points for the class of harmonic solutions					
The vertices of the triangle are at (0.0,0.0), (1.0,0.0), (0.5, 0.5)					
Points	$p = 1$	$p = 2$	$p = 3$	$p = 4$	$p = 5$
1	0.5000000000, 0.0000000000	0.2113248654, 0.0000000000	0.1464466094, 0.0000000000	0.0761088279, 0.0000000000	0.0488705882, 0.0000000000
2		0.7886751346, 0.0000000000	0.5000000000, 0.0000000000	0.3397707358, 0.0000000000	0.2355765633, 0.0000000000
3			0.8535533906, 0.0000000000	0.6602292641, 0.0000000000	0.5000000000, 0.0000000000
4			0.5000000000, 0.5000000000	0.9238911721, 0.0000000000	0.7544234366, 0.0000000000
5				0.5000000000, 0.4887686394	0.9511294118, 0.0000000000
6					0.5000000000, 0.0000000000

Table 1b. Classical superconvergence points for periodic meshes: Elements of degree p , class of harmonic solutions. The superconvergence points for the x_1 -derivative of the error and the class of harmonic solutions for $p = 1, 2, 3, 4, 5$ for the element τ_1 for the Criss-Cross pattern.

Criss-Cross pattern					
Superconvergence points for the class of harmonic solutions					
The vertices of the triangle are at (0.0,0.0), (1.0,0.0), (0.5, 0.5)					
Points	$p = 1$	$p = 2$	$p = 3$	$p = 4$	$p = 5$
1	0.5000000000, 0.5000000000	0.7886751346, 0.5000000000	0.8750000000, 0.2834936534	0.7621420044, 0.3163540210	0.8368698019, 0.2268165908
2			0.8750000000, 0.5000000000	0.9145863153, 0.3966634454	0.7540881642, 0.3397926069
3			0.8750000000, 0.7165063710	0.8970792676, 0.5000000000	0.6883014452, 0.3781734456
4			0.5000000000, 0.5000000000	0.9145863153, 0.6033365546	0.7811733816, 0.4582804499
5				0.7621420044, 0.6836459789	0.9334689552, 0.5000000000
6					0.7811733816, 0.5417195501
7					0.6883014452, 0.6218265544
8					0.7540881642, 0.6602073930
9					0.8368698019, 0.7731834092
10					0.5000000000, 0.5000000000
11					0.7760422930, 0.5000000000

Table 1c. Classical superconvergence points for periodic meshes: Elements of degree p , class of harmonic solutions. The superconvergence points for the x_1 -derivative of the error and the class of harmonic solutions for $p = 1, 2, 3, 4, 5$ for the element τ_2 for the Criss-Cross pattern.

Superconvergence points for the class of general solutions					
Regular pattern					
Points from Table 1a	$p = 1$	$p = 2$	$p = 3$	$p = 4$	$p = 5$
1	yes	yes	no	no	no
2		yes	no	no	no
3		no	yes	no	no
4		no	no	no	no
5			no	no	no
6			no	no	no
7				no	no
8				no	no
9				no	no
10					no

Table 2a. Classical superconvergence points for periodic meshes: Elements of degree p , $1 \leq p \leq 5$, class of general solutions. This Table indicates which of the superconvergence points for the class of harmonic solutions from Table 1a are also superconvergence points for the class of general solutions in element τ in the Regular pattern.

Superconvergence points for the class of general solutions					
Chevron pattern					
Points from Table 1a	$p = 1$	$p = 2$	$p = 3$	$p = 4$	$p = 5$
1	yes	no	no	no	no
2		no	no	no	no
3		no	yes	no	no
4		no	no	no	no
5			no	no	no
6			no	no	no
7				no	no
8				no	no
9				no	no
10					no

Table 2b. Classical superconvergence points for periodic meshes: Elements of degree p , $1 \leq p \leq 5$, class of general solutions. This Table indicates which of the superconvergence points for the harmonic solutions from Table 1a are also superconvergence points for the class of general solutions in element τ in the Chevron pattern.

Superconvergence points for the class of general solutions					
Union-Jack pattern					
Points from Table 1a	$p = 1$	$p = 2$	$p = 3$	$p = 4$	$p = 5$
1	no	no	no	no	no
2		no	no	no	no
3		no	no	no	no
4		no	no	no	no
5			no	no	no
6			no	no	no
7				no	no
8				no	no
9				no	no
10					no

Table 2c. Classical superconvergence points for periodic meshes: Elements of degree p , $1 \leq p \leq 5$, class of general solutions. This Table indicates which of the superconvergence points for the harmonic solutions from Table 1 are also superconvergence points for the class of general solutions in element τ_1 in the Union-Jack pattern.

Superconvergence points for the class of general solutions					
Criss-Cross pattern					
Points from Table 1b (For the element τ_1)	$p = 1$	$p = 2$	$p = 3$	$p = 4$	$p = 5$
1	yes	yes	no	no	no
2		yes	yes	no	no
3			no	no	no
4			no	no	no
5				no	no
6					no

Table 2d. Classical superconvergence points for periodic meshes: Elements of degree p , $1 \leq p \leq 5$, class of general solutions. This Table indicates which of the superconvergence points for the class harmonic solutions from Table 1b are also superconvergence points for the class of general solutions in element τ_1 in the Criss-Cross pattern.

Superconvergence points for the class of general solutions					
Criss-Cross pattern					
Points from Table 1c (For the element τ_2)	$p = 1$	$p = 2$	$p = 3$	$p = 4$	$p = 5$
1	no	no	no	no	no
2			no	no	no
3			no	no	no
4			no	no	no
5				no	no
6					no
7					no
8					no
9					no
10					no
11					no

Table 2e. Classical superconvergence points for periodic meshes: Elements of degree p , $1 \leq p \leq 5$, class of general solutions. This Table indicates which of the superconvergence points for the harmonic solutions from Table 1c are also superconvergence points for the class of general solutions in element τ_2 in the Criss-Cross pattern.

Robustness with respect to the type of solution					
$\bar{\eta}\%(\bar{x}) := \max_{Q \in Q^G} \Theta(\bar{x}; \frac{\partial x}{\partial x_1}; I; Q, z^p, 1, \bar{\tau})$					
Pattern	Regular	Chevron	Union-Jack	Criss-Cross (element τ_1)	Criss-Cross (element τ_2)
Points from Tables 1a, 1b, 1c	$\bar{\eta}\%$	$\bar{\eta}\%$	$\bar{\eta}\%$	$\bar{\eta}\%$	$\bar{\eta}\%$
1	00	100	27	00	18
2	00	100	27	00	
3	21	83	46		
4	25	53	100		

Table 3. Robustness of the superconvergence points with respect to the type of solution: Quadratic elements, cubic general polynomial solutions. Value of $\eta\%$ -error in the x_1 -derivative of the solution, at the various points corresponding to the superconvergence points for harmonic solutions.

Robustness with respect to the distortion of the mesh						
$\bar{\eta}\%(\bar{x}) := \max_{Q \in Q^H} \Theta(\bar{x}; \frac{\partial u}{\partial x_1}; I; Q, z^p, 1, \bar{\tau}'),$ $\bar{\tau}' = \mathcal{F}(\bar{\tau}), \quad \bar{x}' = \mathcal{F}(x)$						
Points from Table 1a	Mesh 1 (Fig. 14a)		Mesh 2 (Fig. 14c)		Mesh 3 (Fig. 14d)	
	Harmonic Solution	General Solution	Harmonic Solution	General Solution	Harmonic Solution	General Solution
	$\bar{\eta}\%$	$\bar{\eta}\%$	$\bar{\eta}\%$	$\bar{\eta}\%$	$\bar{\eta}\%$	$\bar{\eta}\%$
1	18.1	28.0	8.7	75.2	10.7	94.1
2	19.2	45.7	16.8	61.7	37.1	55.5
3	14.1	66.8	12.2	50.7	26.8	48.8
4	2.7	17.1	9.6	61.5	22.9	36.9

Table 4. Robustness of the superconvergence points with respect to the distortion of the mesh: Quadratic elements, cubic polynomial solutions. For the meshes of Fig. 13a, Fig. 13c, Fig. 13d, obtained by displacing the central node of the Regular pattern, the value of $\bar{\eta}\%$ -error for the x_1 -derivative of the error is given at the points in the element τ which correspond to the superconvergence points for the undistorted Regular pattern and the class of harmonic solutions, for: (a) Harmonic solutions; (b) General solutions.

$\eta\%$-error at a random set of 10%-superconvergence points		
$\eta\% = \Theta(\bar{x}; \frac{\partial u}{\partial x_1}; u, u_h, h, \tau) \cdot 100\%$		
Point	Value of $\eta\%$ for $u = u_1$	Value of $\eta\%$ for $u = u_2$
1	4.422	3.592
2	2.027	6.461
3	8.512	4.917
4	2.463	0.671
5	2.801	3.449
6	5.884	12.513
7	3.369	6.129
8	2.862	4.335
9	2.594	1.559
10	2.527	1.489
11	1.859	1.914
12	2.337	1.433
13	6.109	5.971
14	10.337	11.140
15	6.456	5.545
16	4.648	11.874
17	7.086	2.353
18	9.935	14.901
19	9.848	7.306
20	2.779	0.875
21	2.882	4.376
22	6.195	5.591

Table 5a. Robustness of the $\eta\%$ -superconvergence points in practical computations: Relative error at the 10%-superconvergence points for the x_1 -derivative for linear elements ($p = 1$). These points were randomly selected from the 10%-superconvergence regions, as shown in Fig. 43a.

$\eta\%$ -error at a random set of 10%-superconvergence points		
$\eta\% = \Theta(\bar{x}; \frac{\partial u}{\partial x_1}; u, u_h, h, \tau) \cdot 100\%$		
Point	Value of $\eta\%$ for $u = u_1$	Value of $\eta\%$ for $u = u_2$
1	11.936	2.963
2	8.743	0.094
3	4.372	6.474
4	0.582	5.564
5	4.585	1.350
6	0.053	6.036
7	2.086	6.719
8	1.944	6.918
9	7.722	0.882
10	5.030	6.854
11	5.764	0.962
12	5.331	0.705
13	4.308	0.852
14	1.447	7.988
15	6.811	2.824
16	6.317	3.555
17	6.956	0.047
18	8.101	2.136
19	7.564	4.765
20	6.637	0.570
21	3.569	1.081
22	5.423	1.578
23	8.373	0.432
24	7.065	5.188
25	1.589	5.472
26	4.162	1.309
27	7.696	0.494

Table 5b. Robustness of the $\eta\%$ -superconvergence points in practical computations: Relative error at the 10%-superconvergence points for the x_1 -derivative for quadratic elements ($p = 2$). These points were randomly selected from the 10%-superconvergence regions, as shown in Fig. 43b.

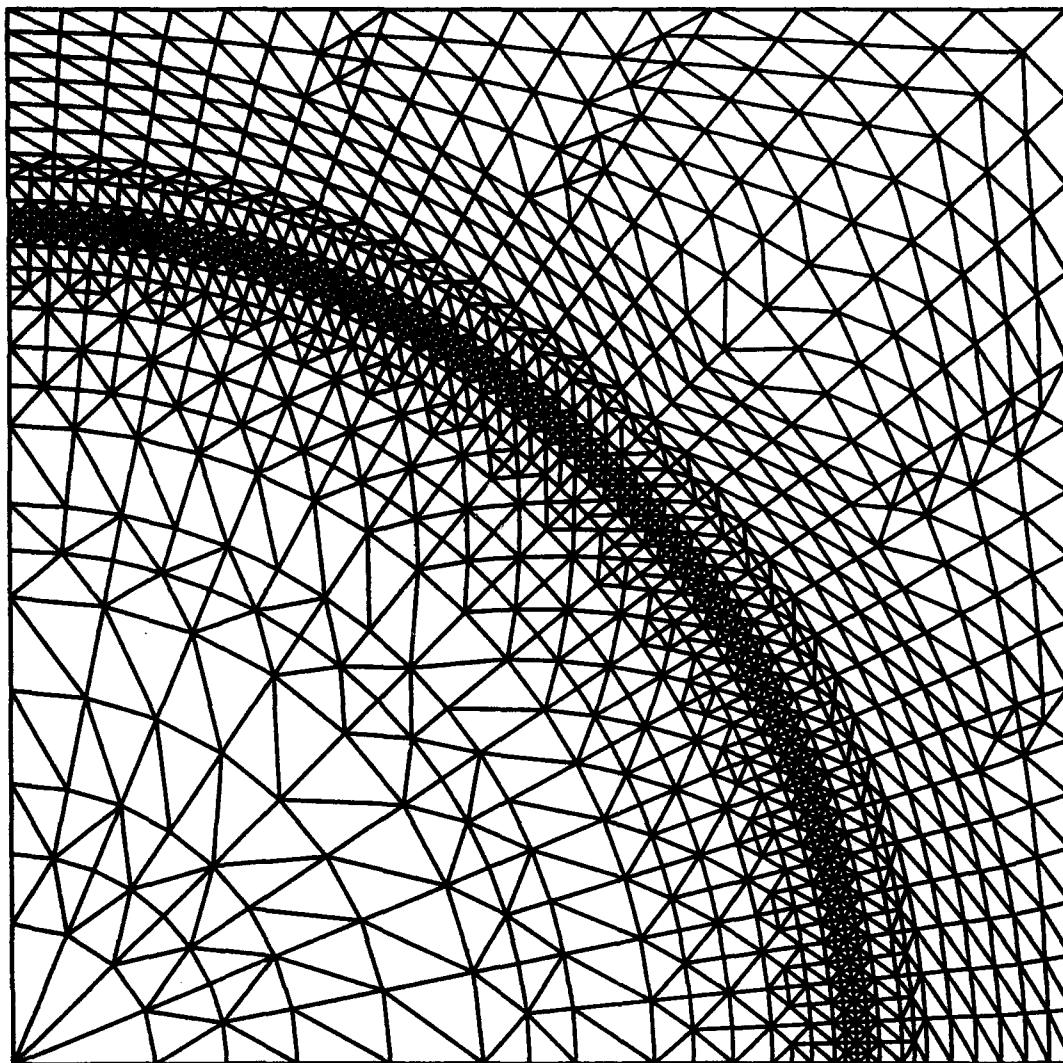


Fig. 1

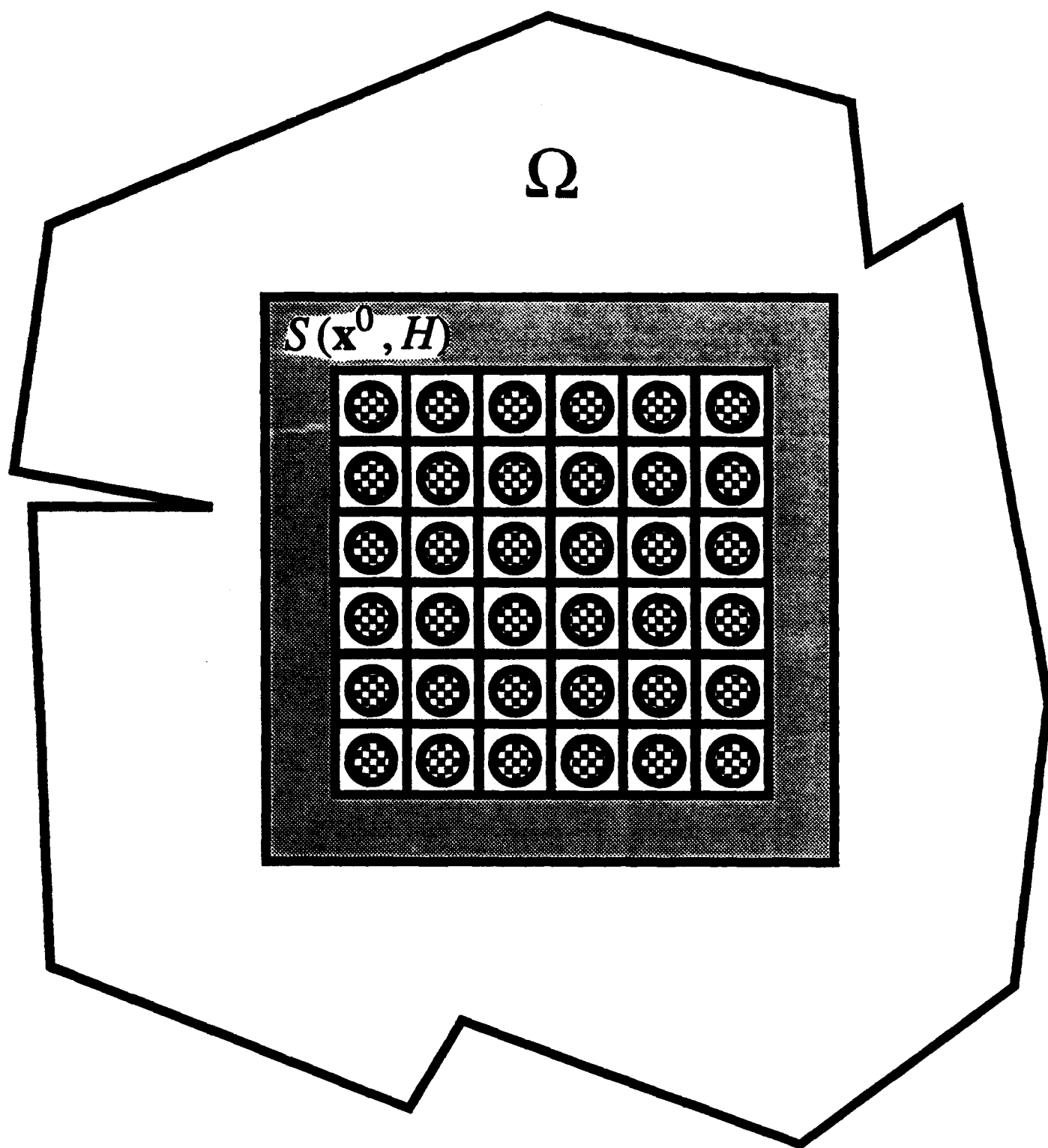


Fig. 2a

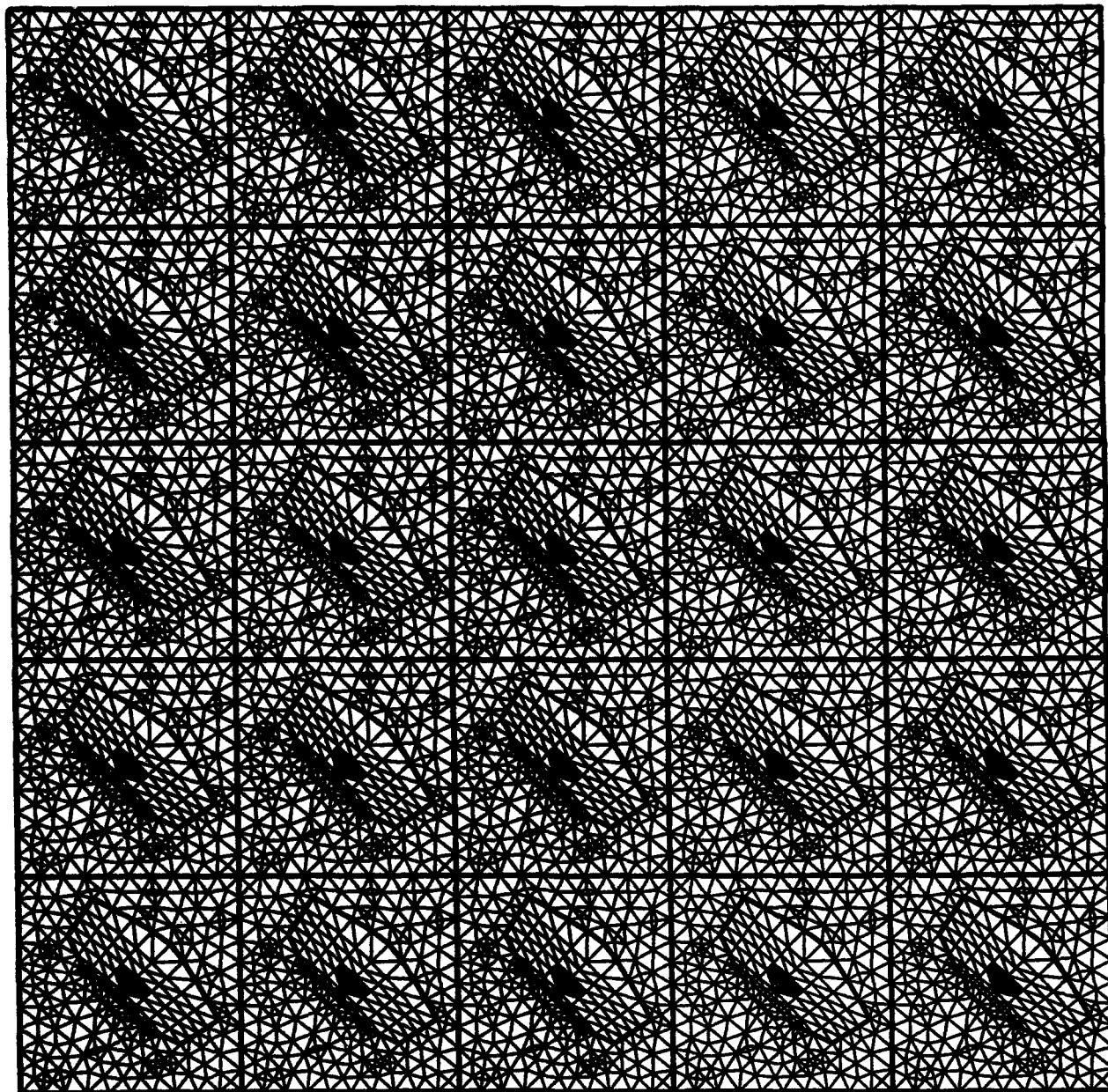


Fig. 2b

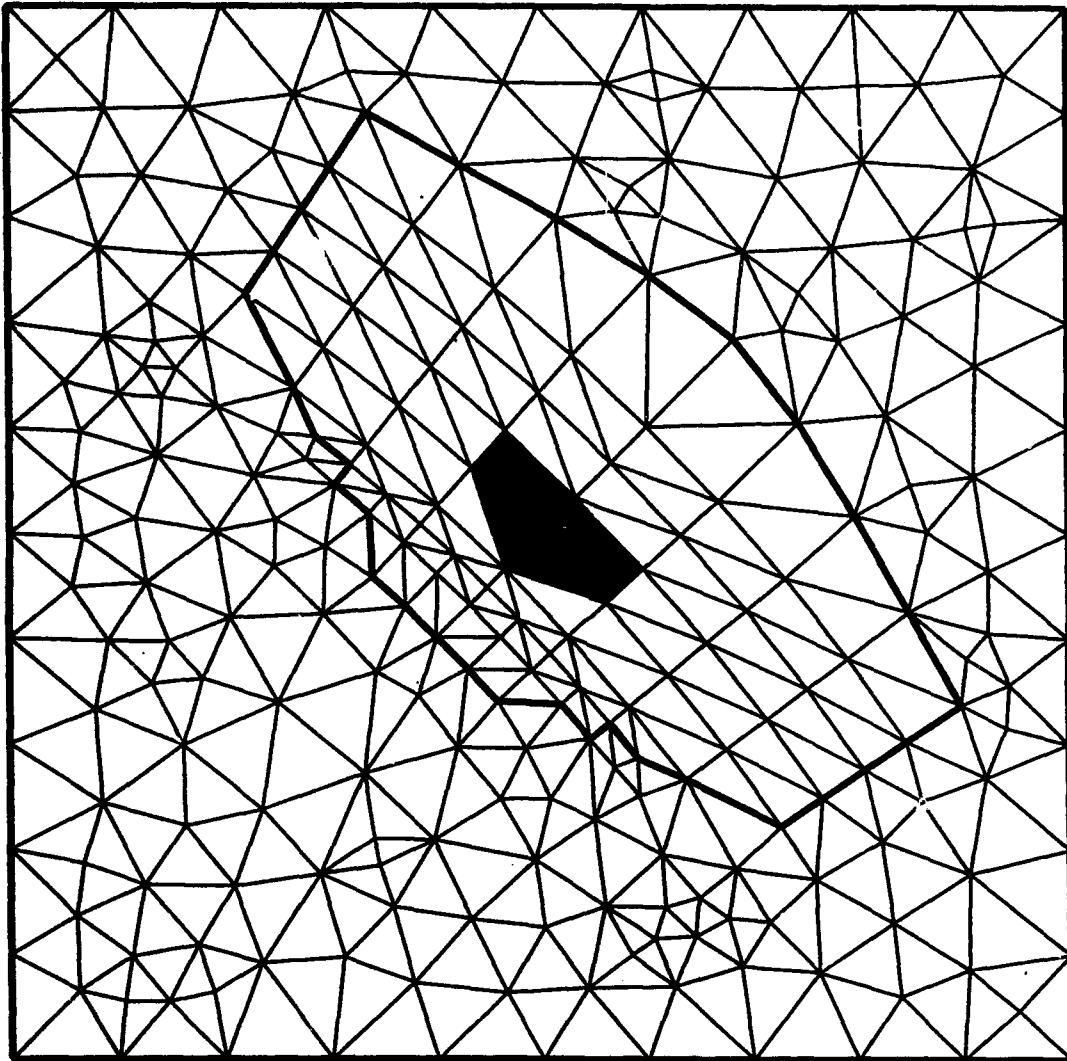


Fig.2c

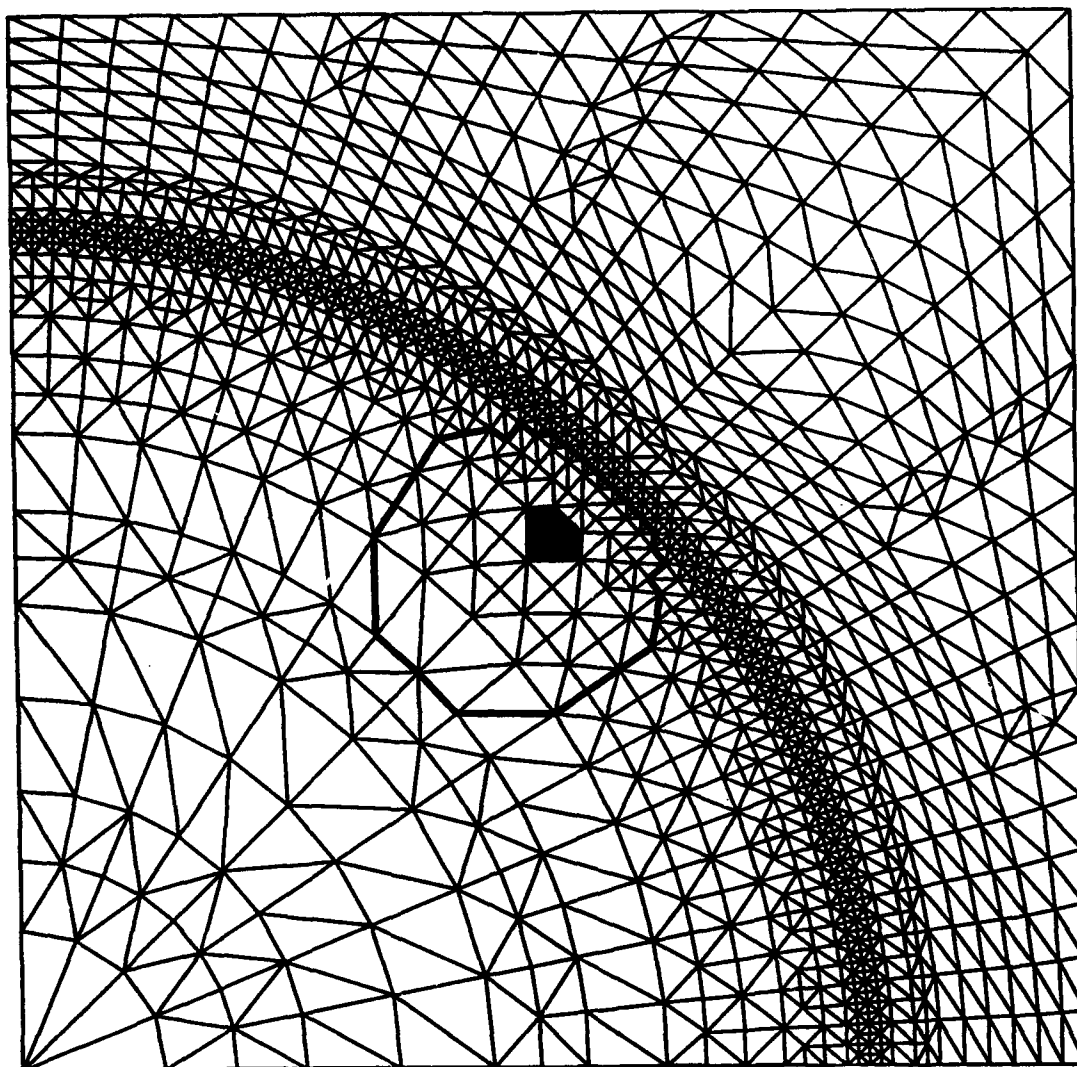


Fig. 3a

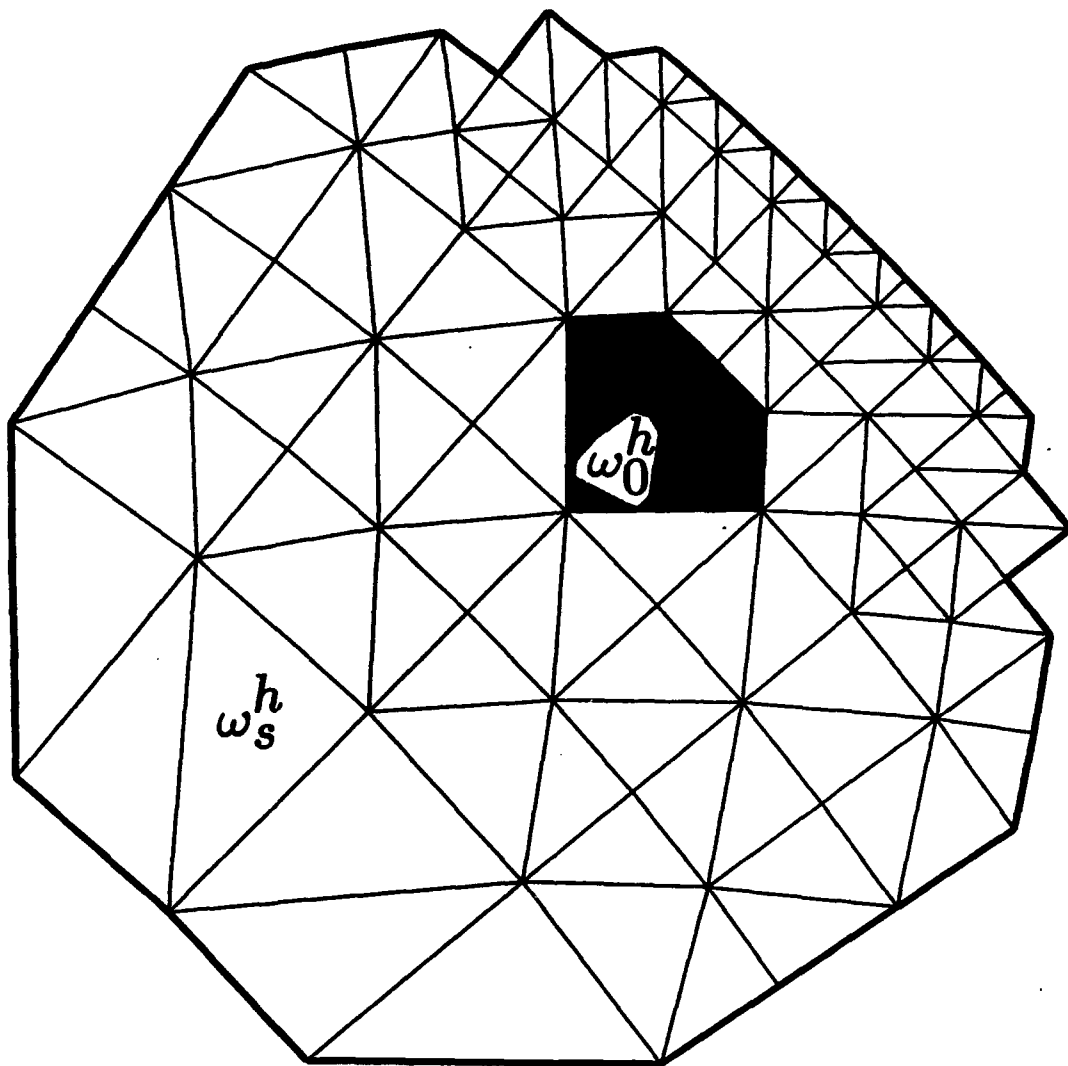


Fig. 3b

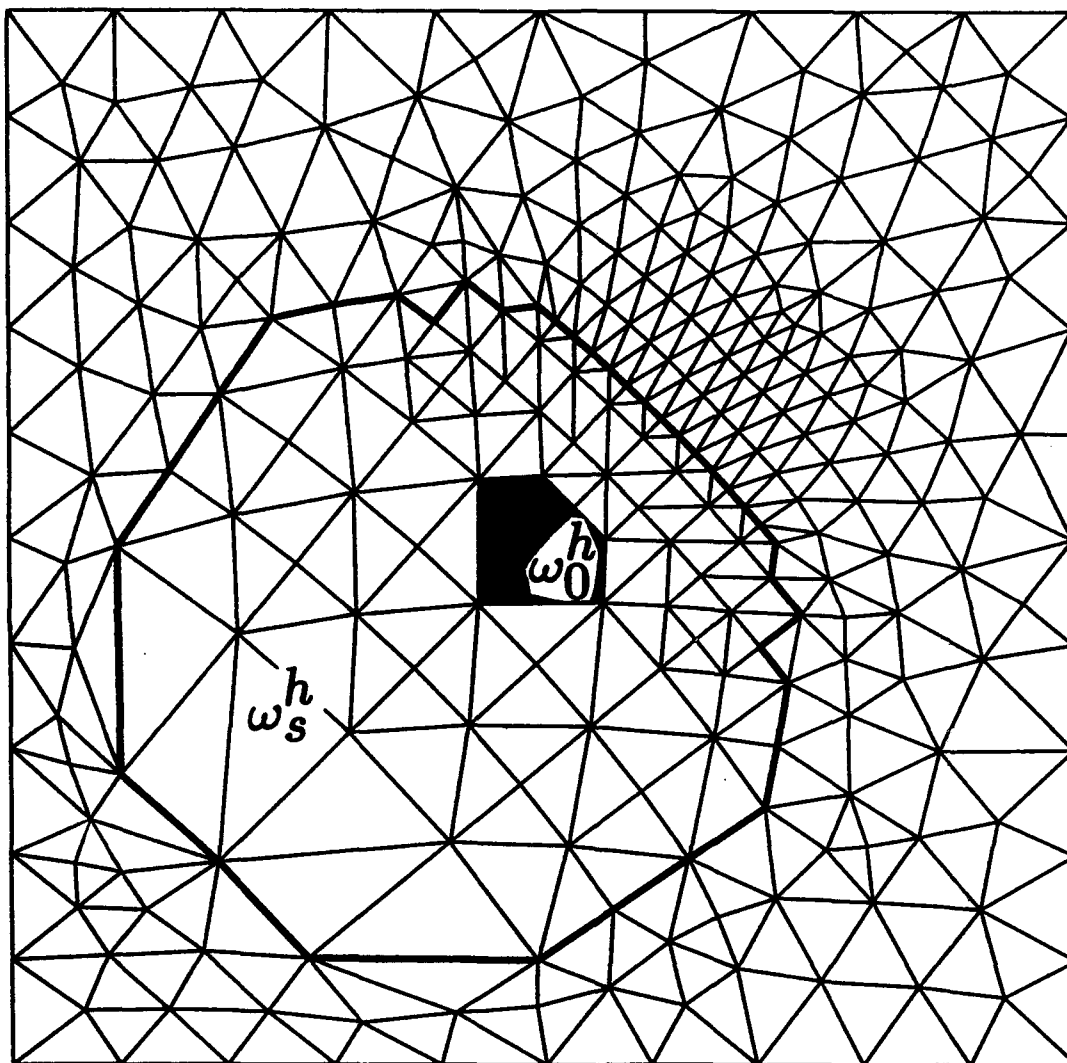


Fig. 3c

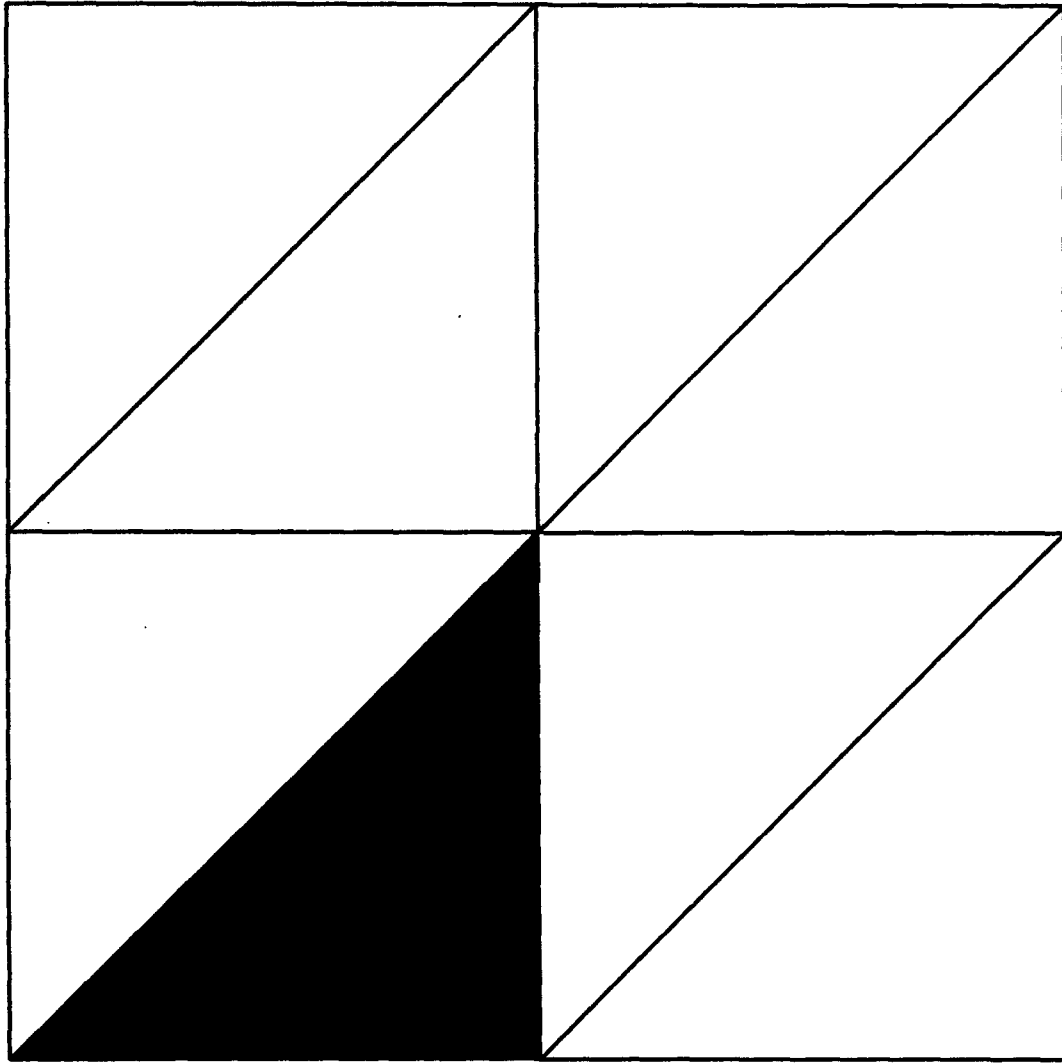


Fig. 4a

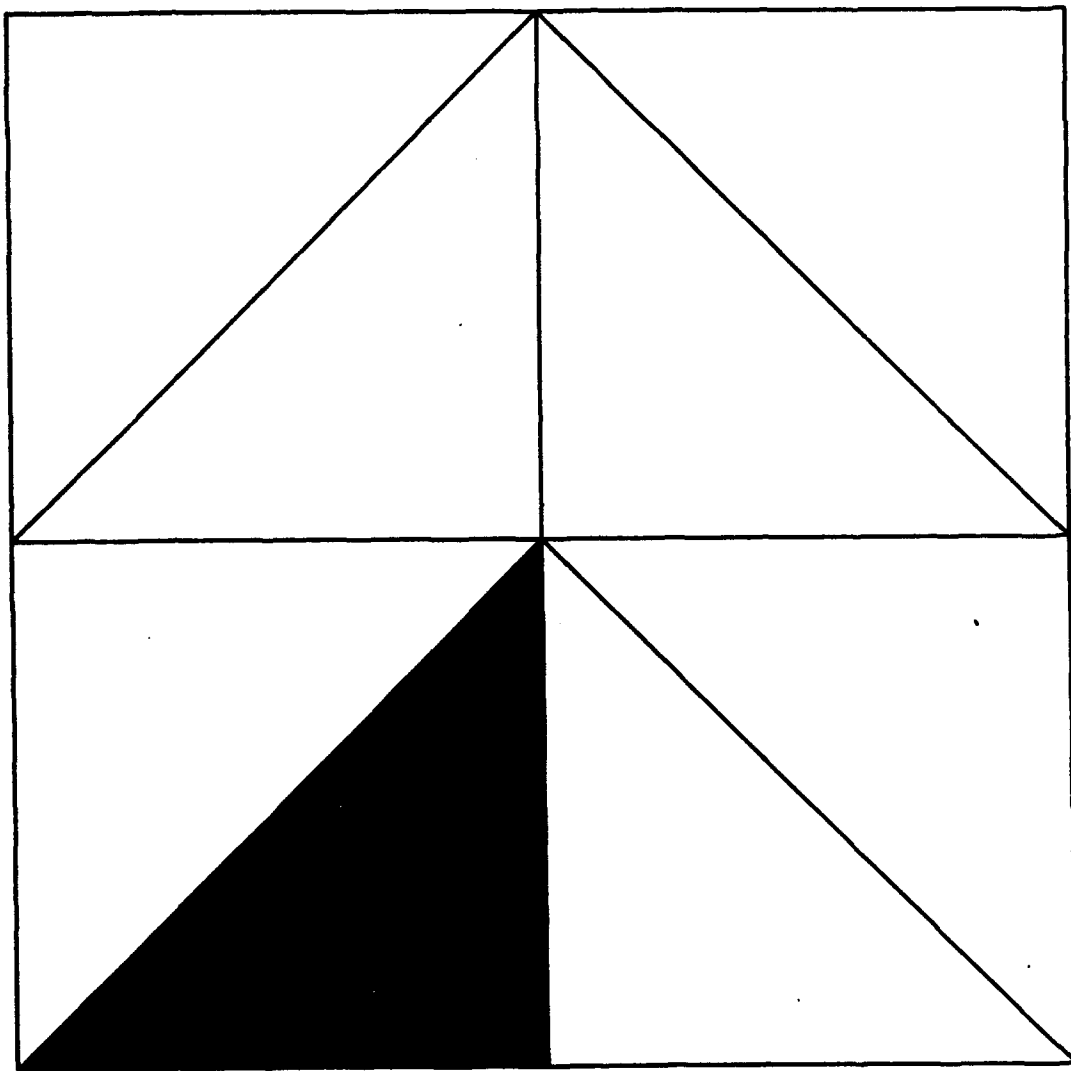


Fig. 4b

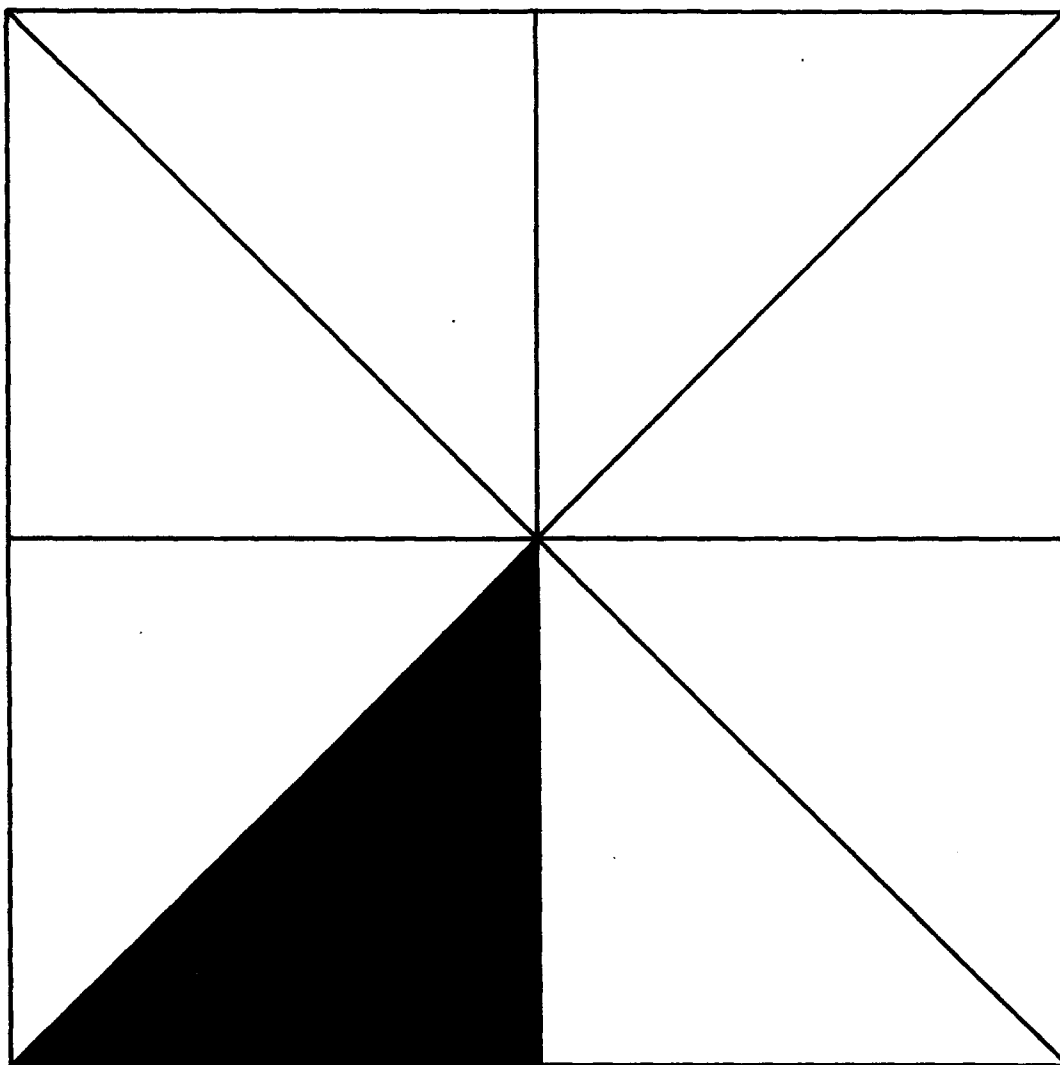


Fig. 4c

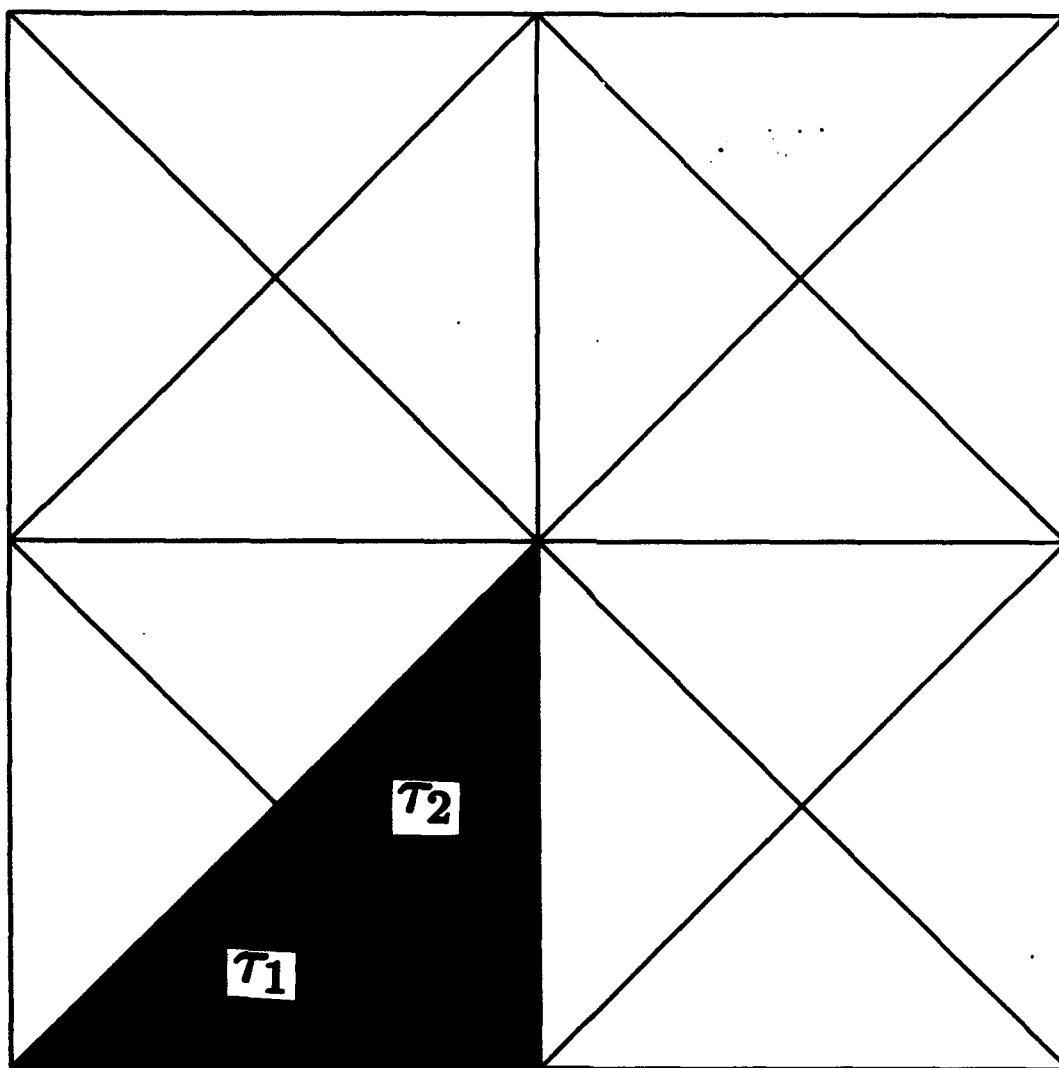
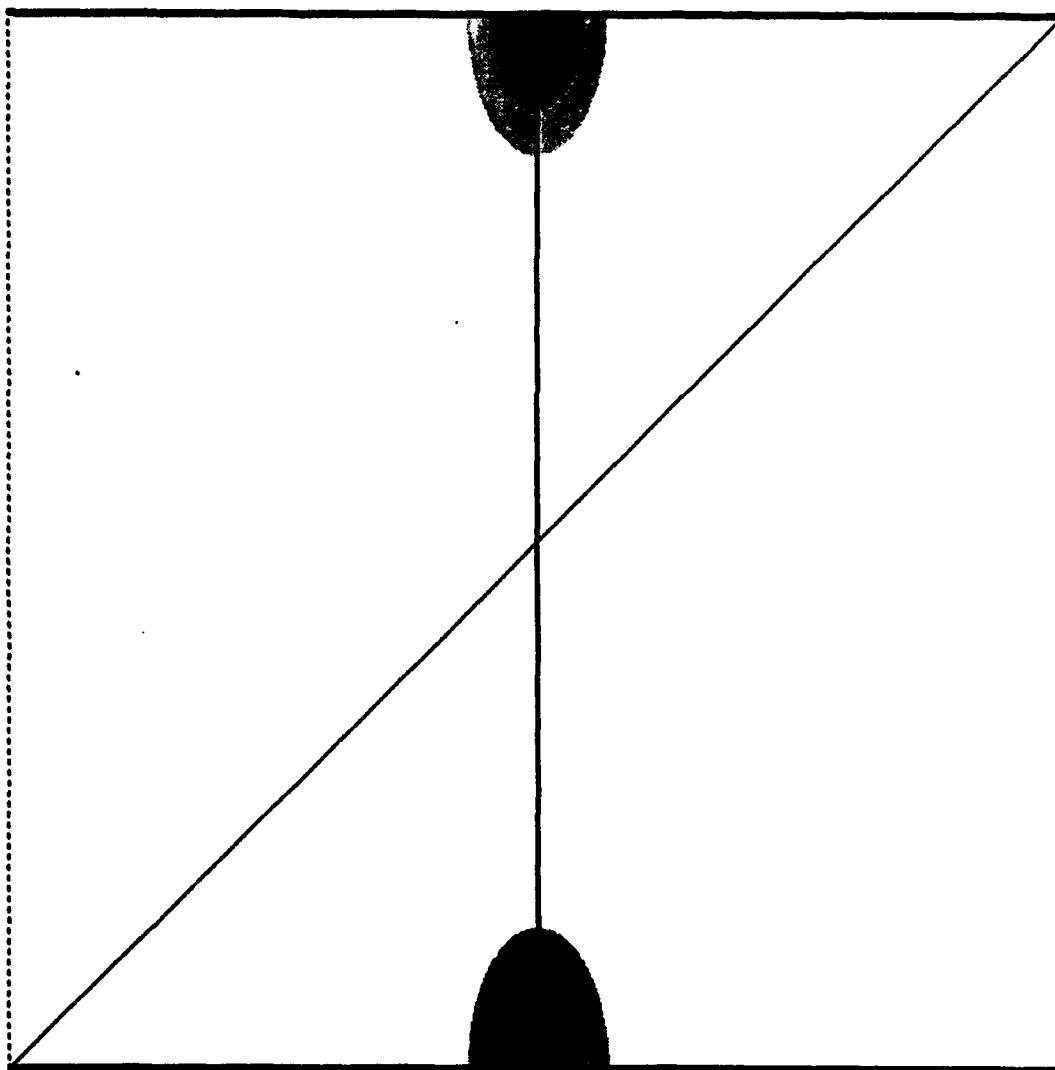


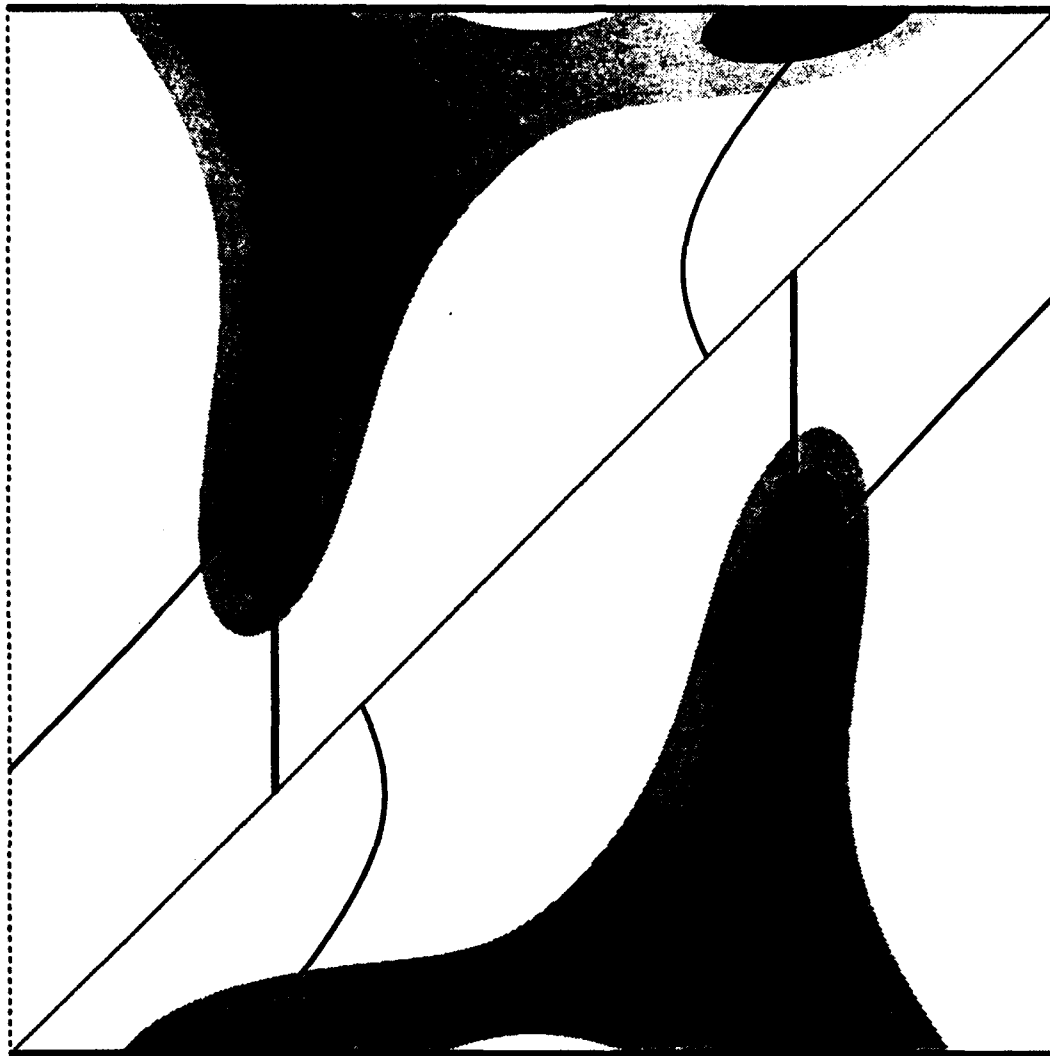
Fig. 4d



Harmonic solution $P = 1$
SIMPLIFIED L2 APPROACH

— *Function Q1*
 — *Function Q2*

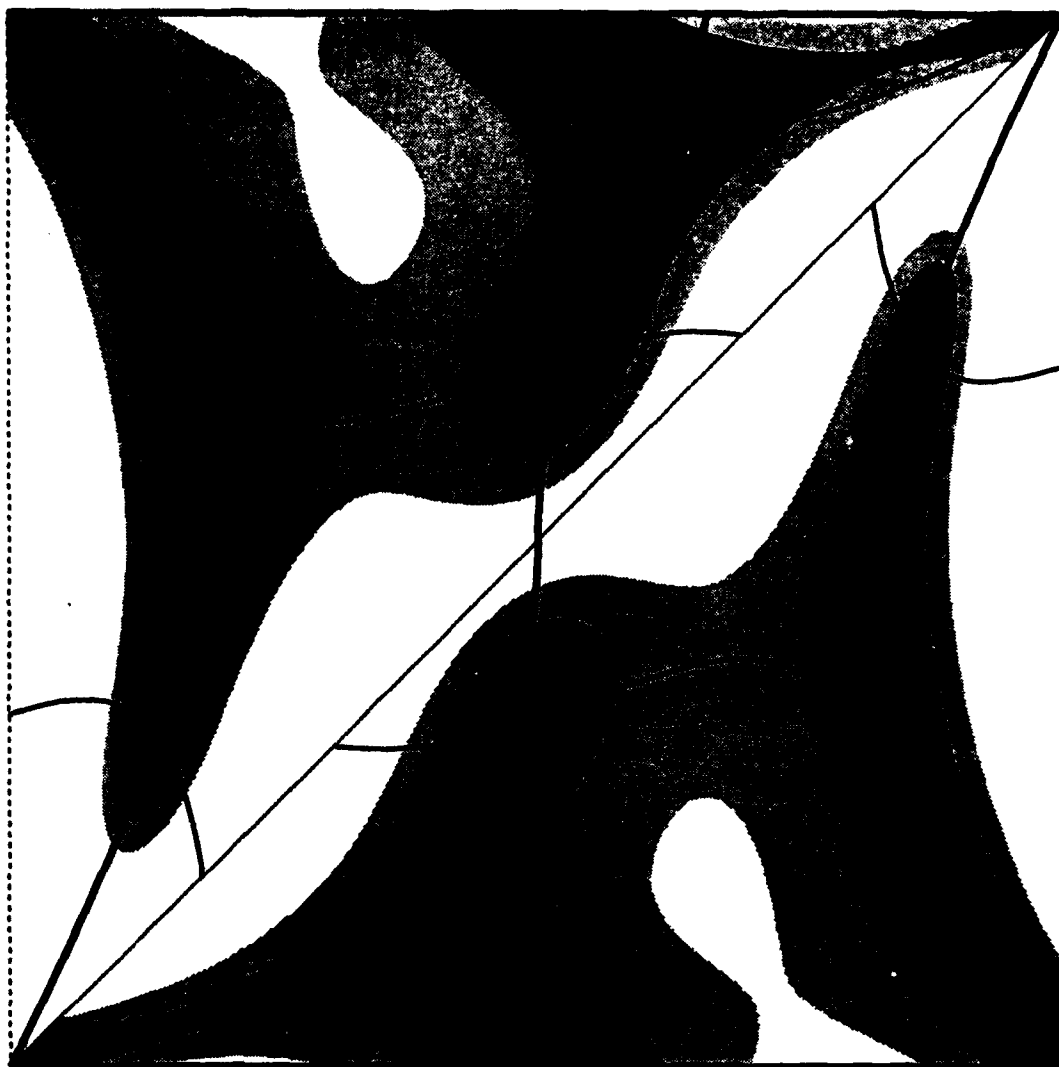
Fig. 5a



Harmonic solution **$P = 2$**
SIMPLIFIED L2 APPROACH

— ***Function Q1***
— ***Function Q2***

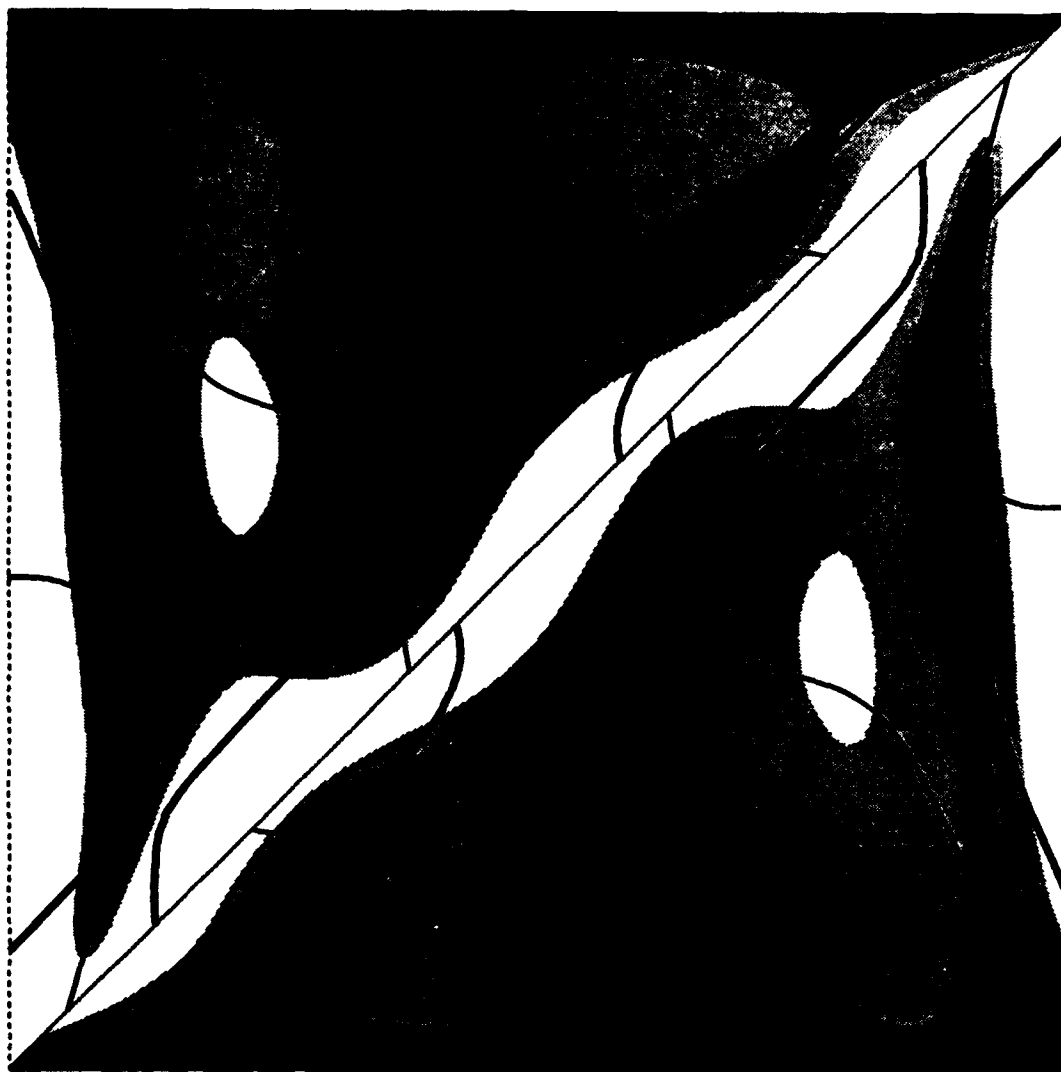
Fig. 5b



Harmonic solution $P = 3$
SIMPLIFIED L2 APPROACH

— *Function Q1*
 — *Function Q2*

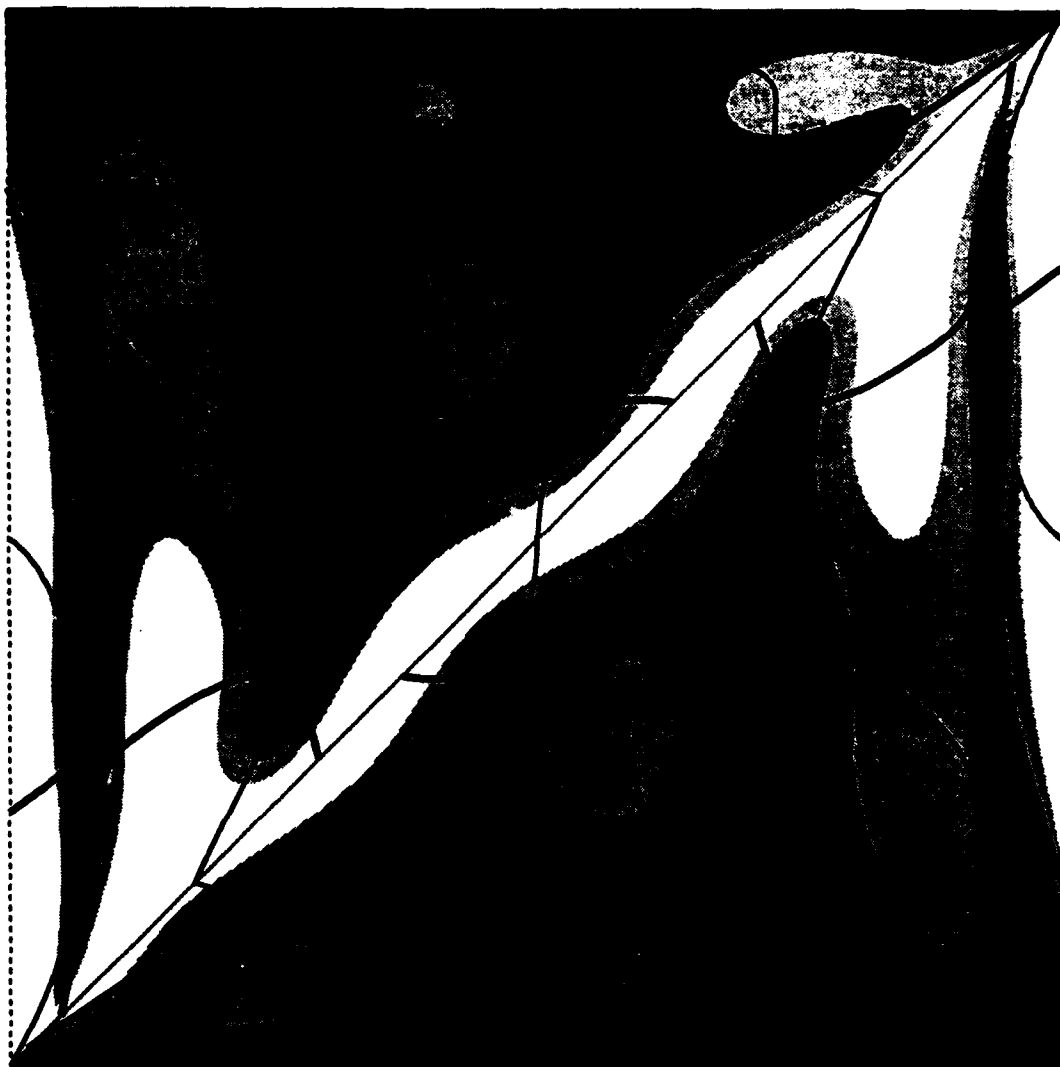
Fig. 5c



Harmonic solution $P = 4$
SIMPLIFIED L2 APPROACH

— *Function Q1*
 — *Function Q2*

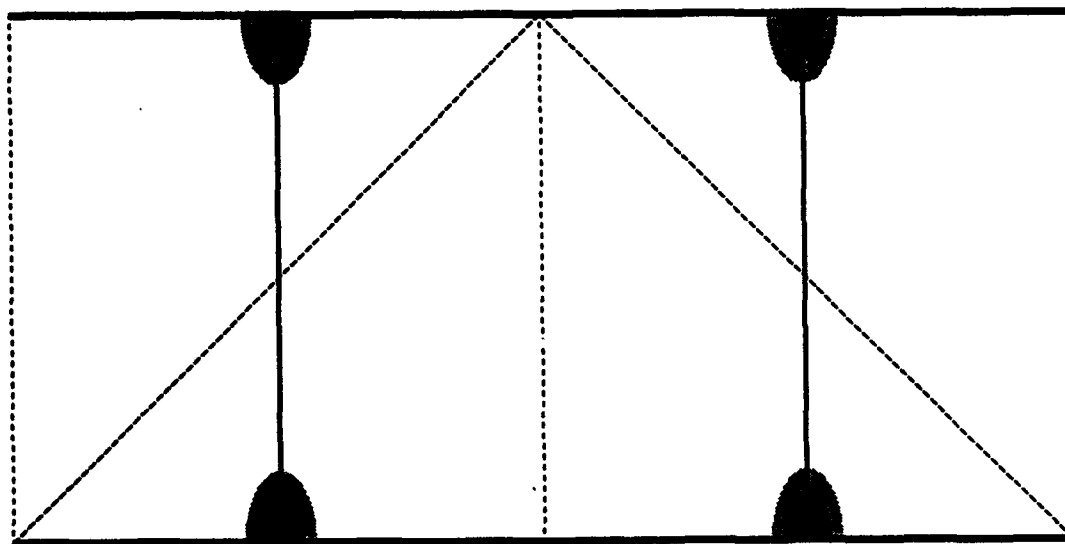
Fig. 5d



Harmonic solution $P = 5$
SIMPLIFIED L2 APPROACH

— *Function Q1*
— *Function Q2*

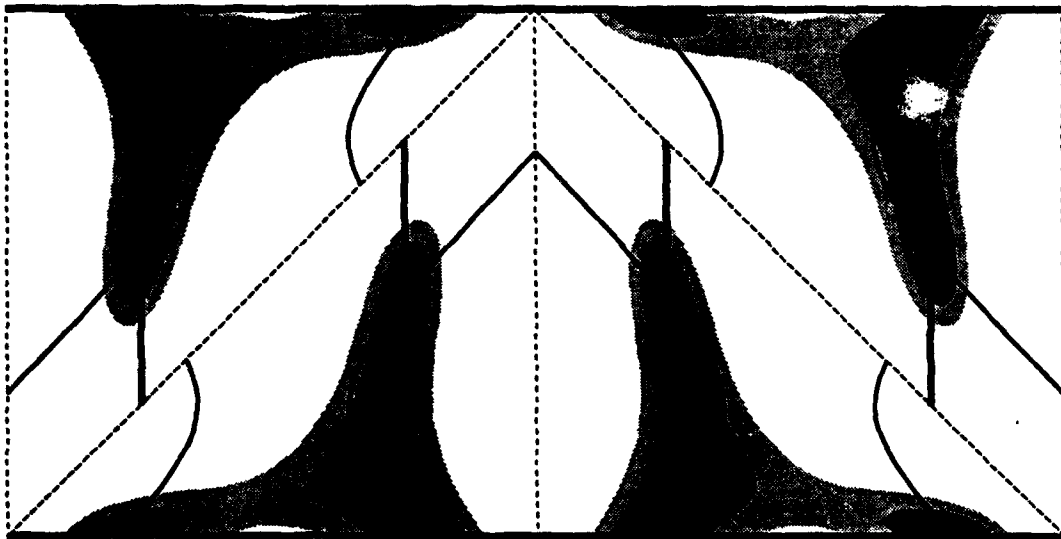
Fig.5e



Harmonic solution **P = 1**
SIMPLIFIED L2 APPROACH

— ***Function Q1***
 — ***Function Q2***

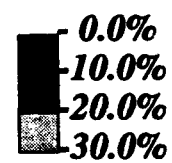
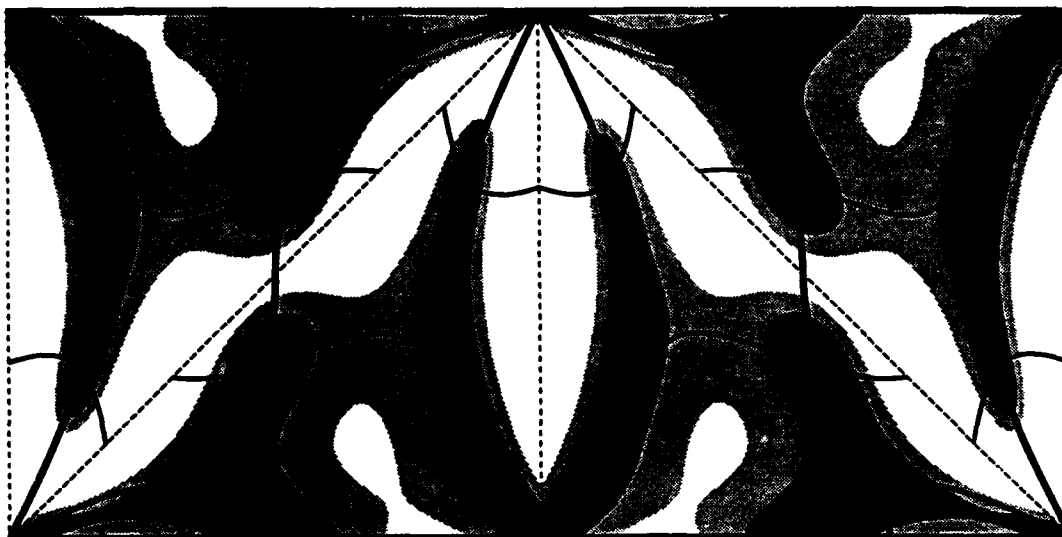
Fig. 6a



Harmonic solution $P = 2$
SIMPLIFIED L2 APPROACH

— *Function Q1*
 - - - *Function Q2*

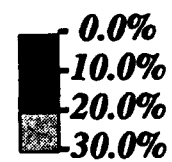
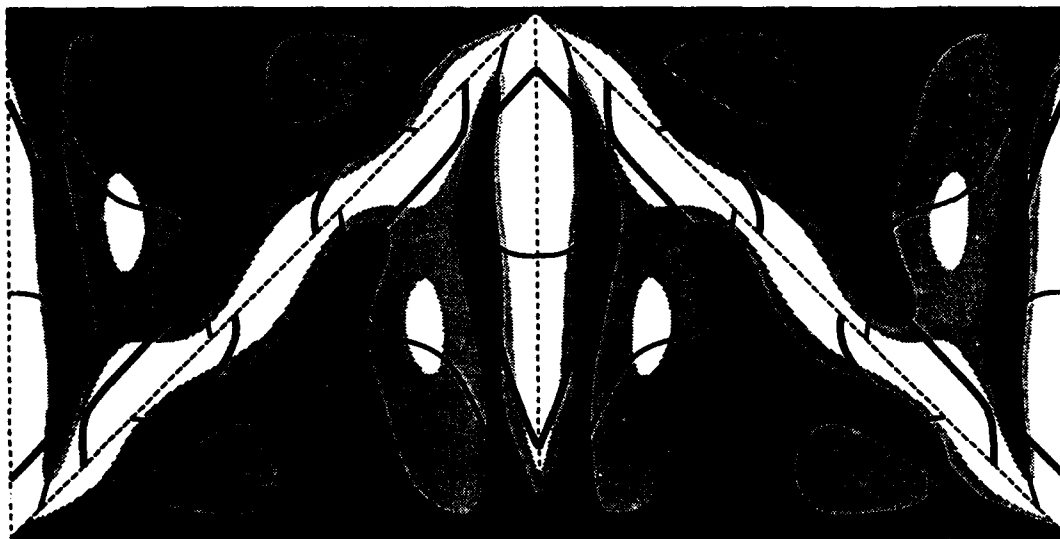
Fig. 6b



Harmonic solution $P = 3$
SIMPLIFIED L2 APPROACH

— *Function Q1*
— *Function Q2*

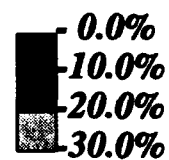
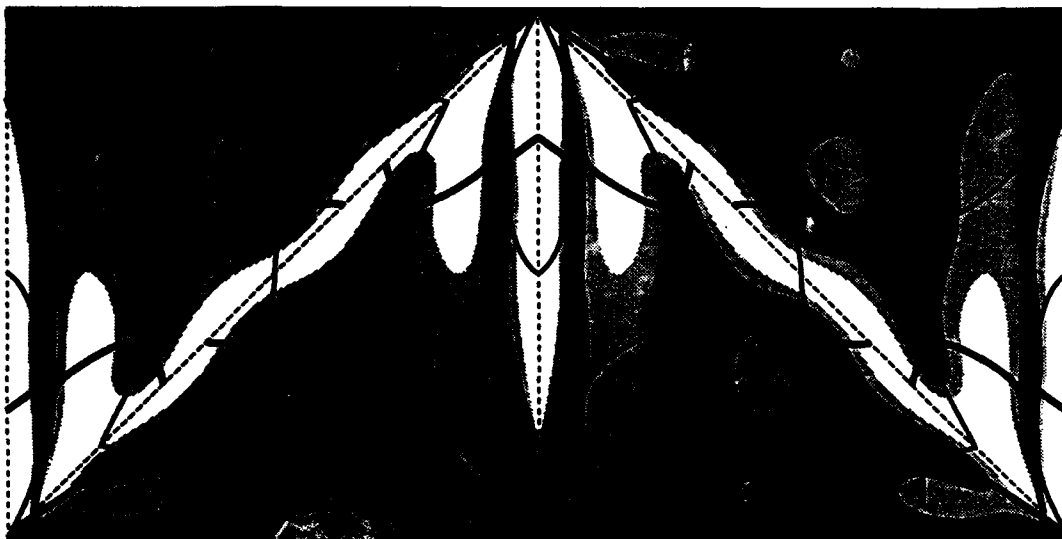
Fig. 6c



Harmonic solution $P = 4$
SIMPLIFIED L2 APPROACH

— *Function Q1*
— *Function Q2*

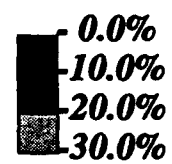
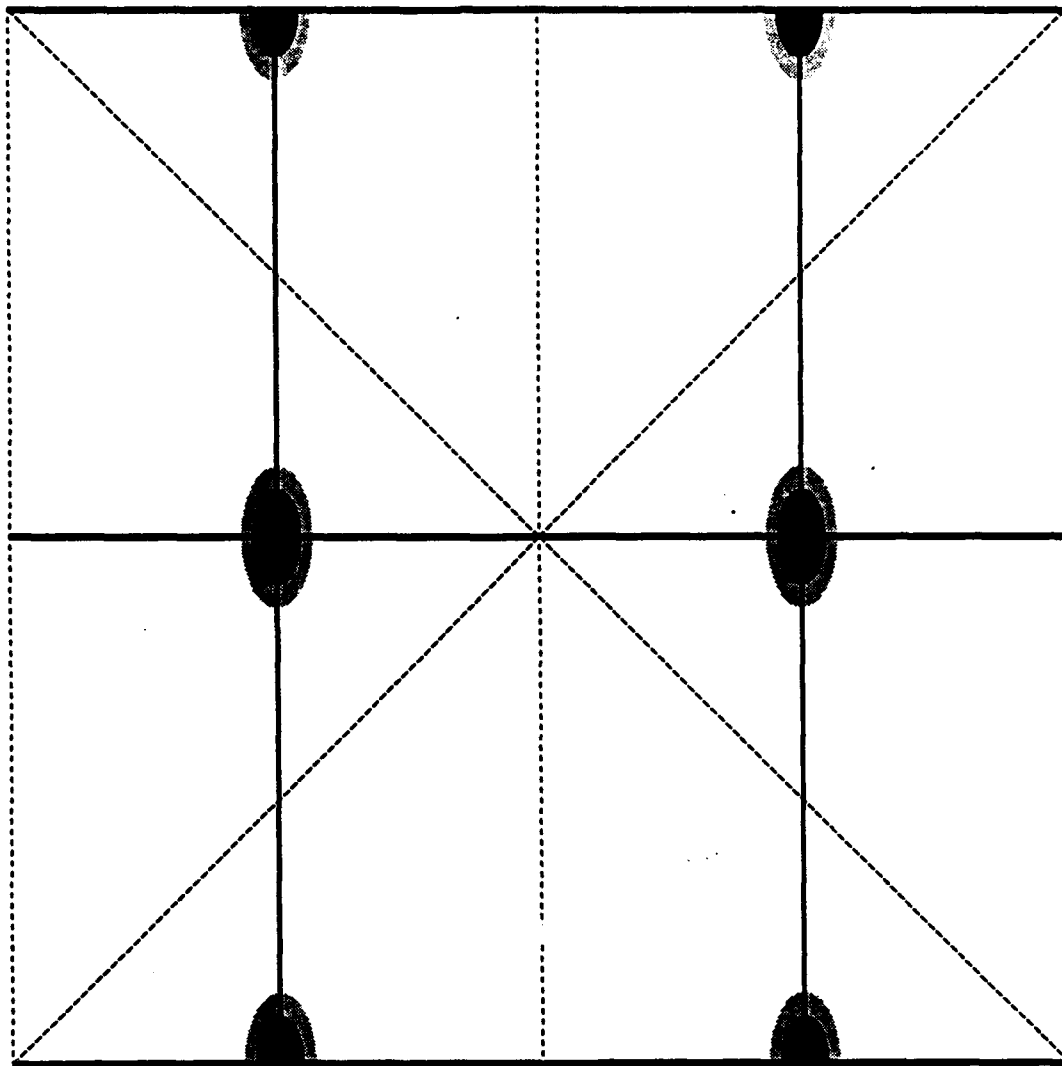
Fig. 6d



Harmonic solution $P = 5$
SIMPLIFIED L2 APPROACH

— *Function Q1*
— *Function Q2*

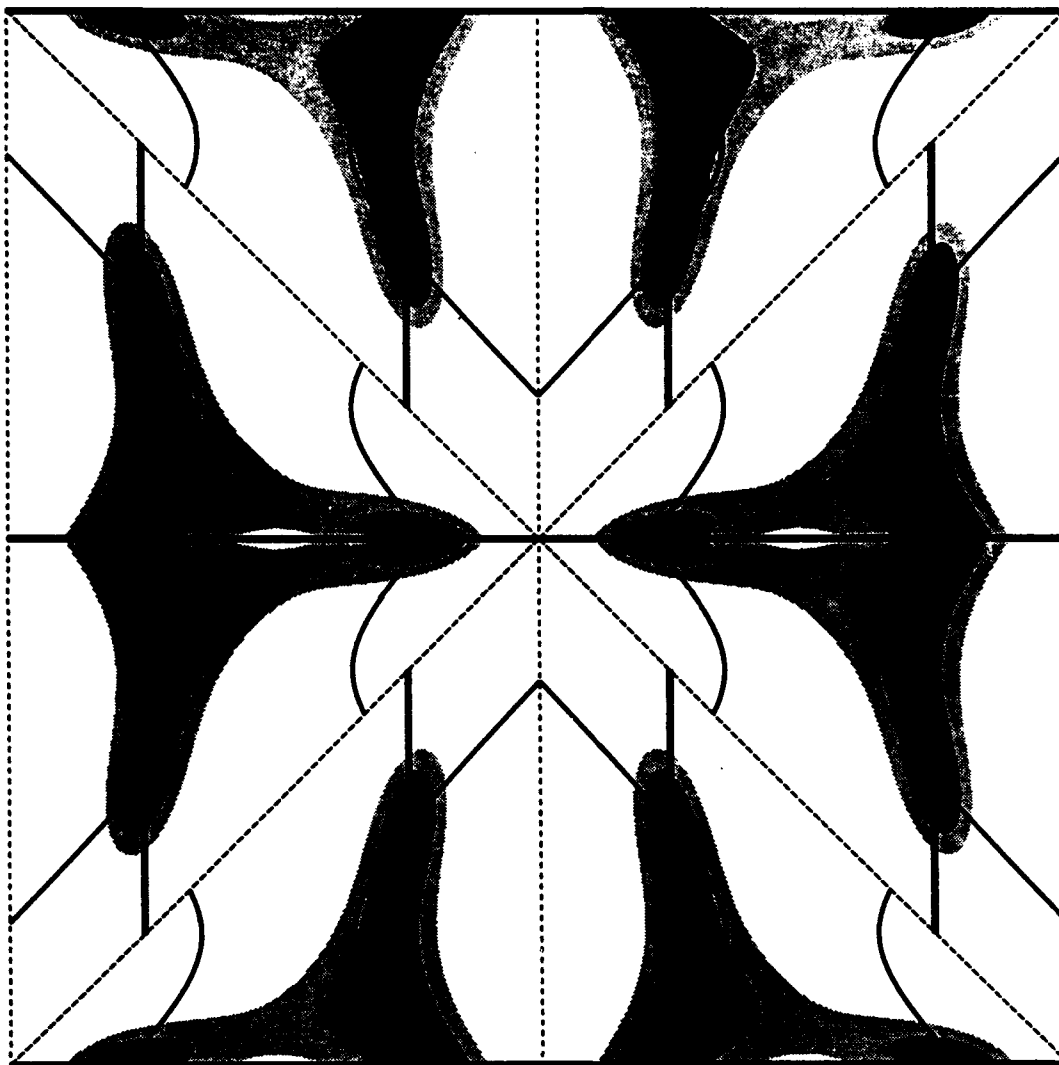
Fig.6e



Harmonic solution $P = 1$
SIMPLIFIED L2 APPROACH

— *Function Q1*
 — *Function Q2*

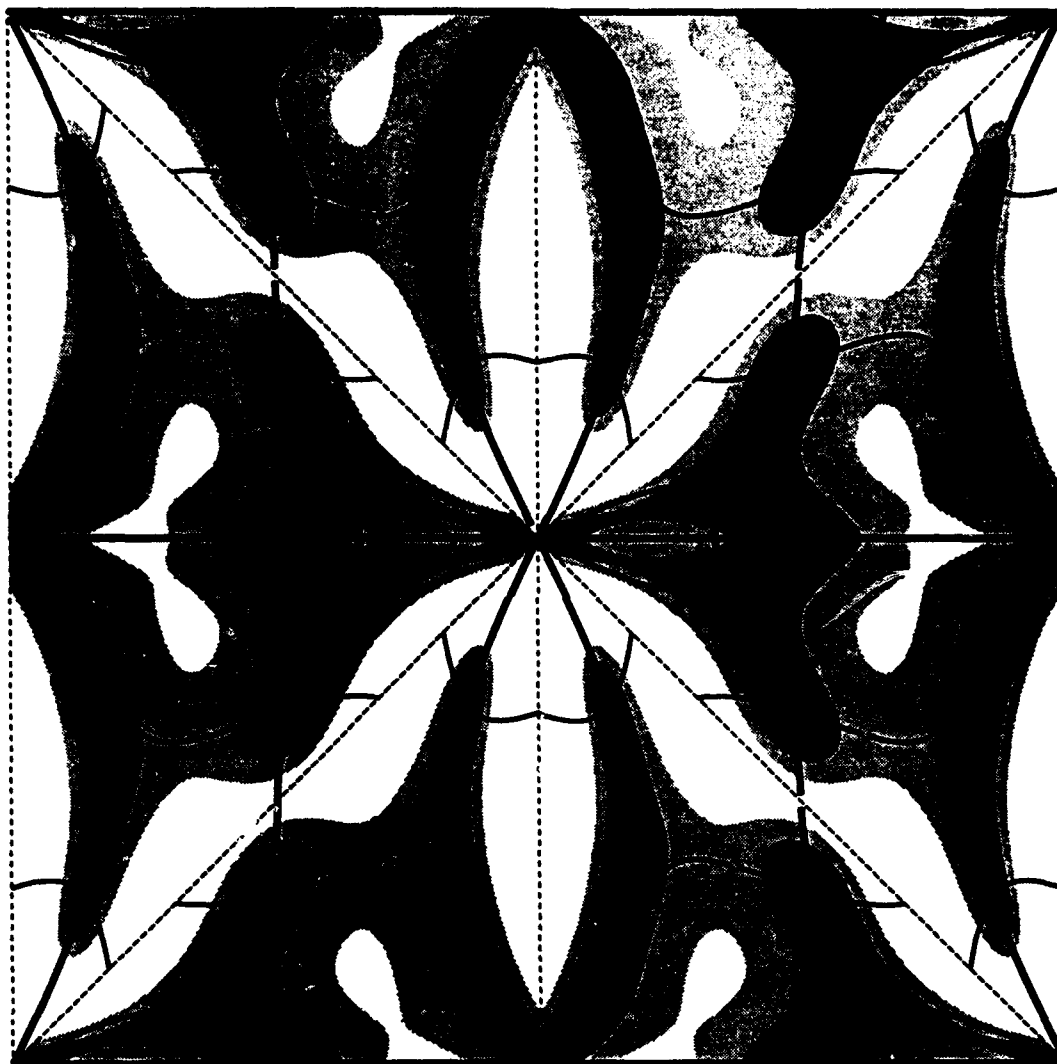
Fig. 7a



Harmonic solution $P = 2$
SIMPLIFIED L2 APPROACH

— *Function Q1*
— *Function Q2*

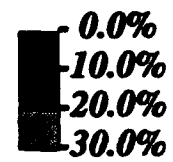
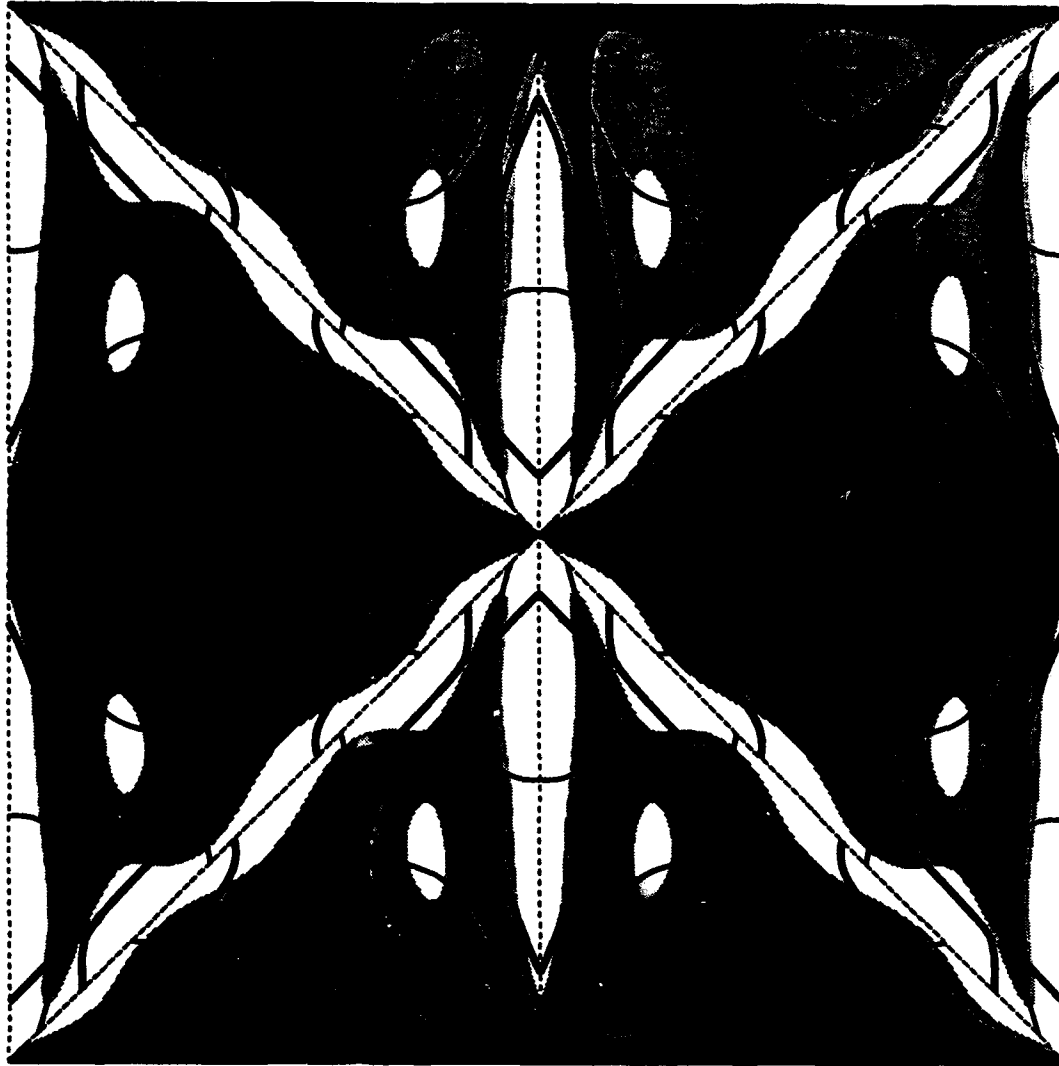
Fig. 7b



Harmonic solution $P = 3$
SIMPLIFIED L2 APPROACH

— *Function Q1*
 — *Function Q2*

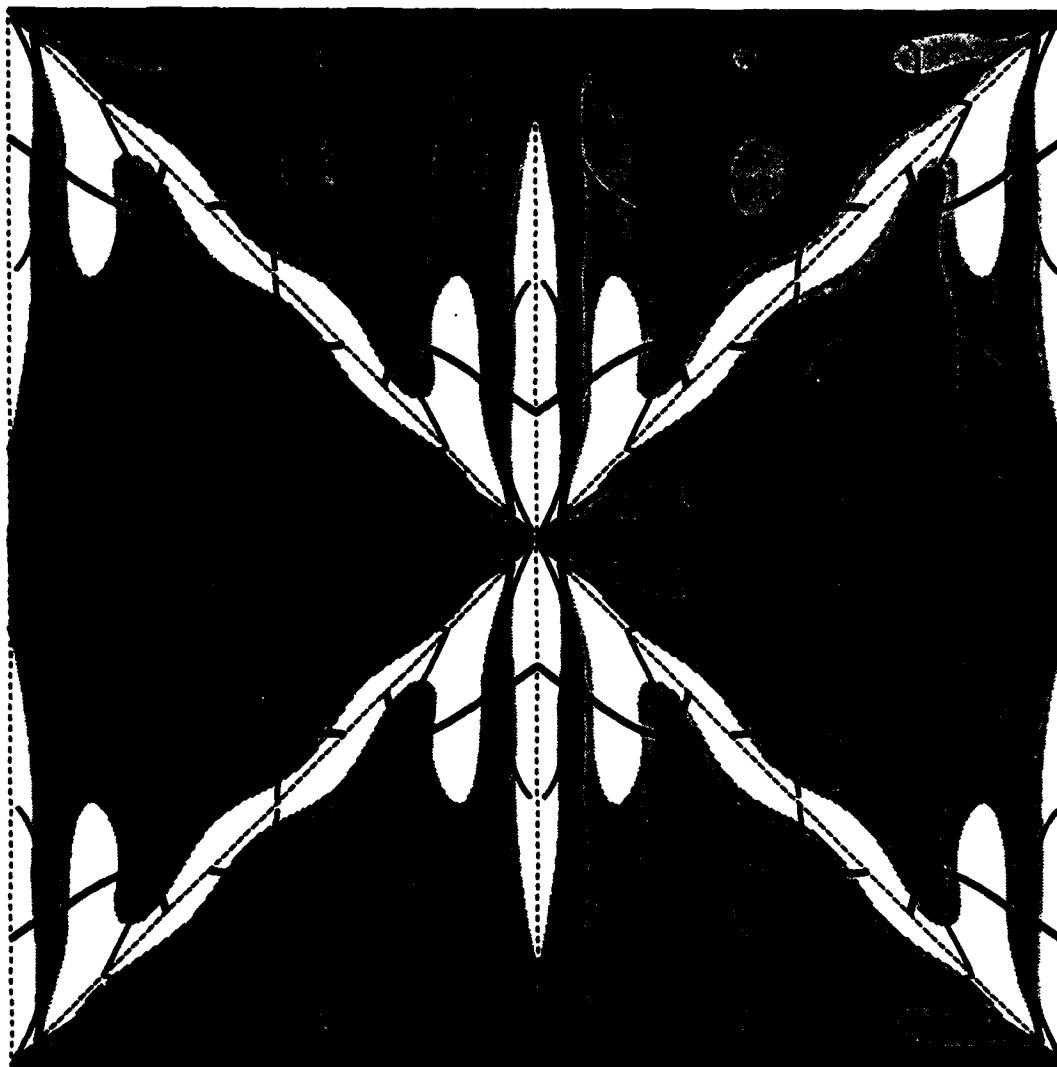
Fig. 7c



Harmonic solution $P = 4$
SIMPLIFIED L2 APPROACH

— *Function Q1*
 — *Function Q2*

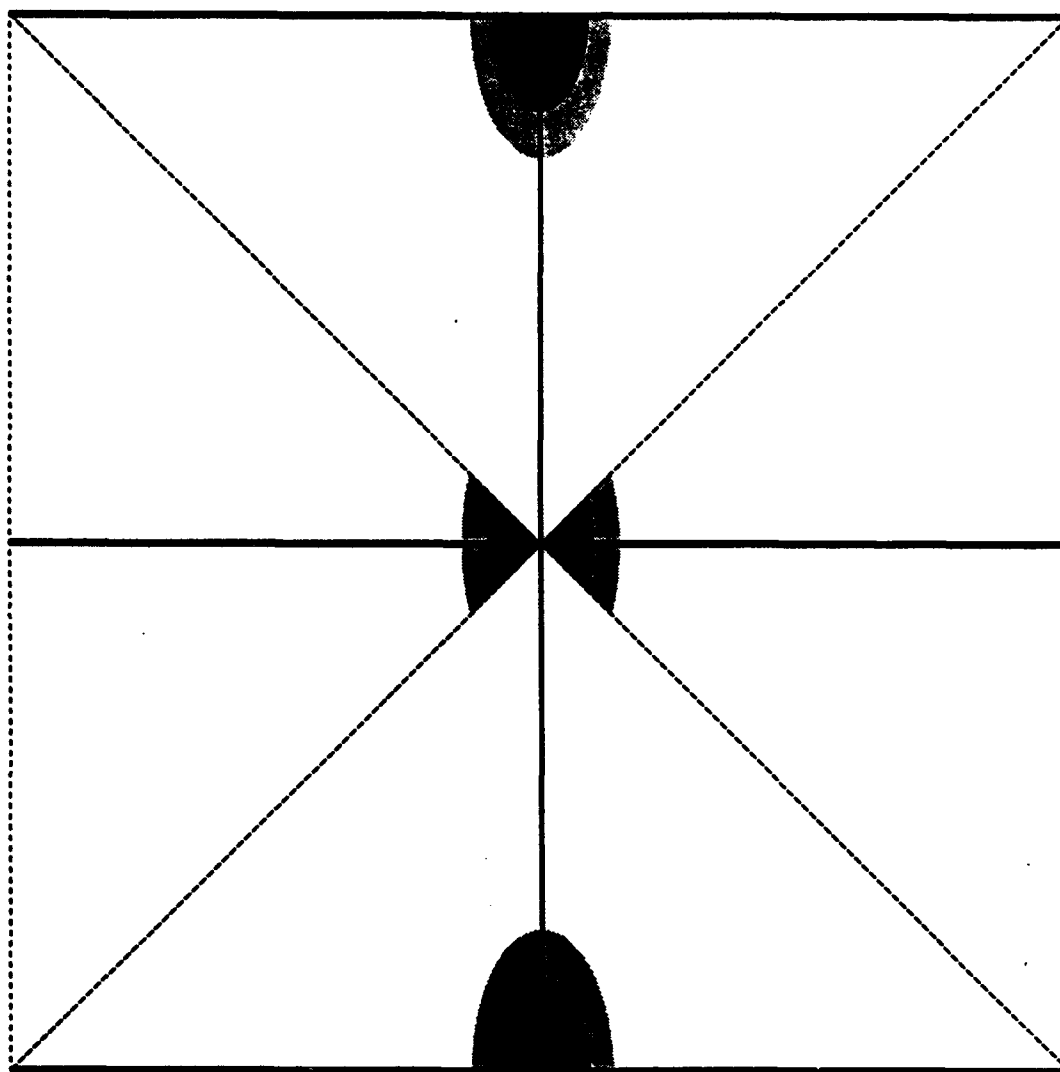
Fig. 7d



Harmonic solution $P = 5$
SIMPLIFIED L2 APPROACH

— *Function Q1*
 — *Function Q2*

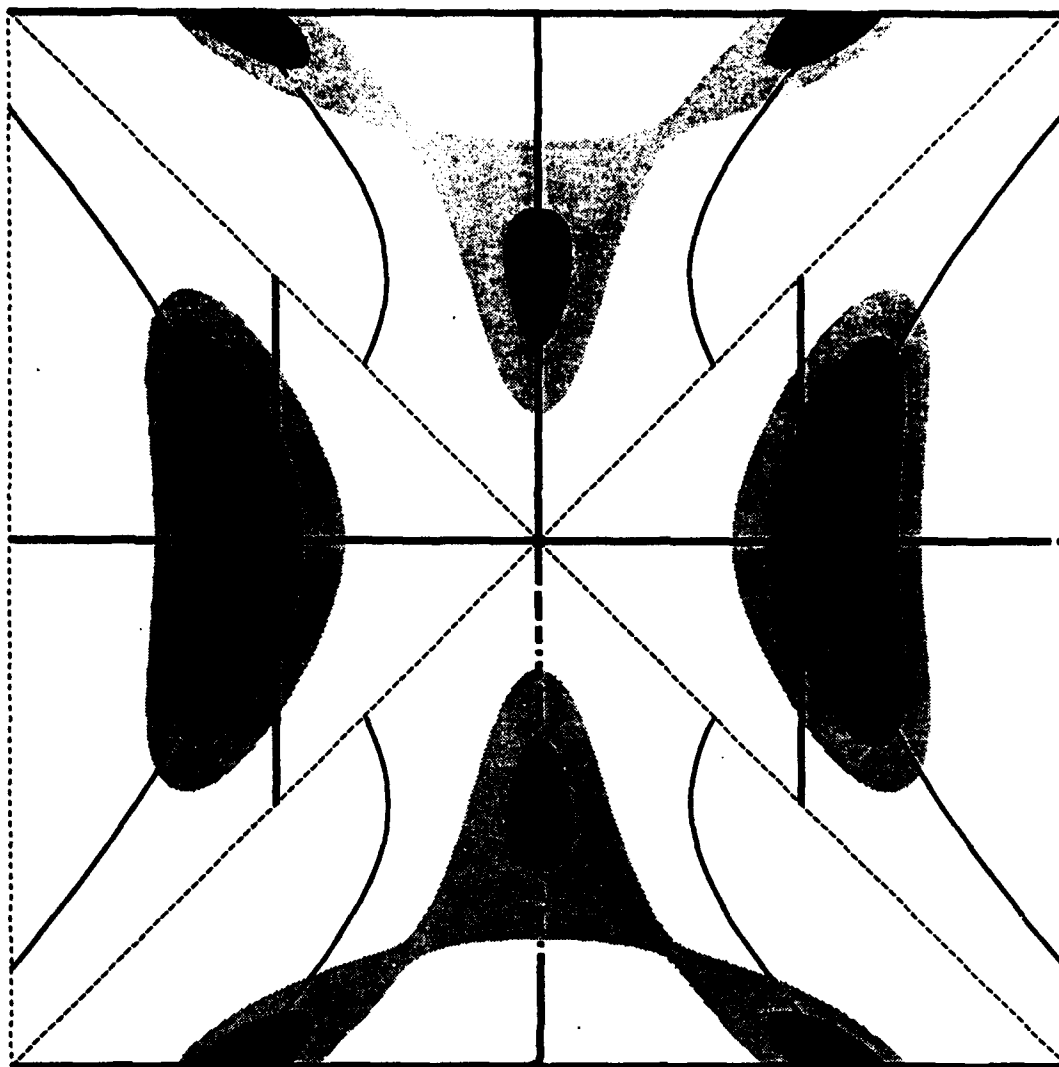
Fig.7e



Harmonic solution $P = 1$
SIMPLIFIED L2 APPROACH

— *Function Q1*
 — *Function Q2*

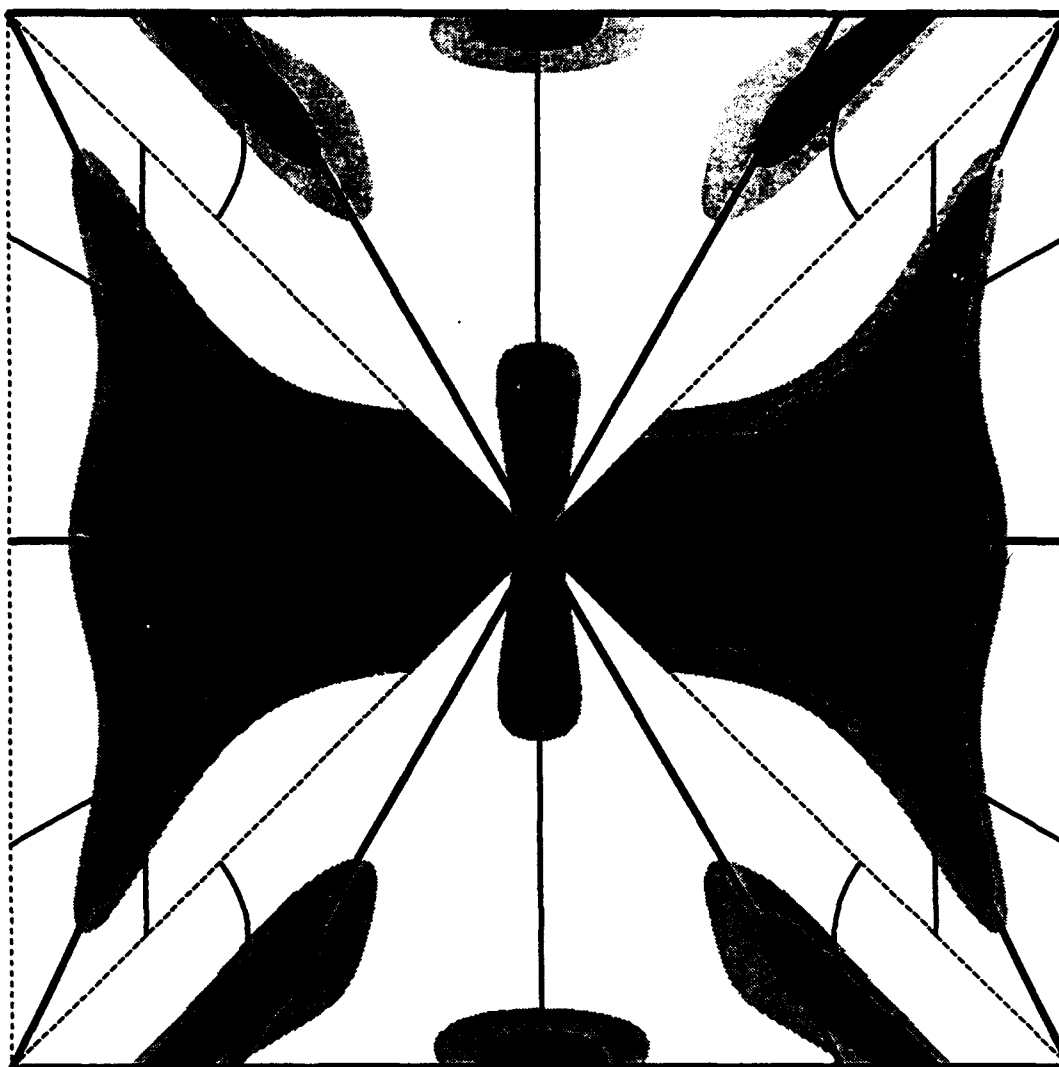
Fig. 8a



Harmonic solution $P = 2$
SIMPLIFIED L2 APPROACH

— *Function Q1*
— *Function Q2*

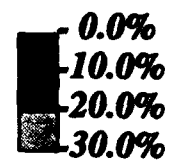
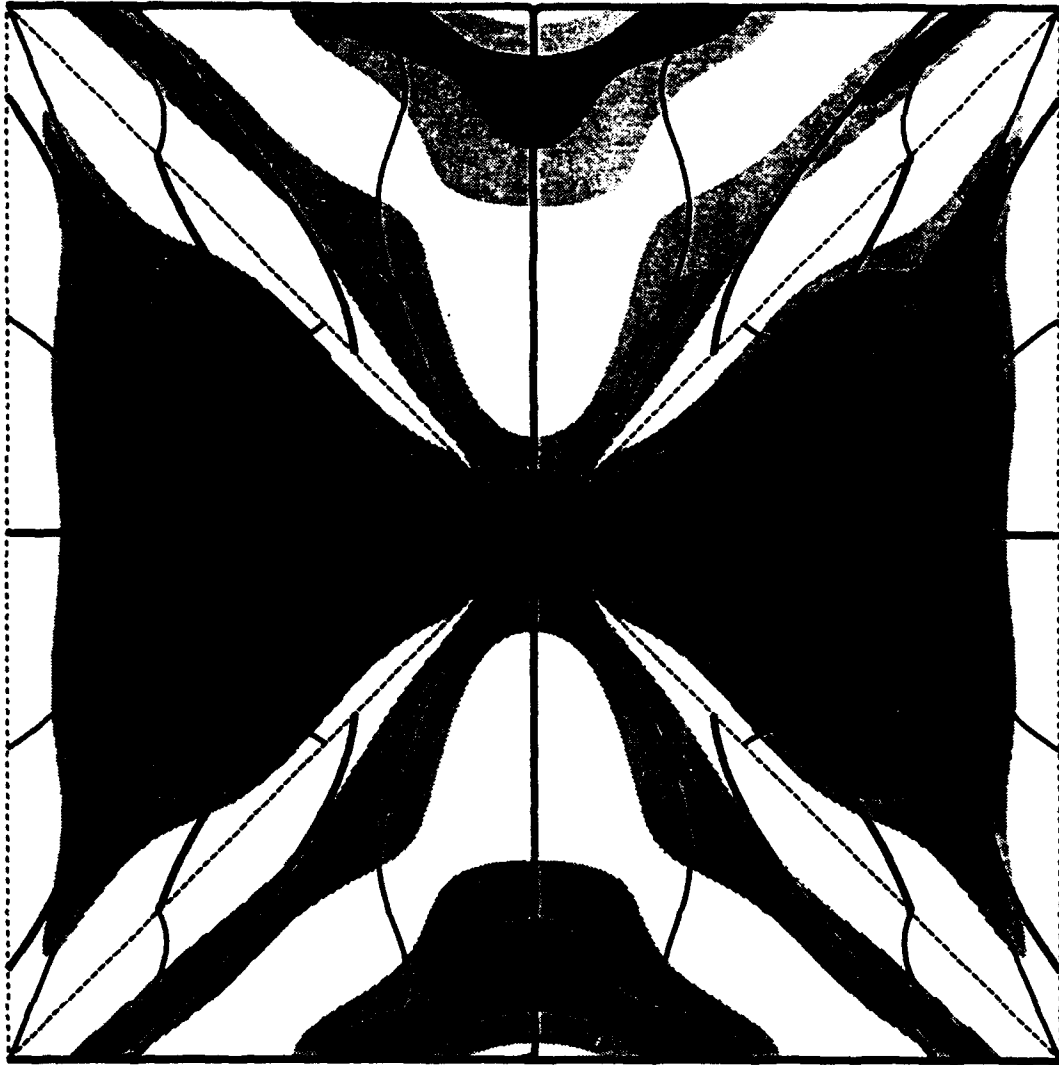
Fig. 8b



Harmonic solution $P = 3$
SIMPLIFIED L2 APPROACH

— *Function Q1*
— *Function Q2*

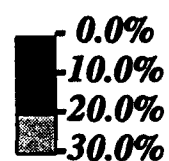
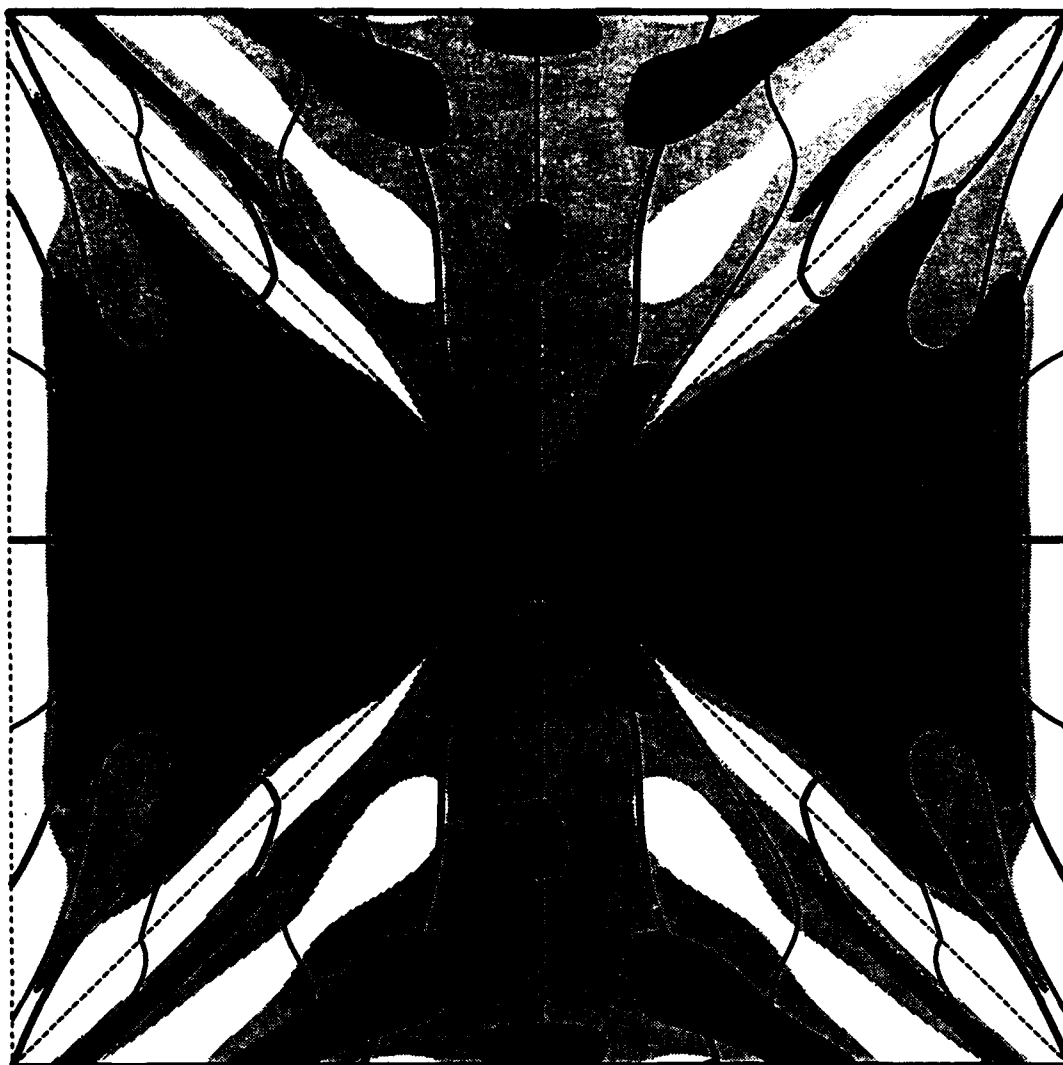
Fig. 8c



Harmonic solution $P = 4$
SIMPLIFIED L2 APPROACH

— *Function Q1*
 — *Function Q2*

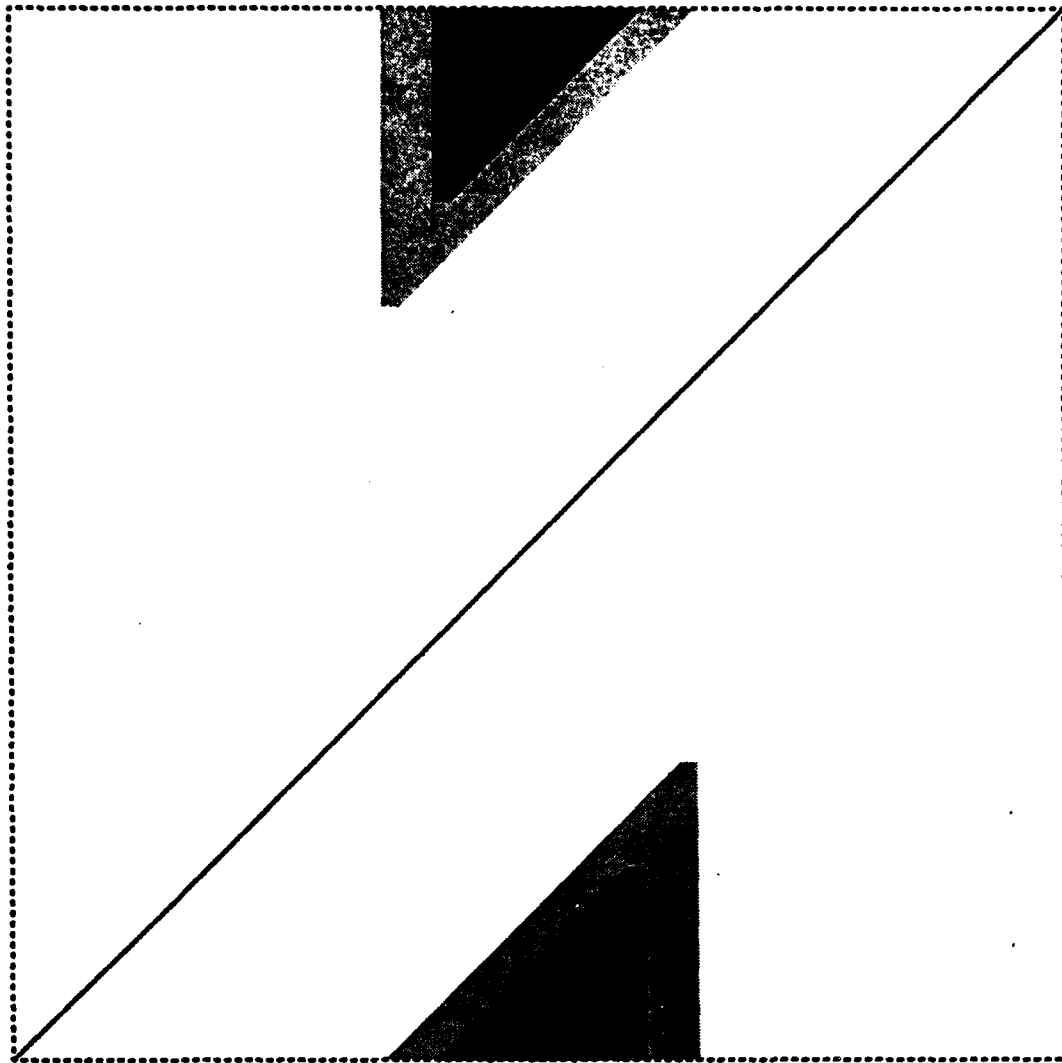
Fig. 8d



Harmonic solution $P = 5$
SIMPLIFIED L2 APPROACH

— *Function Q1*
 — *Function Q2*

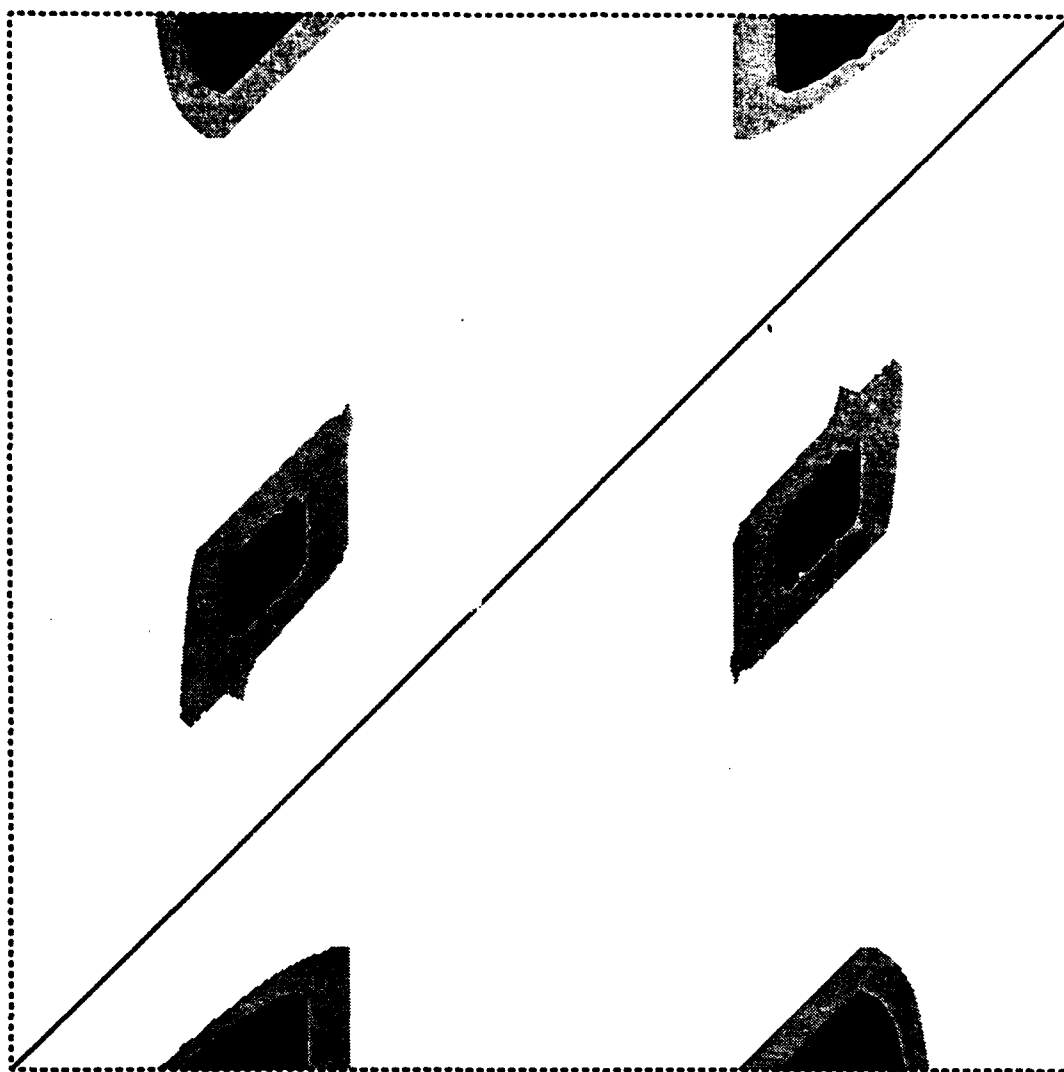
Fig.8e



General solution $P = 1$
DIRECT OPTIMISATION



Fig. 9a



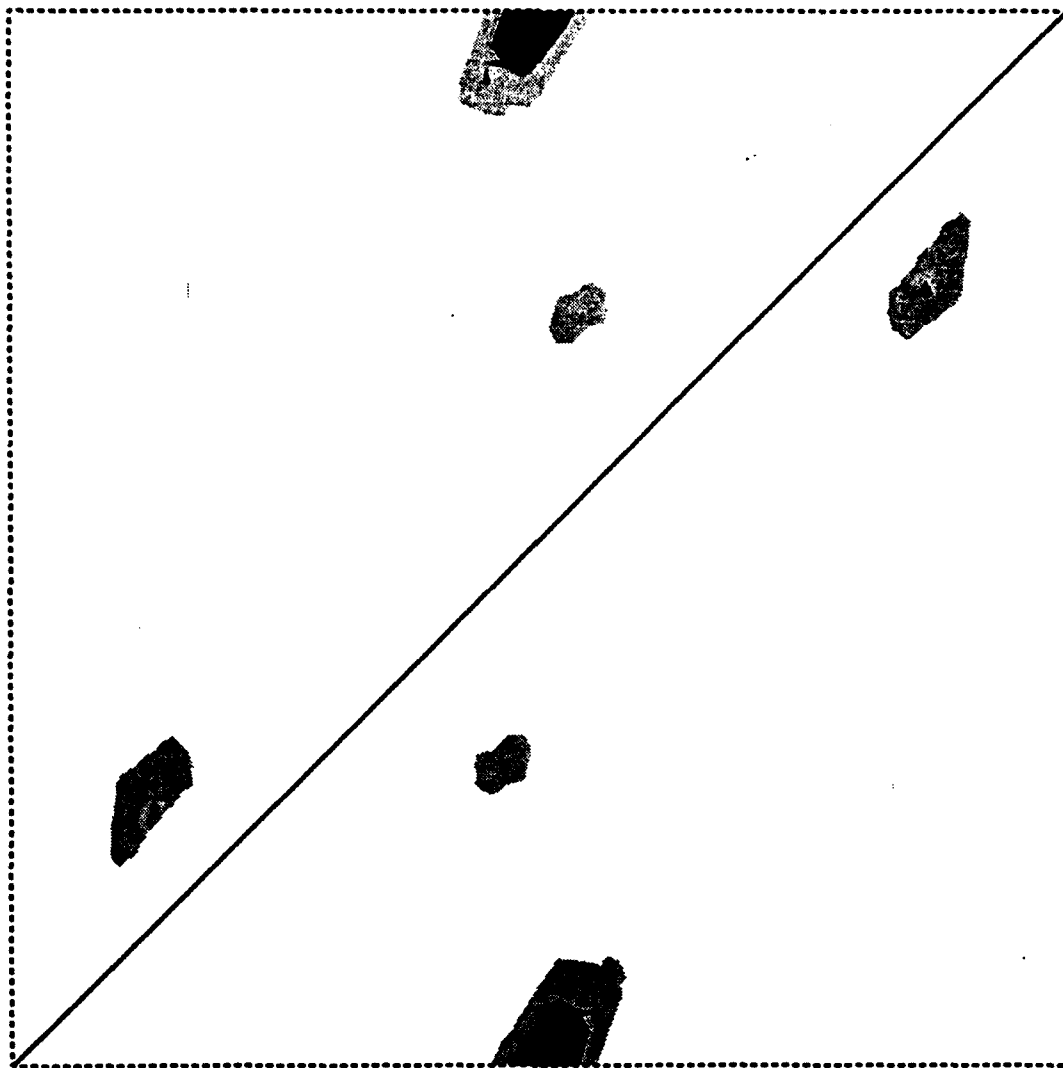
General solution

$P = 2$

DIRECT OPTIMISATION



Fig. 9b



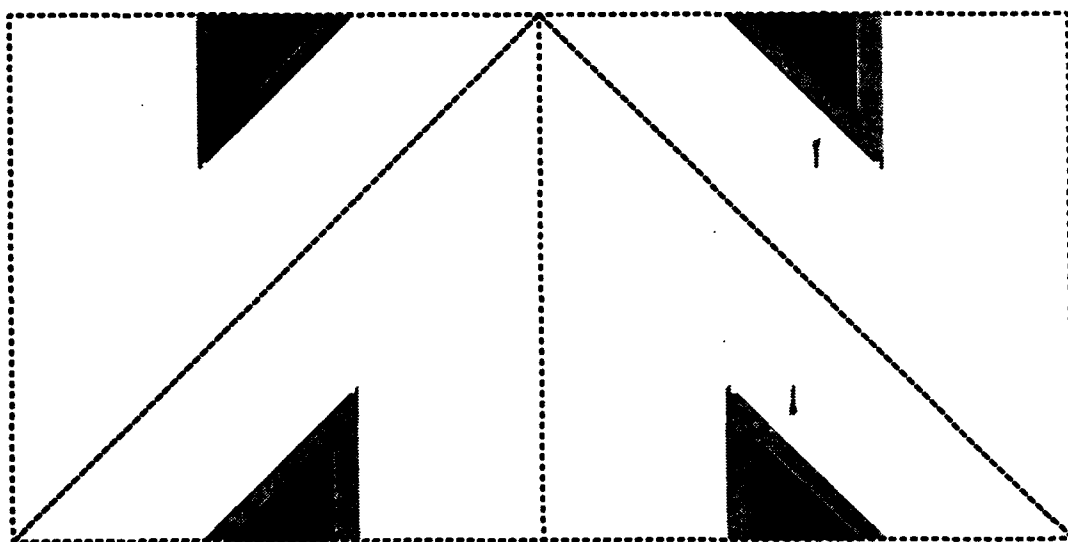
General solution

$P = 3$

DIRECT OPTIMISATION



Fig. 9c



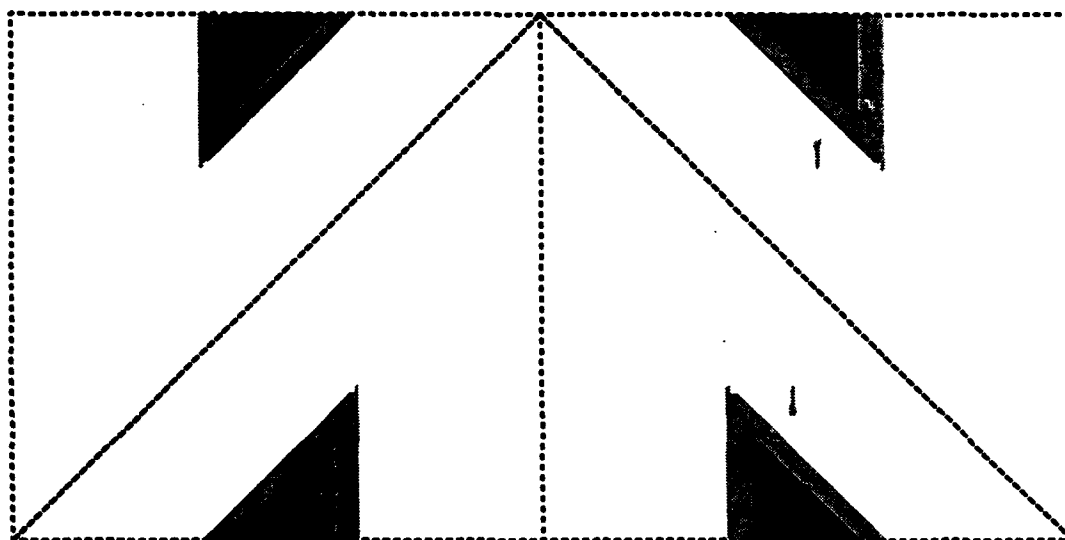
General solution

$P = 1$

DIRECT OPTIMISATION



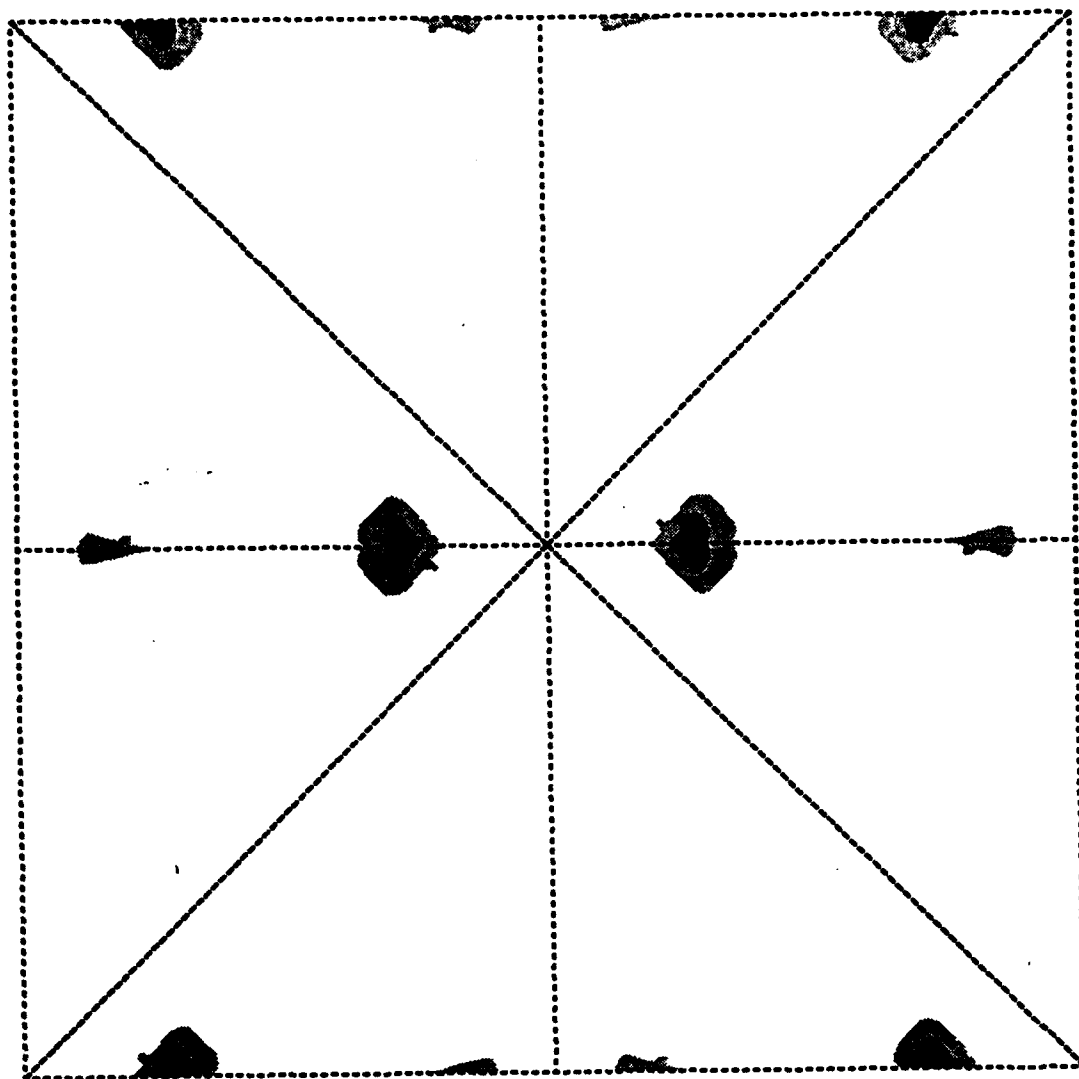
Fig. 10a



General solution $P = 1$
DIRECT OPTIMISATION



Fig. 10a



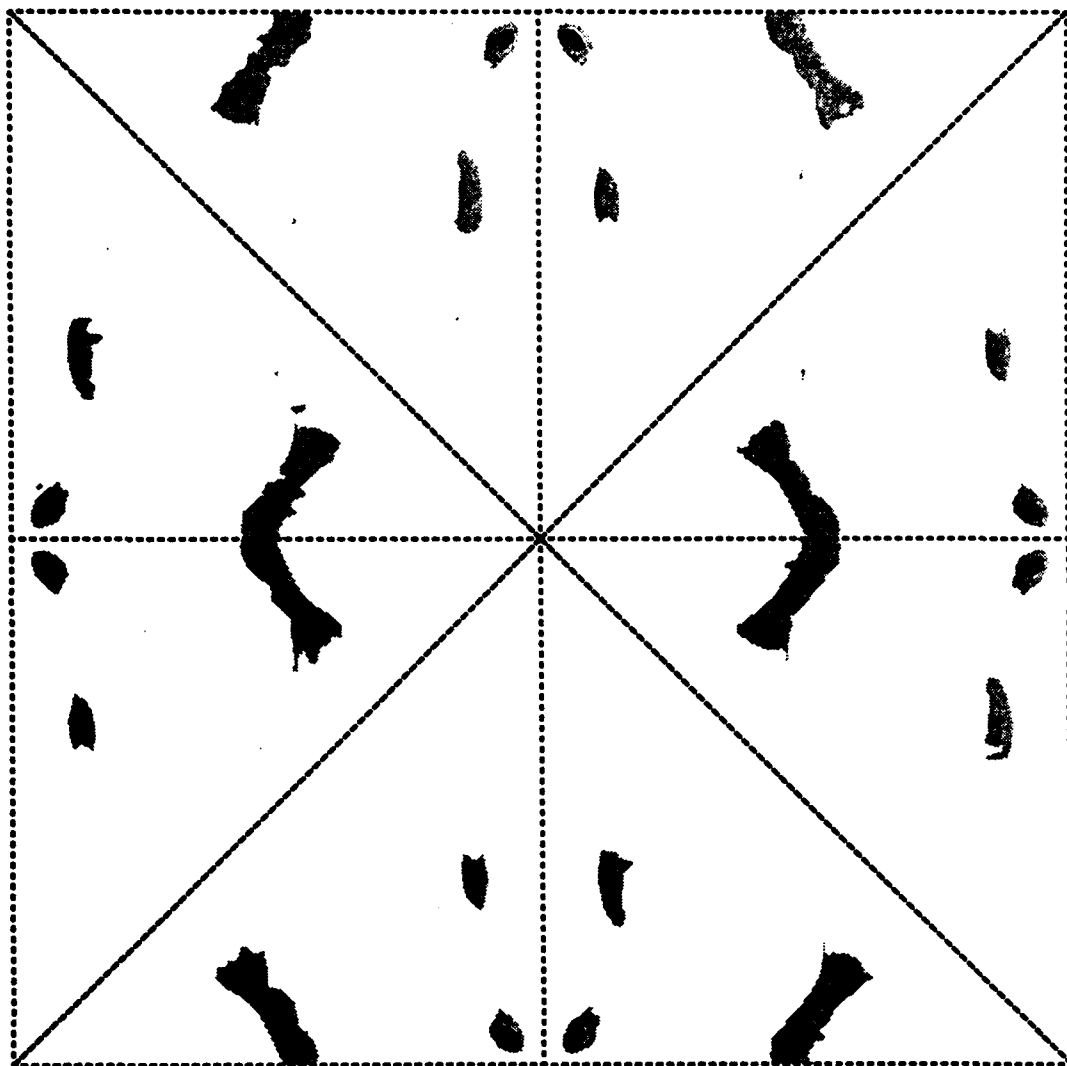
General solution

$P = 2$

DIRECT OPTIMISATION



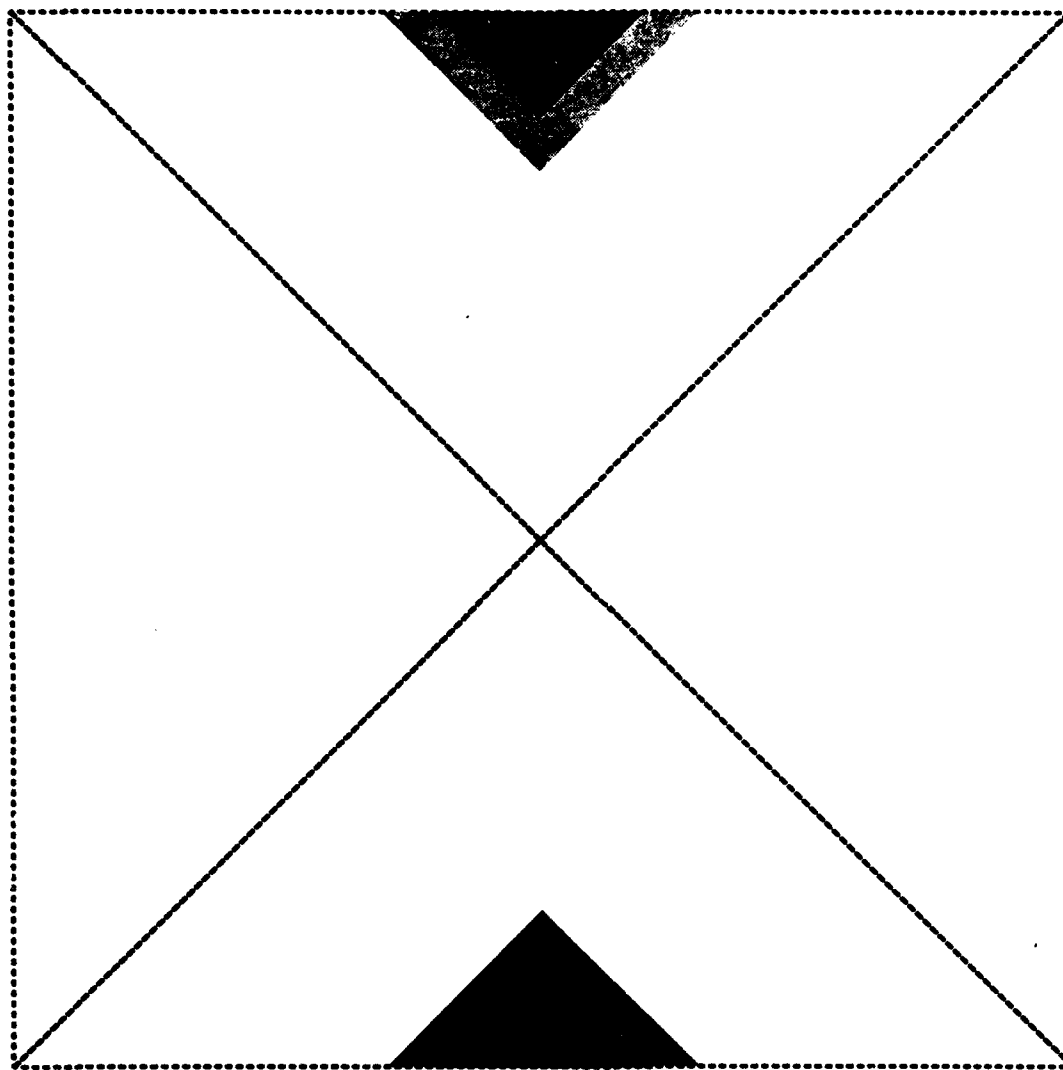
Fig. 11a



General solution **P = 3**
DIRECT OPTIMISATION



Fig. 11b



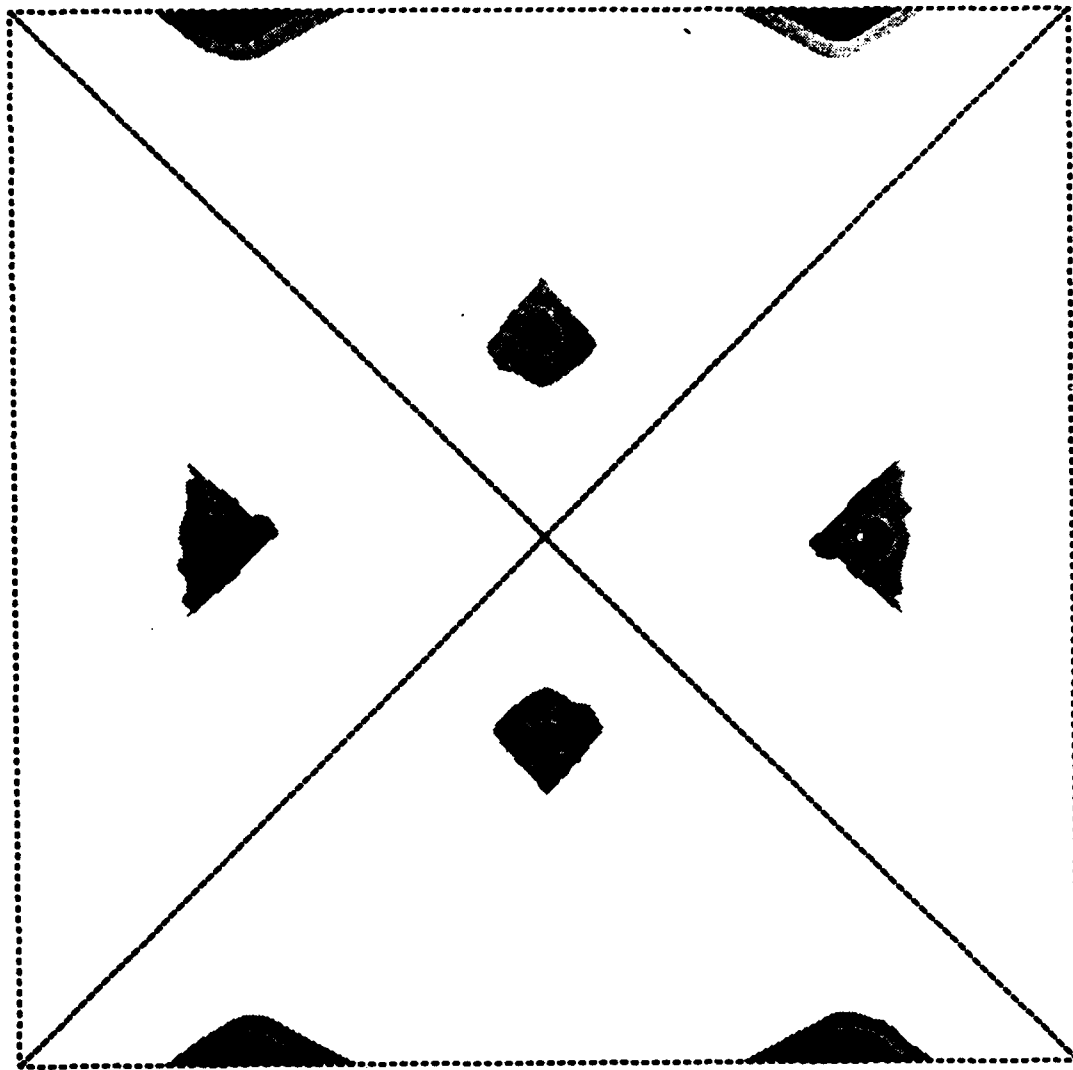
General solution

$P = 1$

DIRECT OPTIMISATION



Fig. 12a



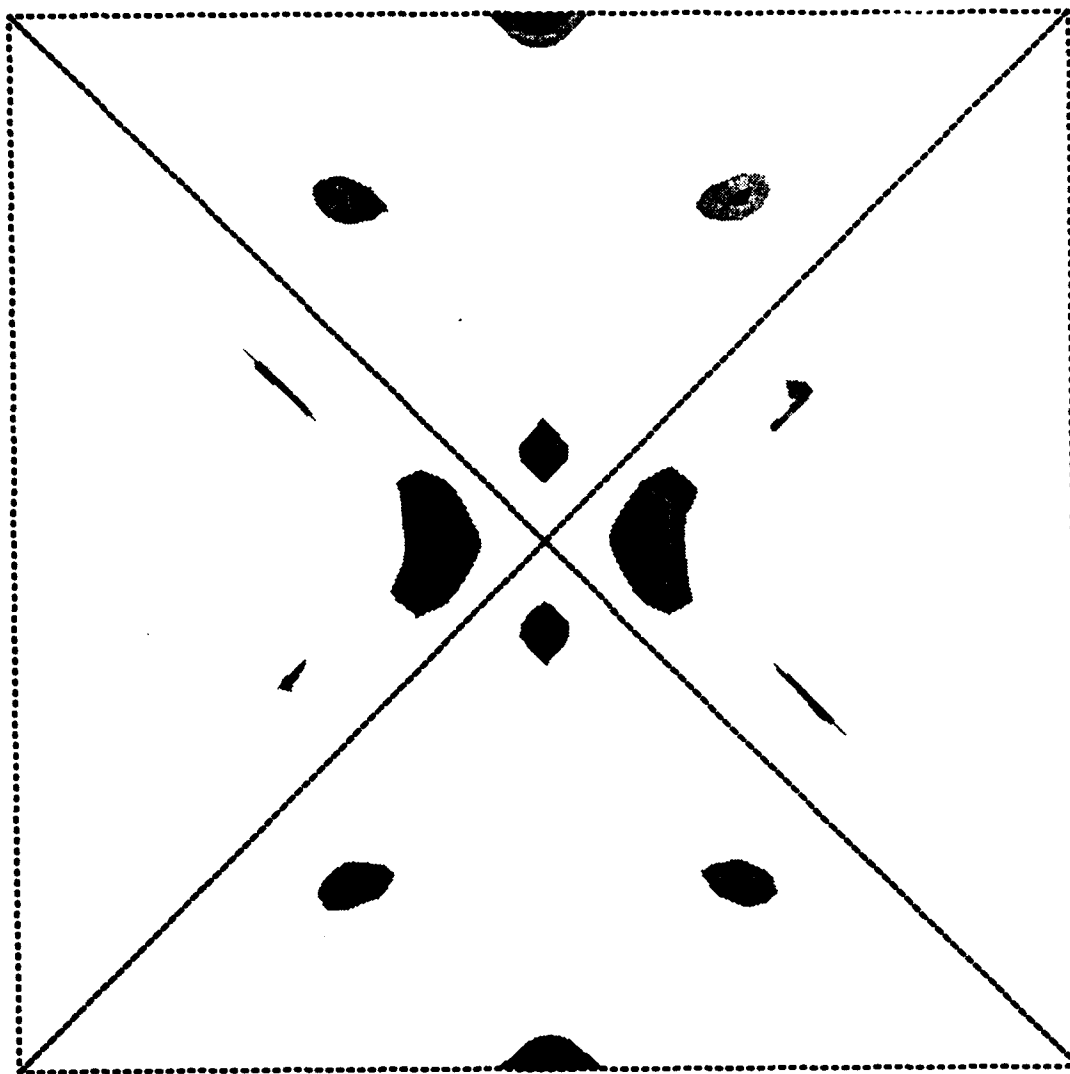
General solution

$P = 2$

DIRECT OPTIMISATION



Fig. 12b



General solution

$P = 3$

DIRECT OPTIMISATION



Fig. 12c

Fig. 17c

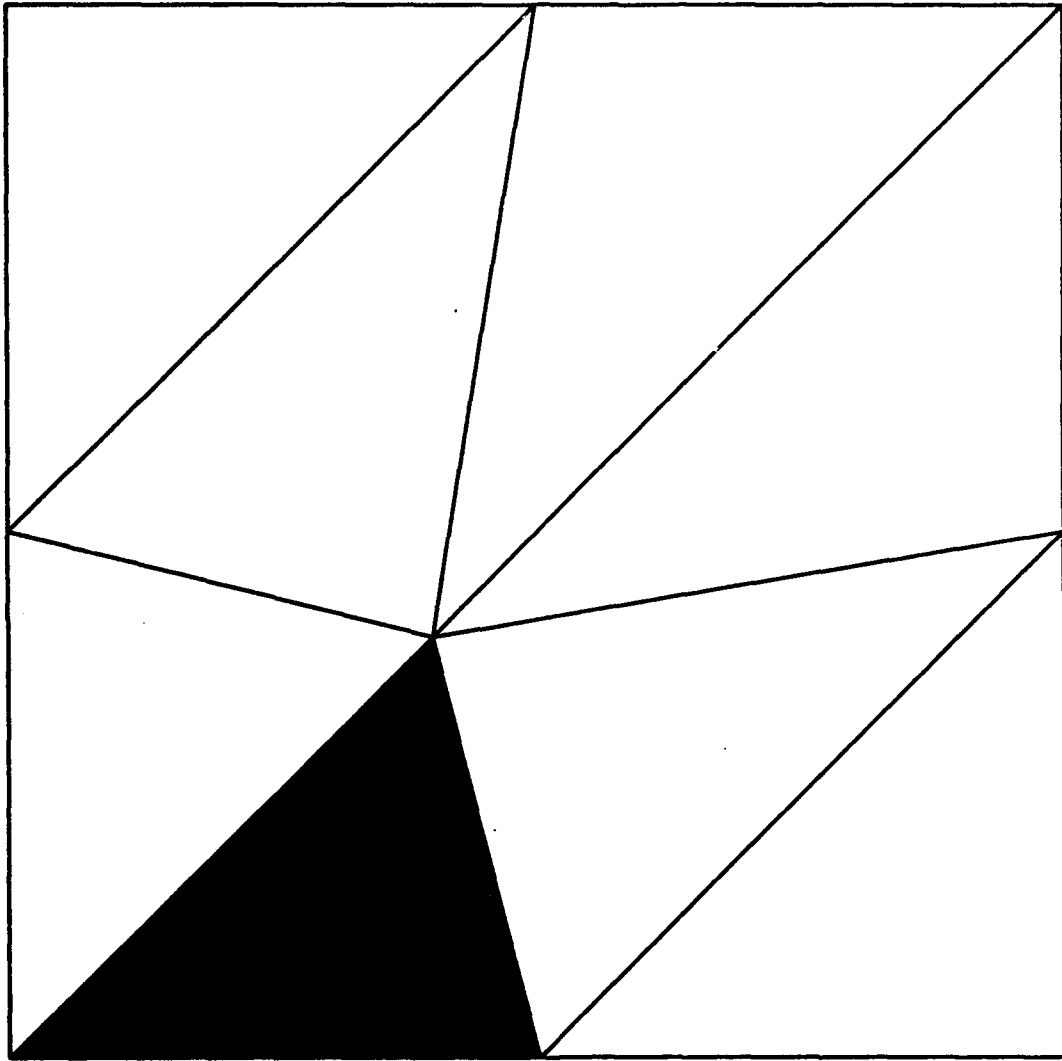


Fig. 13a

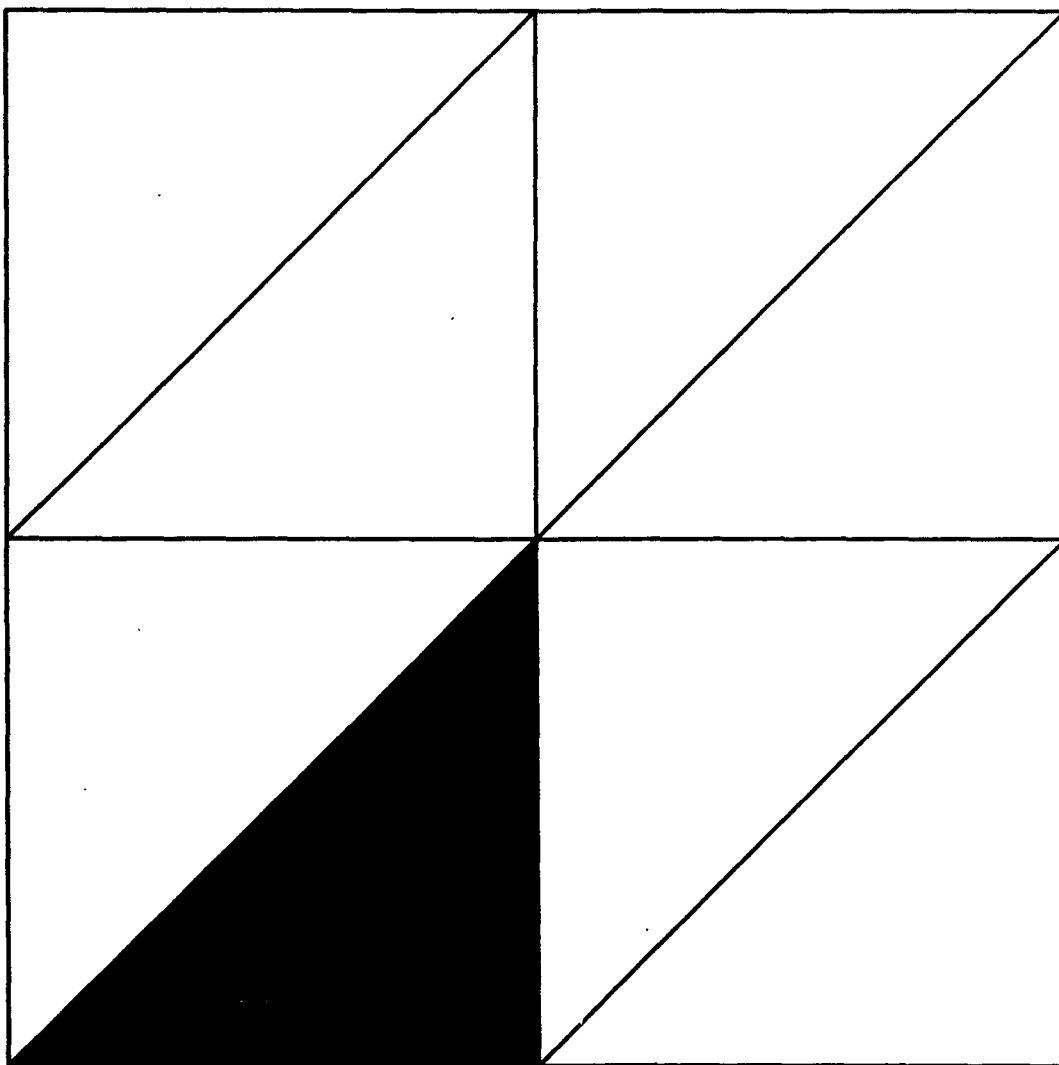


Fig. 13b

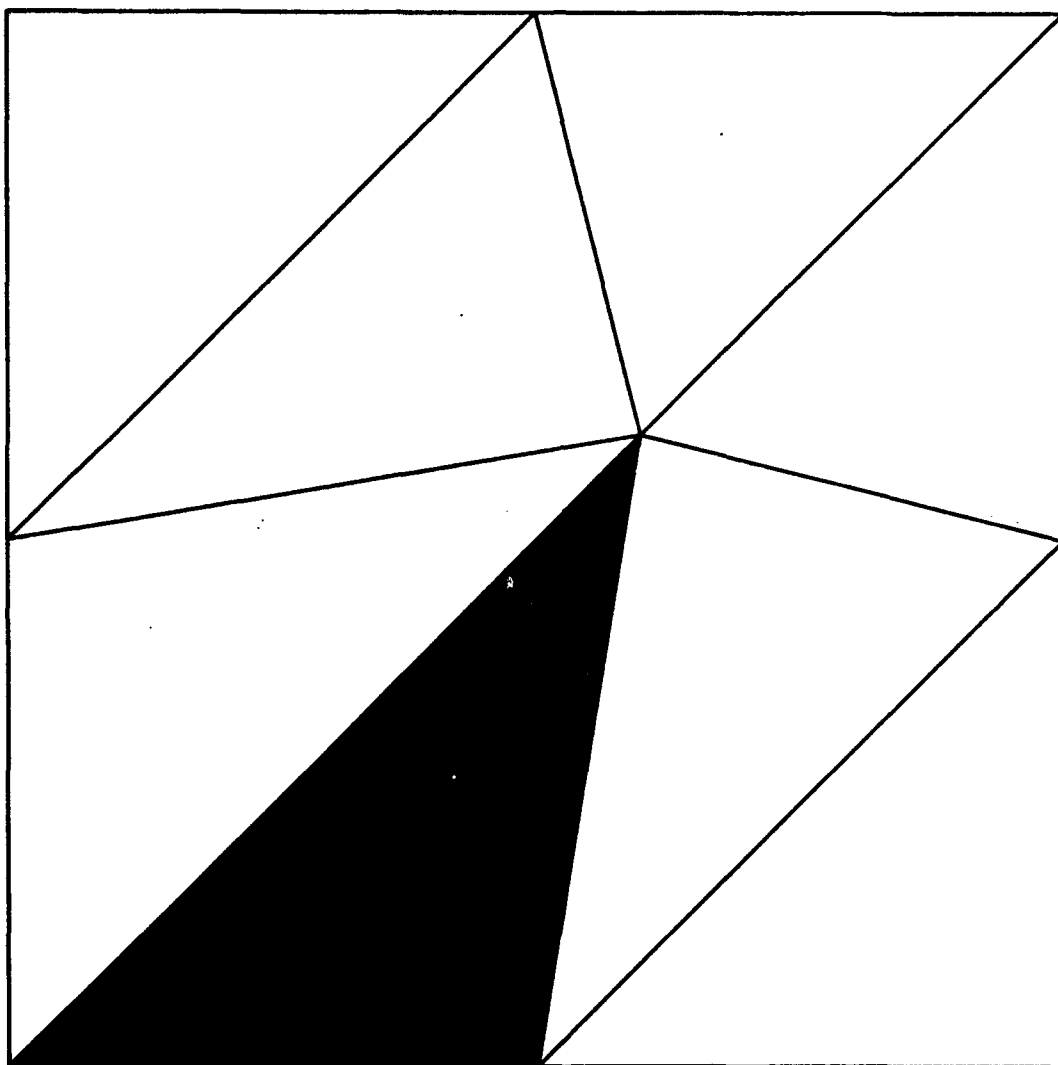


Fig. 13c

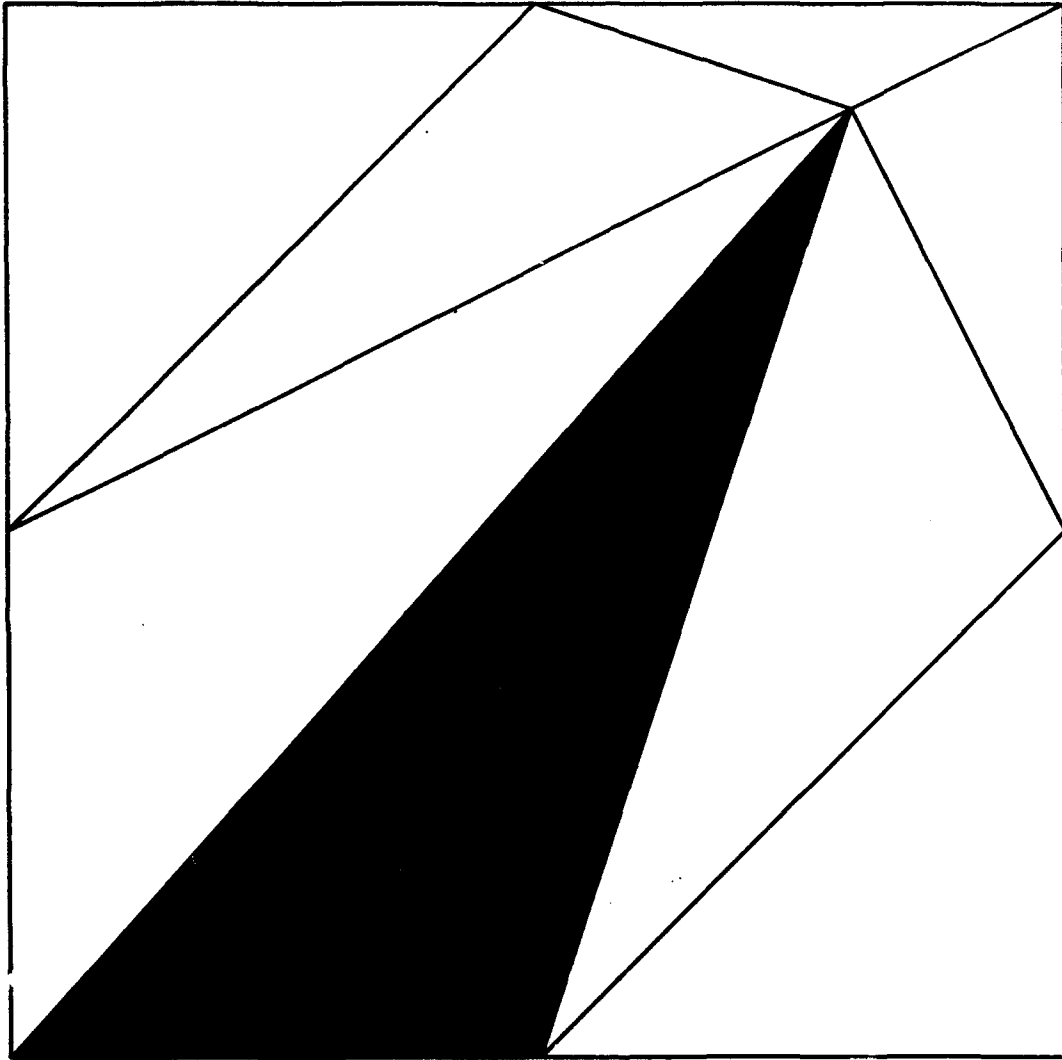


Fig. 13d

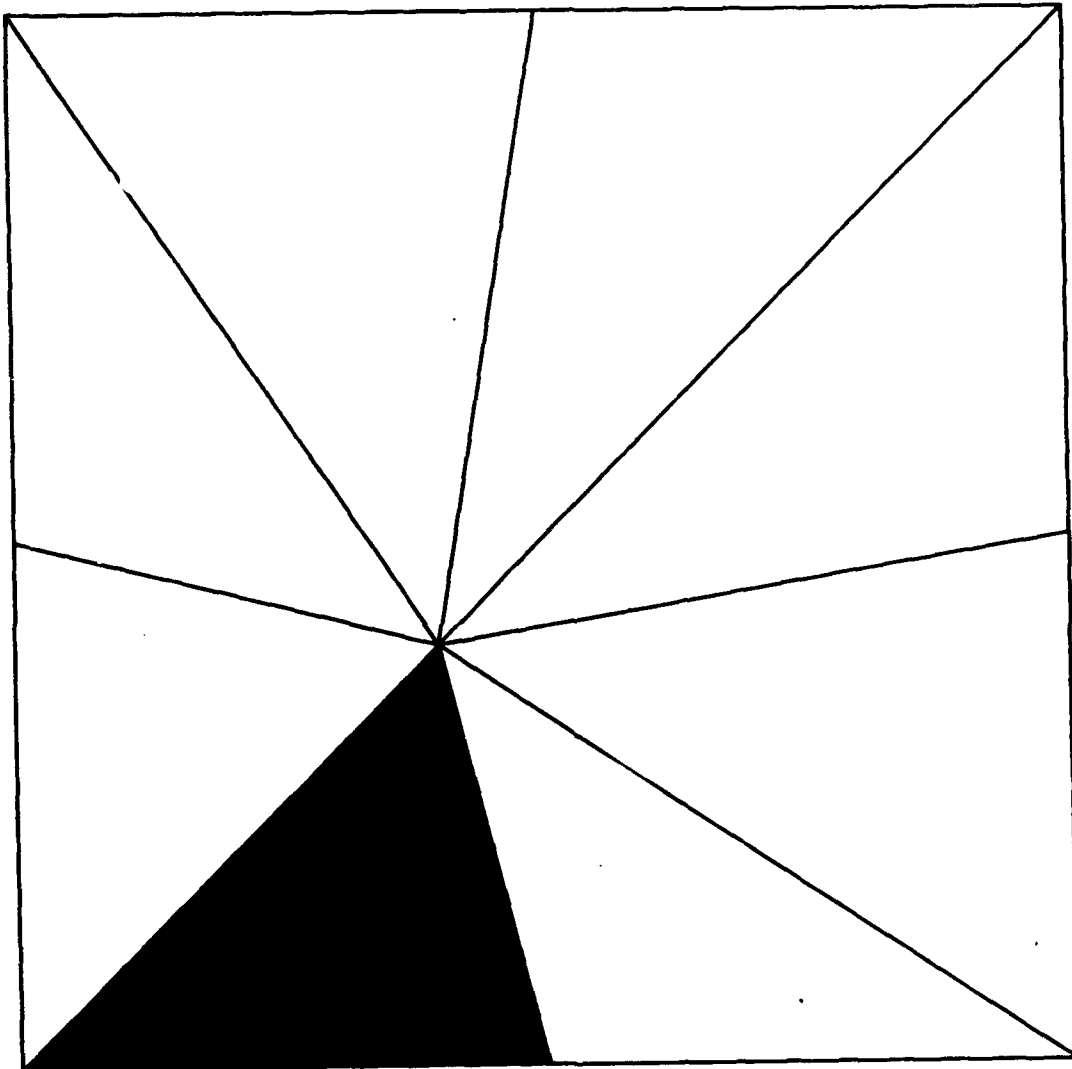


Fig. 13e

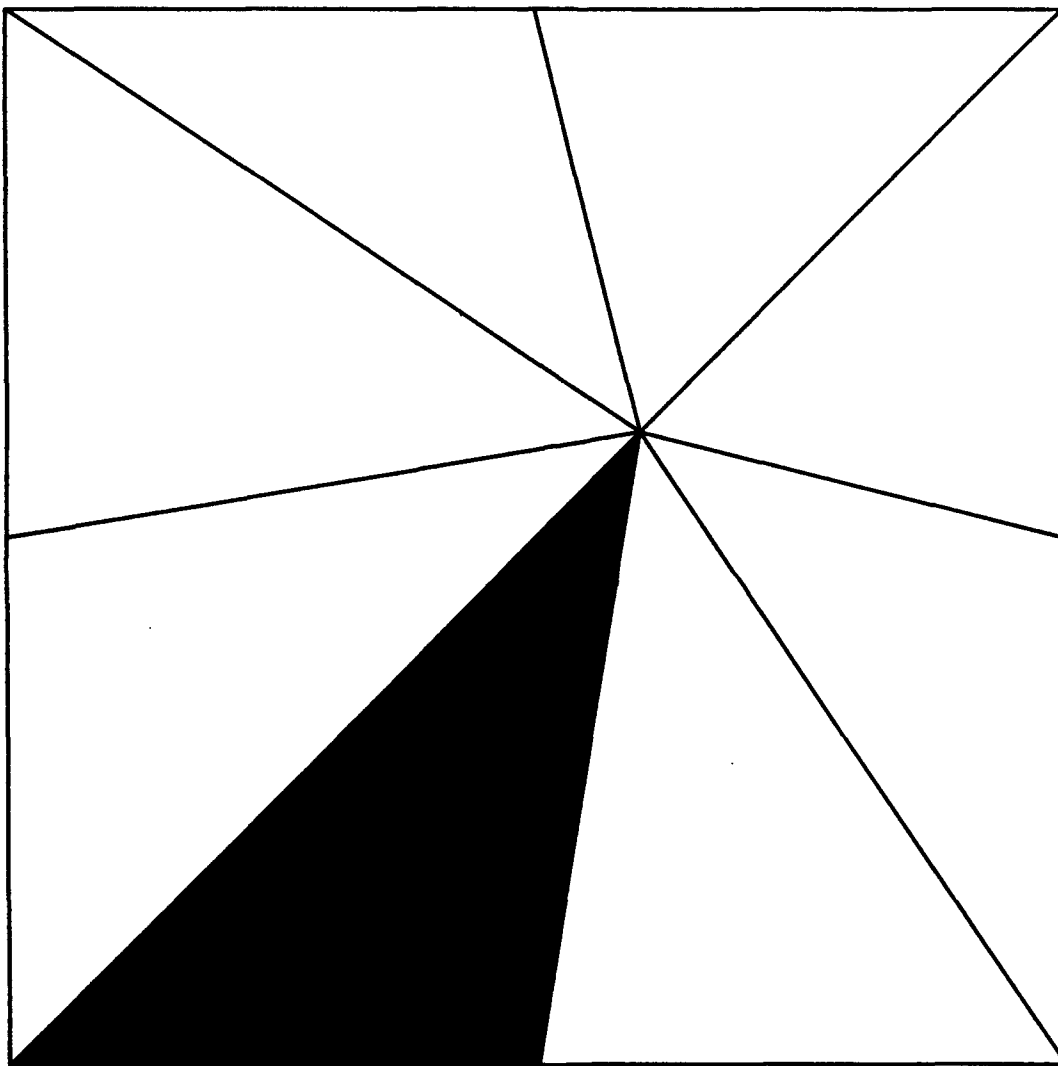


Fig. 13g

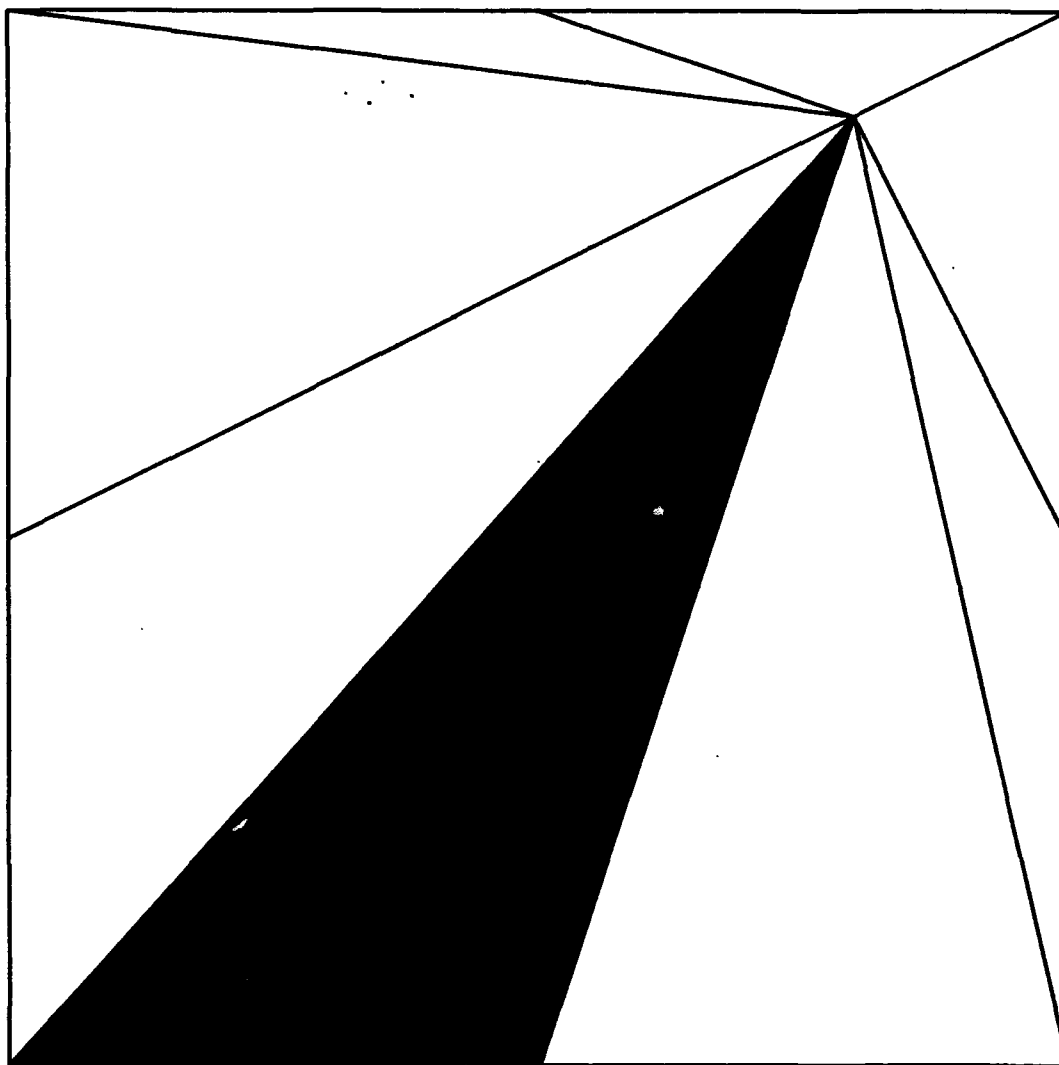
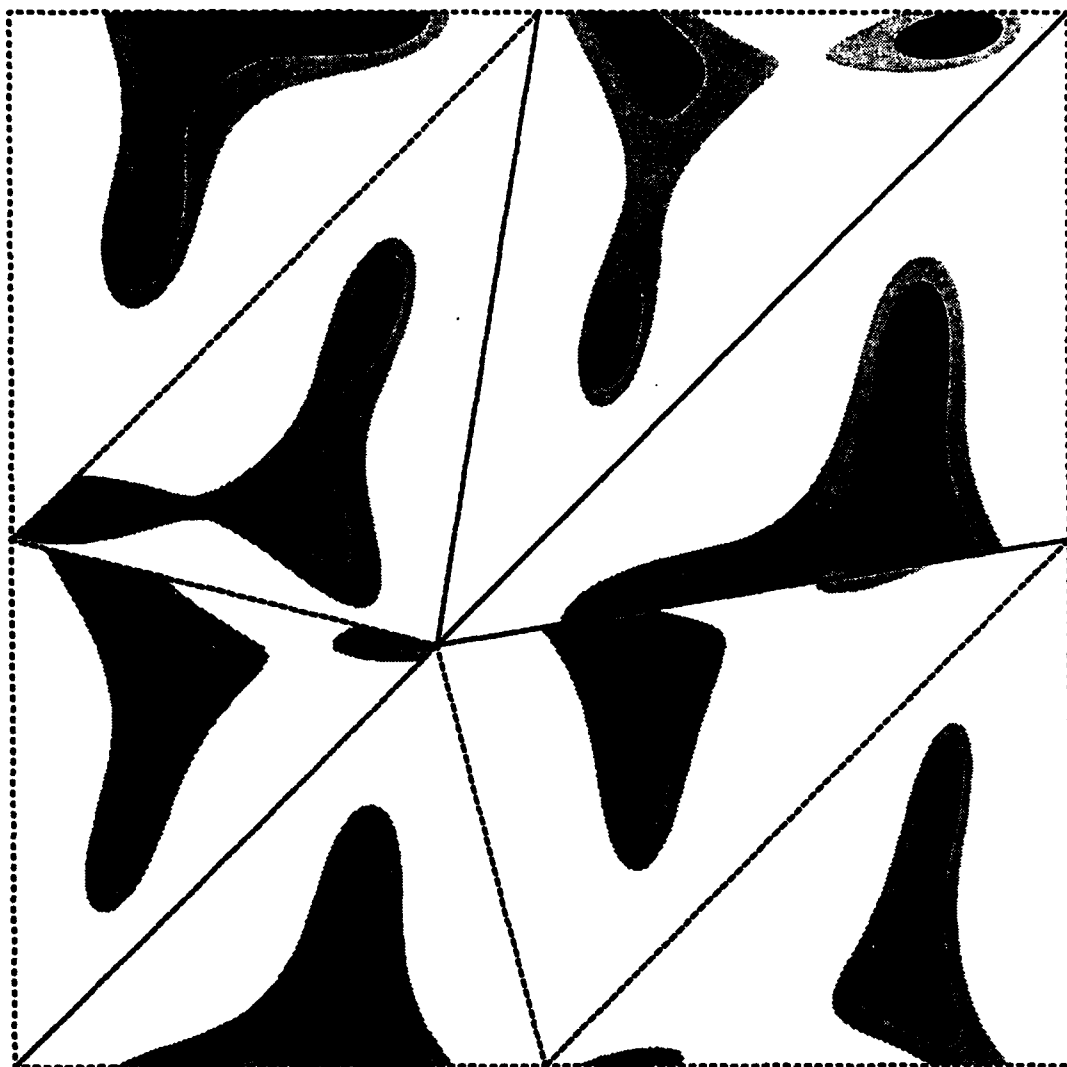


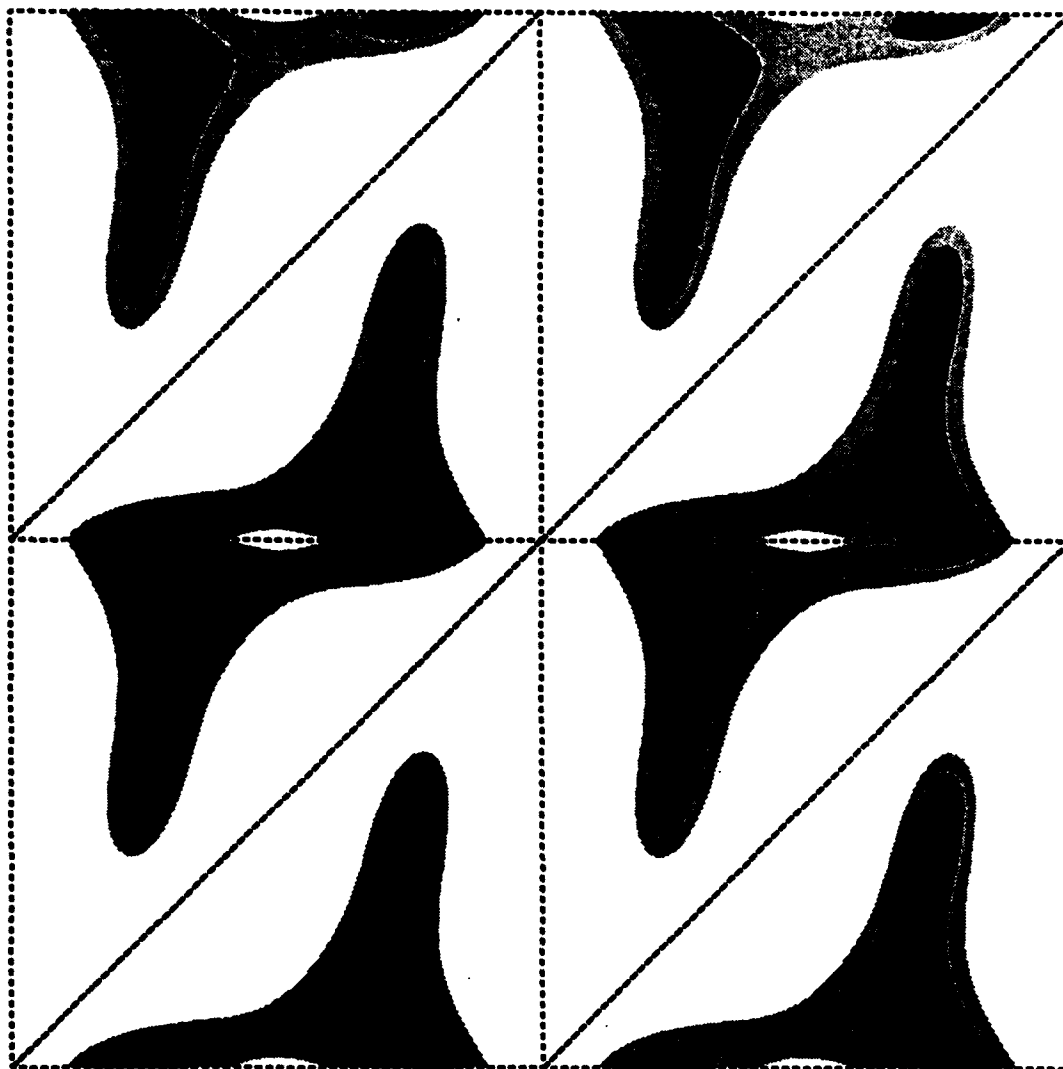
Fig. 13h



Harmonic solution $P = 2$
SIMPLIFIED L2 APPROACH



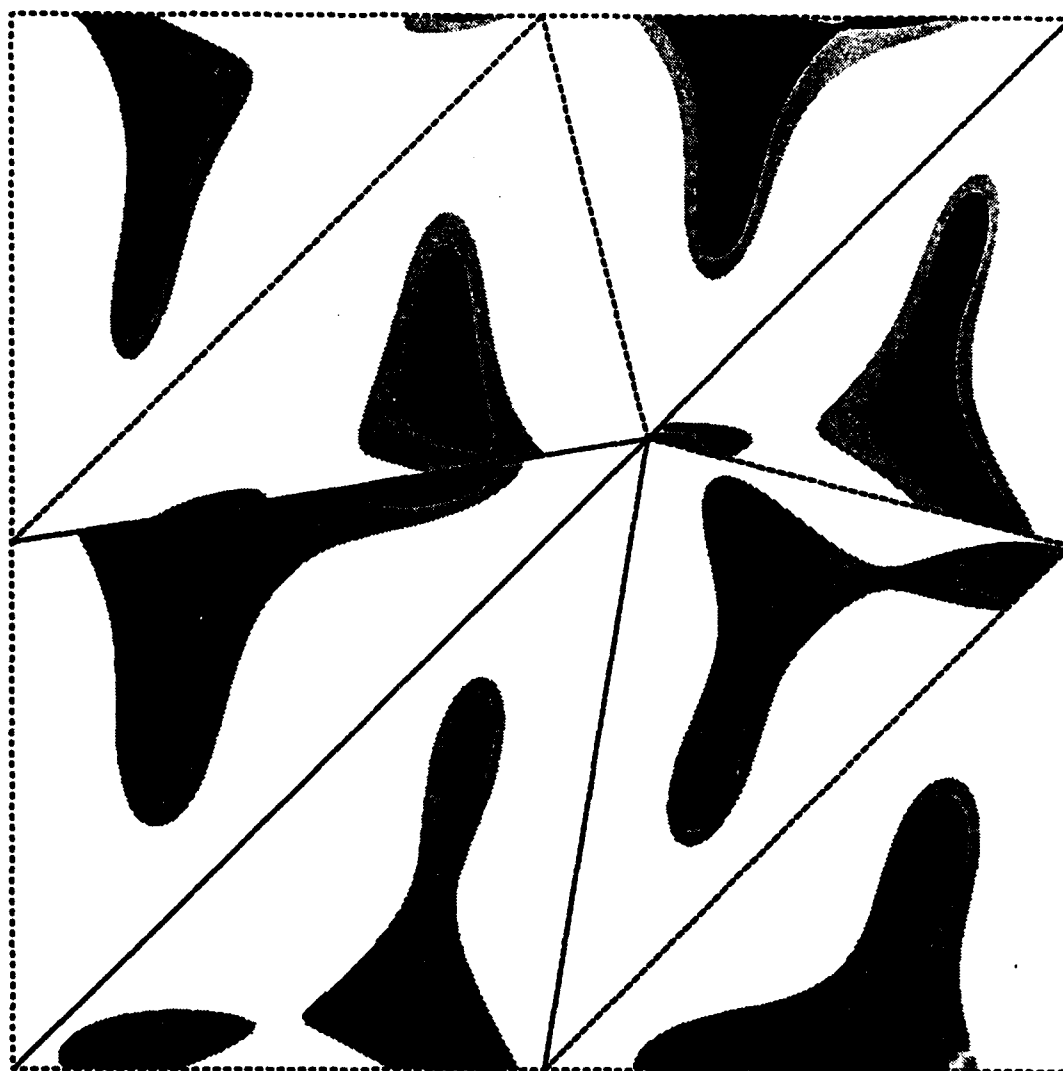
Fig. 14a



Harmonic solution $P = 2$
SIMPLIFIED L2 APPROACH



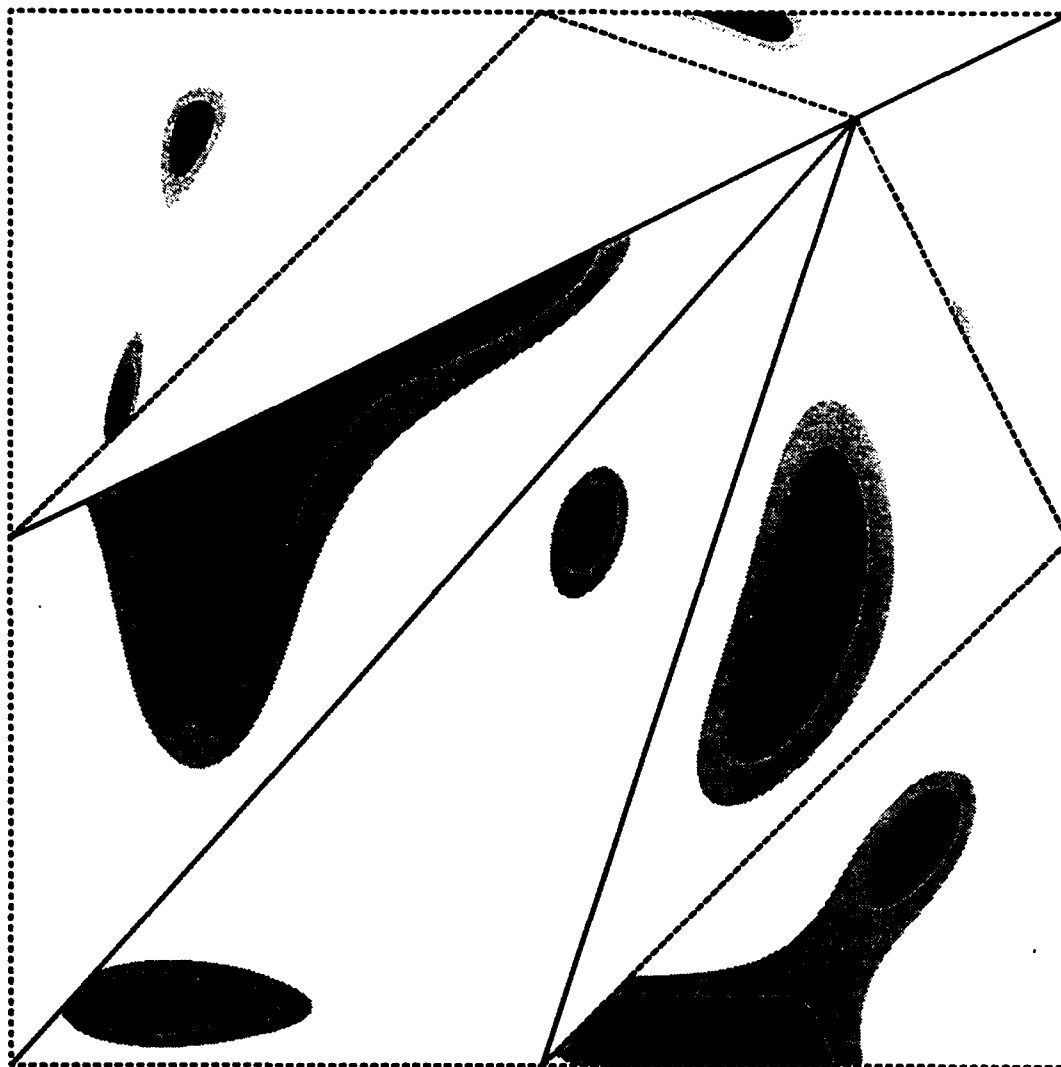
Fig. 14b



Harmonic solution $P = 2$
SIMPLIFIED L2 APPROACH



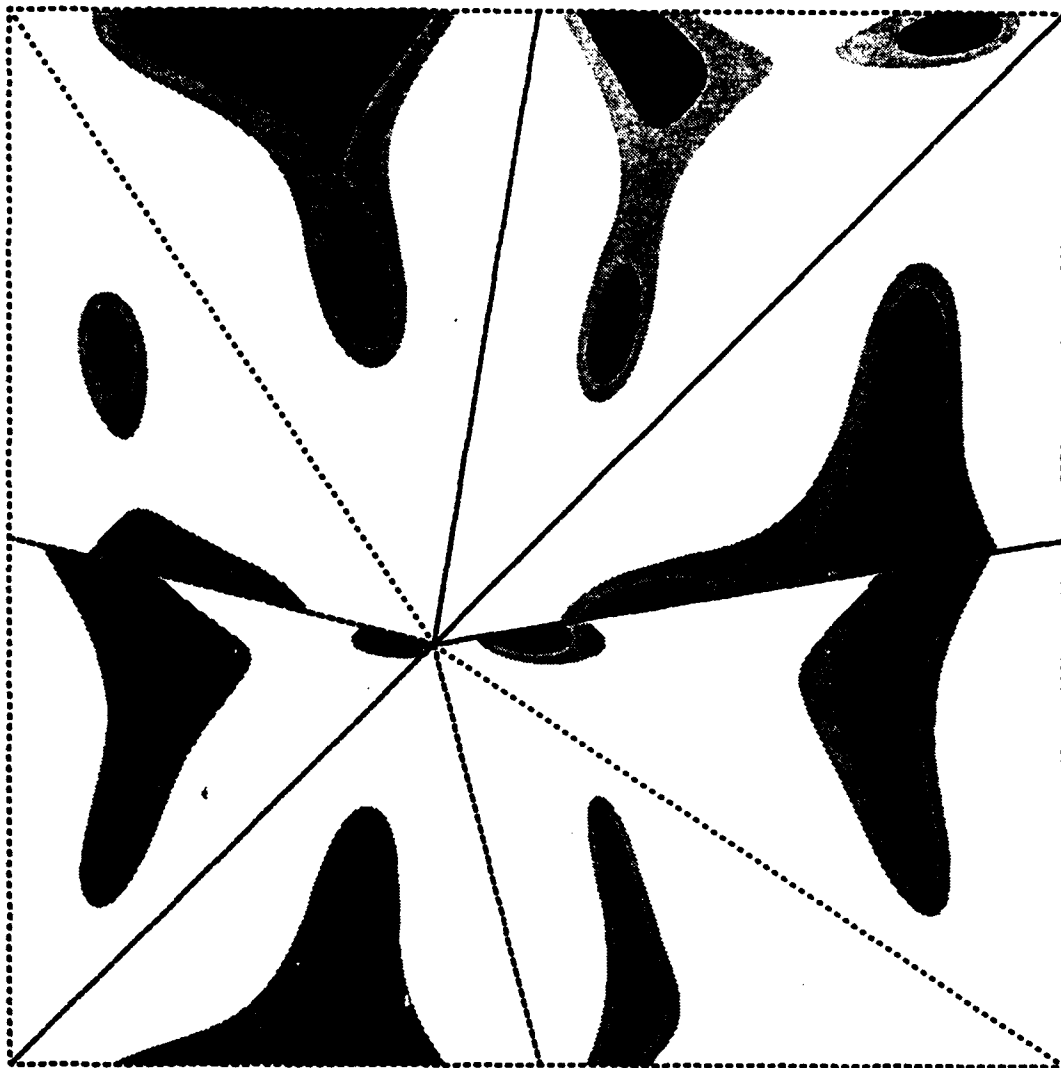
Fig. 14c



Harmonic solution $P = 2$
SIMPLIFIED L2 APPROACH



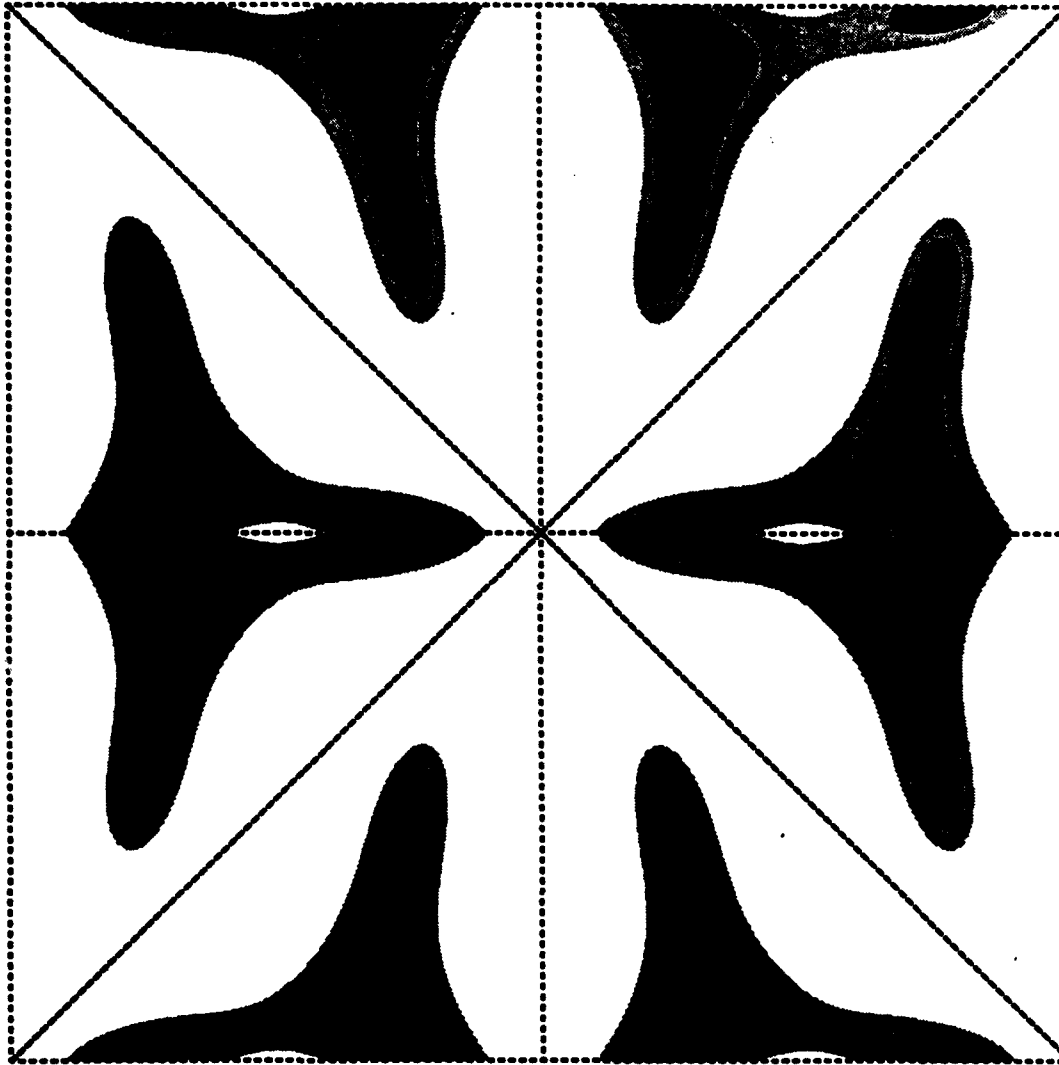
Fig. 14d



Harmonic solution $P = 2$
SIMPLIFIED L2 APPROACH

0.0%
10.0%
20.0%
30.0%

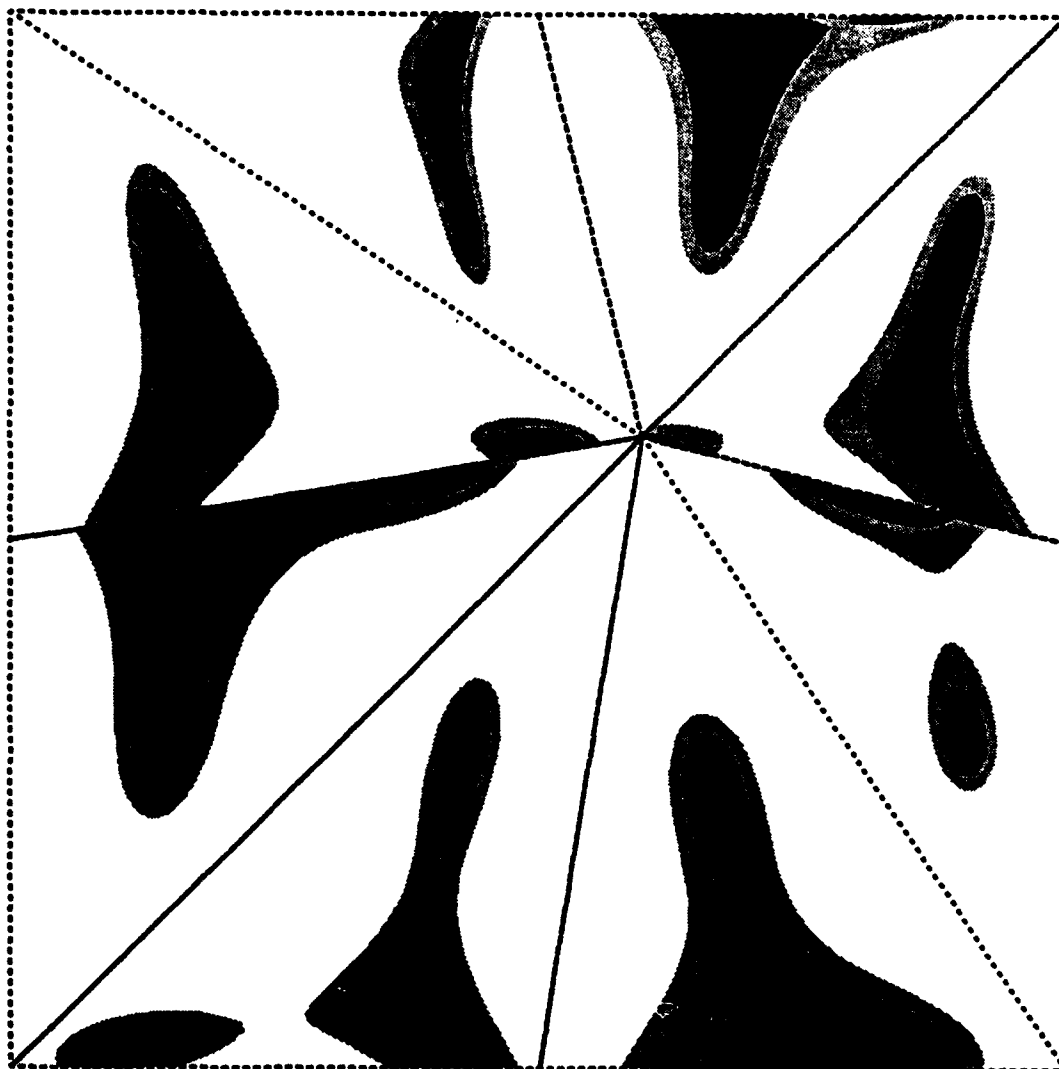
Fig. 15a



Harmonic solution $P = 2$
SIMPLIFIED L2 APPROACH



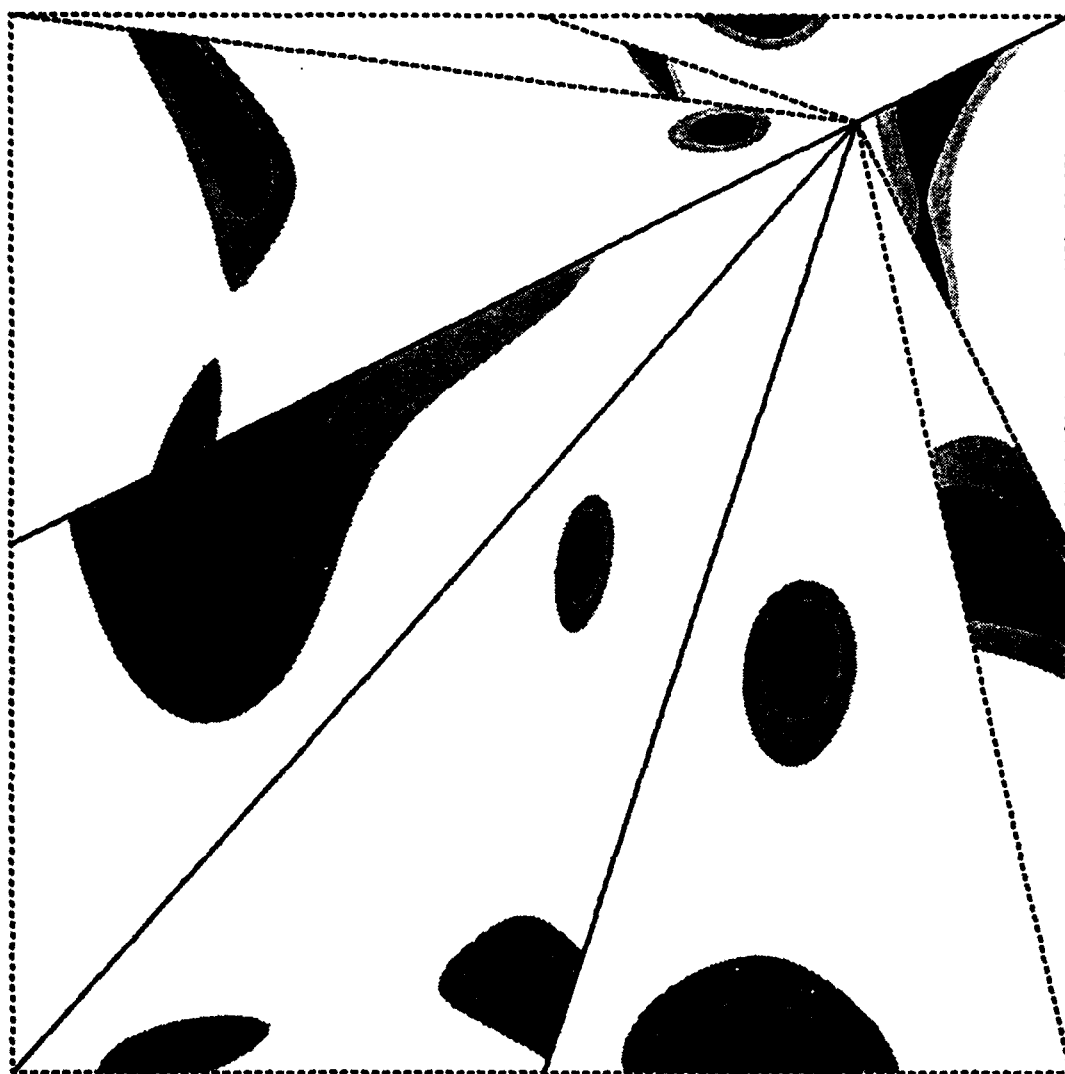
Fig. 15b



Harmonic solution $P = 2$
SIMPLIFIED L2 APPROACH



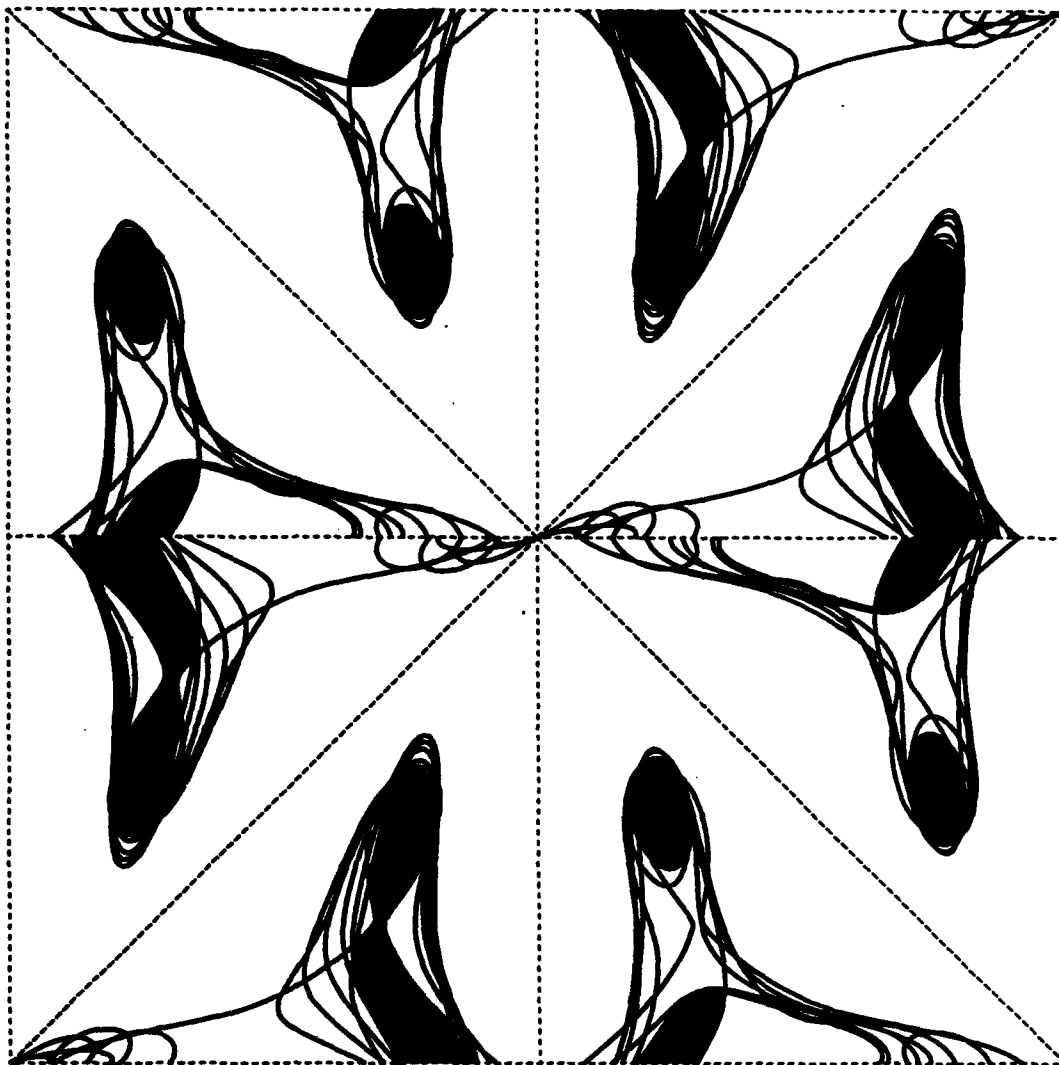
Fig. 15c



Harmonic solution $P = 2$
SIMPLIFIED L2 APPROACH

0.0%
10.0%
20.0%
30.0%

Fig. 15d

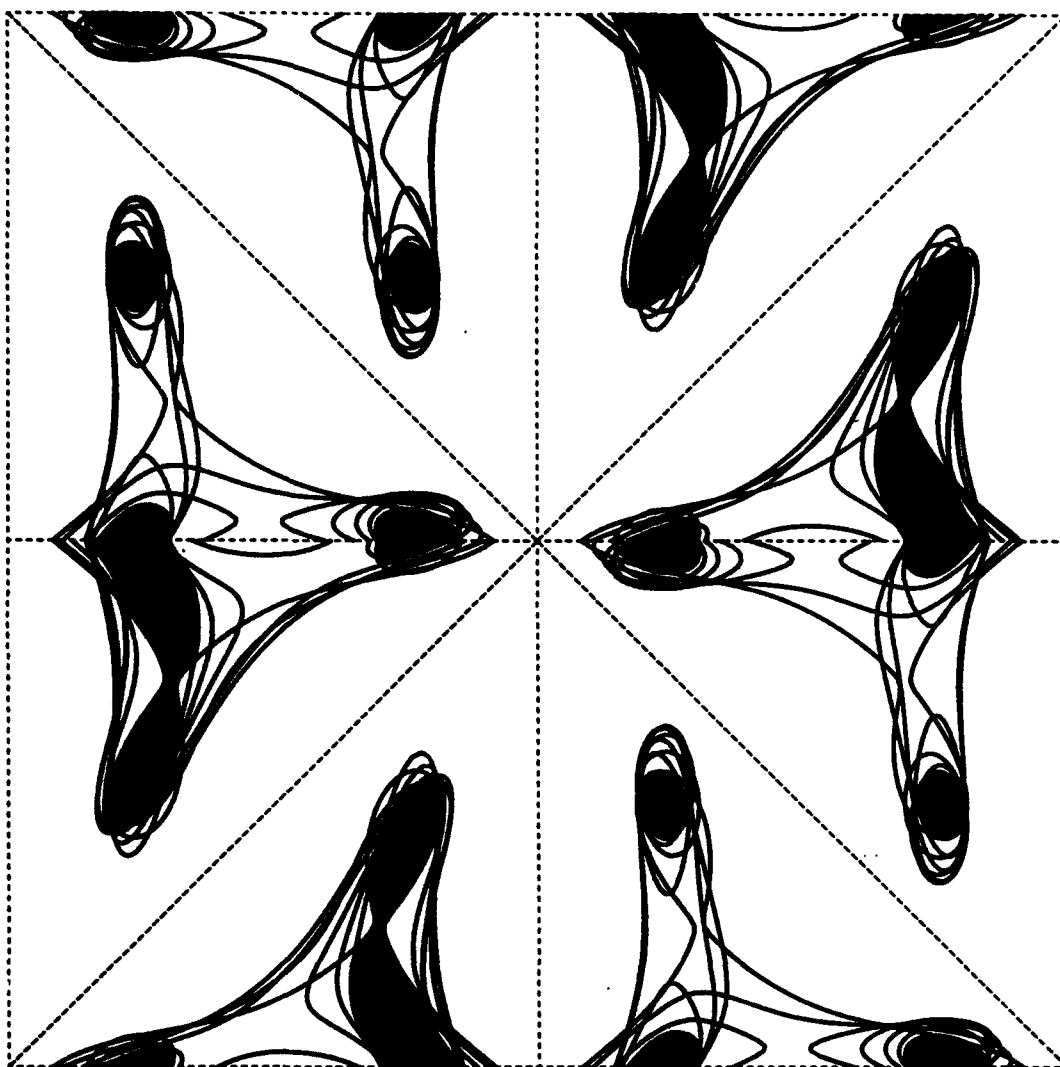


Harmonic solution

$P = 2$

— 25.0 % contour

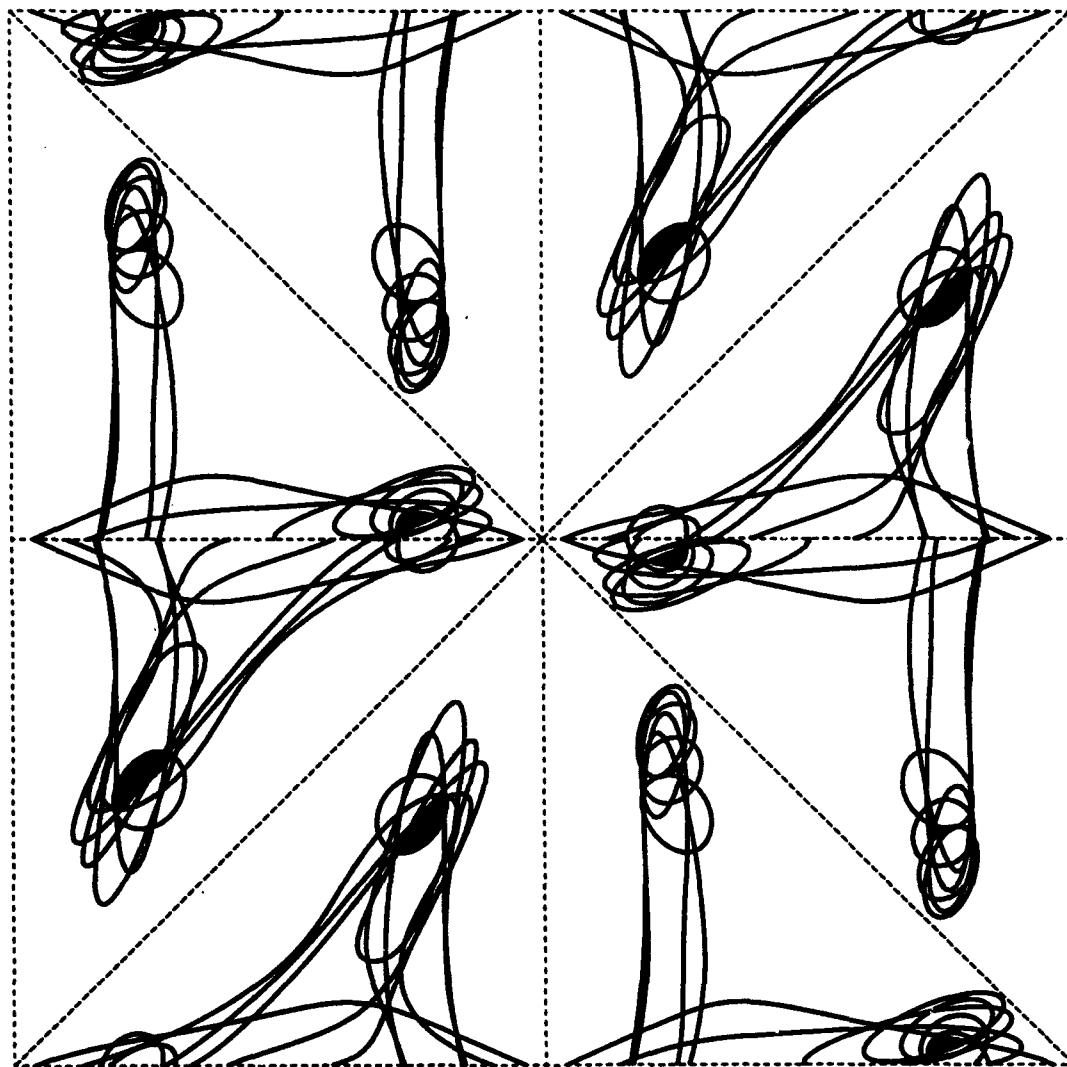
Fig. 16



Harmonic solution

Fig. 17

— 25.0 % contour



Harmonic solution

$P = 2$

— 25.0 % contour

Fig. 18

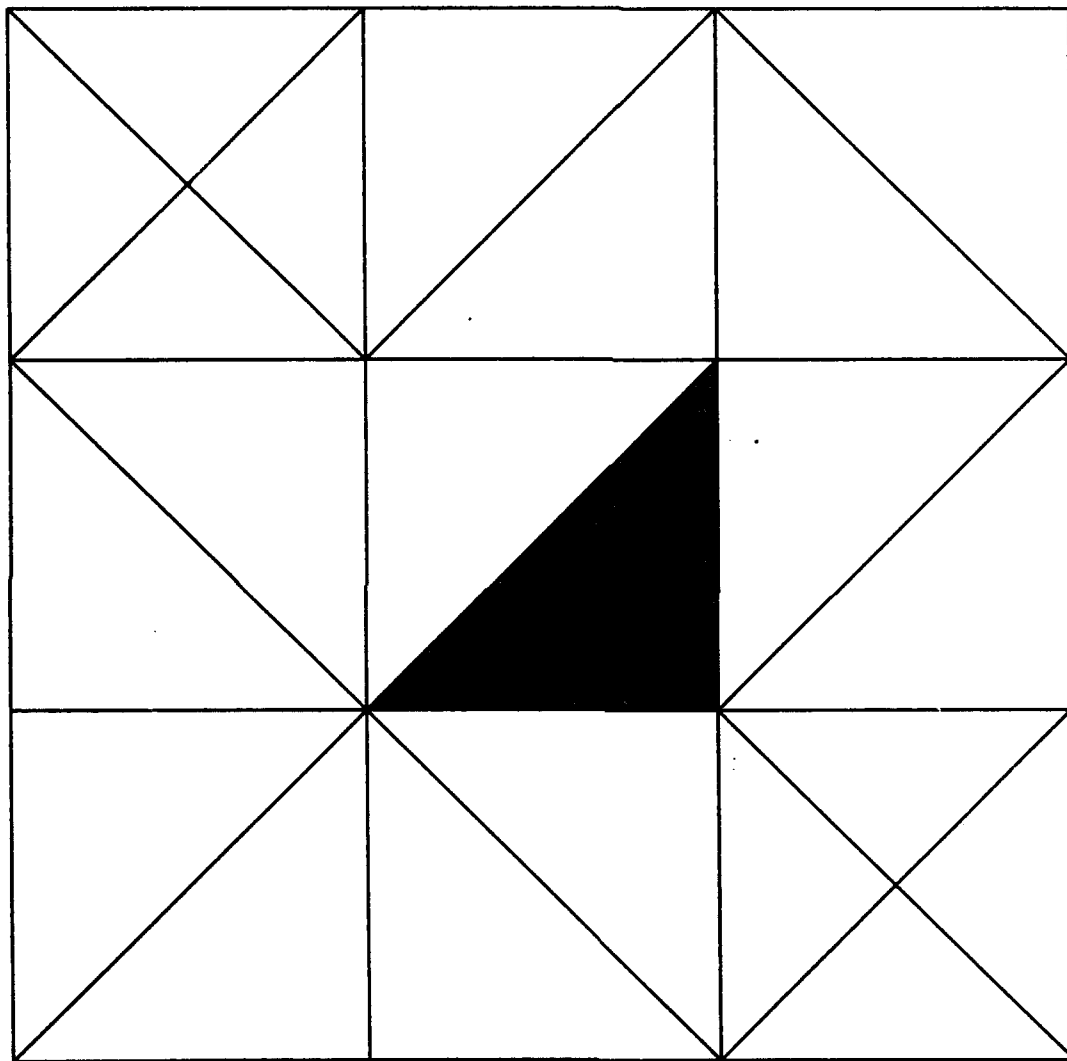


Fig. 19a

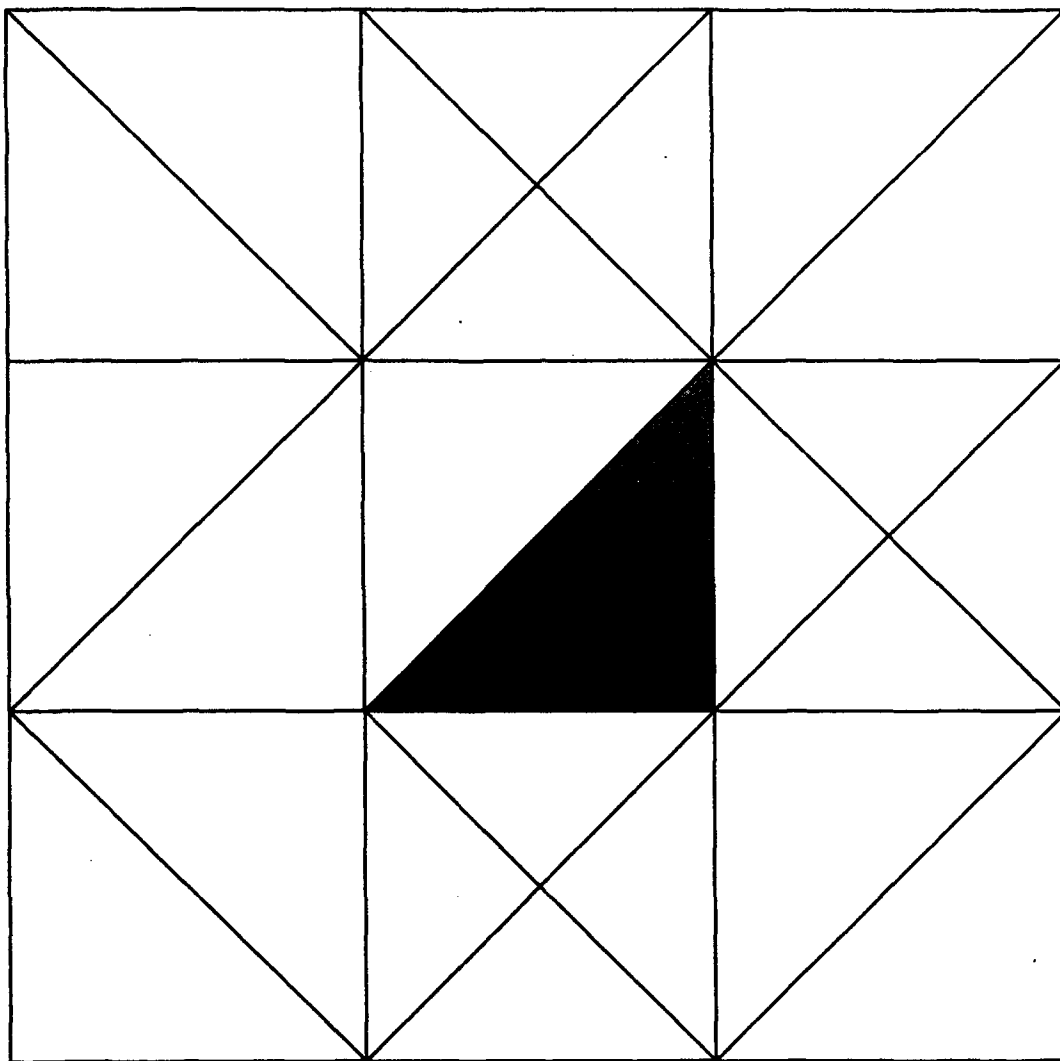


Fig. 19b

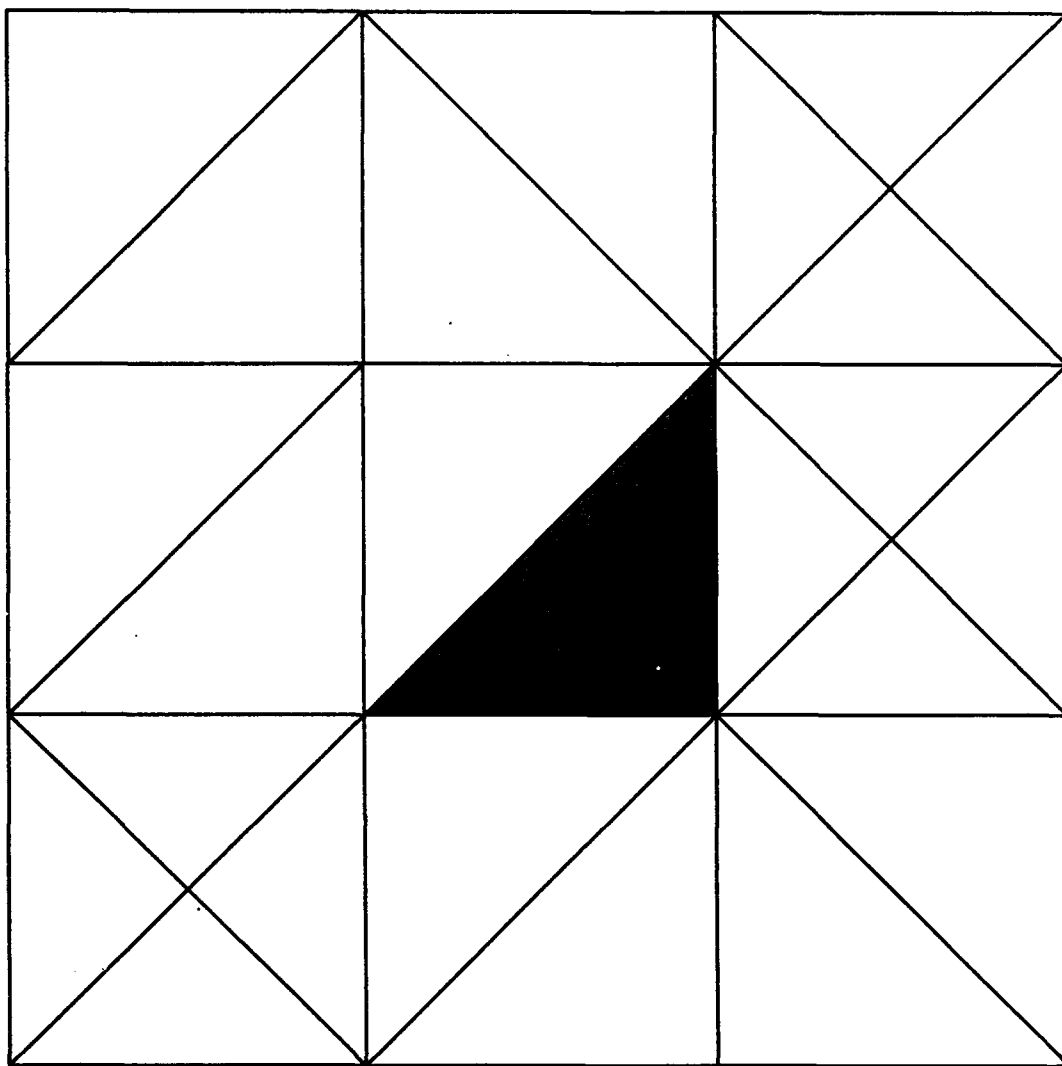


Fig. 19c

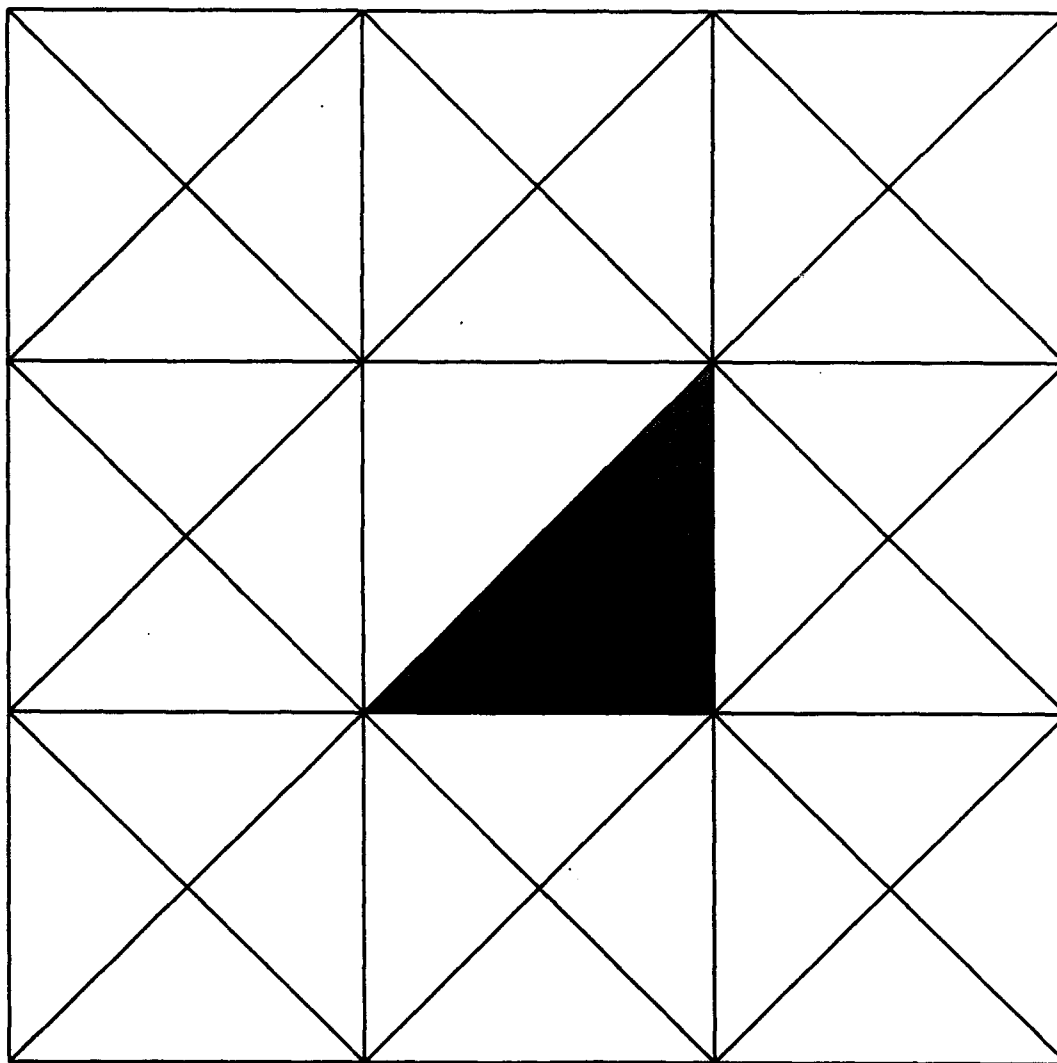


Fig. 19d

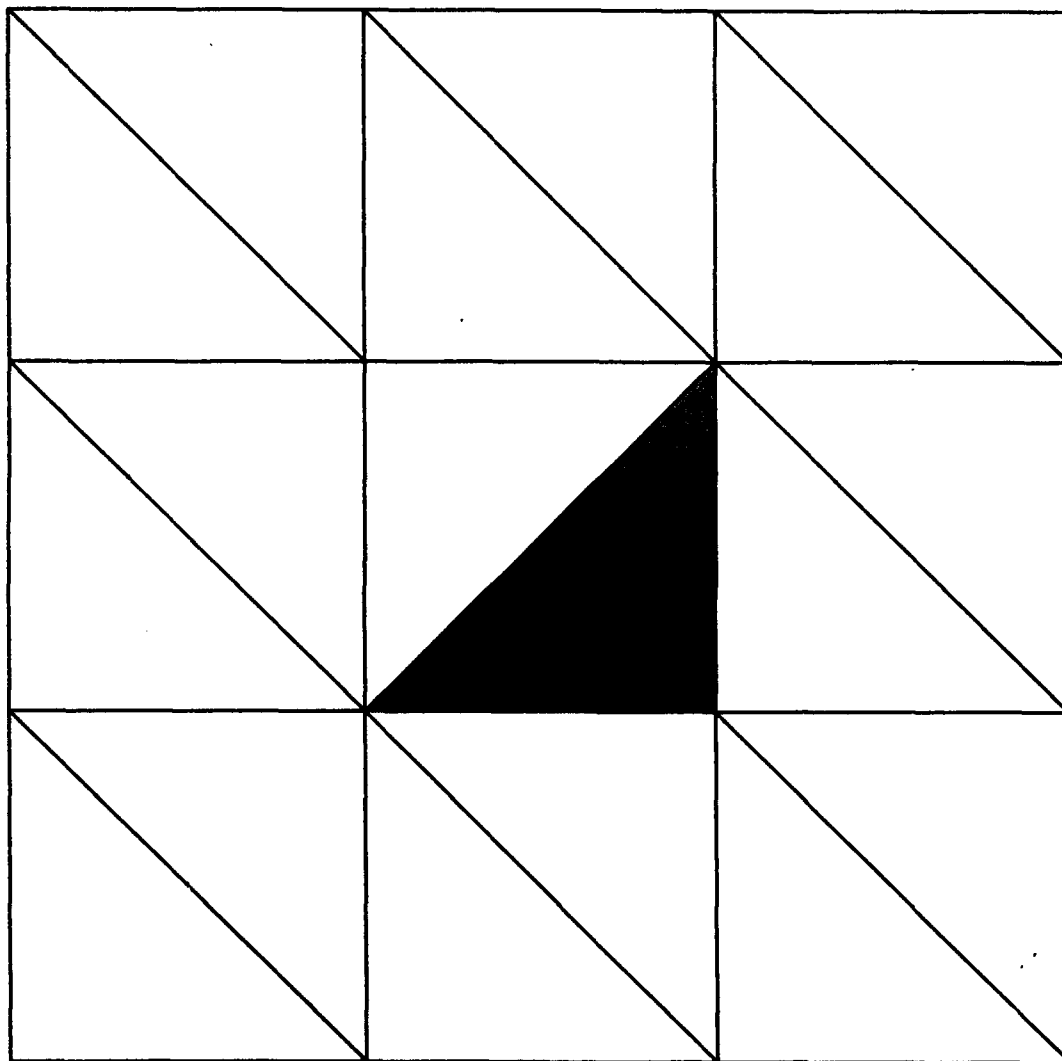
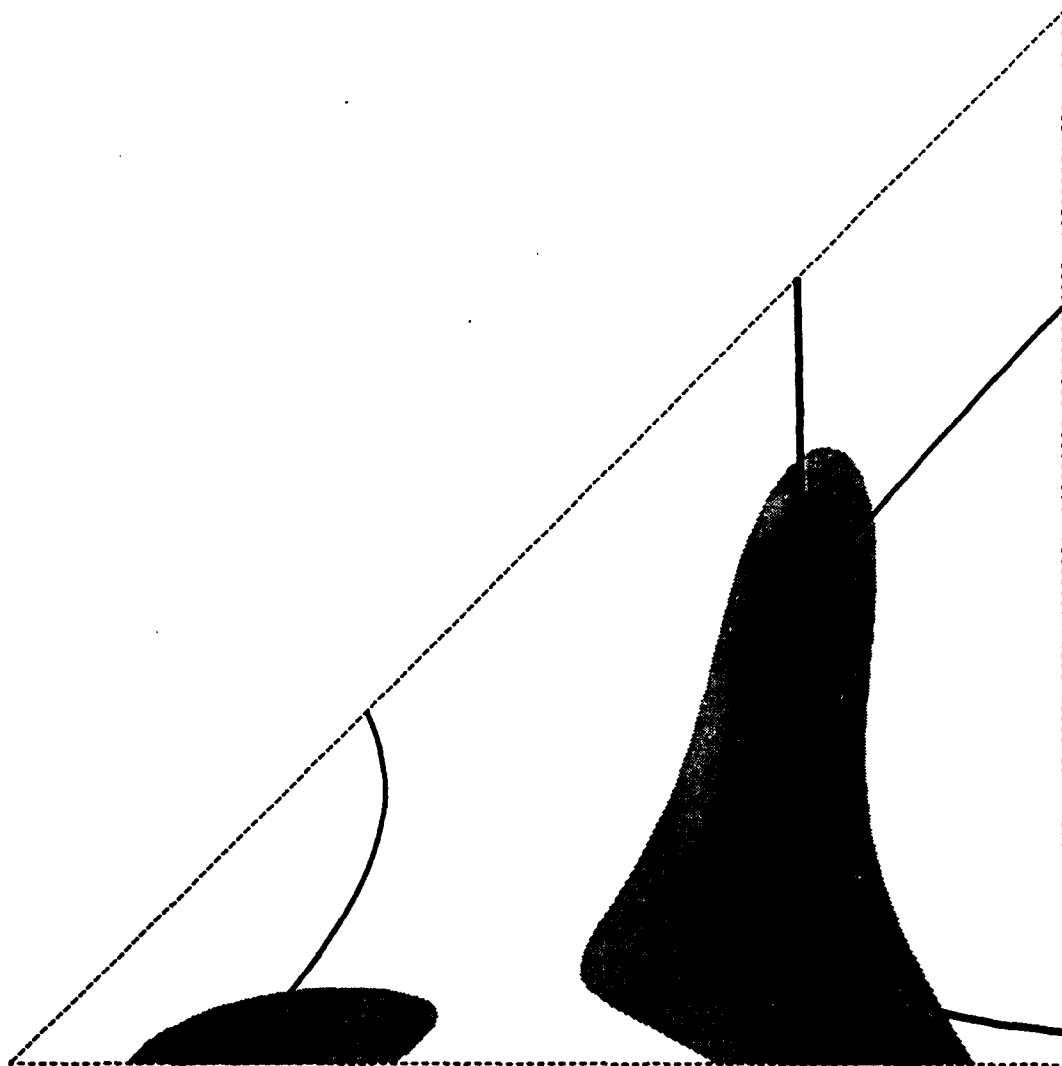


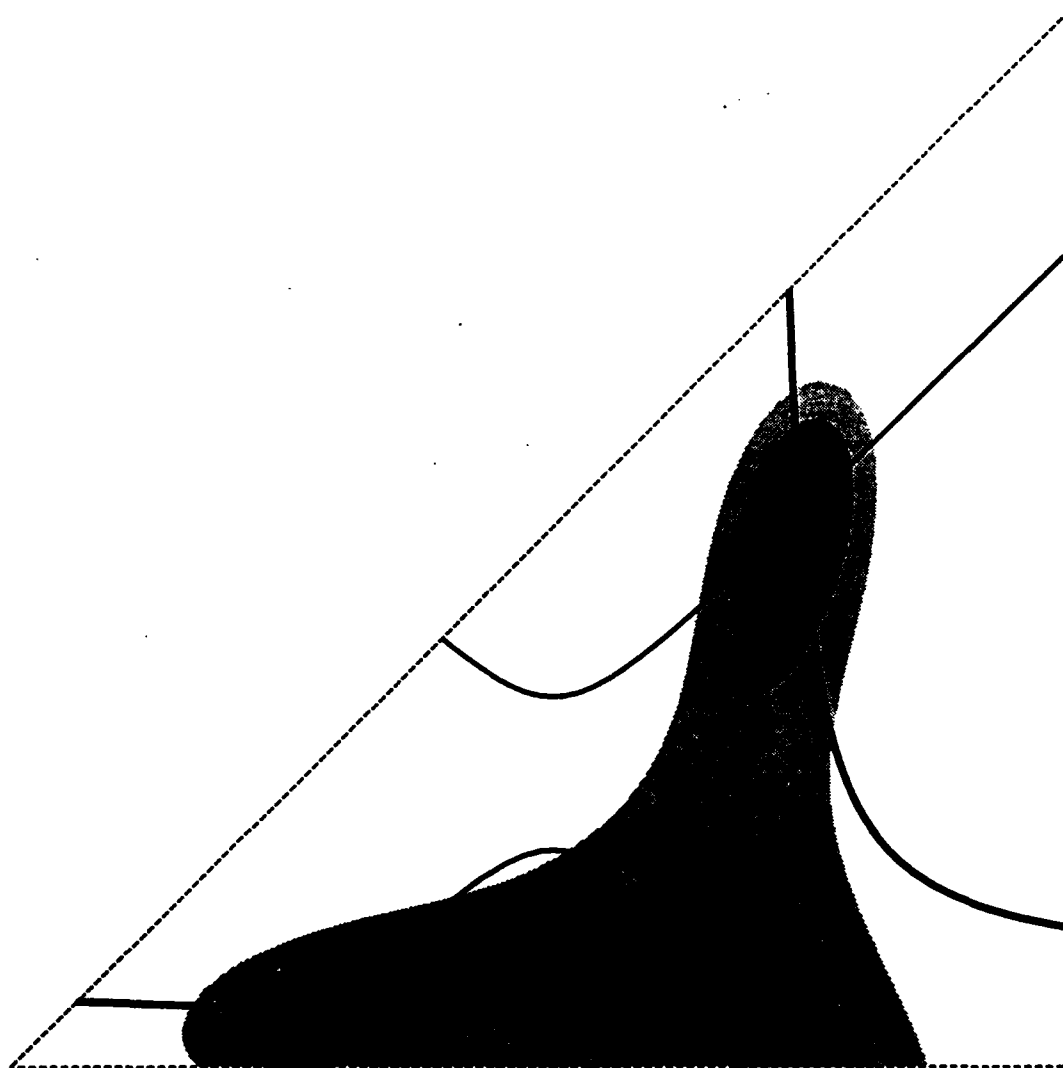
Fig. 19e



Harmonic solution **P = 2**
SIMPLIFIED L2 APPROACH

— **Function Q1**
 — **Function Q2**

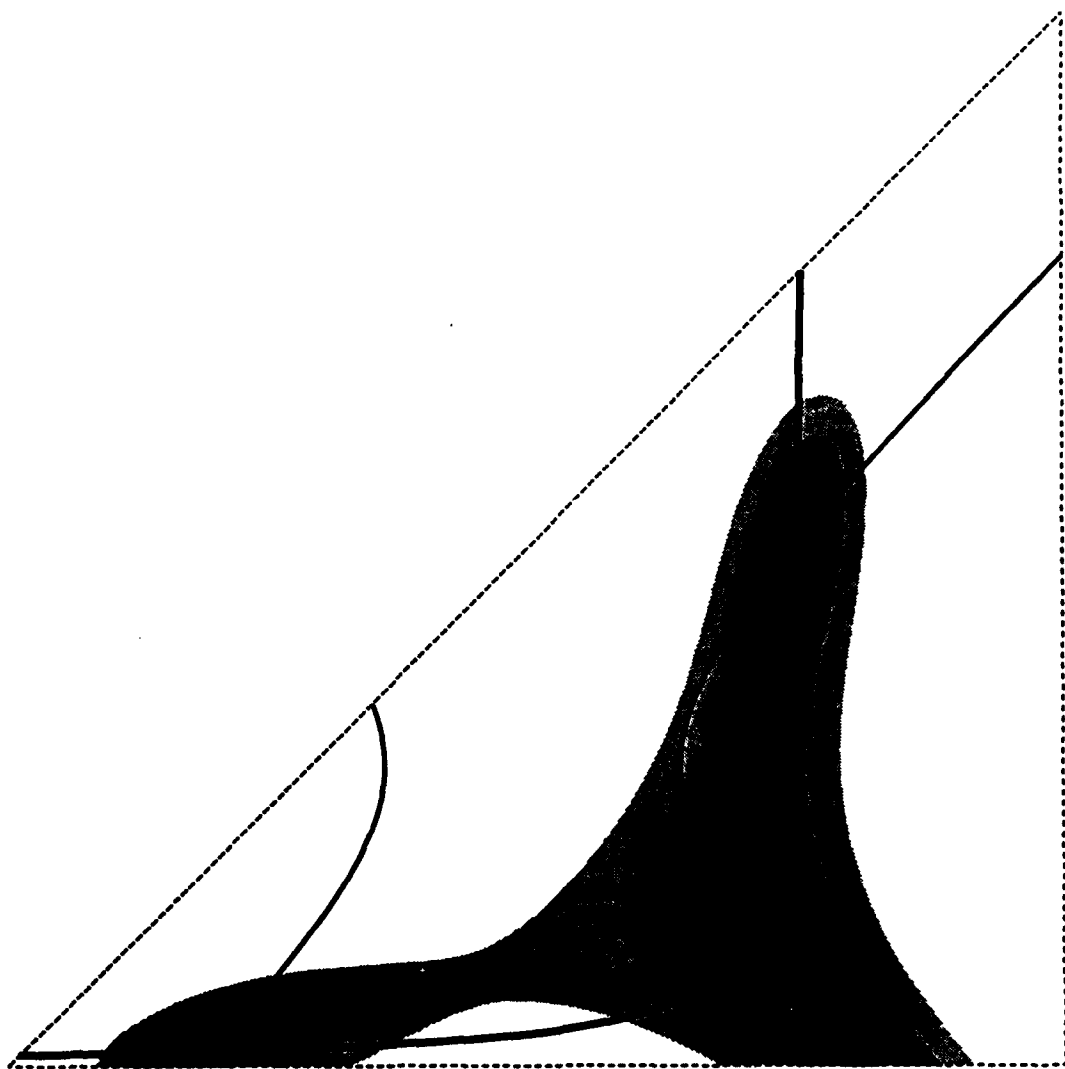
Fig. 20a



Harmonic solution $P = 2$
SIMPLIFIED L2 APPROACH

— *Function Q1*
 — *Function Q2*

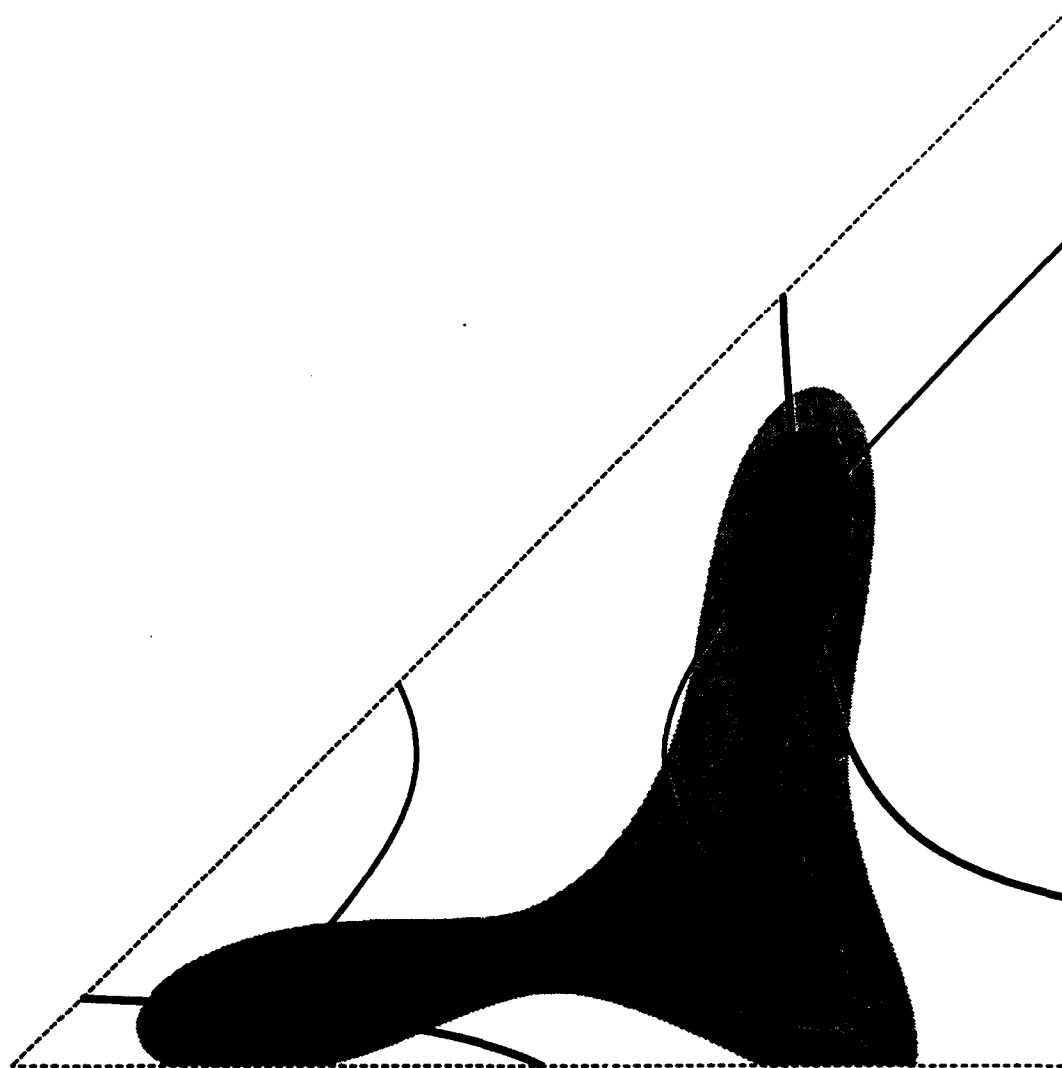
Fig. 20b



Harmonic solution $P = 2$
SIMPLIFIED L2 APPROACH

— *Function Q1*
 — *Function Q2*

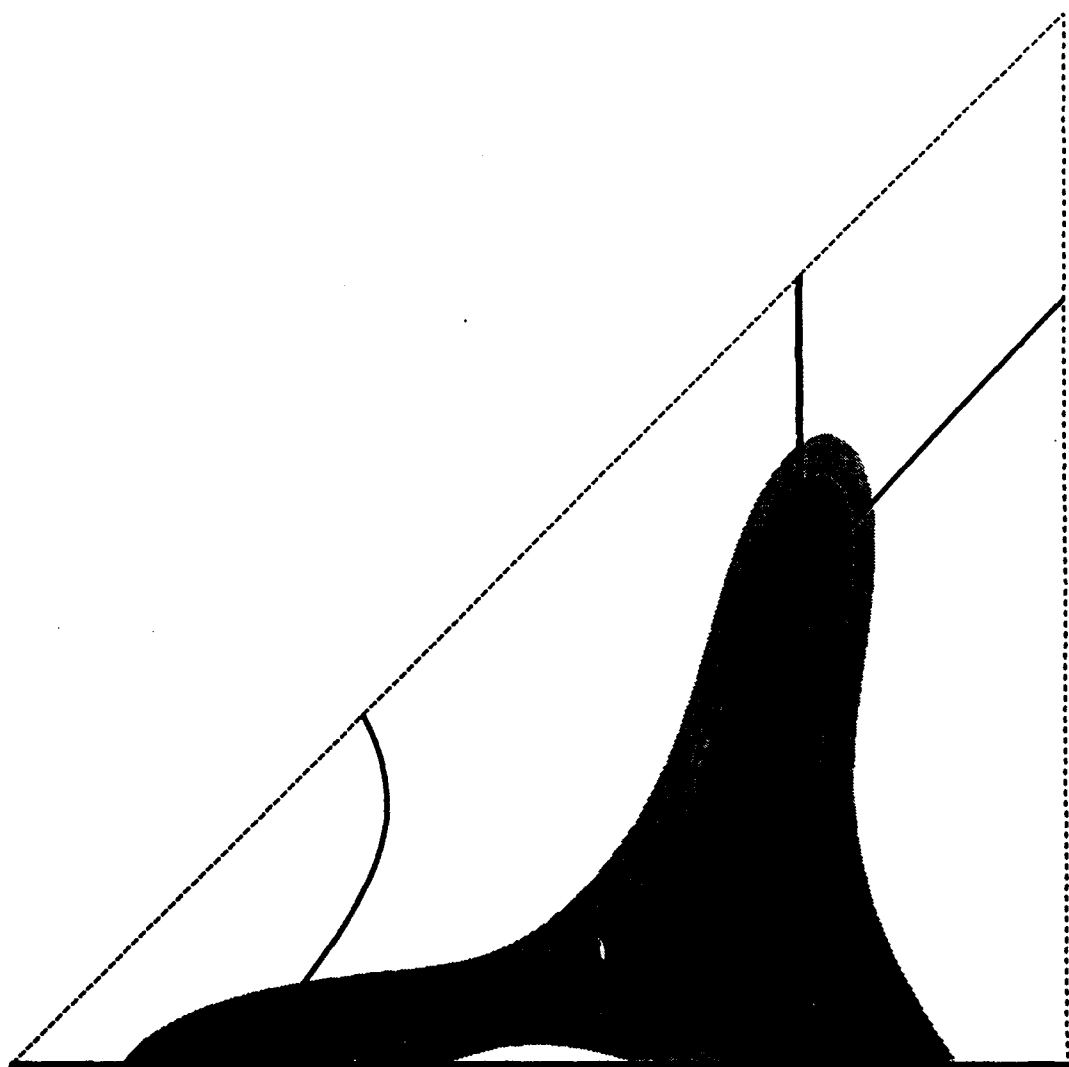
Fig. 20c



Harmonic solution **$P = 2$**
SIMPLIFIED L2 APPROACH

— ***Function Q1***
 — ***Function Q2***

Fig. 20d

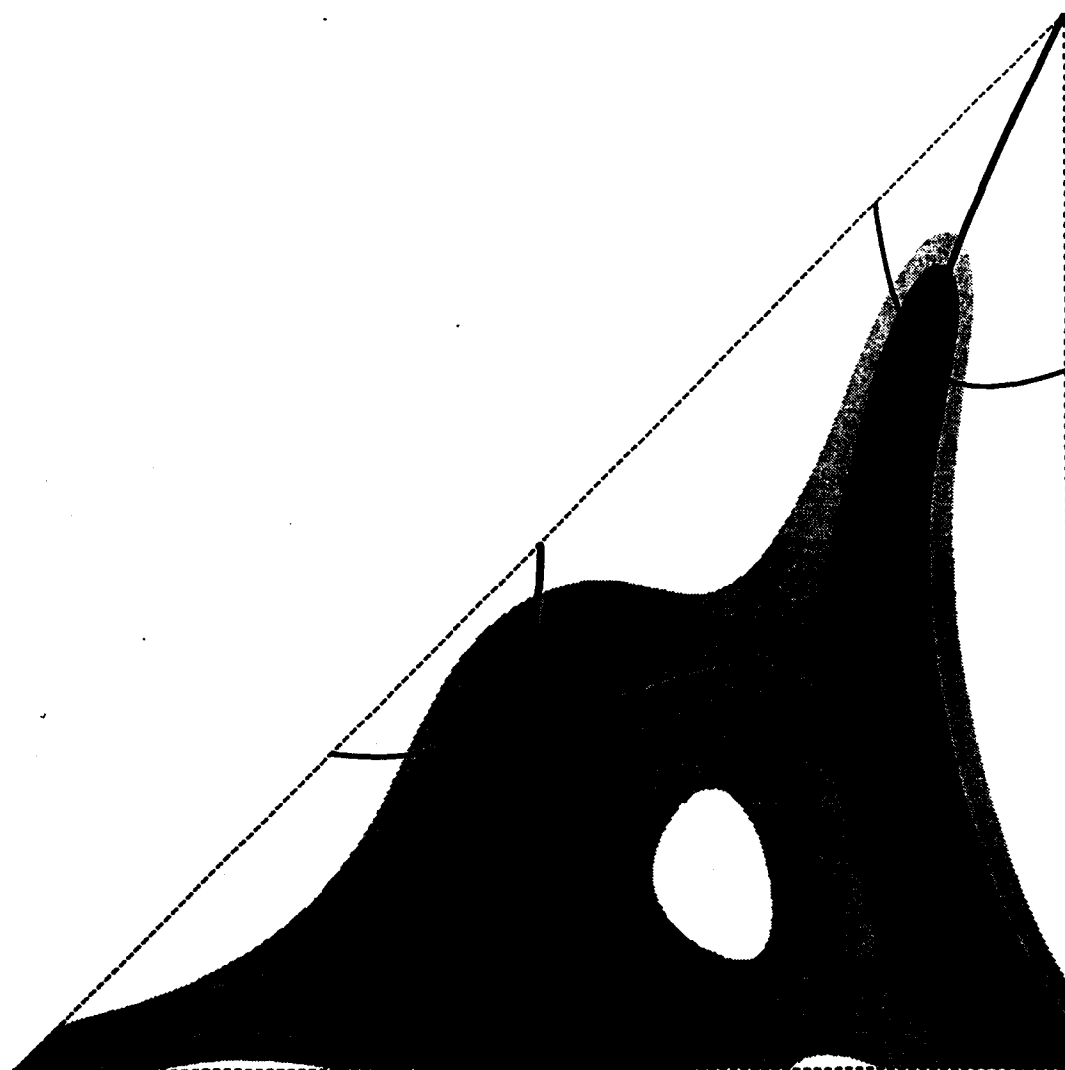


Harmonic solution **P = 2**
SIMPLIFIED L2 APPROACH



— **Function Q1**
 — **Function Q2**

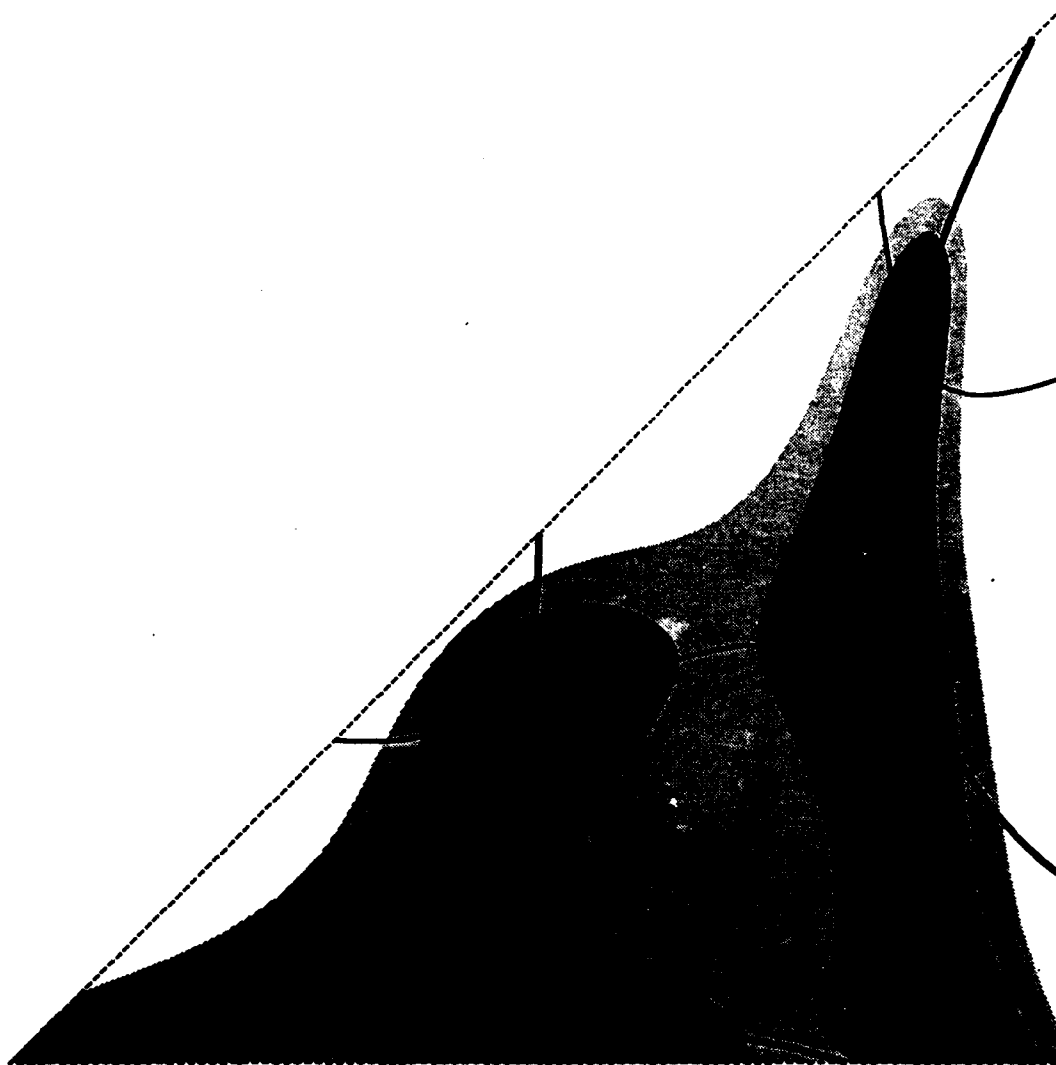
Fig. 20e



Harmonic solution $P = 3$
SIMPLIFIED L2 APPROACH

— *Function Q1*
— *Function Q2*

Fig. 21a

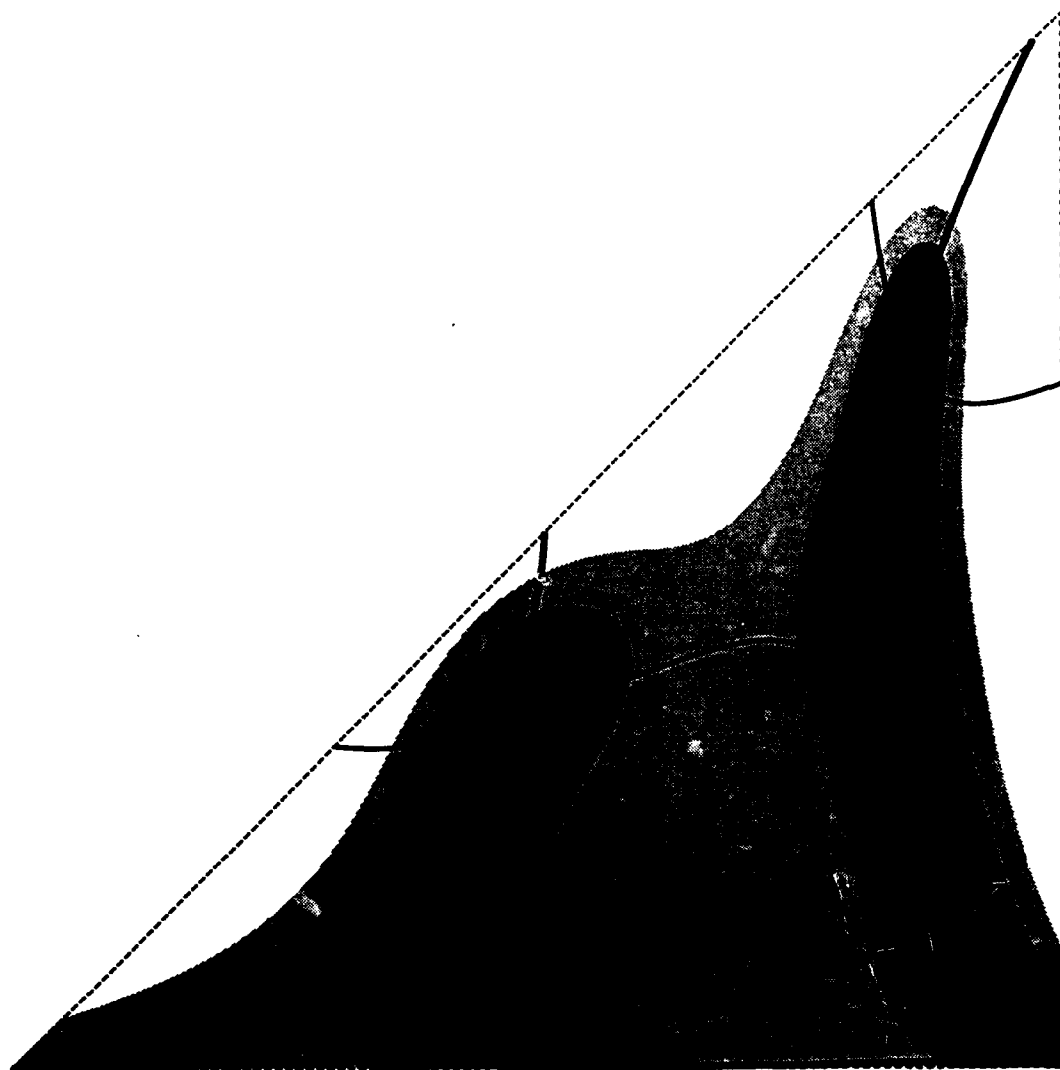


Harmonic solution $P = 3$
SIMPLIFIED L2 APPROACH



— *Function Q1*
 — *Function Q2*

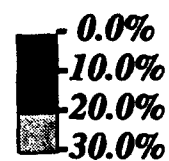
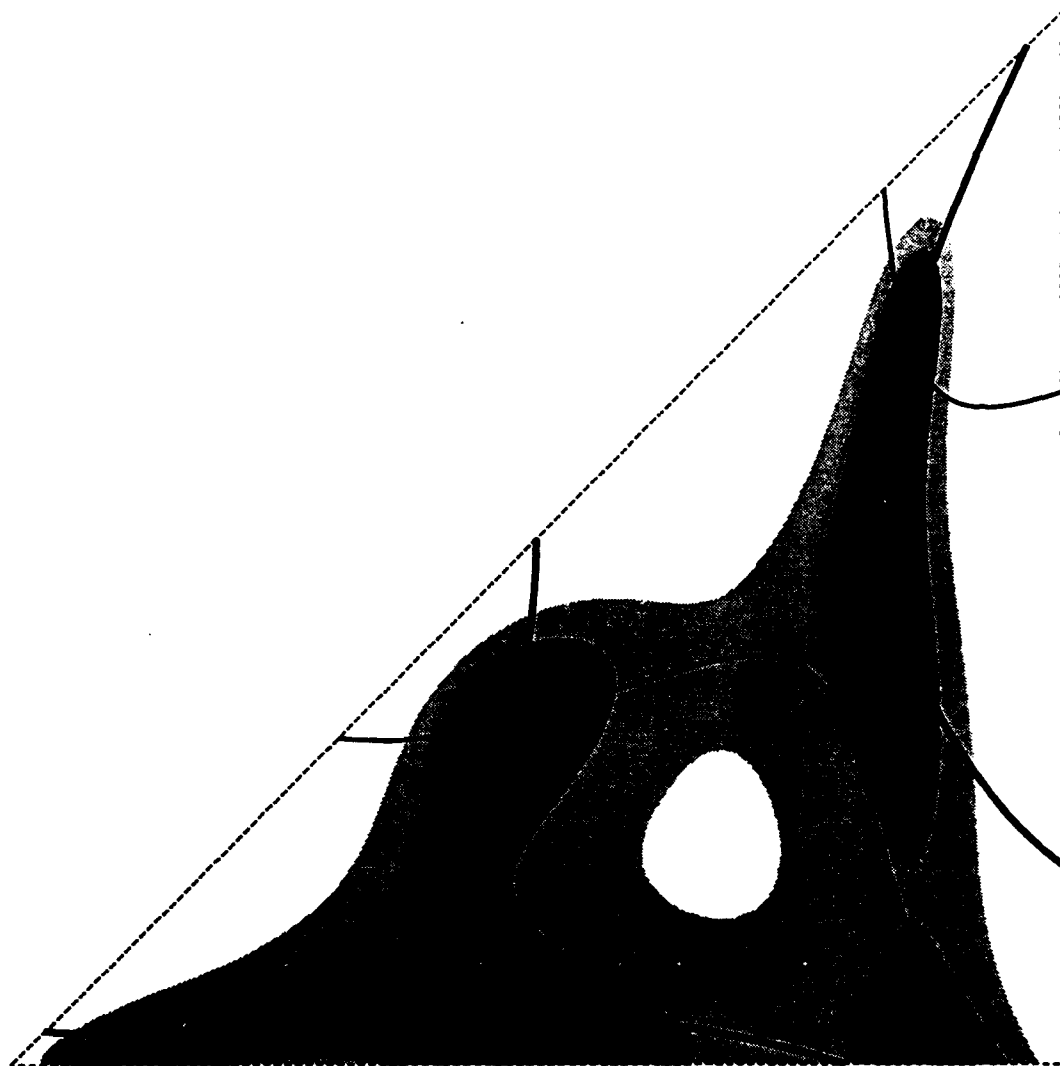
Fig. 21b



Harmonic solution $P = 3$
SIMPLIFIED L2 APPROACH

— *Function Q1*
 — *Function Q2*

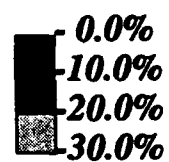
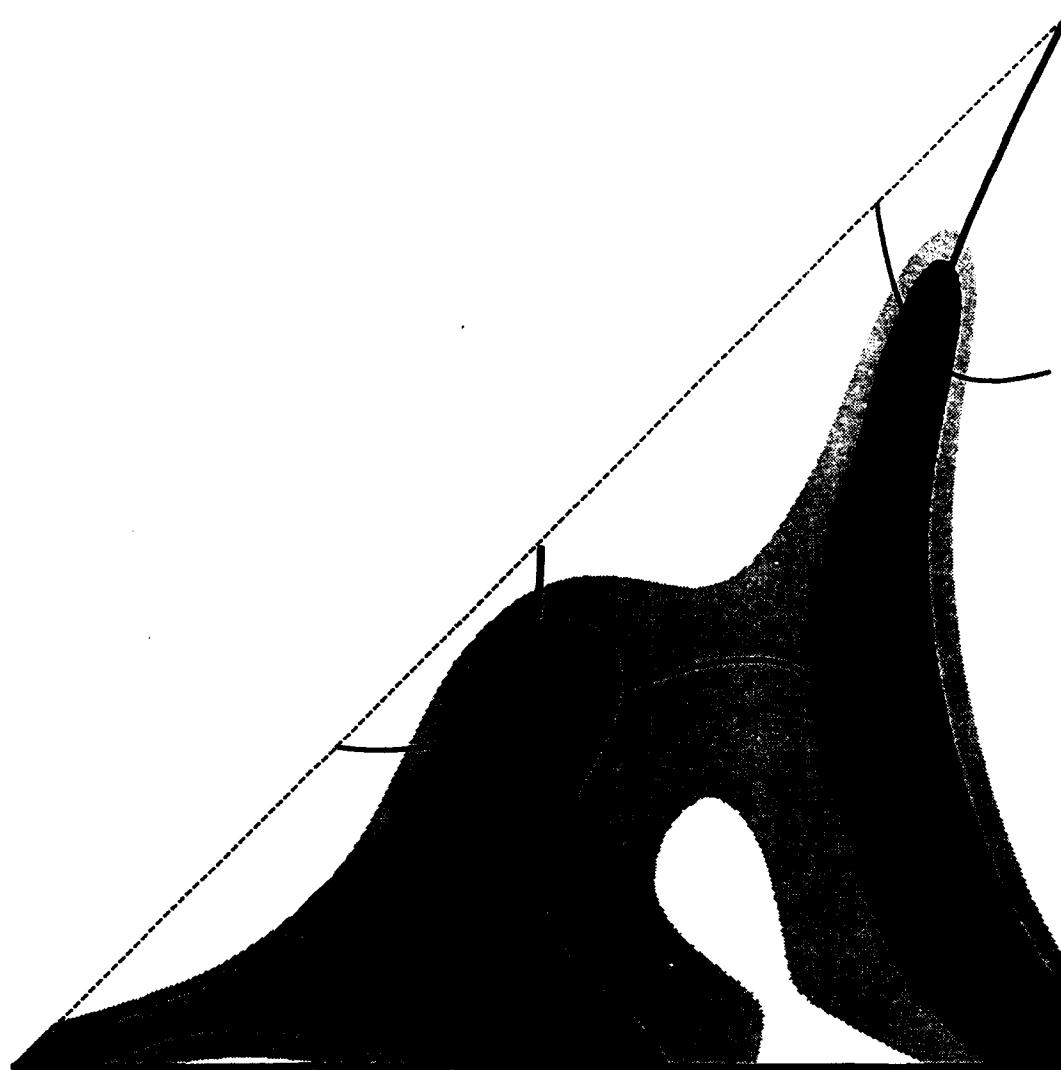
Fig. 21c



Harmonic solution $P = 3$
SIMPLIFIED L2 APPROACH

— *Function Q1*
 — *Function Q2*

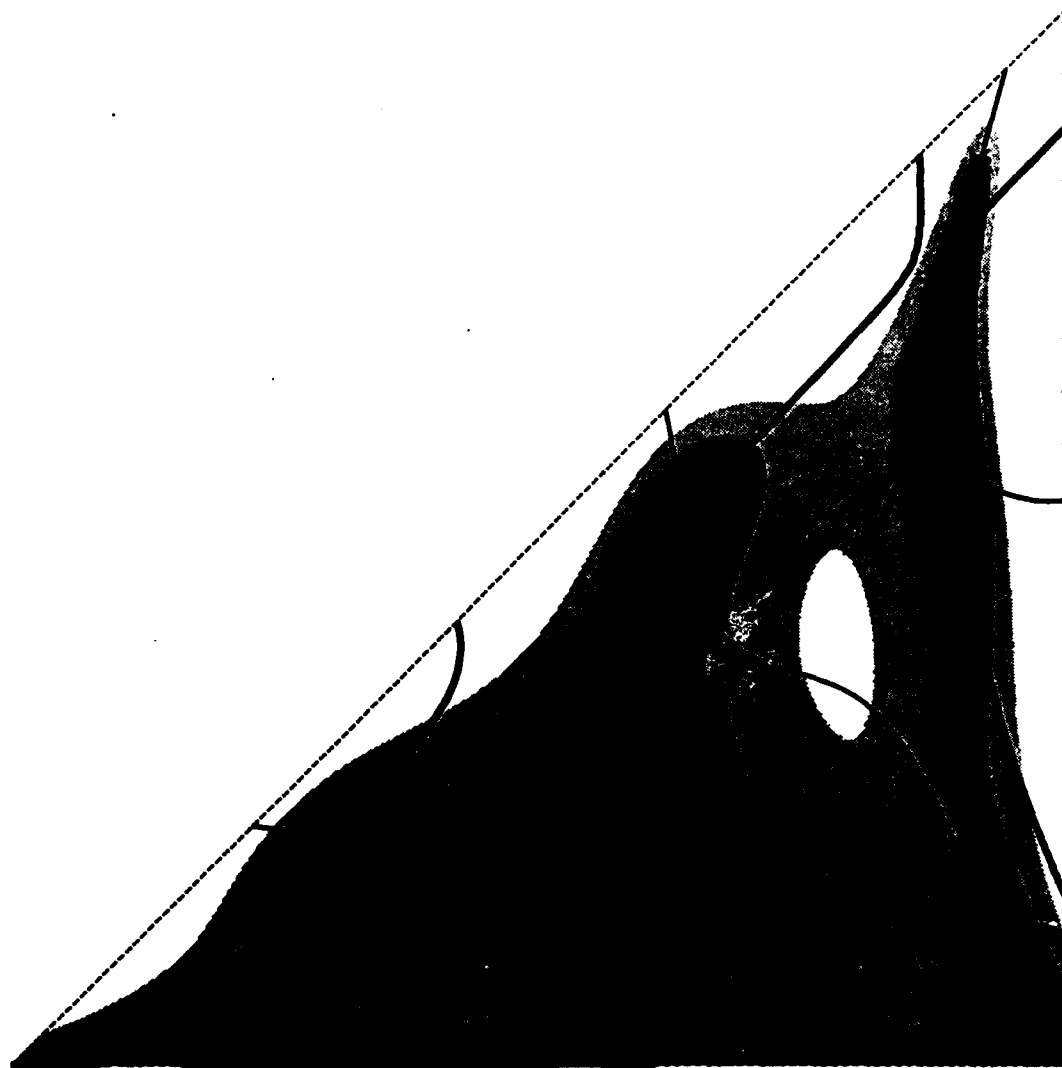
Fig. 21d



Harmonic solution $P = 3$
SIMPLIFIED L2 APPROACH

— *Function Q1*
 — *Function Q2*

Fig. 21e

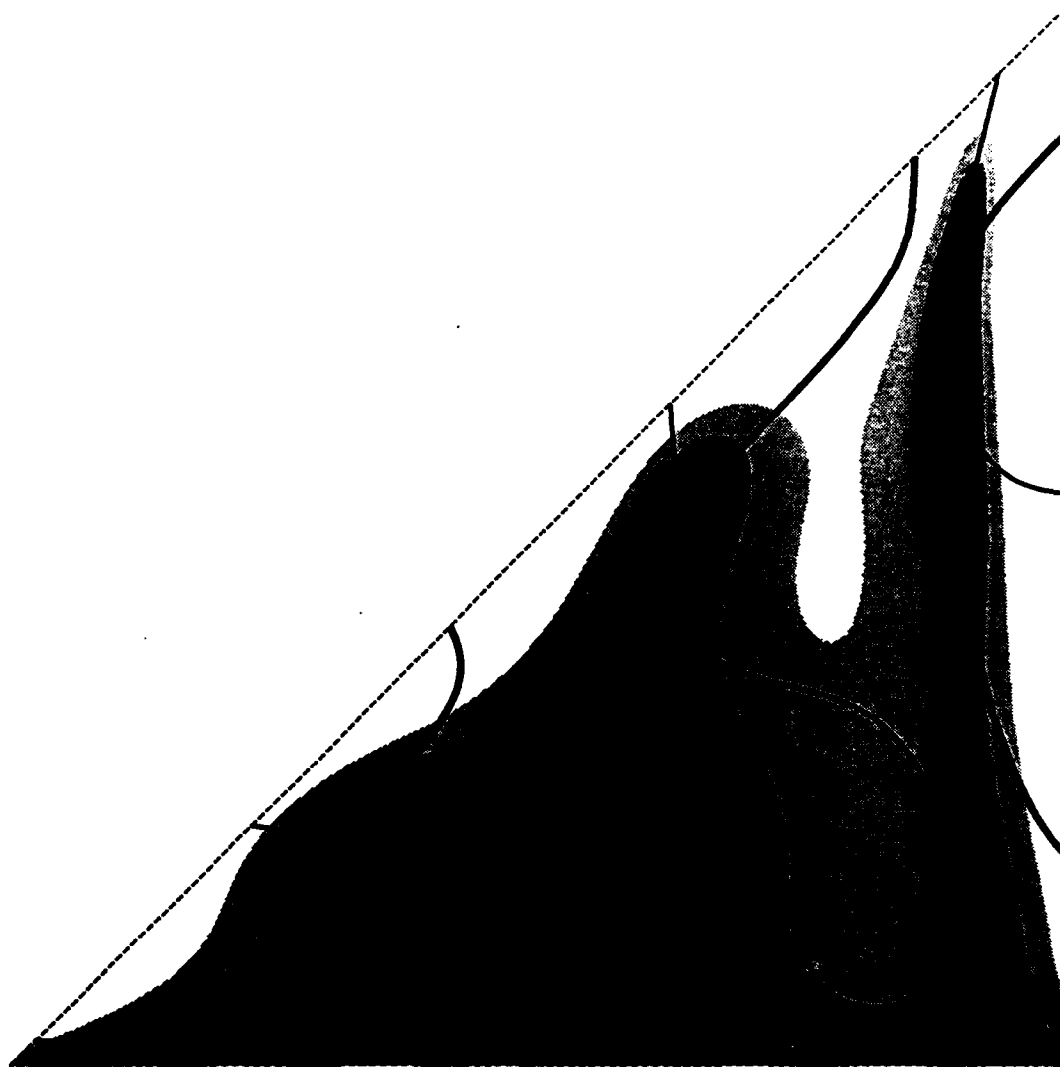


Harmonic solution $P = 4$
SIMPLIFIED L2 APPROACH

— 0.0%
 — 10.0%
 — 20.0%
 — 30.0%

— *Function Q1*
 — *Function Q2*

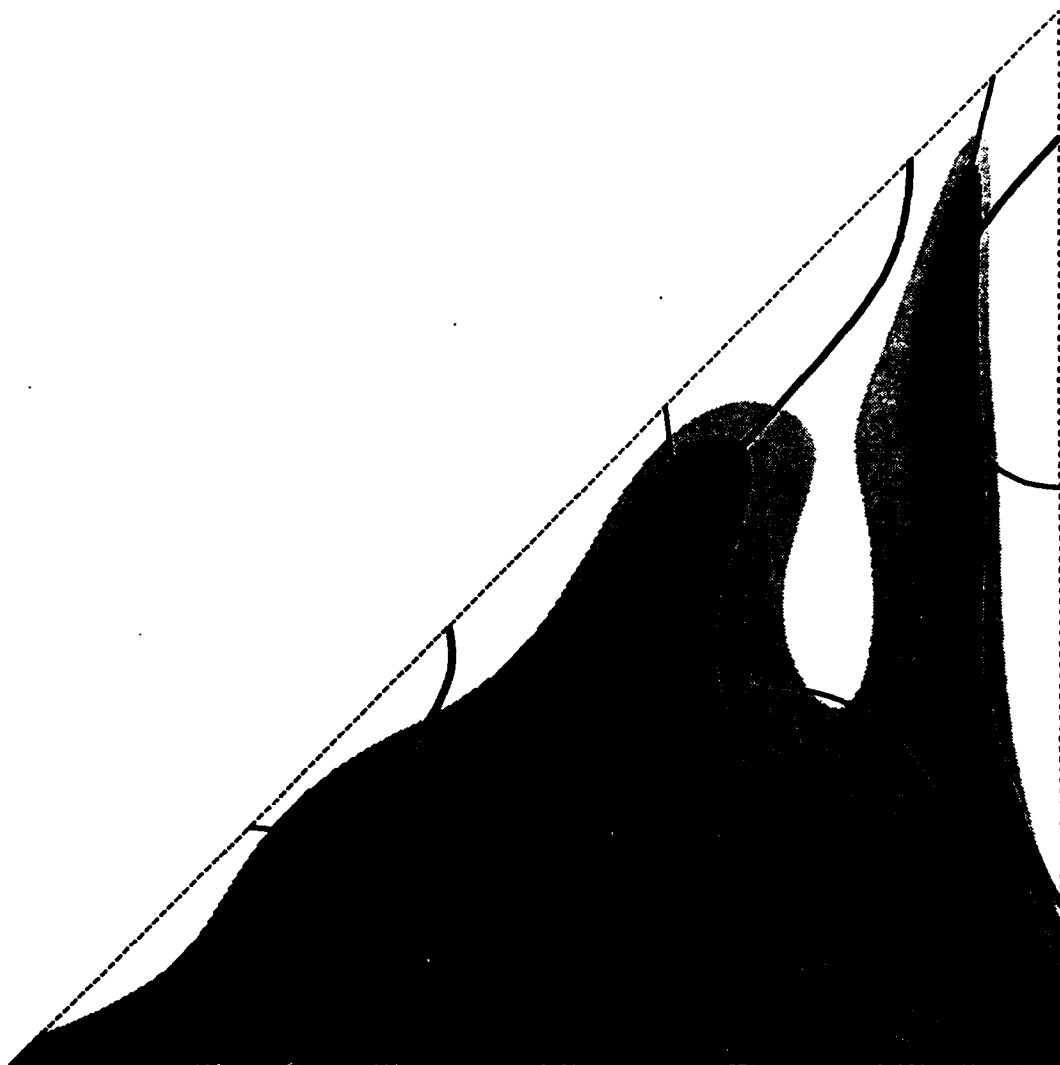
Fig. 22a



Harmonic solution $P = 4$
SIMPLIFIED L2 APPROACH

— *Function Q1*
 — *Function Q2*

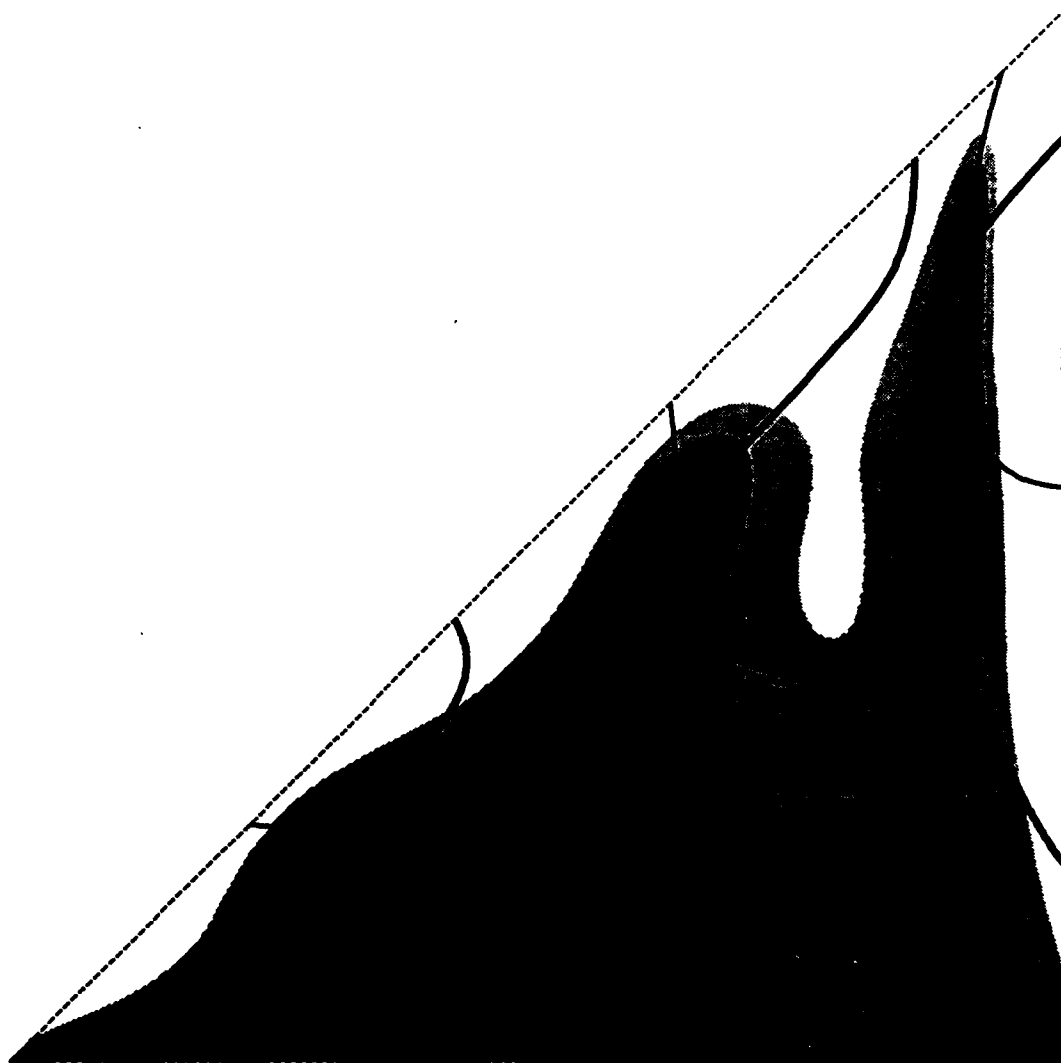
Fig. 22b



Harmonic solution $P = 4$
SIMPLIFIED L2 APPROACH

— *Function Q1*
 — *Function Q2*

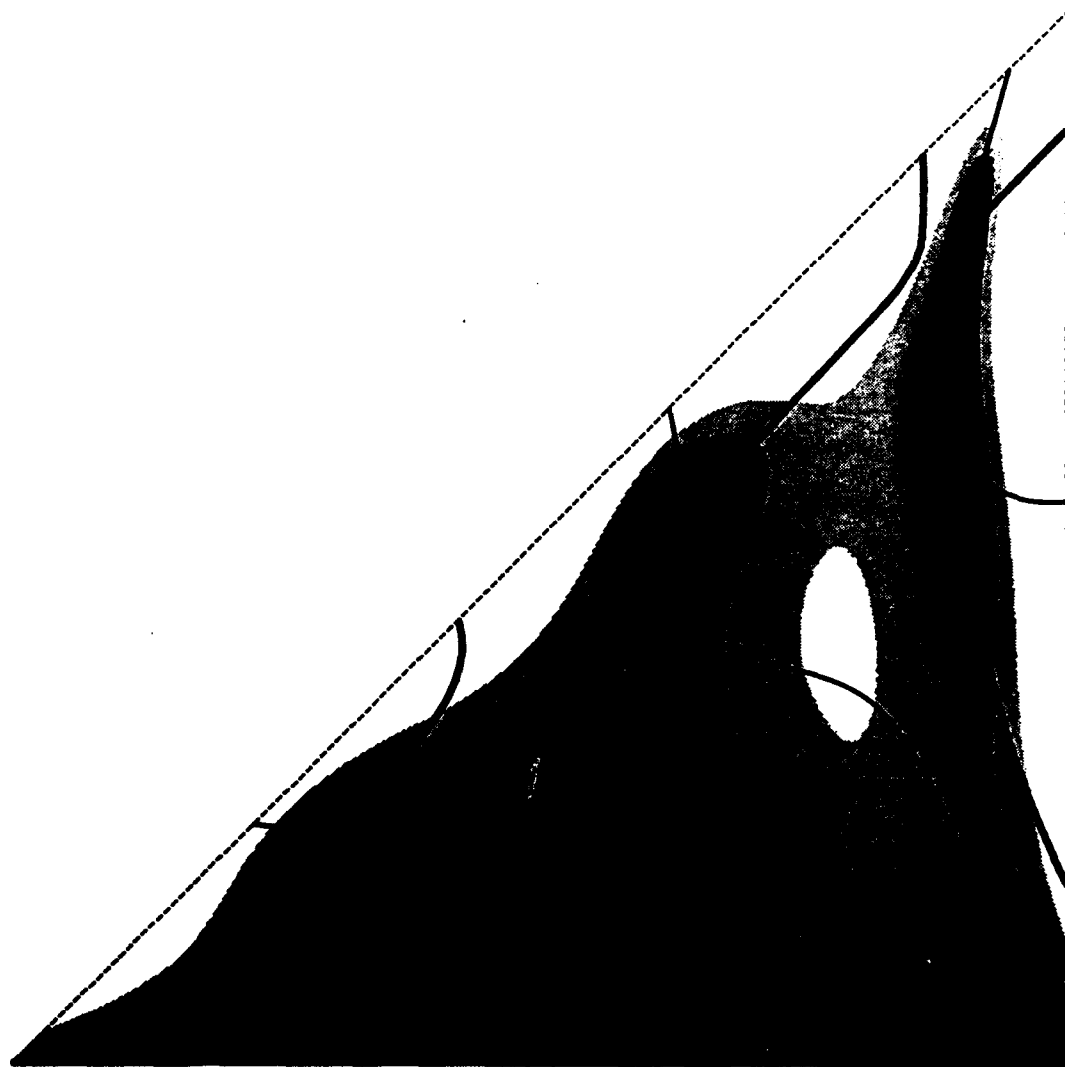
Fig. 22c



Harmonic solution $P = 4$
SIMPLIFIED L2 APPROACH

— *Function Q1*
 — *Function Q2*

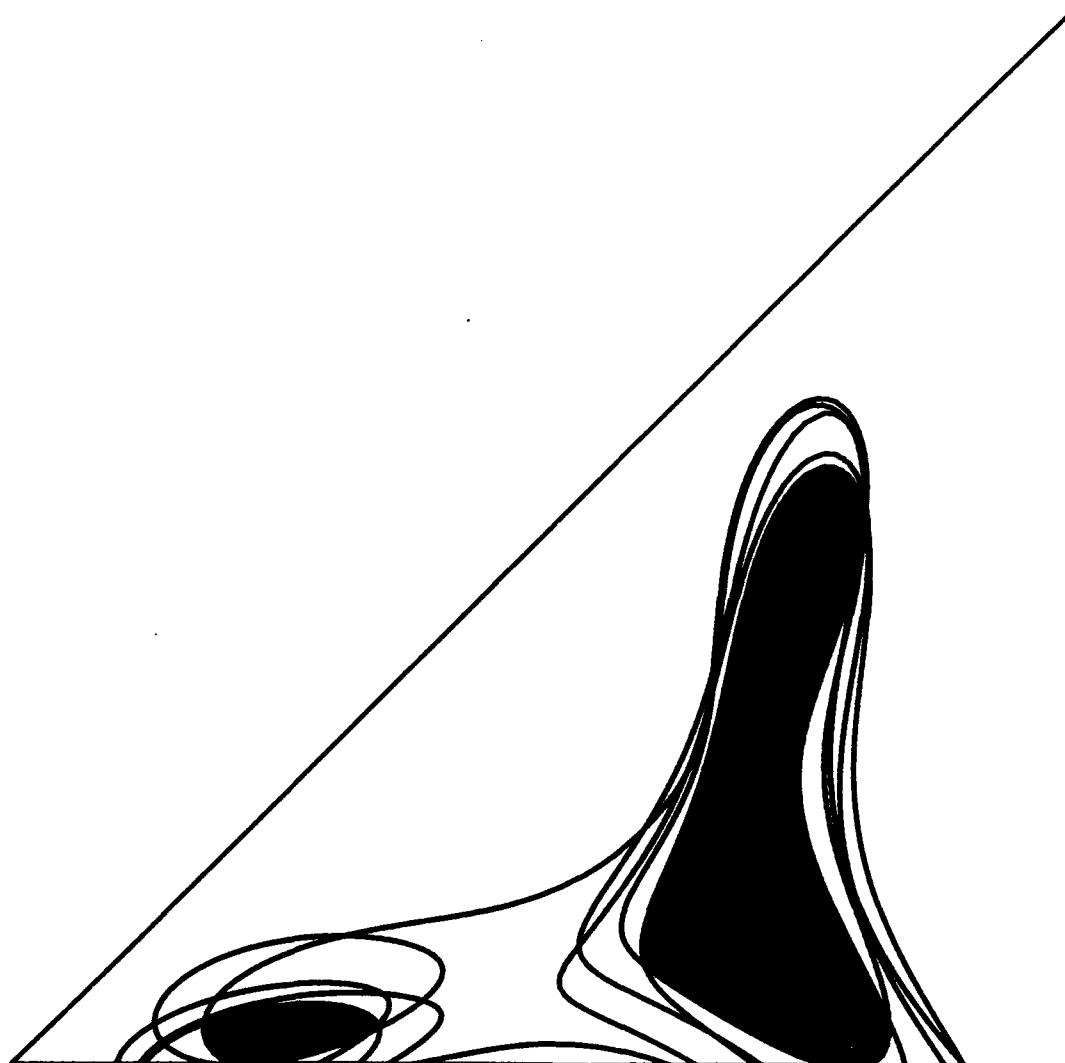
Fig. 22d



Harmonic solution $P = 4$
SIMPLIFIED L2 APPROACH

— *Function Q1*
— *Function Q2*

Fig. 22e



Harmonic solution

$P = 2$

— 25.0 % contour

Fig. 23a



Harmonic solution

$P = 3$

— 25.0 % contour

Fig. 23b

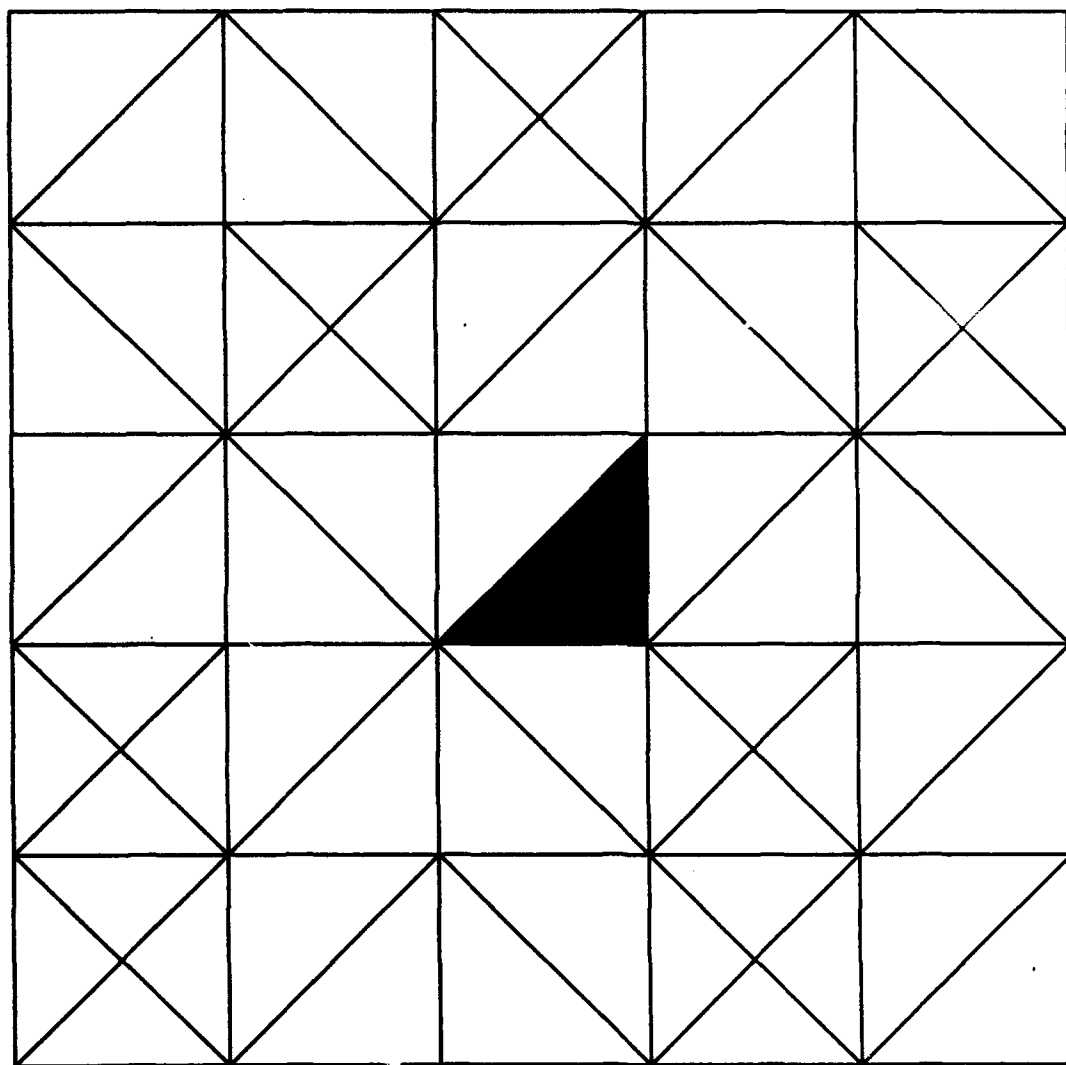


Fig. 24a

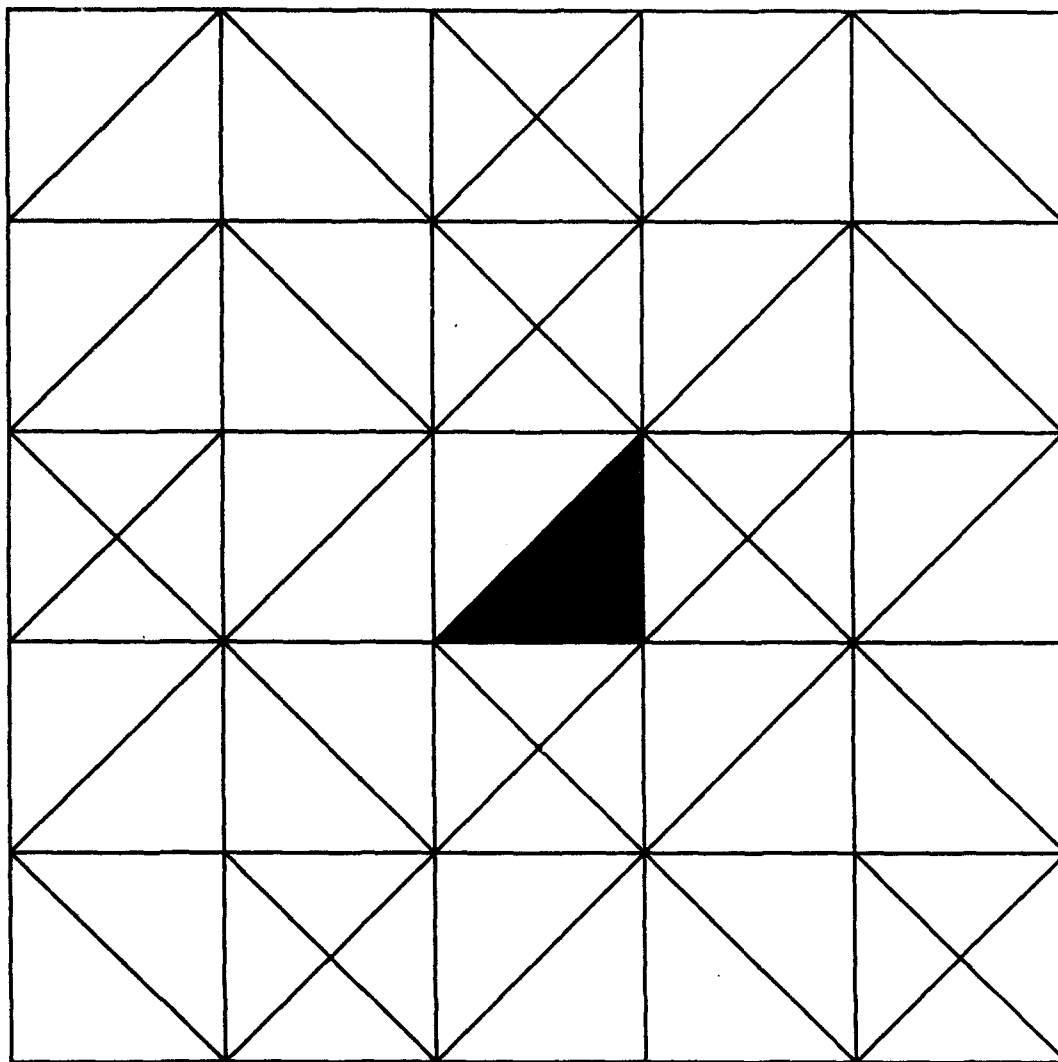


Fig. 24b

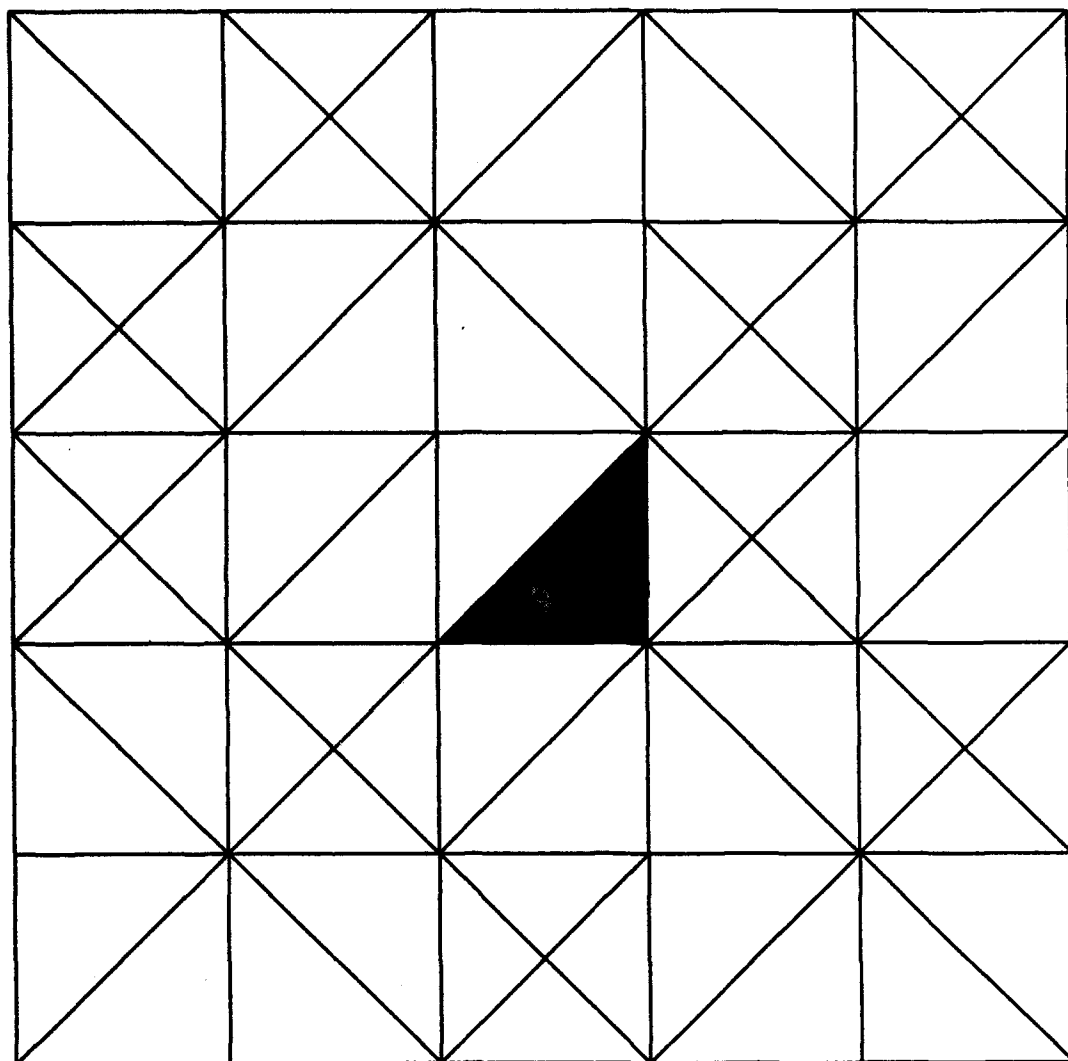


Fig. 24c

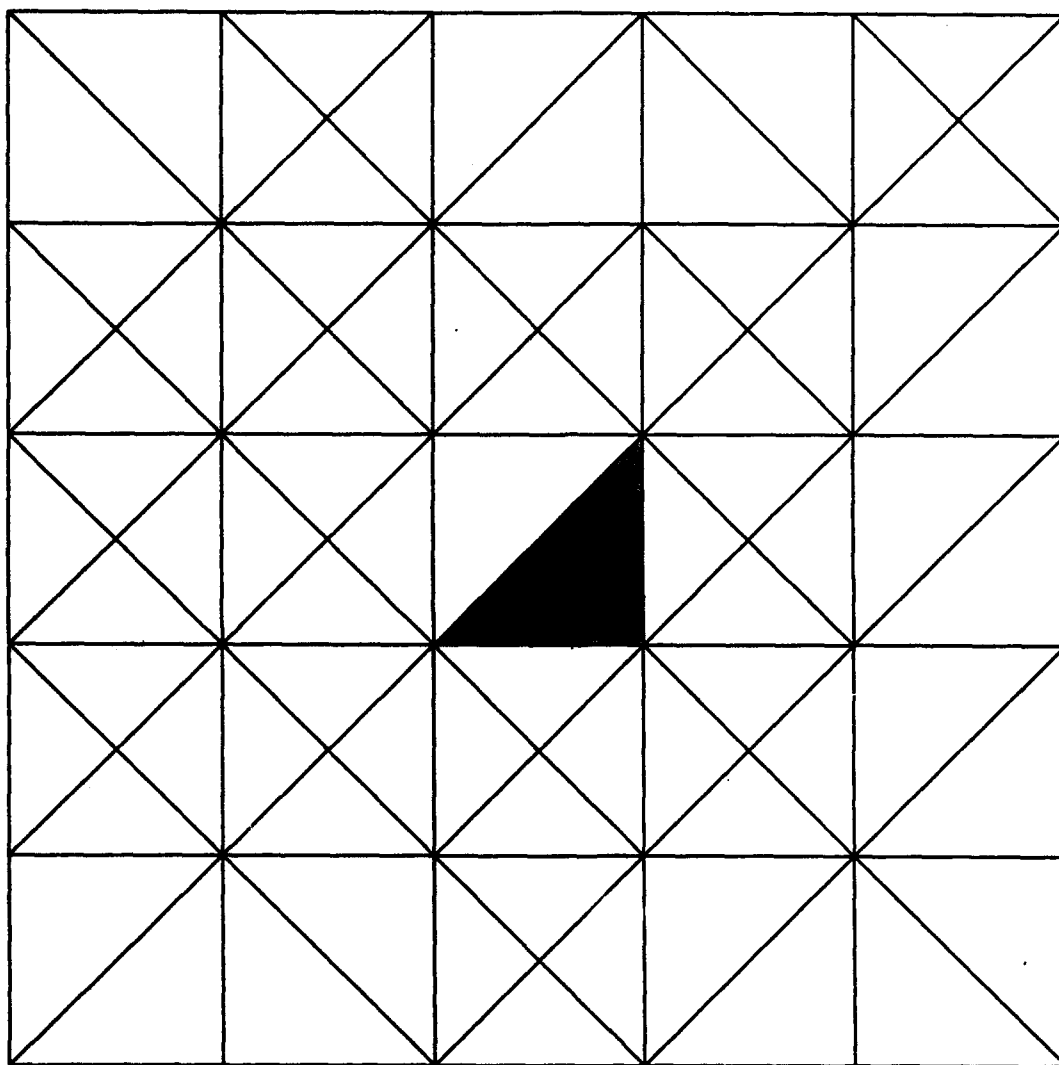


Fig. 24d

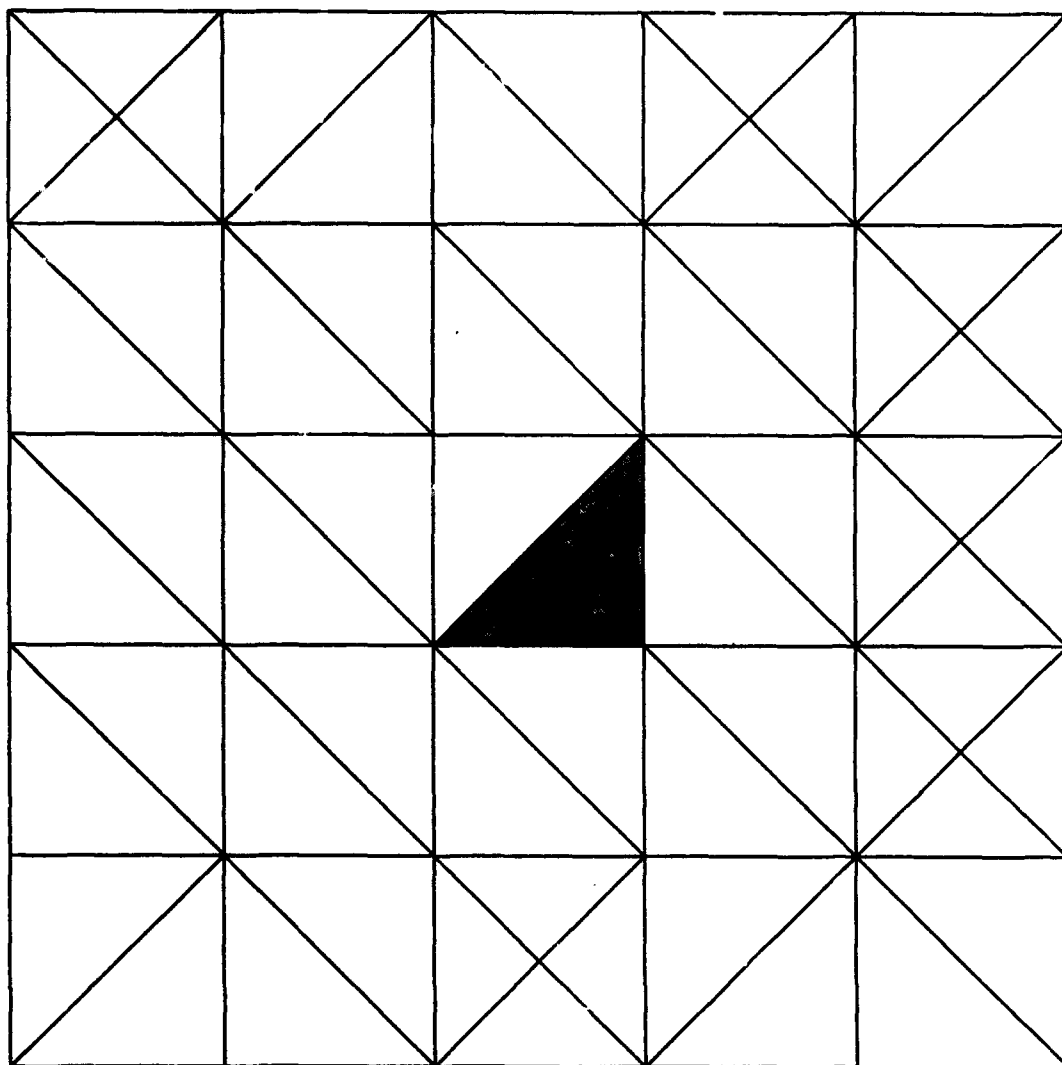
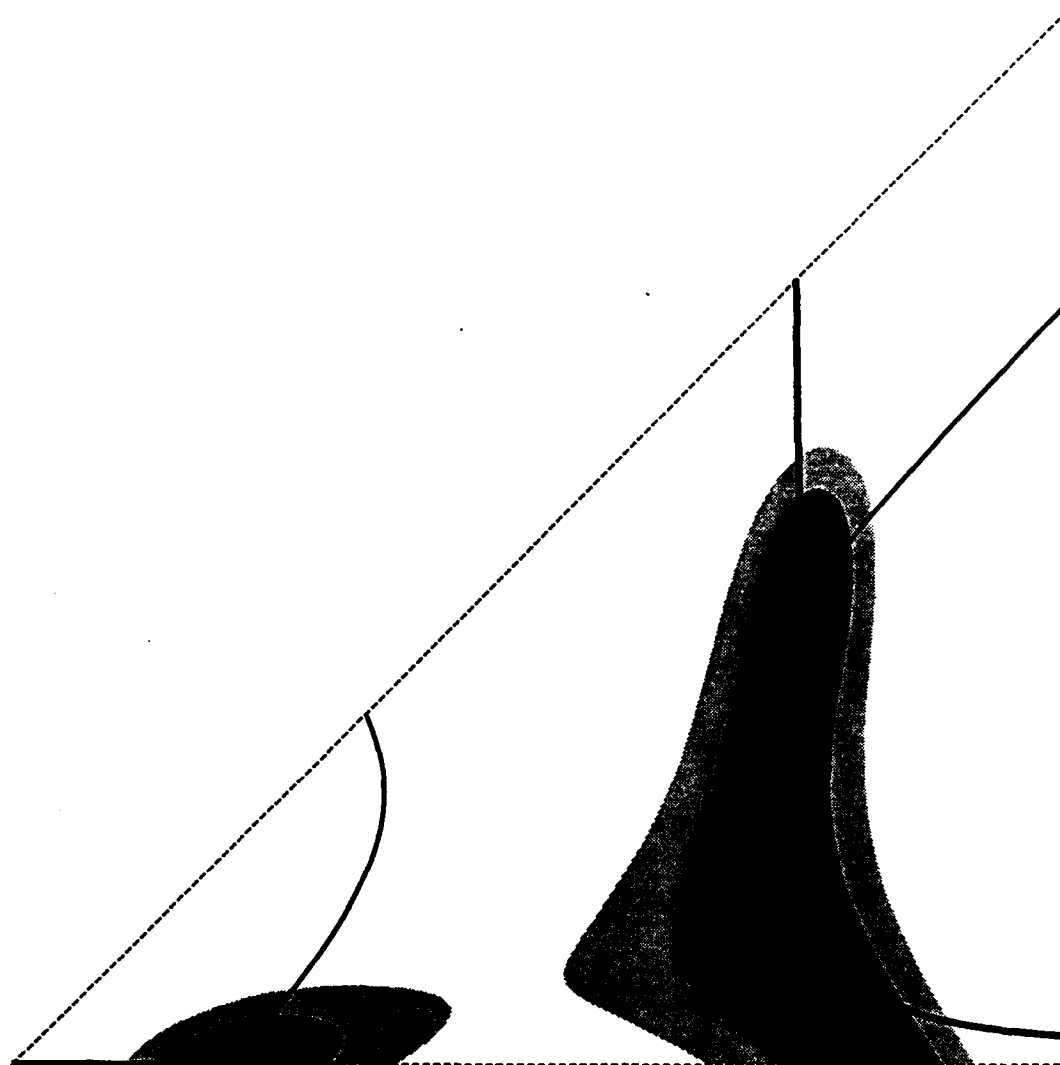


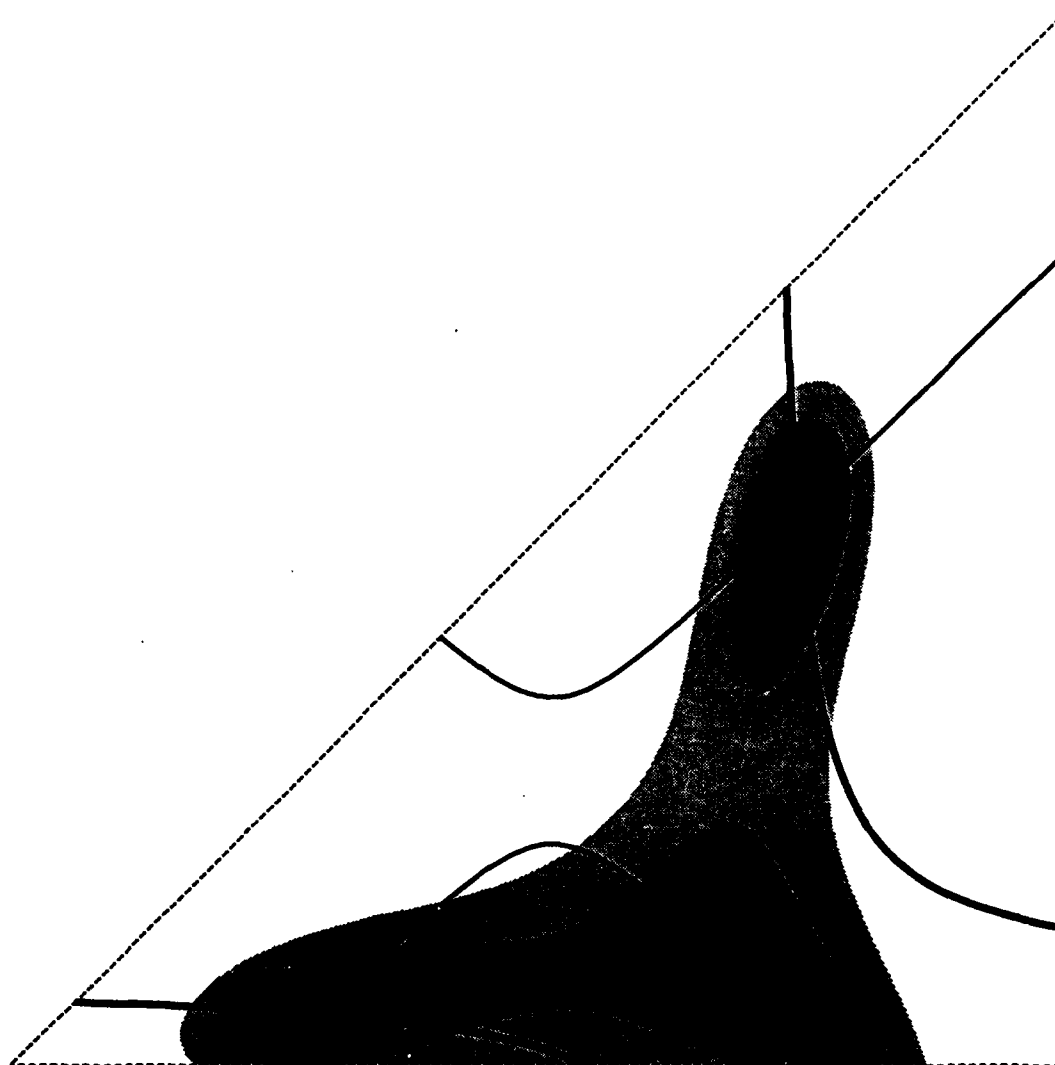
Fig. 24e



Harmonic solution $P = 2$
SIMPLIFIED L2 APPROACH

— *Function Q1*
— *Function Q2*

Fig. 25a

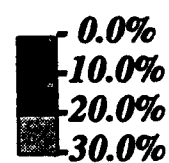
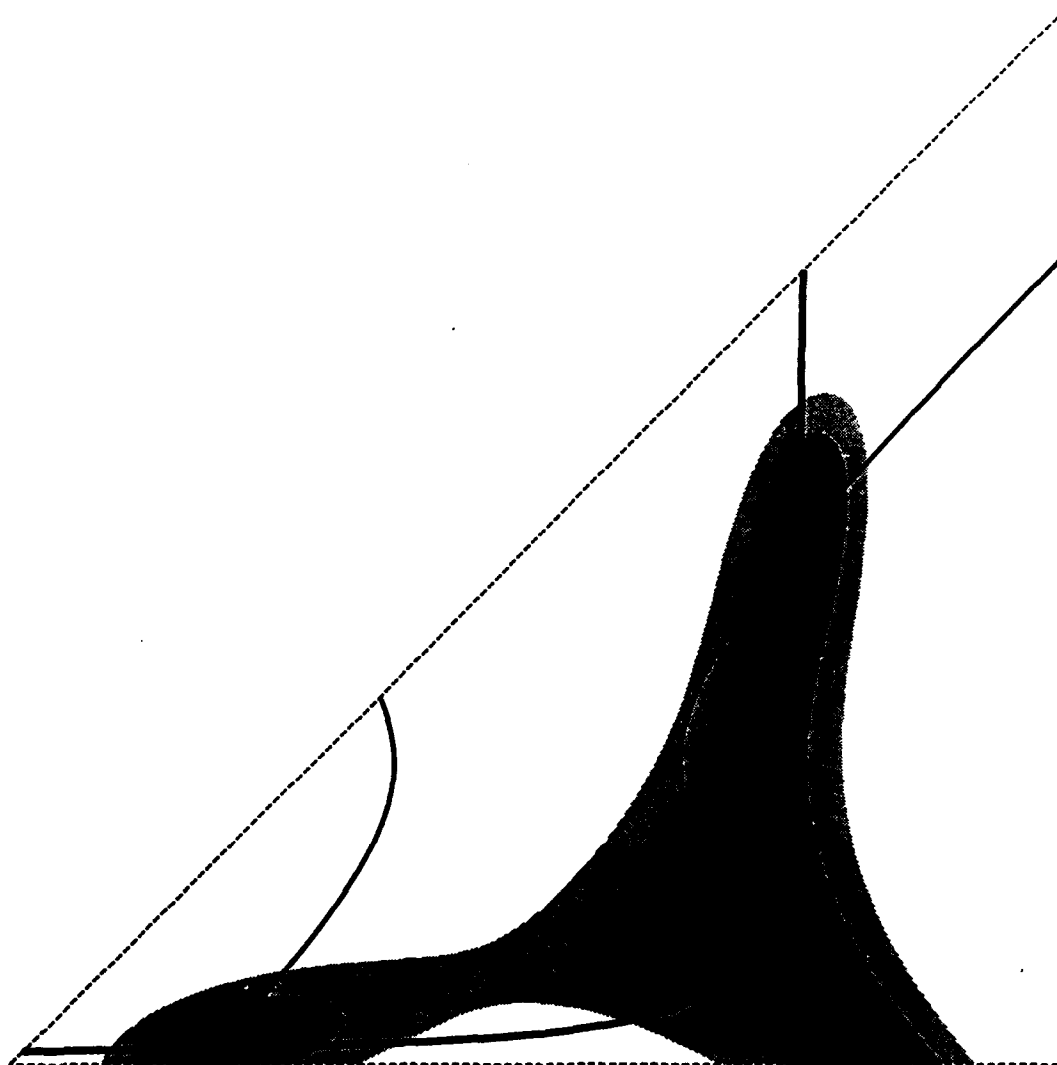


Harmonic solution $P = 2$
SIMPLIFIED L2 APPROACH

— 0.0%
 — 10.0%
 — 20.0%
 — 30.0%

— *Function Q1*
 — *Function Q2*

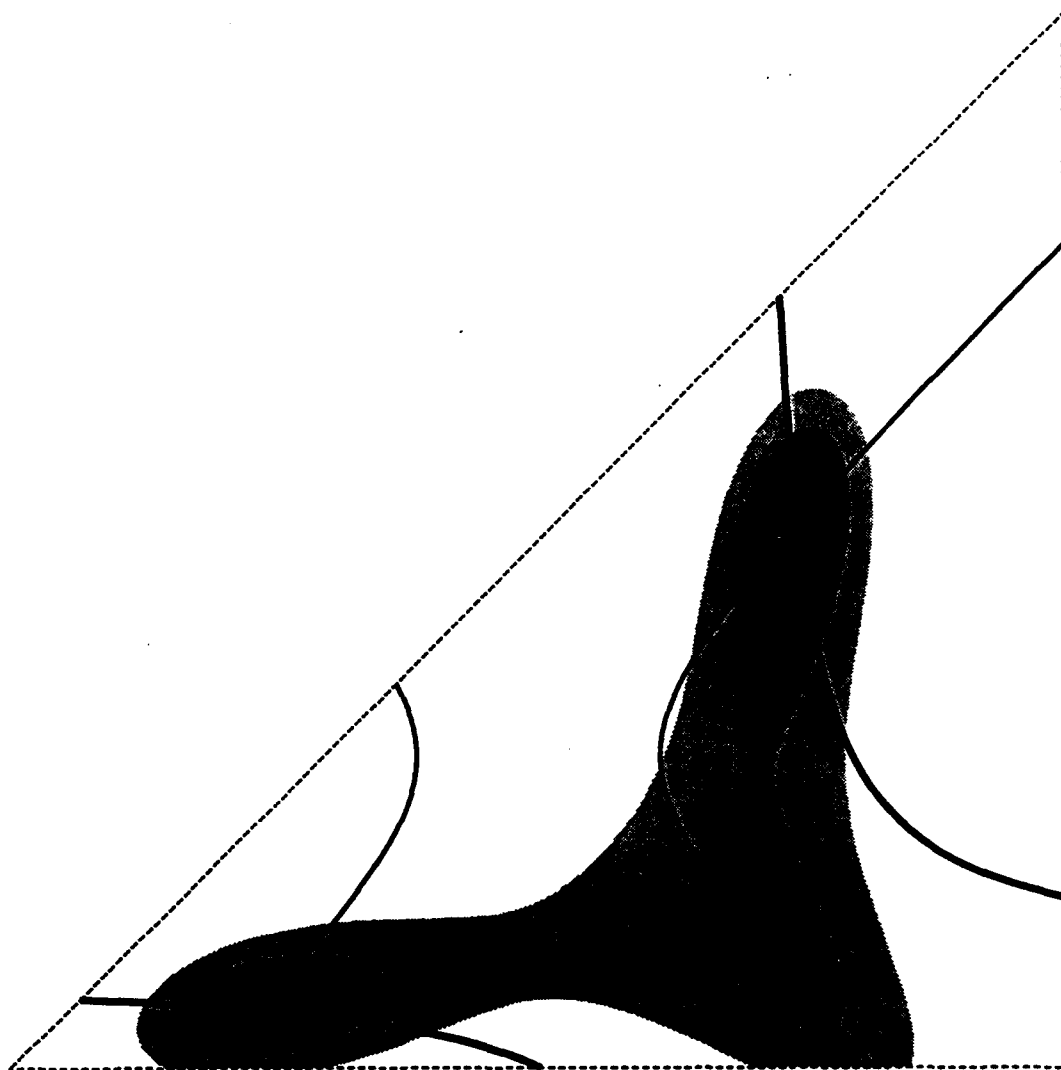
Fig. 25b



Harmonic solution $P = 2$
SIMPLIFIED L2 APPROACH

— *Function Q1*
— *Function Q2*

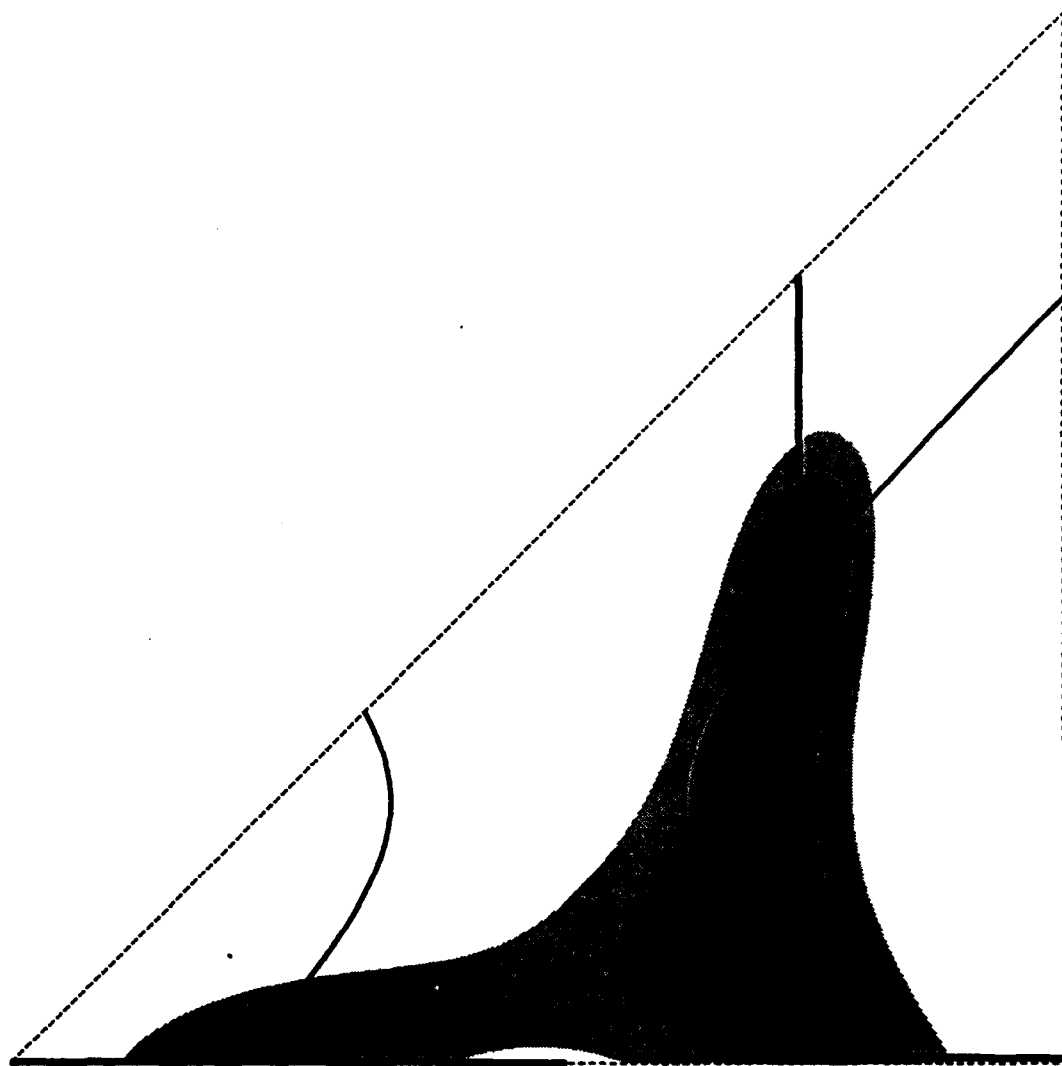
Fig. 25c



Harmonic solution $P = 2$
SIMPLIFIED L2 APPROACH

— *Function Q1*
 — *Function Q2*

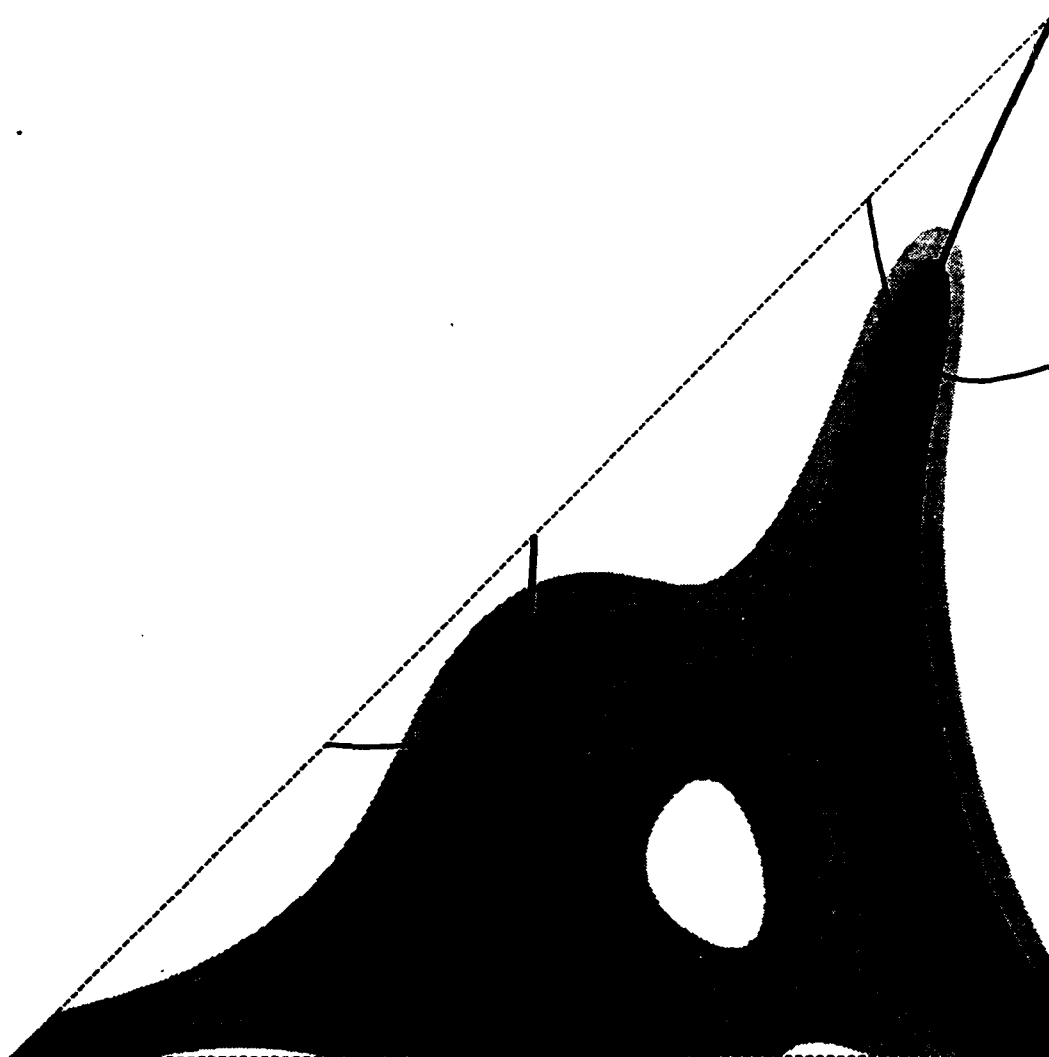
Fig. 25d



Harmonic solution $P = 2$
SIMPLIFIED L2 APPROACH

— *Function Q1*
— *Function Q2*

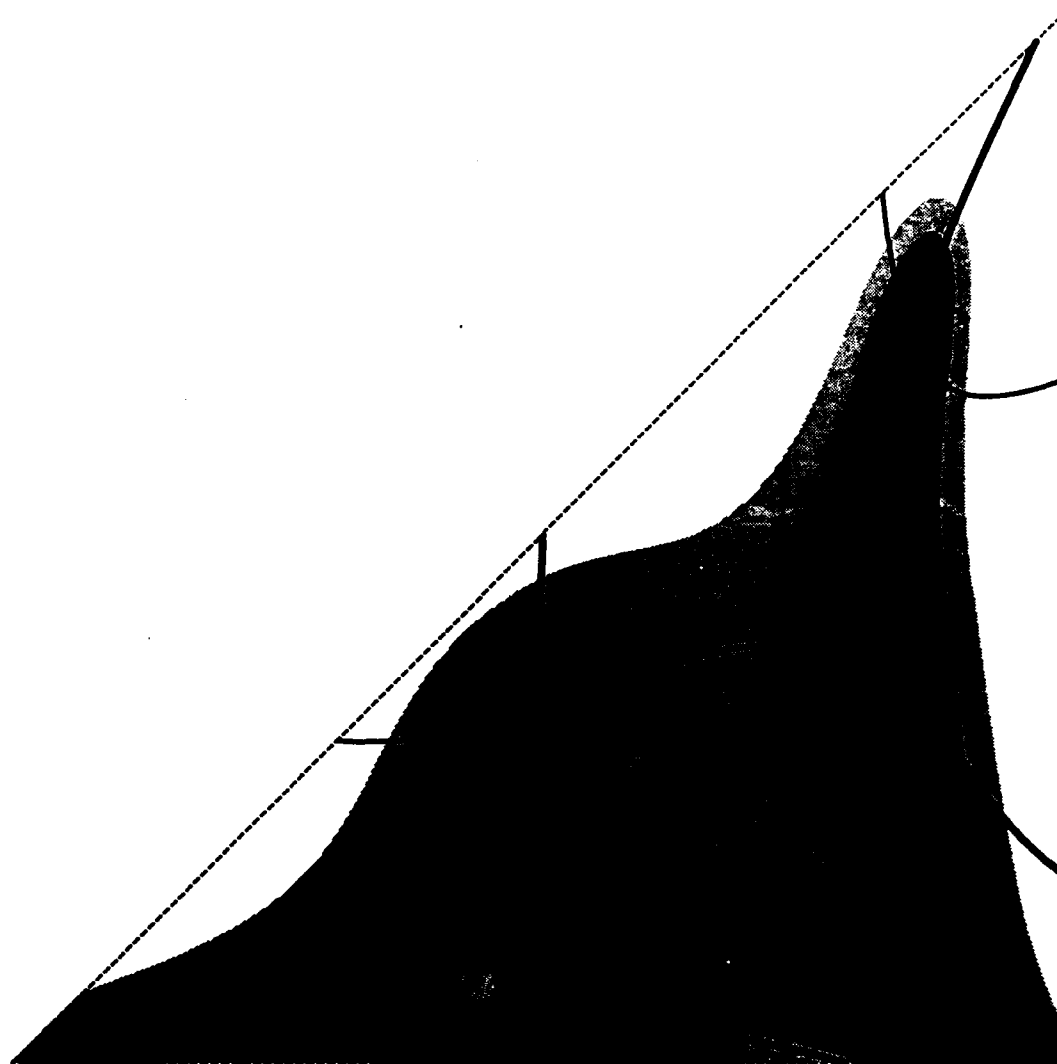
Fig. 25e



Harmonic solution $P = 3$
SIMPLIFIED L2 APPROACH

— *Function Q1*
 — *Function Q2*

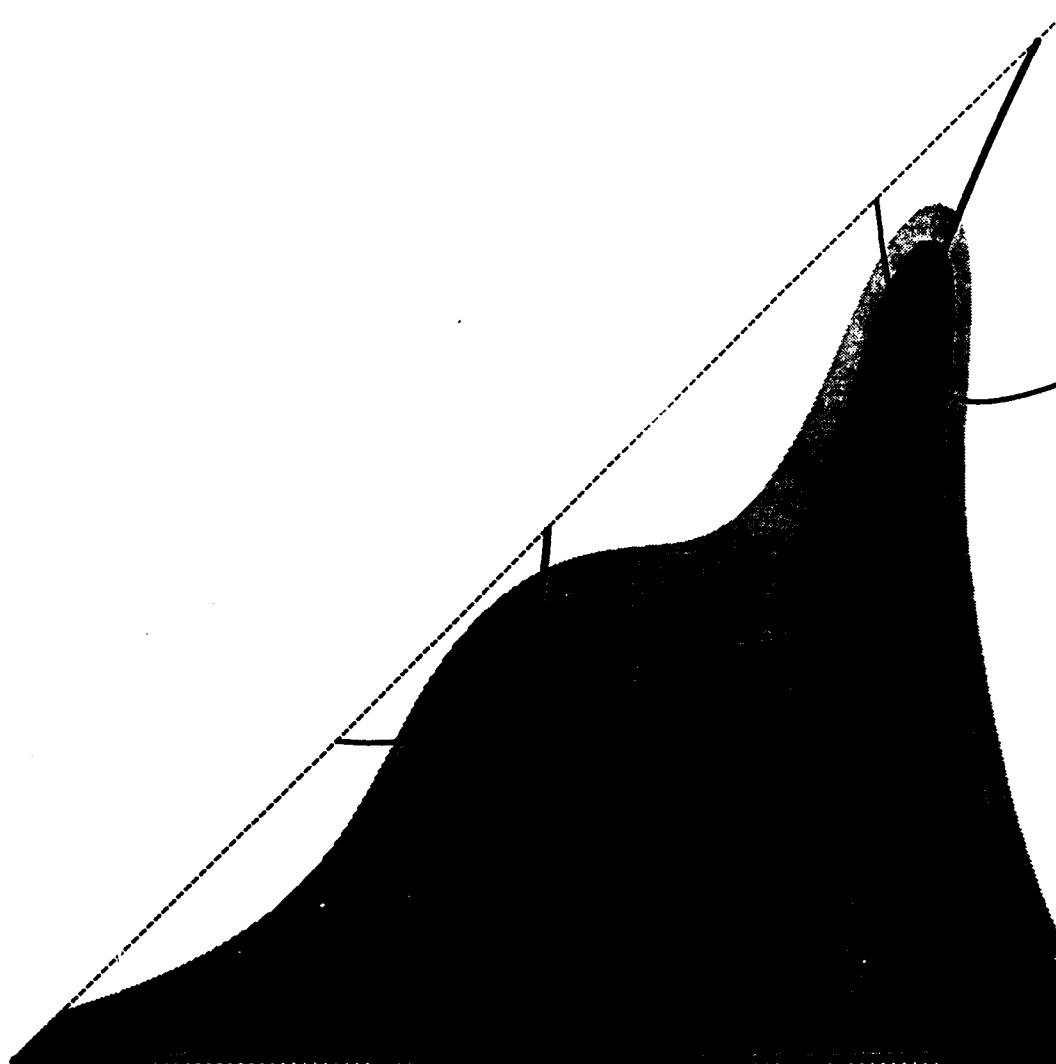
Fig. 26a



Harmonic solution $P = 3$
SIMPLIFIED L2 APPROACH

— *Function Q1*
— *Function Q2*

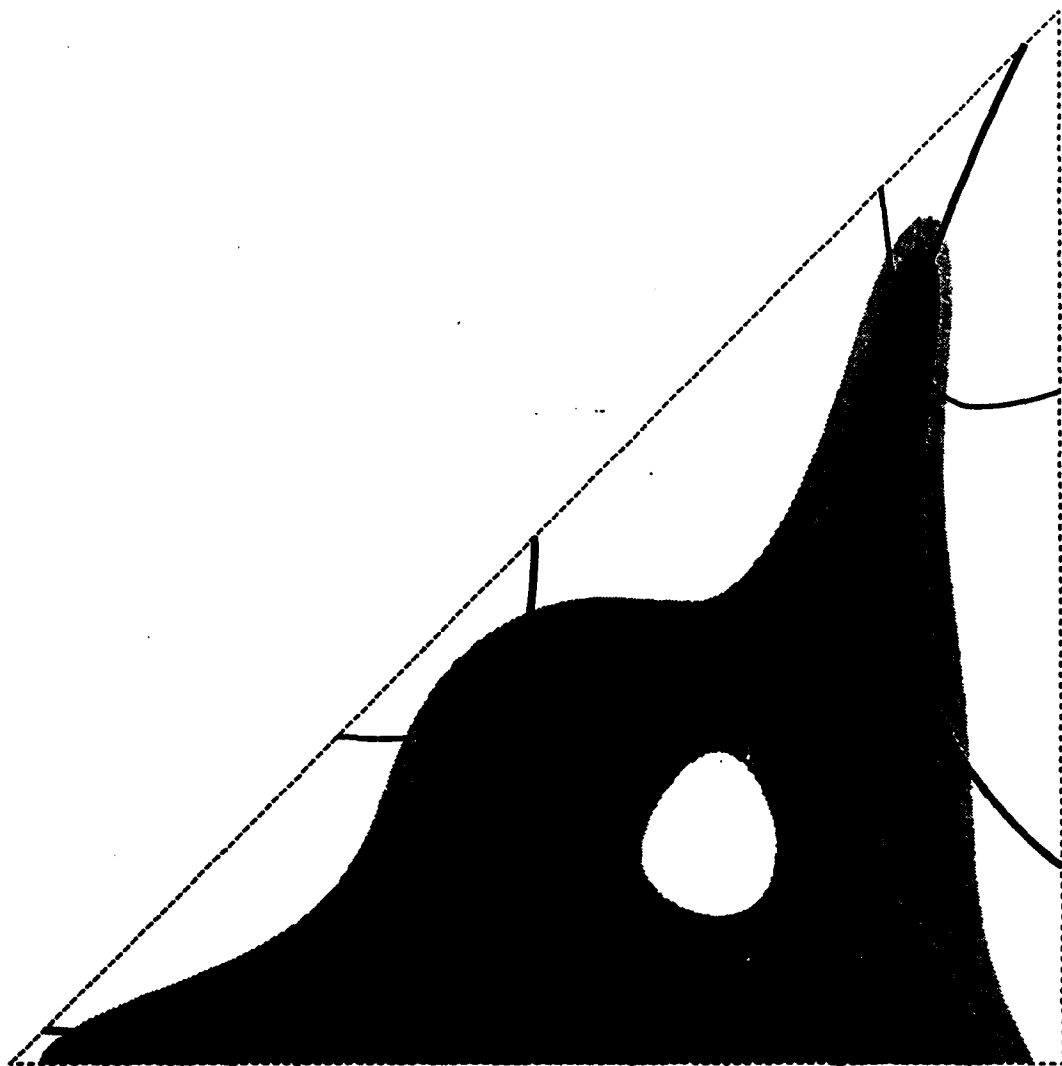
Fig. 26b



Harmonic solution $P = 3$
SIMPLIFIED L2 APPROACH

— *Function Q1*
 — *Function Q2*

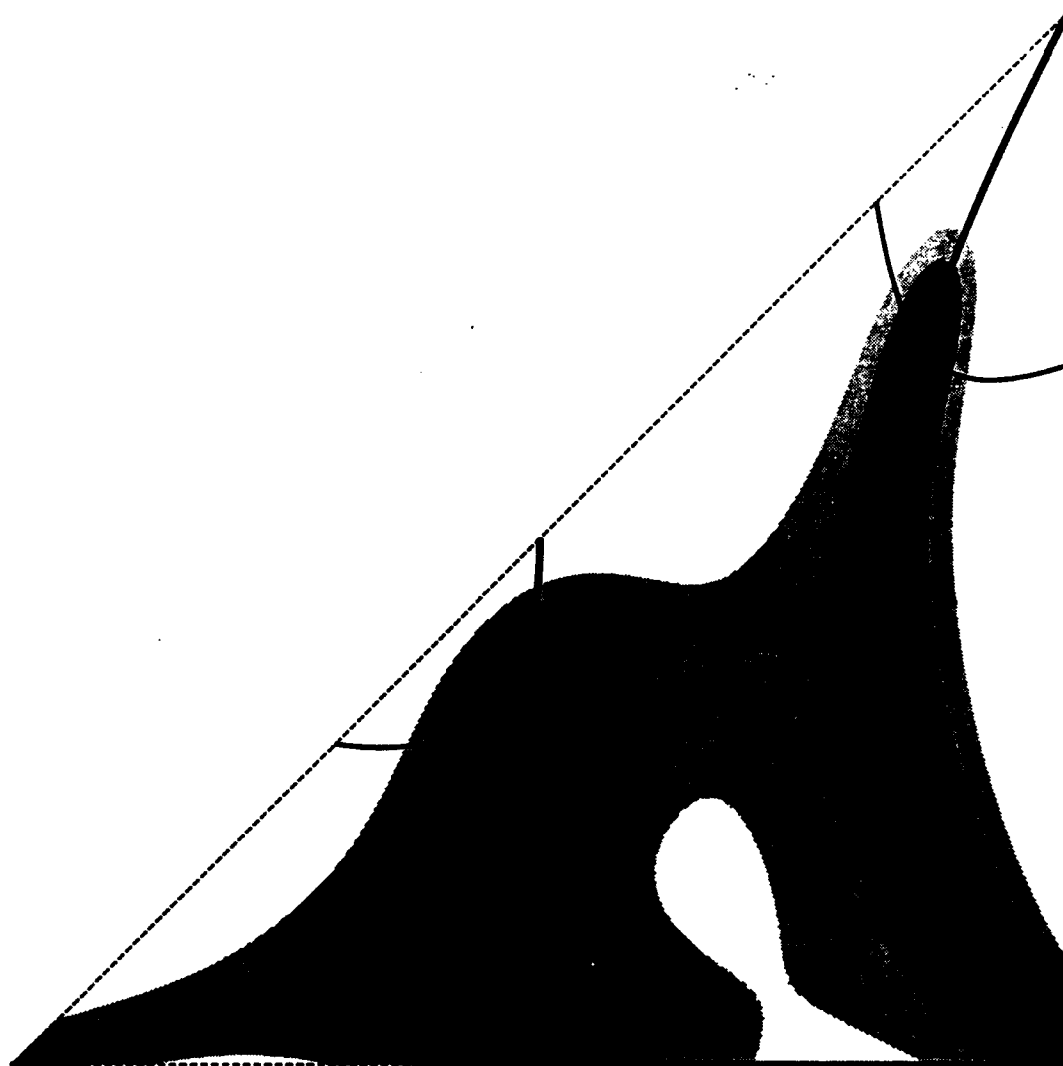
Fig. 26c



Harmonic solution **P = 3**
SIMPLIFIED L2 APPROACH

— **Function Q1**
 — **Function Q2**

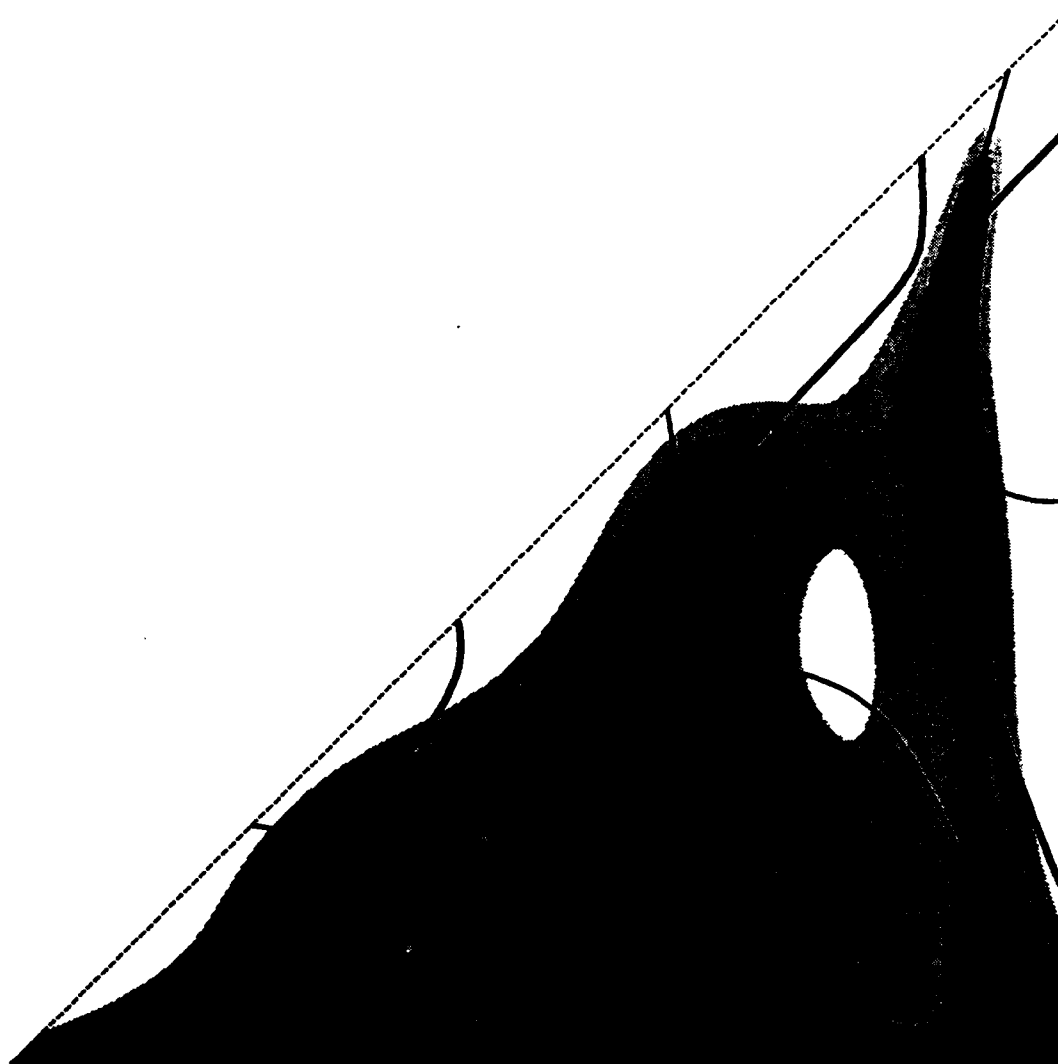
Fig. 26d



Harmonic solution **P = 3**
SIMPLIFIED L2 APPROACH

— **Function Q1**
 — **Function Q2**

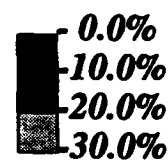
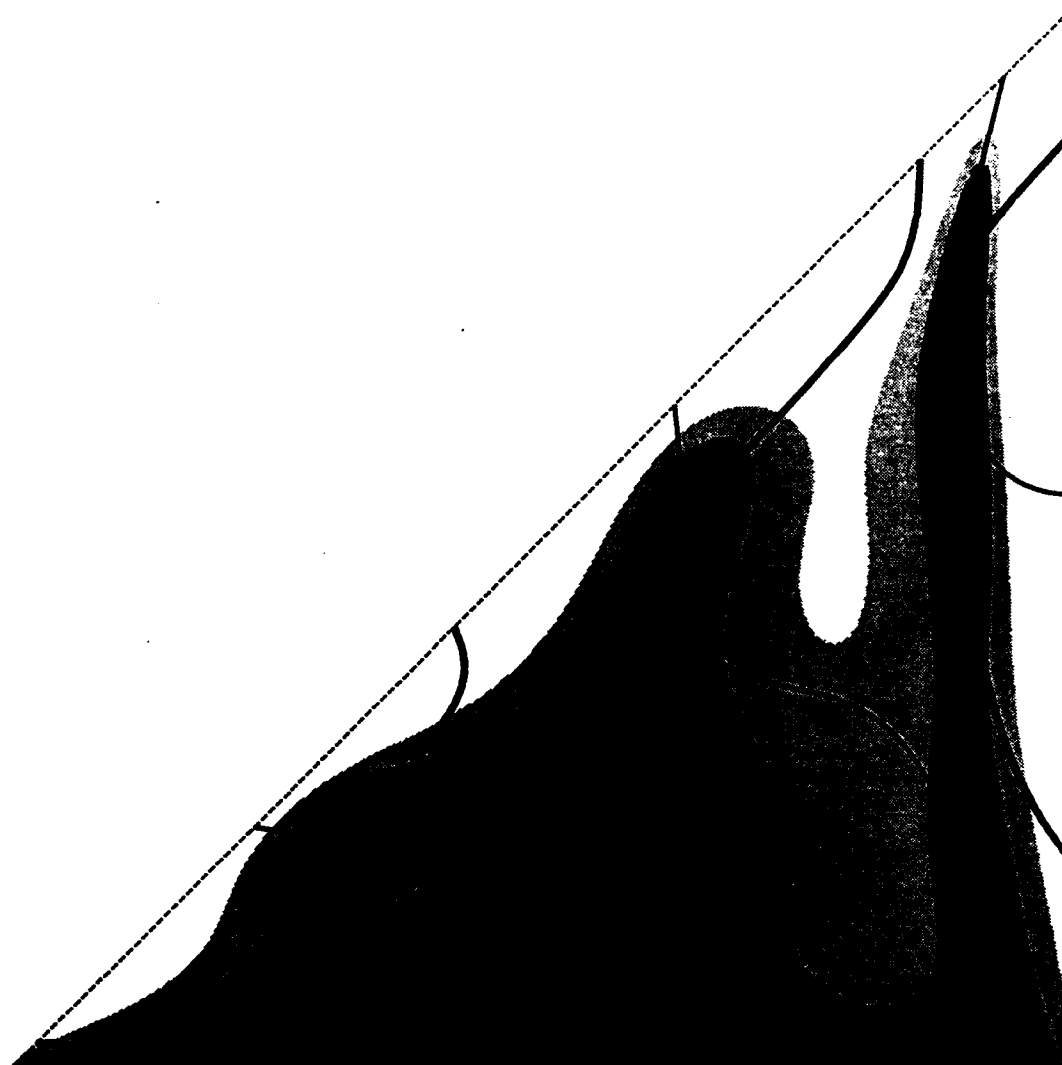
Fig. 26e



Harmonic solution $P = 4$
SIMPLIFIED L2 APPROACH

— *Function Q1*
 — *Function Q2*

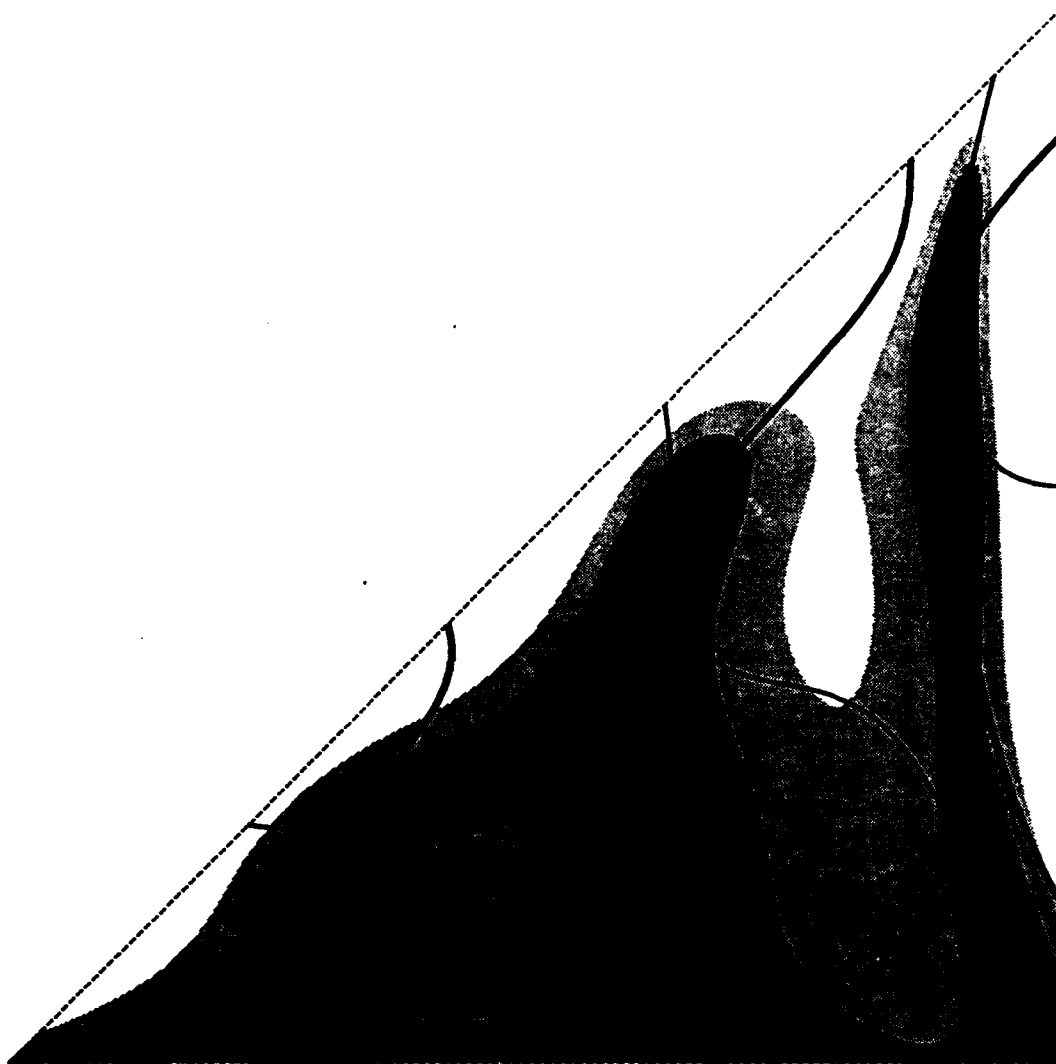
Fig. 27a



Harmonic solution $P = 4$
SIMPLIFIED L2 APPROACH

— *Function Q1*
 — *Function Q2*

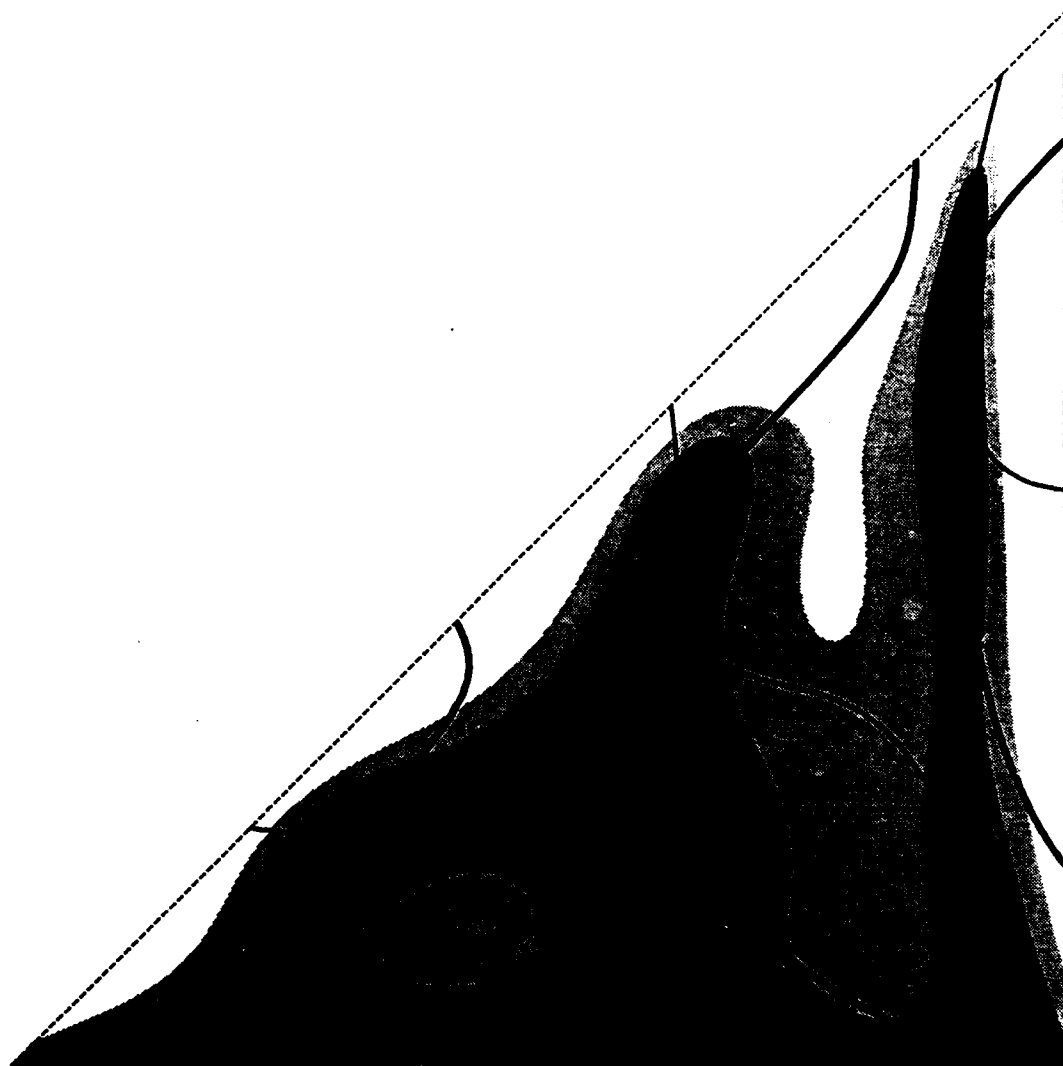
Fig. 27b



Harmonic solution $P = 4$
SIMPLIFIED L2 APPROACH

— *Function Q1*
— *Function Q2*

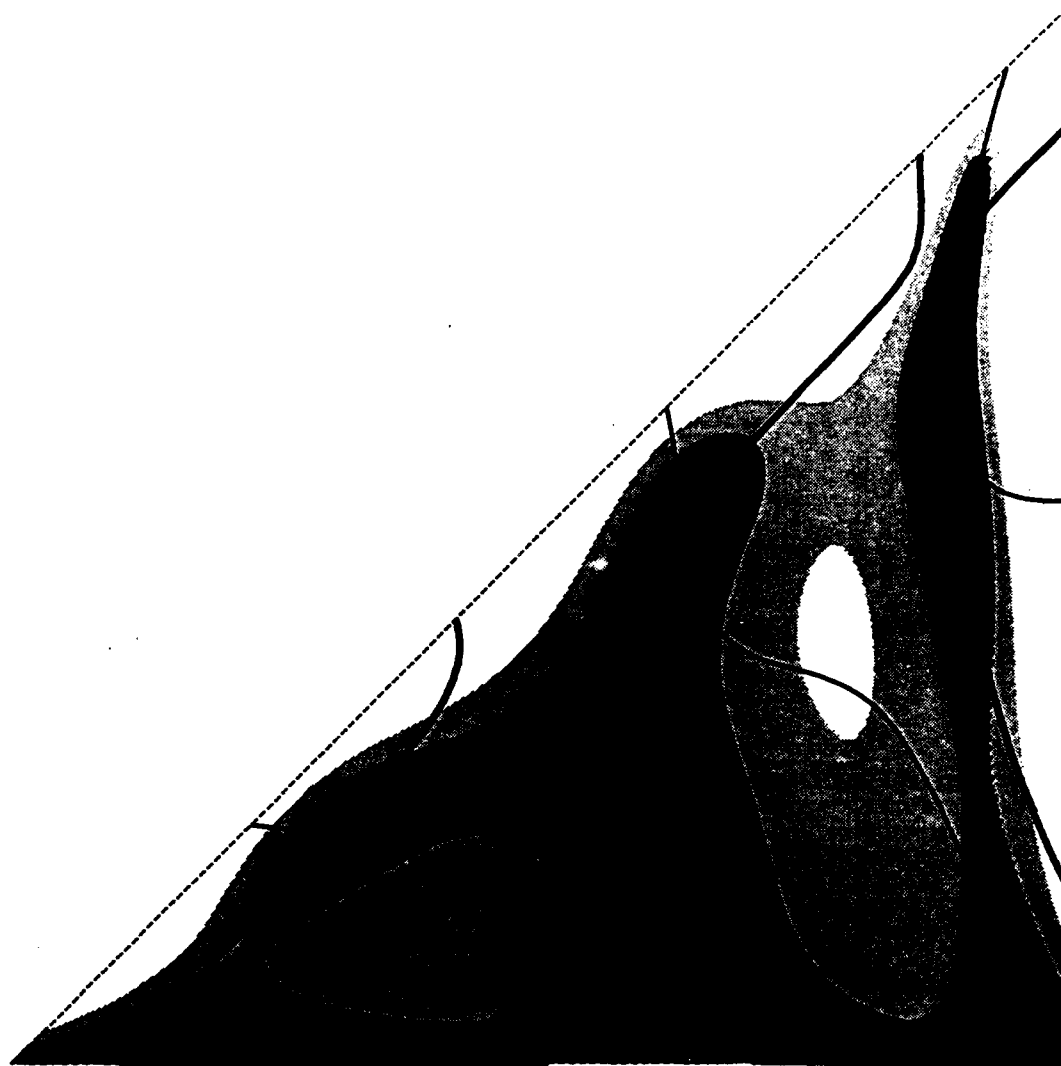
Fig. 27c



Harmonic solution $P = 4$
SIMPLIFIED L2 APPROACH

— *Function Q1*
 — *Function Q2*

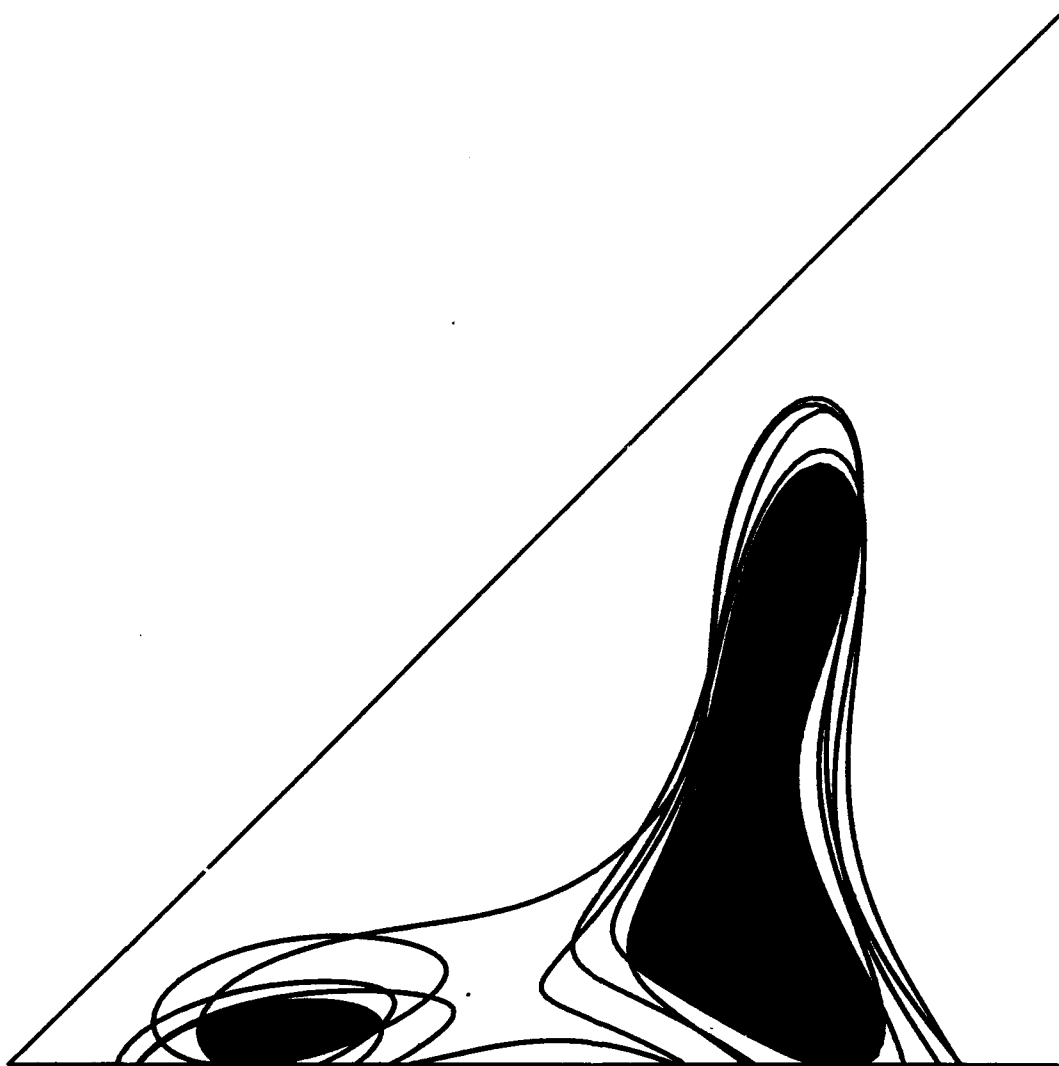
Fig. 27d



Harmonic solution $P = 4$
SIMPLIFIED L2 APPROACH

— *Function Q1*
 — *Function Q2*

Fig. 27e



Harmonic solution

$P = 2$

— 25.0 % contour

Fig. 28a



Harmonic solution

$P = 3$

— 25.0 % contour

Fig. 28b

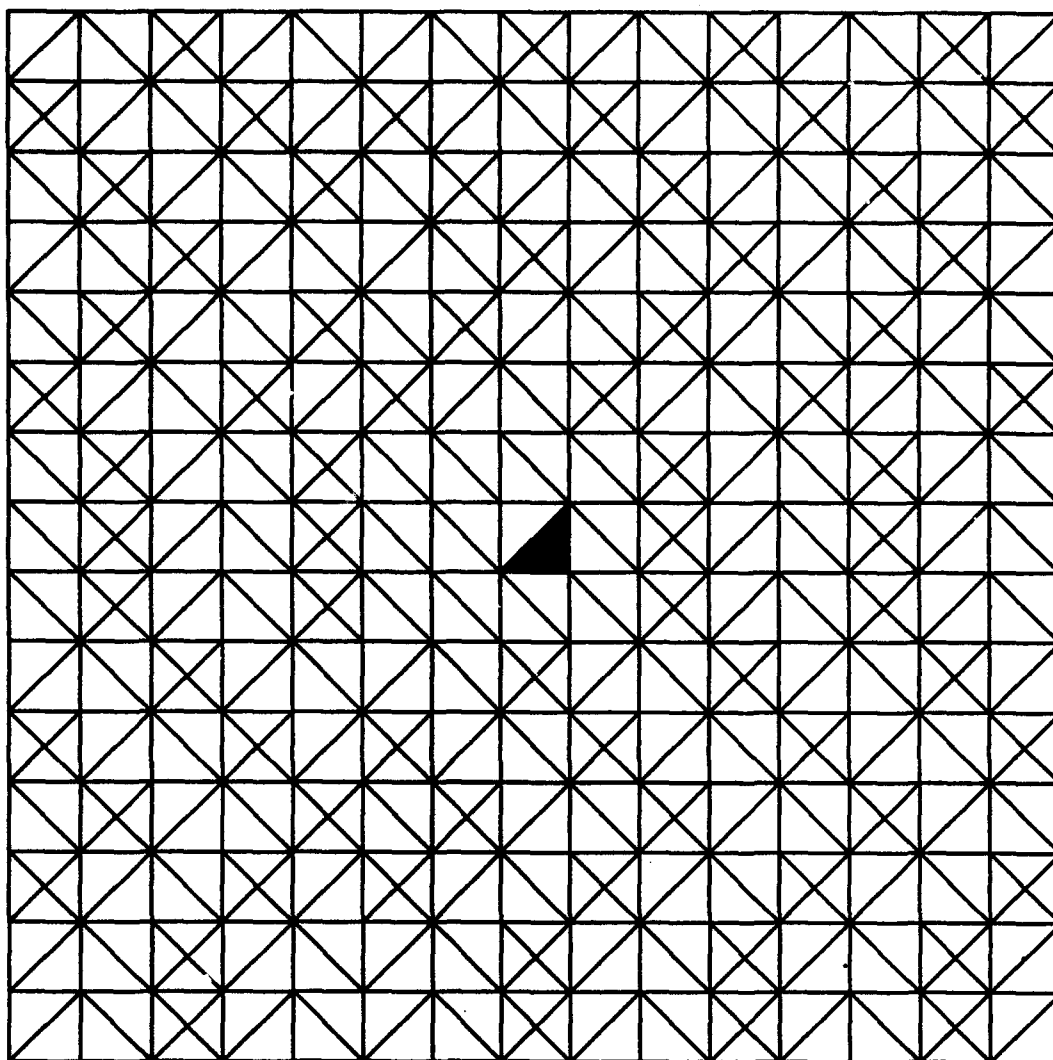
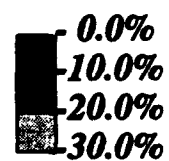
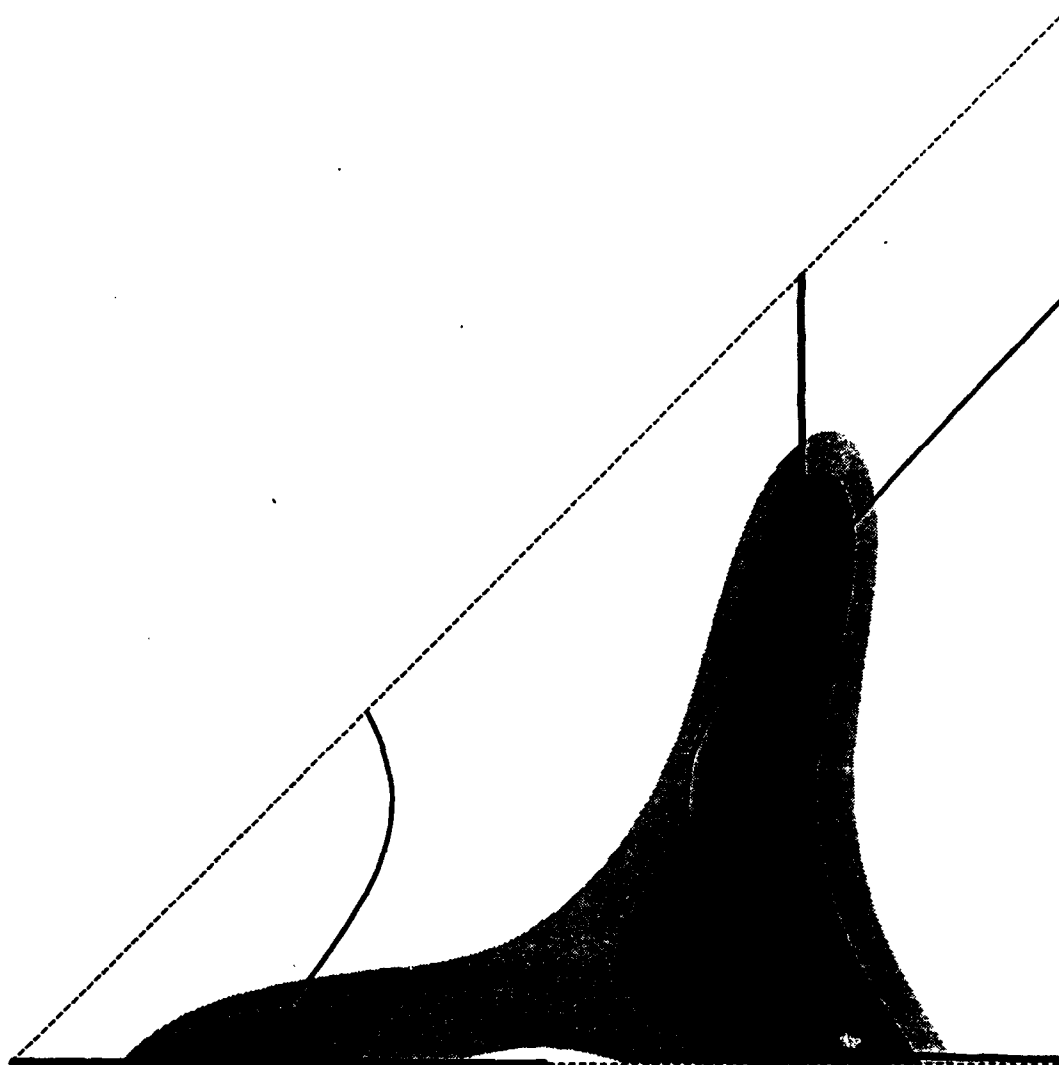


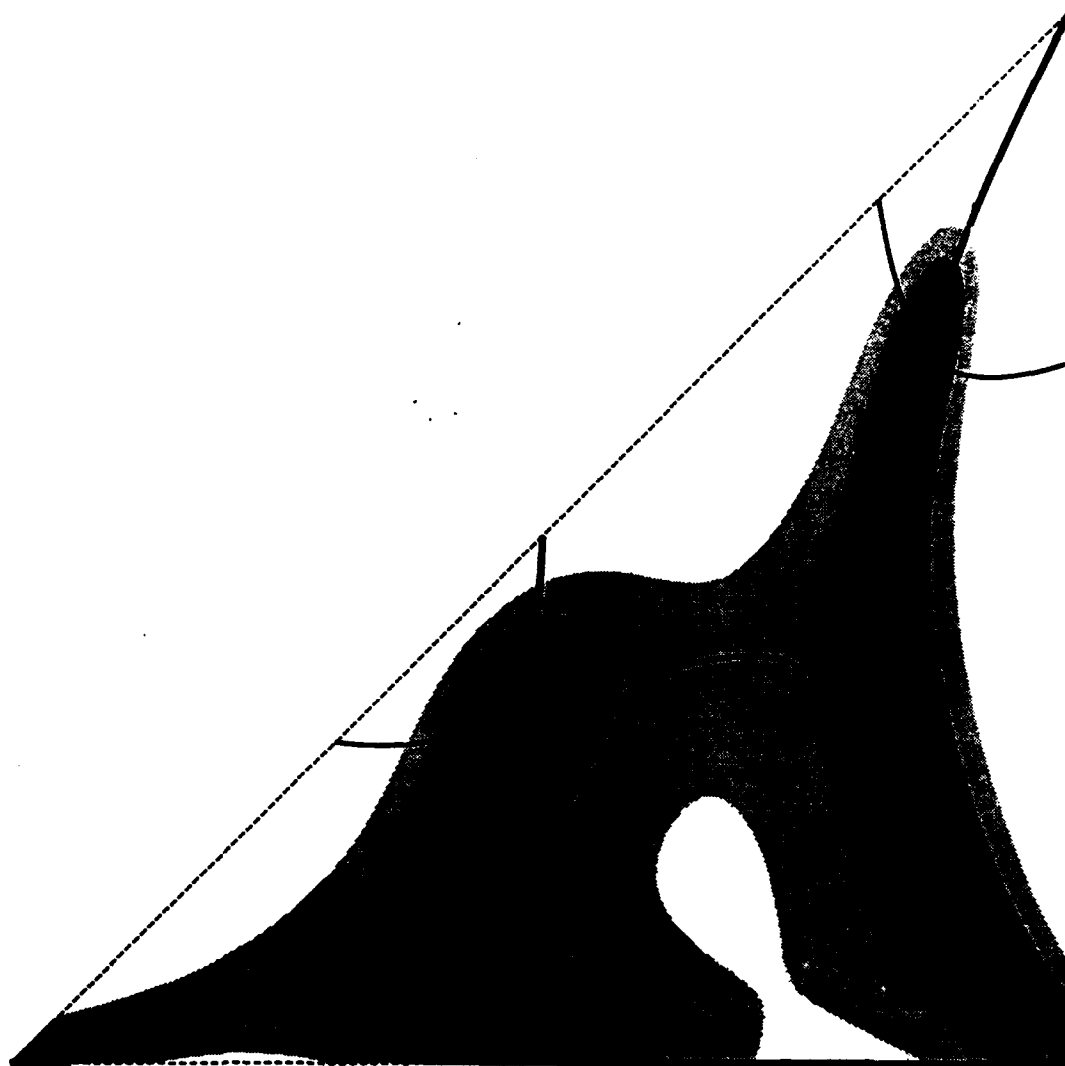
Fig. 29



Harmonic solution $P = 2$
SIMPLIFIED L2 APPROACH

— *Function Q1*
— *Function Q2*

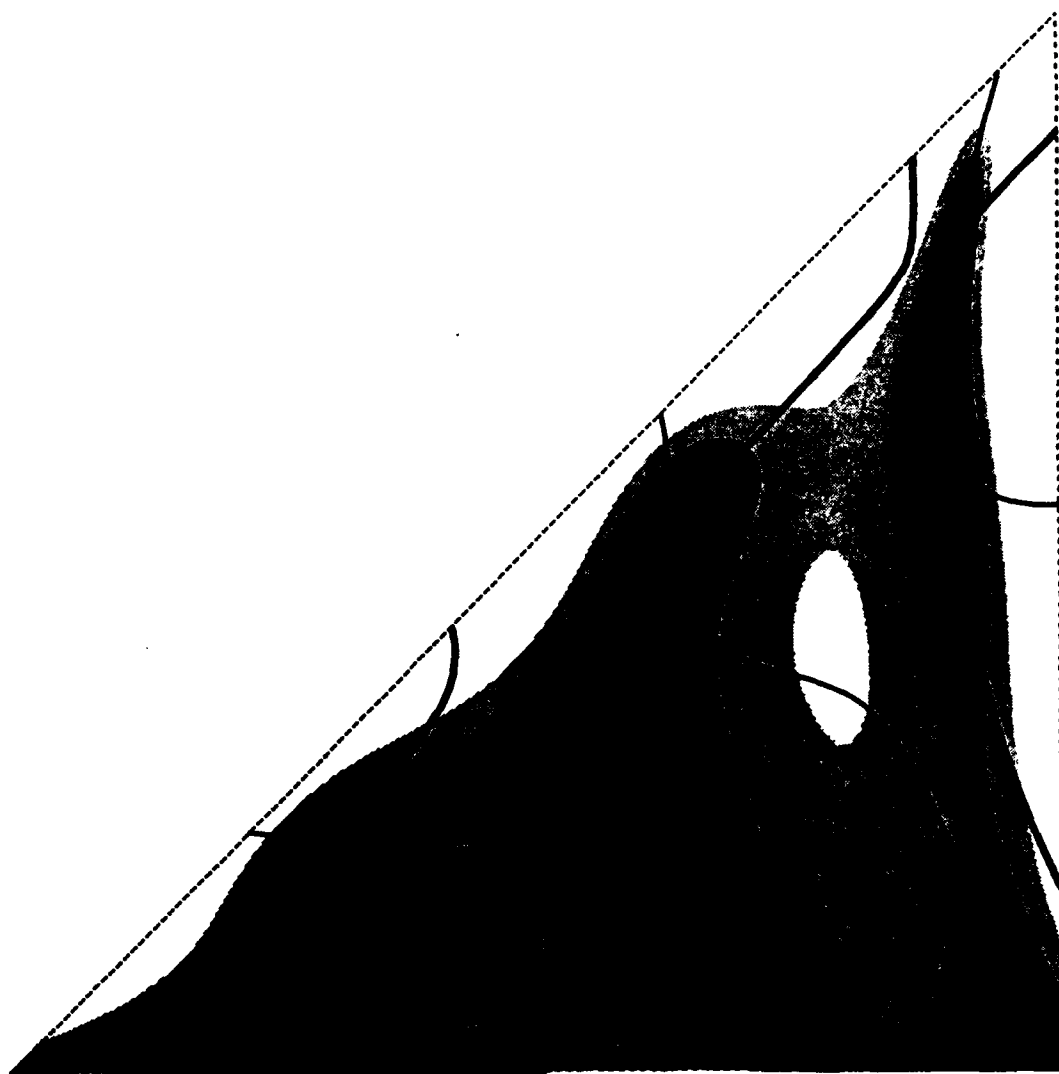
Fig. 30a



Harmonic solution $P = 3$
SIMPLIFIED L2 APPROACH

— *Function Q1*
 — *Function Q2*

Fig. 30b



Harmonic solution $P = 4$
SIMPLIFIED L2 APPROACH

— *Function Q1*
 - - - *Function Q2*

Fig. 30c

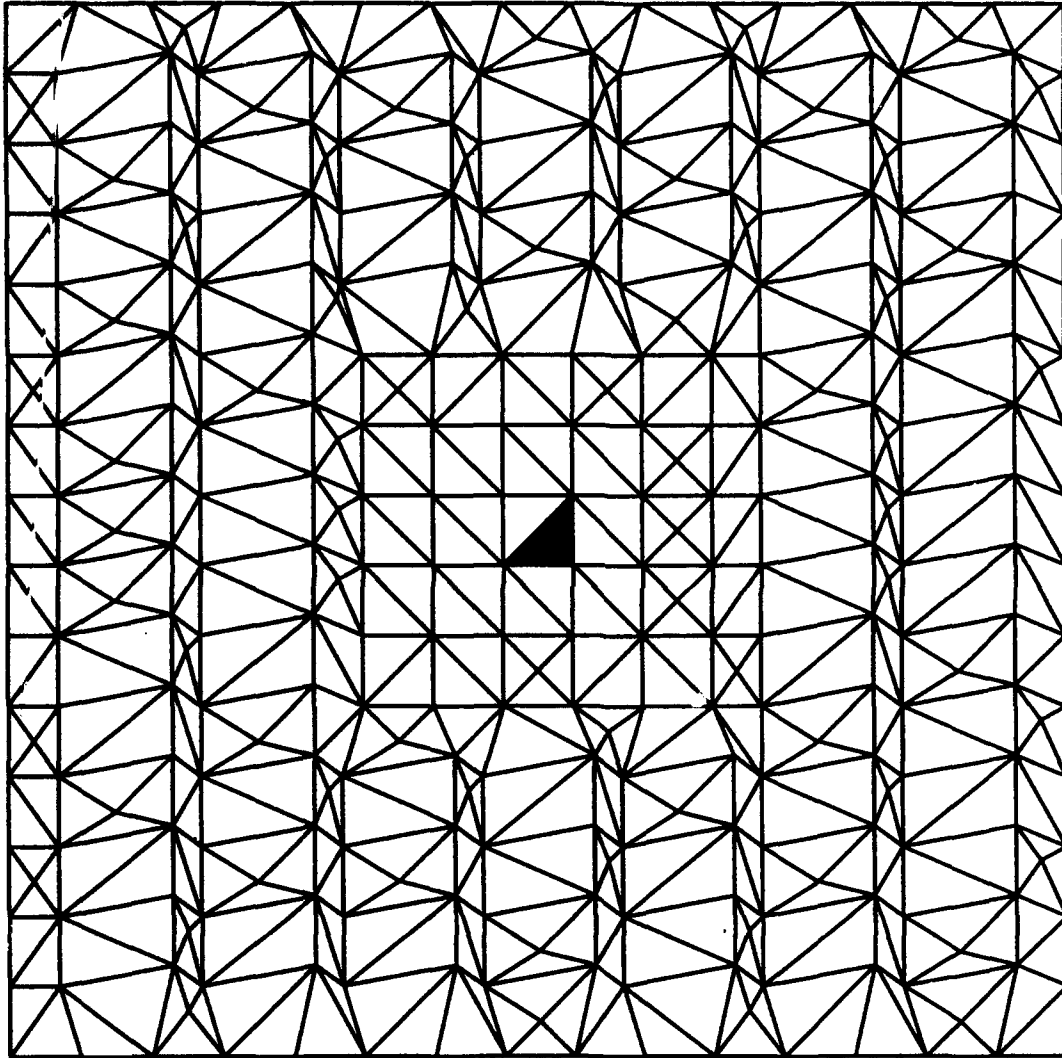
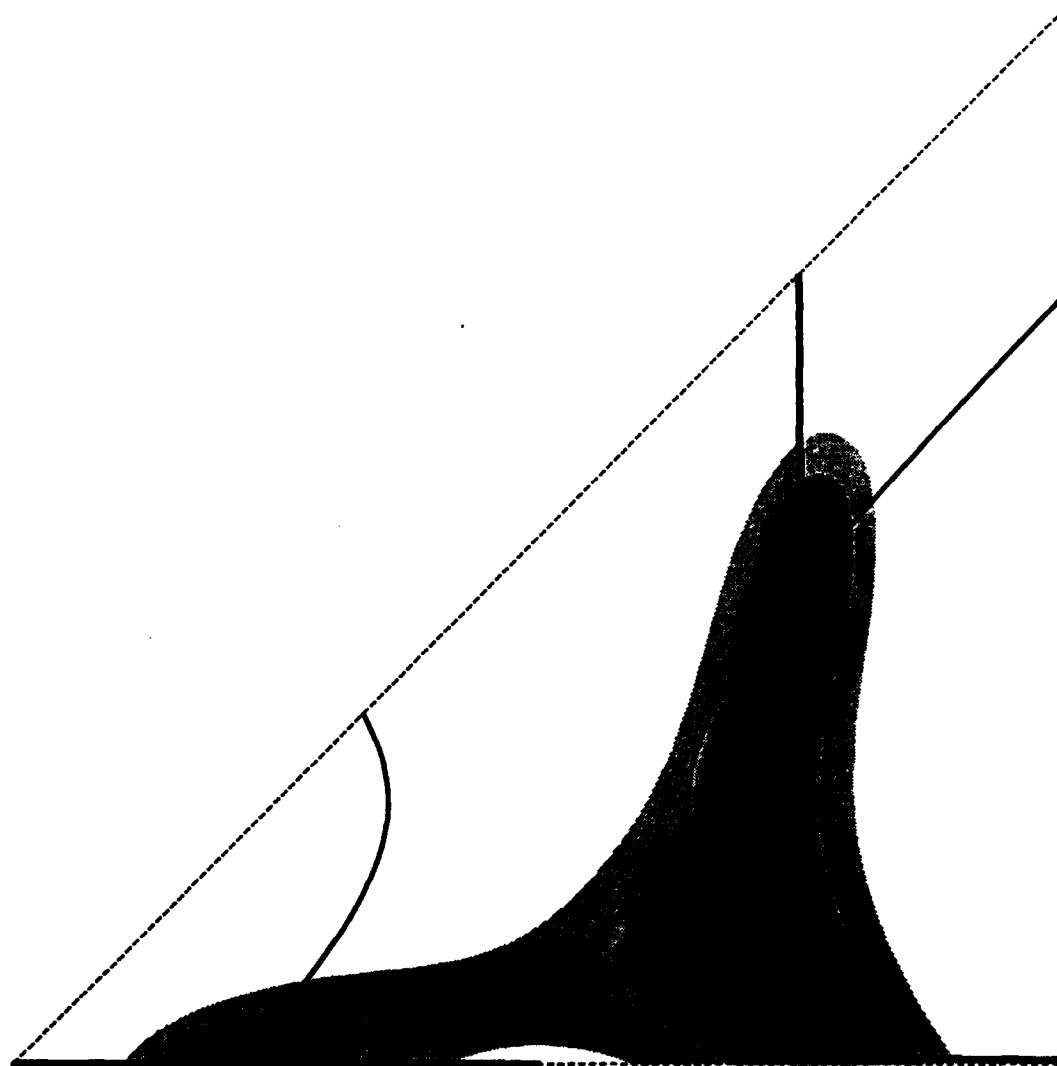


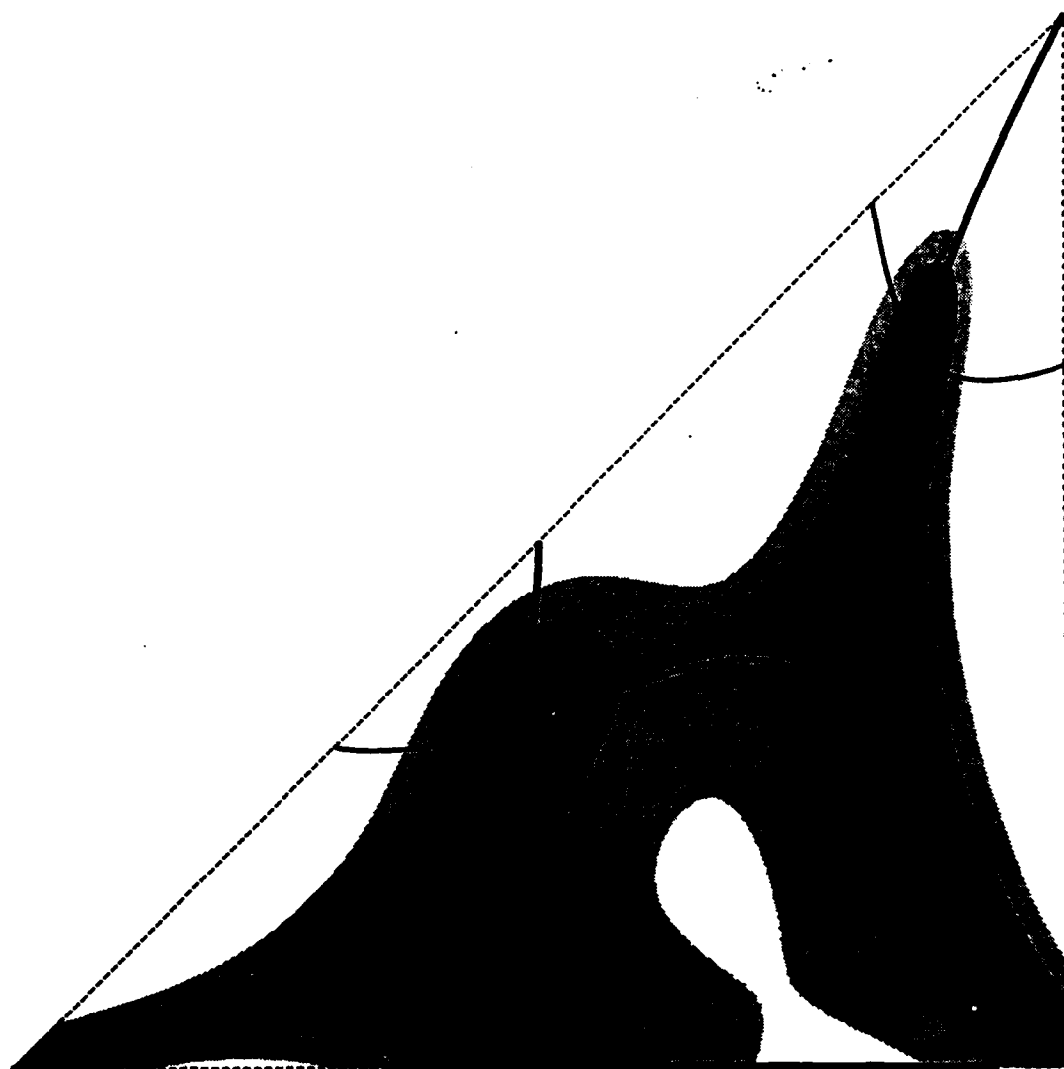
Fig. 31



Harmonic solution $P = 2$
SIMPLIFIED L2 APPROACH

— *Function Q1*
— *Function Q2*

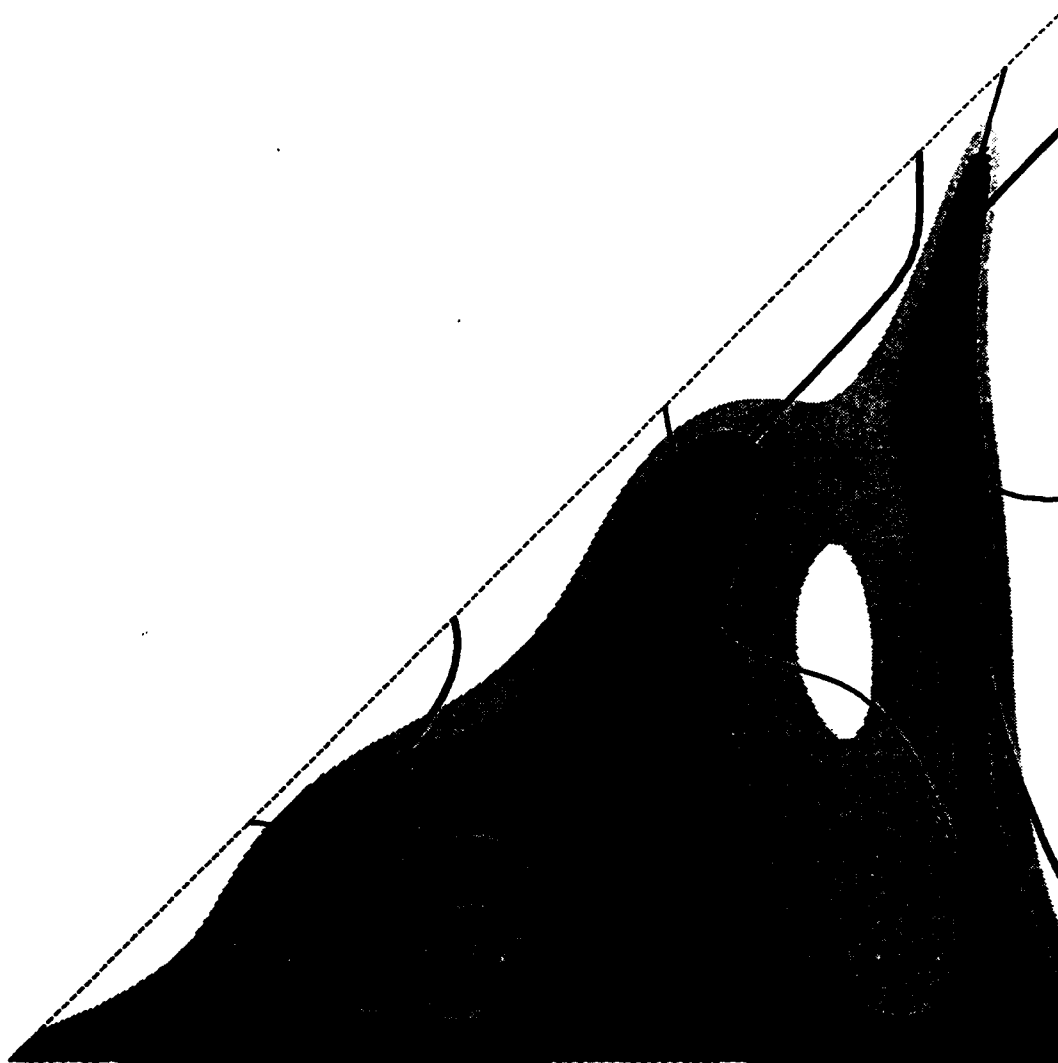
Fig. 32a



Harmonic solution $P = 3$
SIMPLIFIED L2 APPROACH

— *Function Q1*
 — *Function Q2*

Fig. 32b



Harmonic solution $P = 4$
SIMPLIFIED L2 APPROACH

— *Function Q1*
— *Function Q2*

Fig. 32c

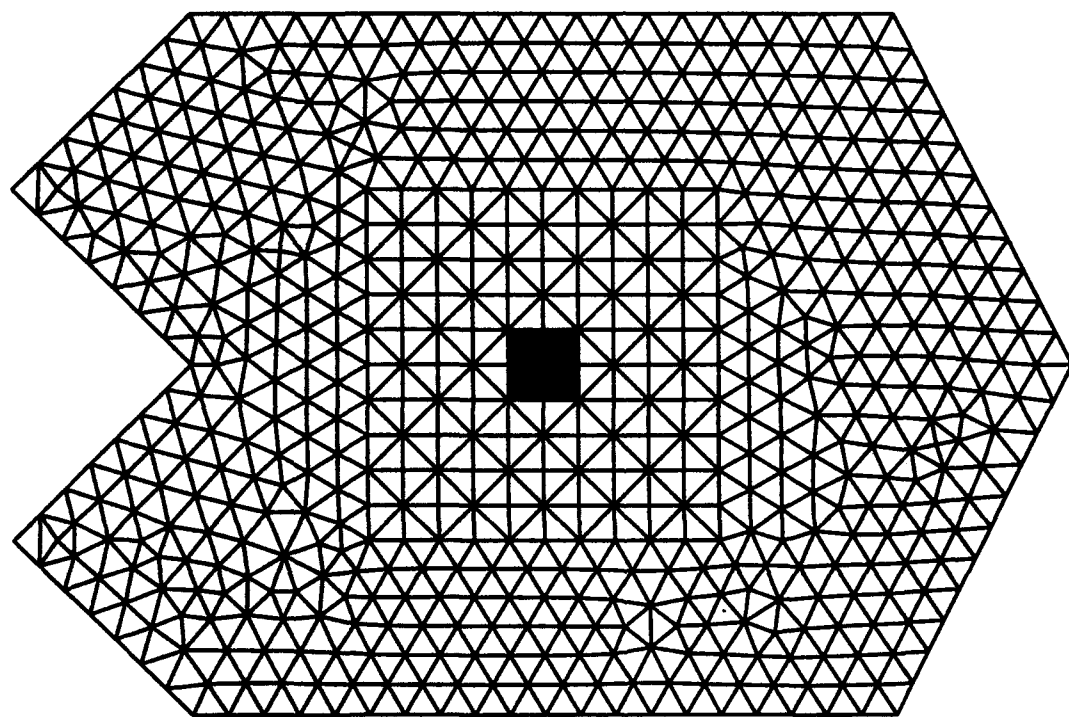


Fig. 33a

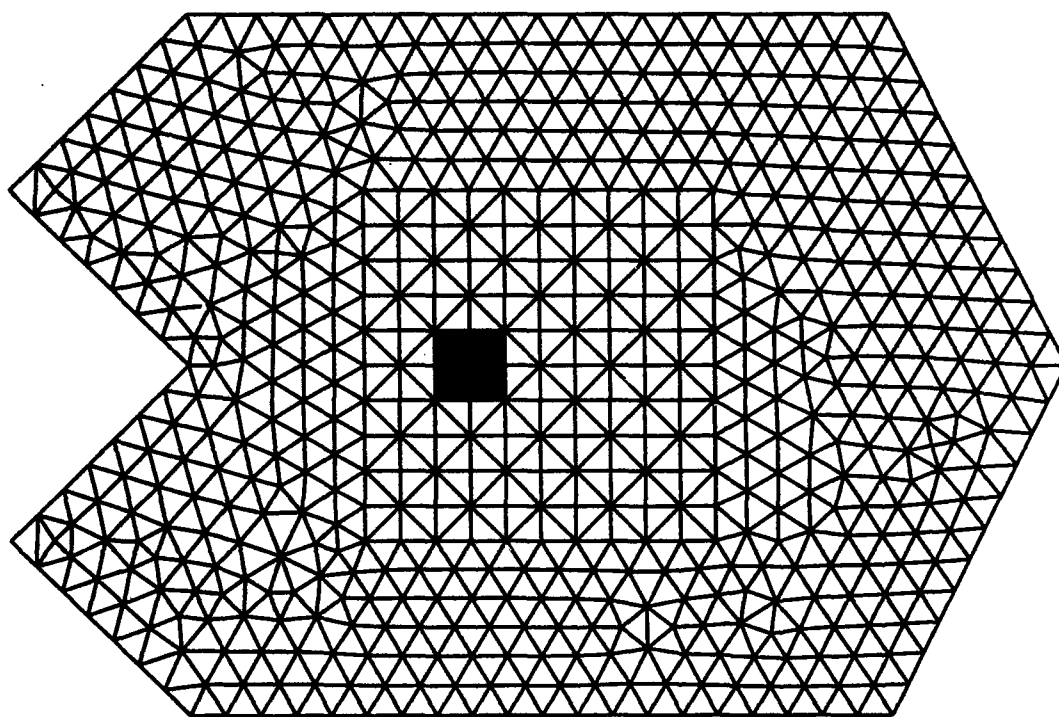


Fig. 33b

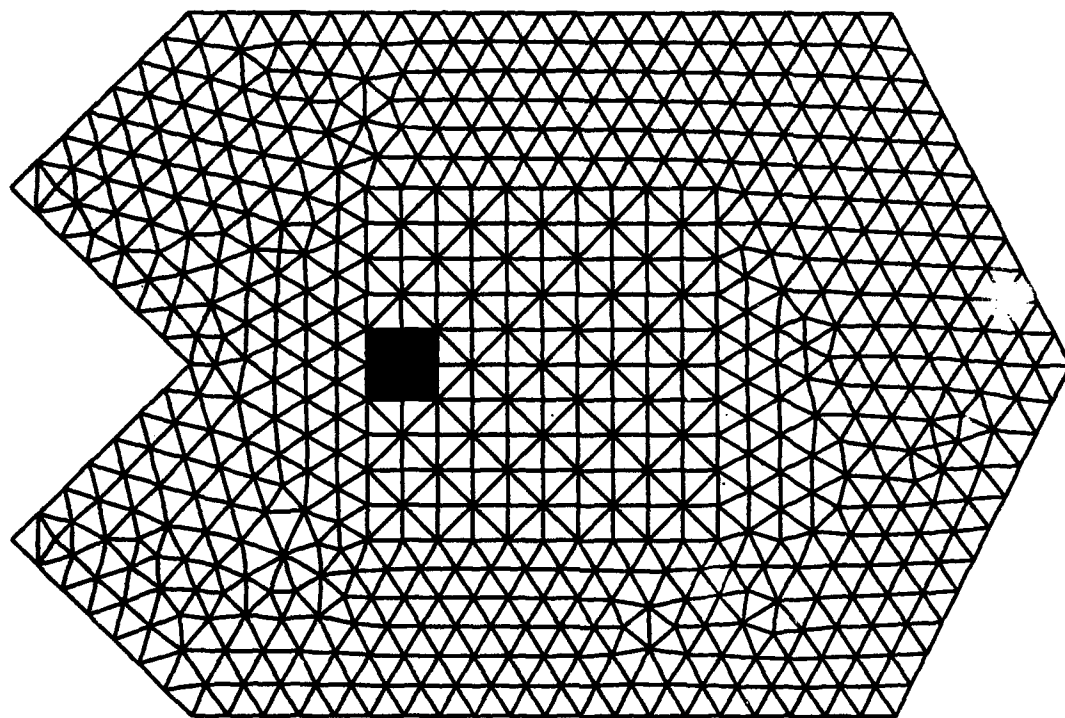
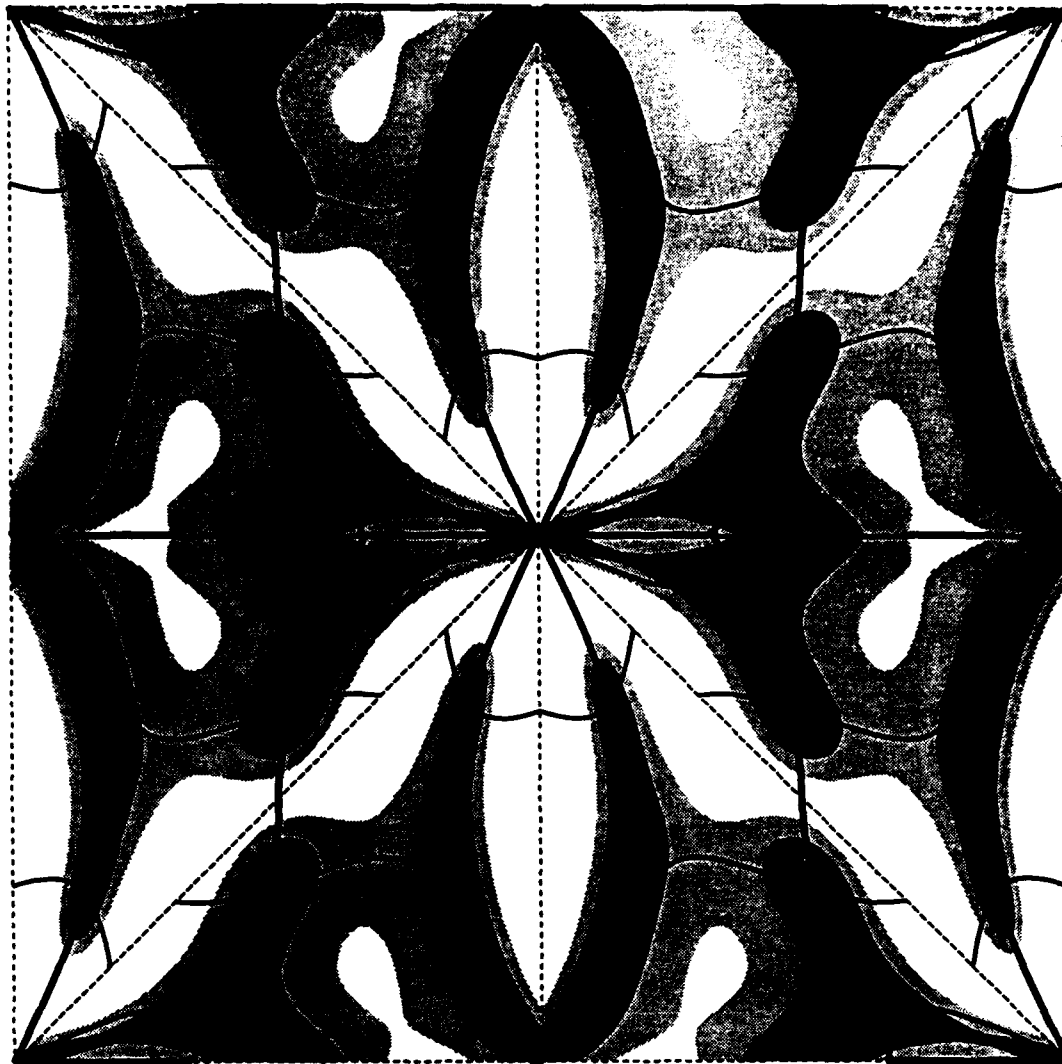


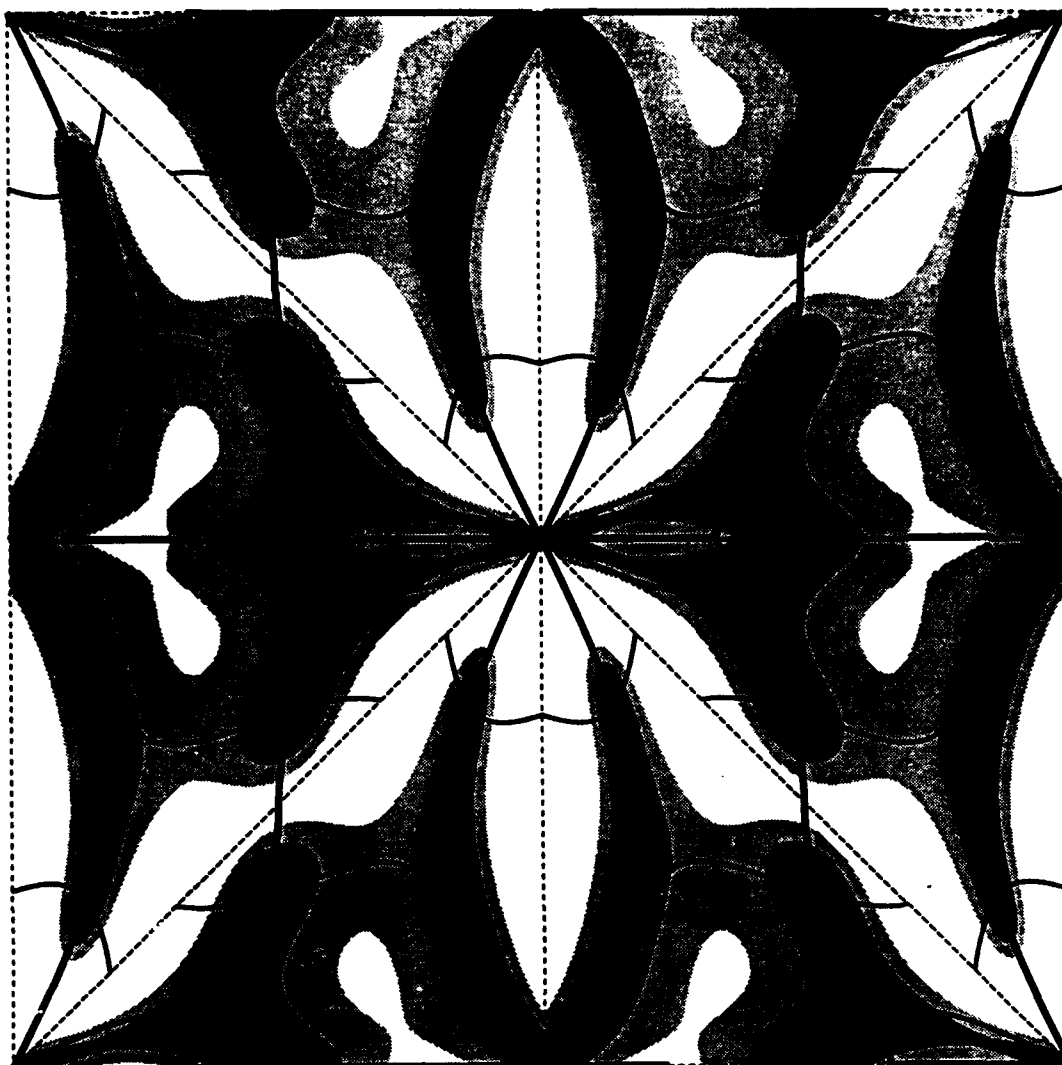
Fig. 33c



Harmonic solution $P = 3$
SIMPLIFIED L2 APPROACH

— *Function Q1*
— *Function Q2*

Fig. 34a



Harmonic solution $P = 3$
SIMPLIFIED L2 APPROACH

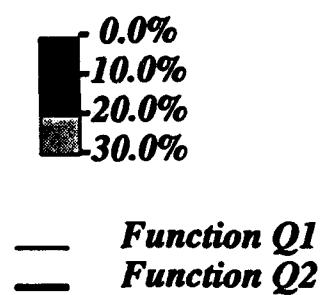
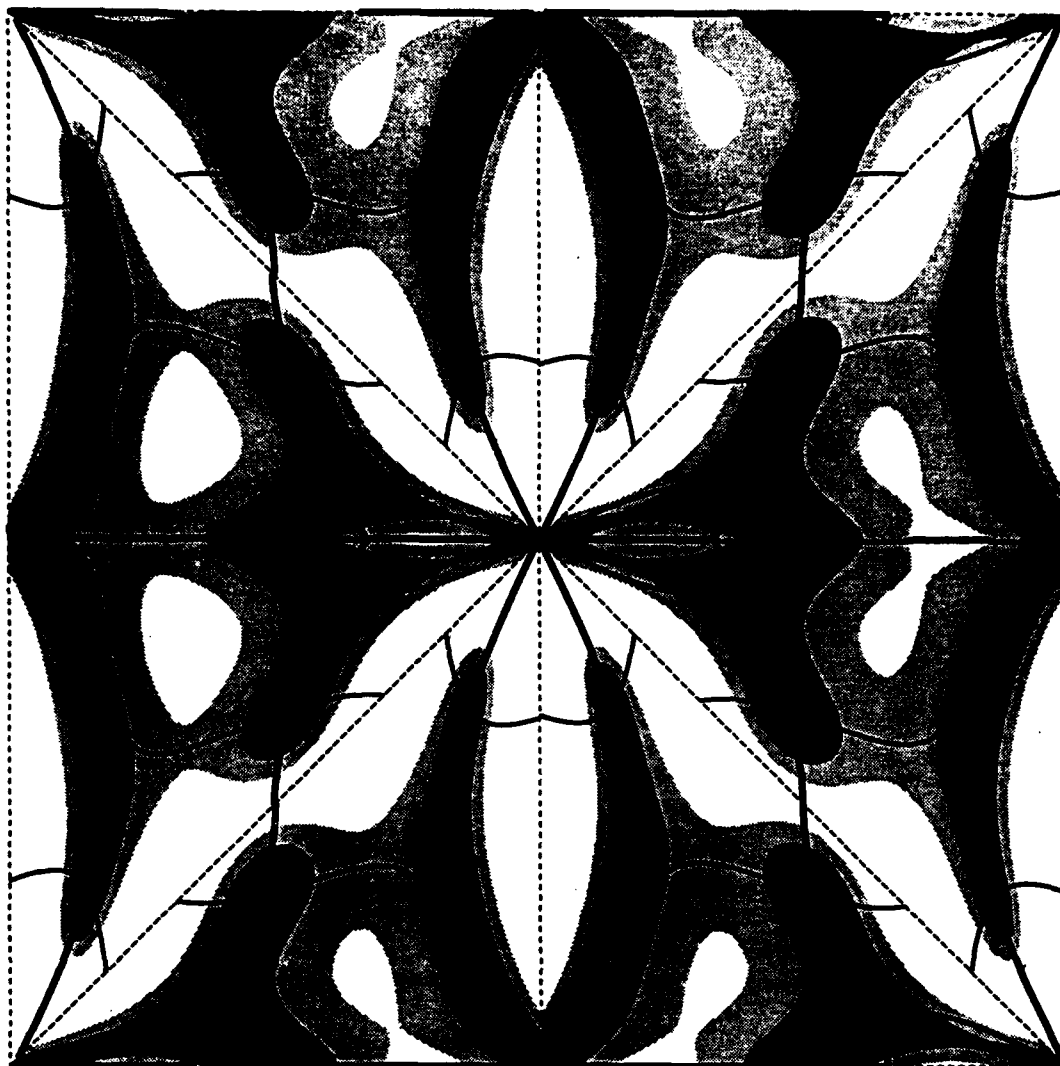


Fig. 34b



Harmonic solution $P = 3$
SIMPLIFIED L2 APPROACH

— *Function Q1*
— *Function Q2*

Fig. 34c

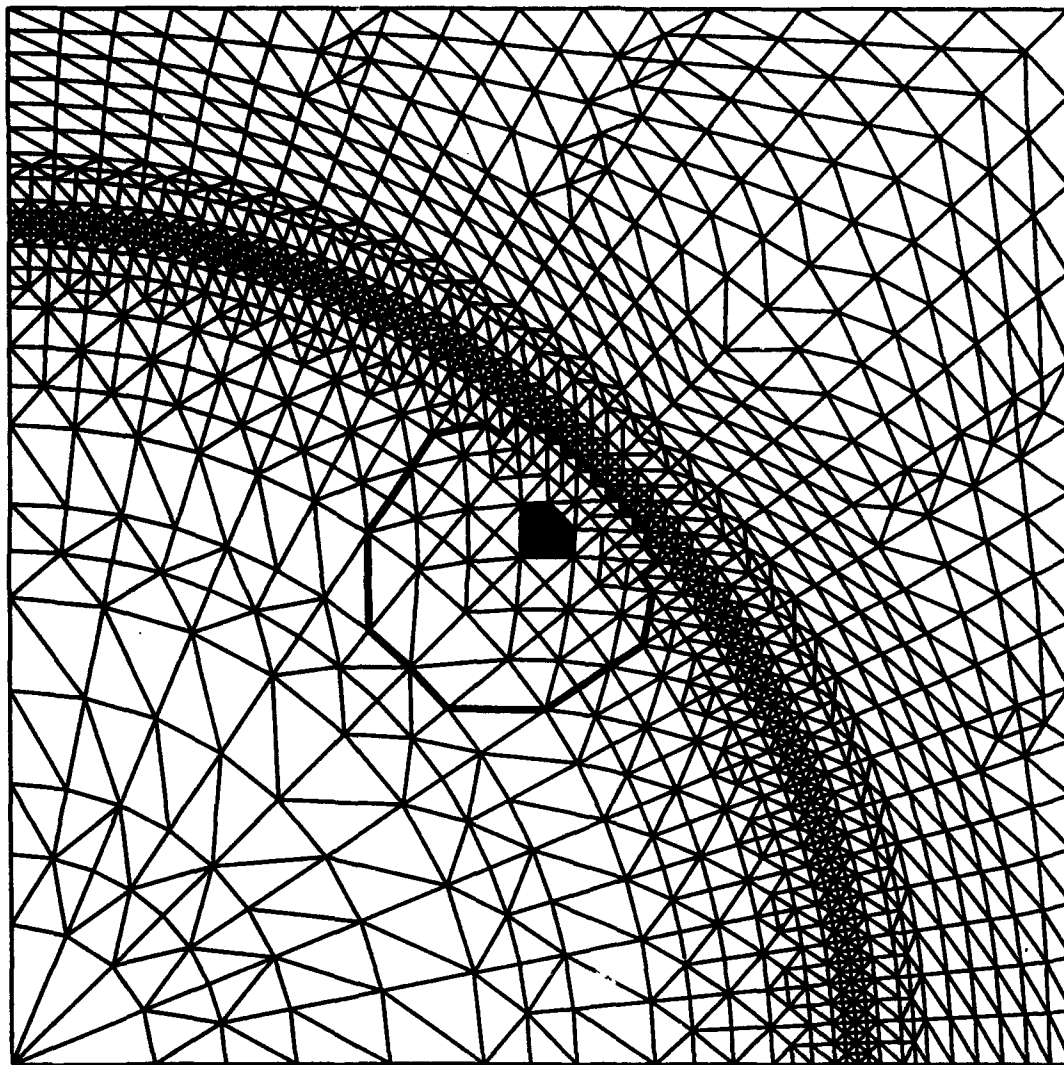


Fig. 35a

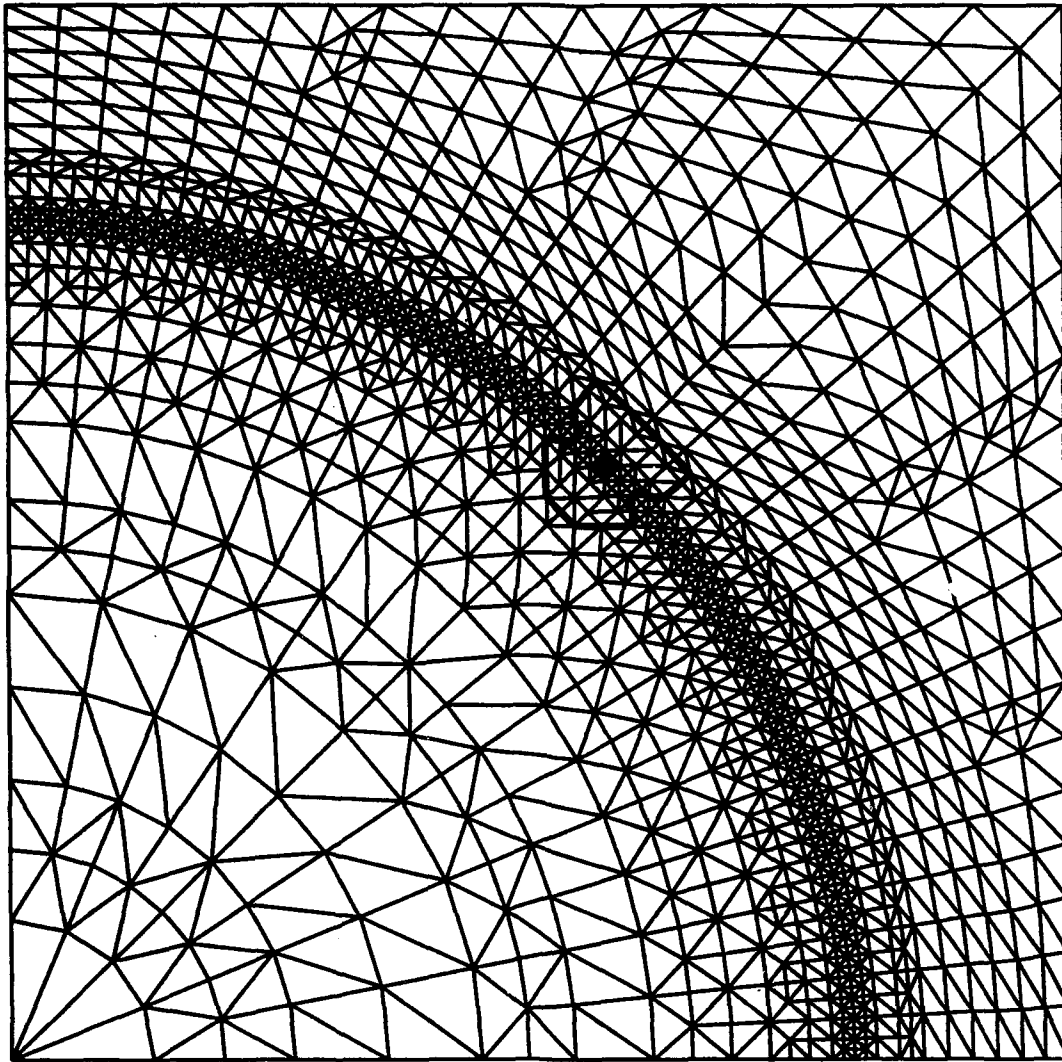


Fig. 35b

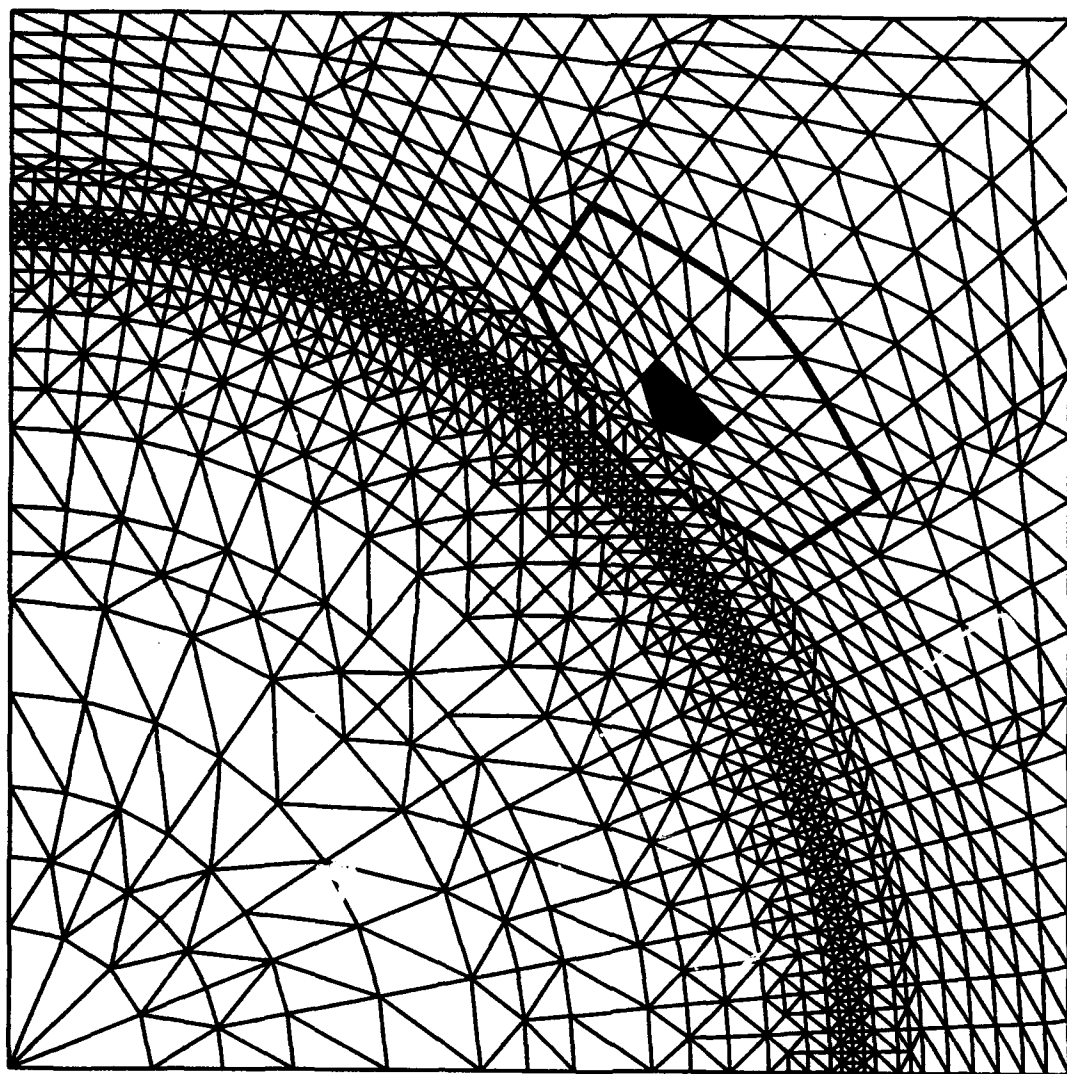


Fig. 35c

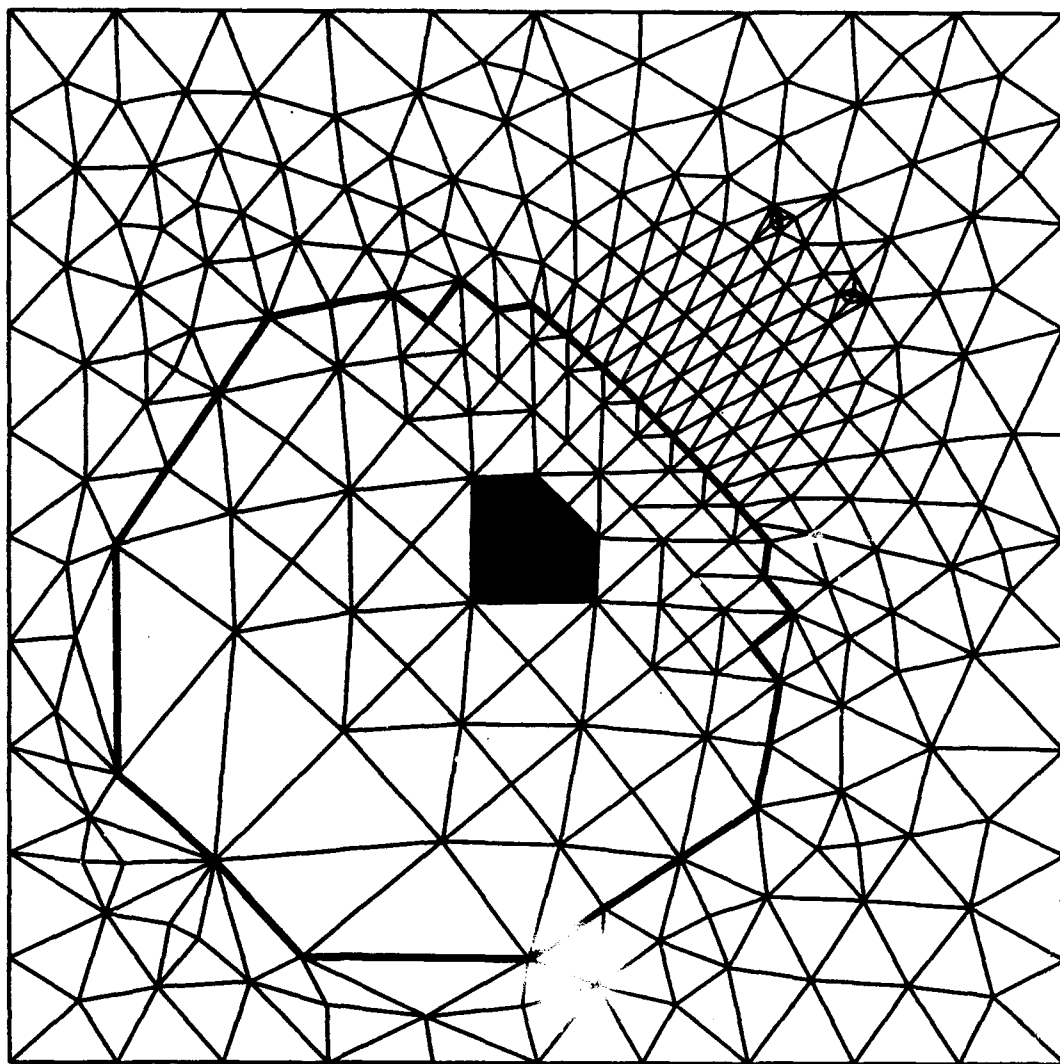


Fig. 36a

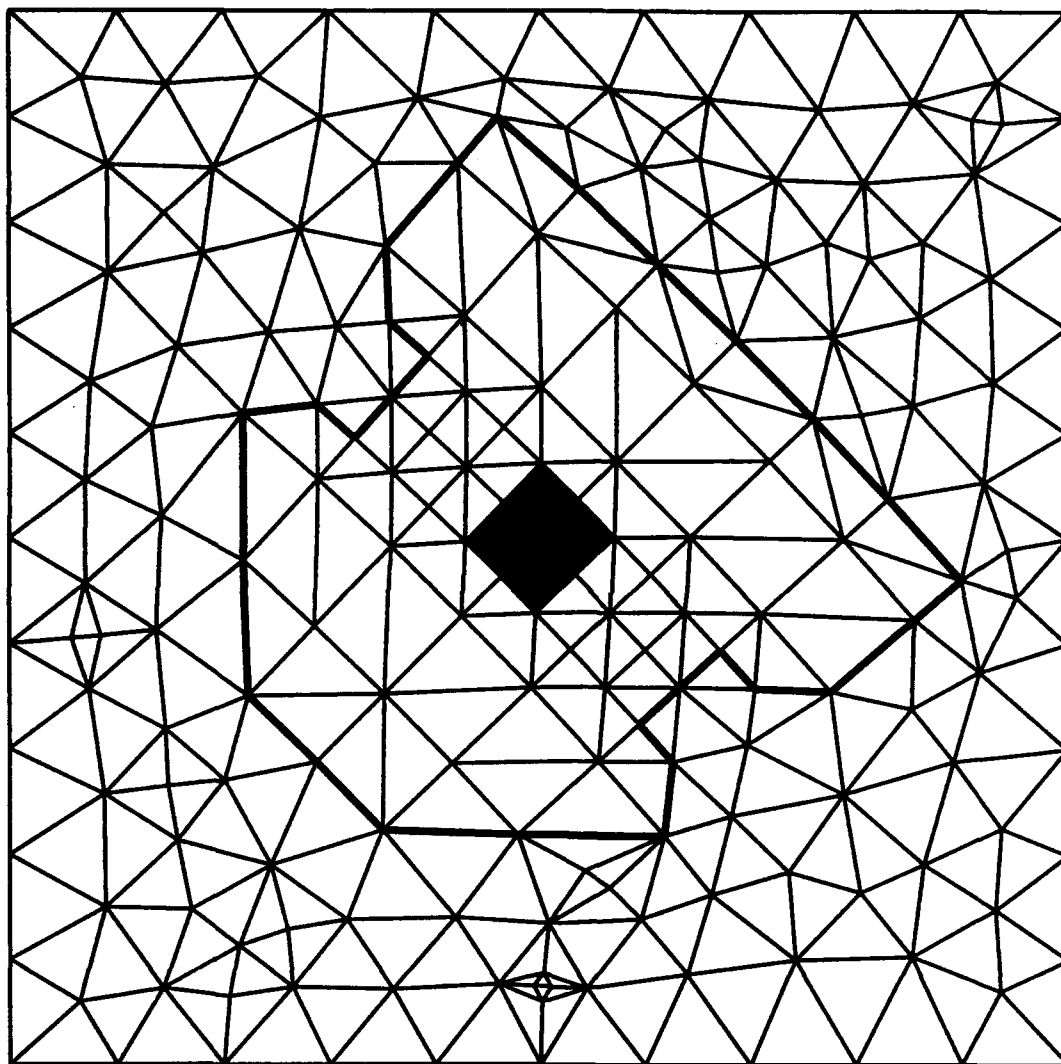


Fig. 36b

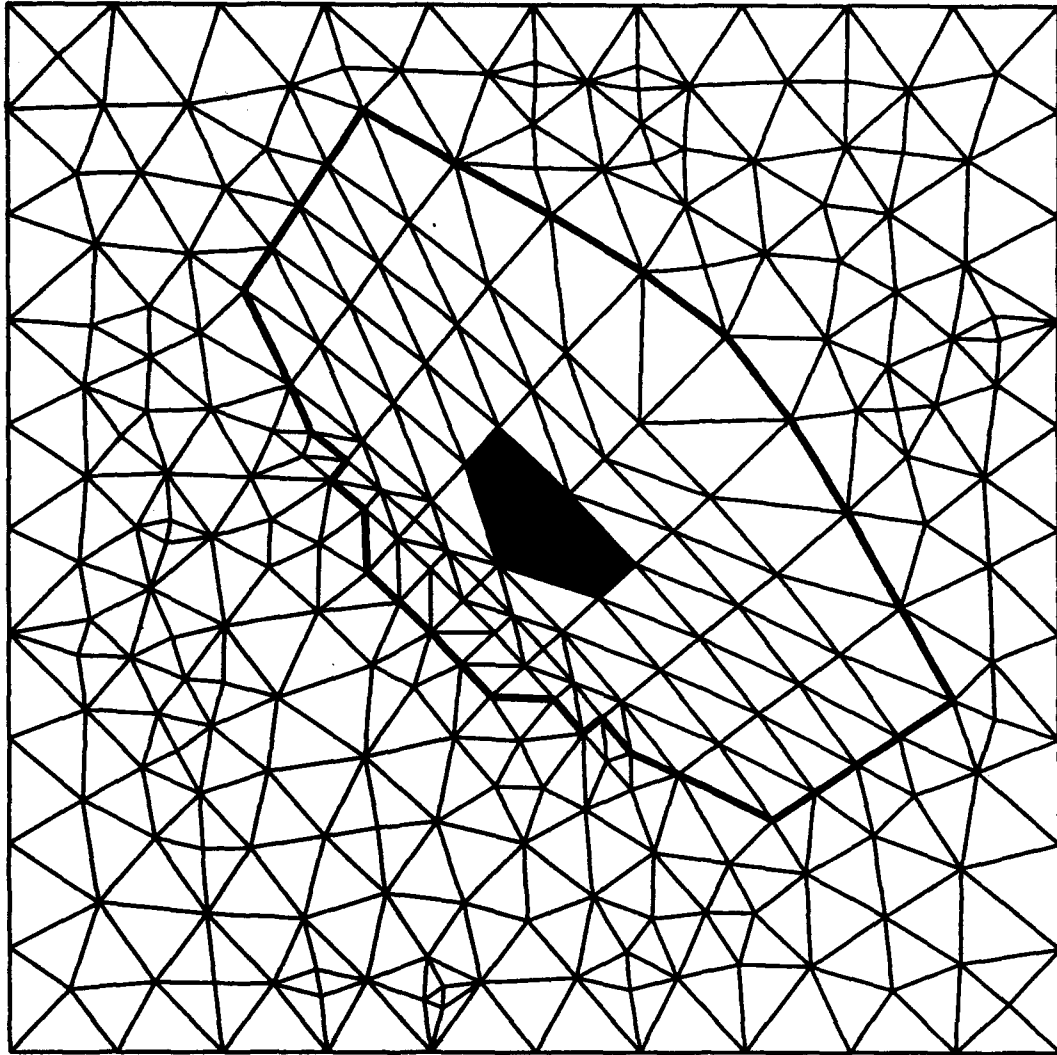
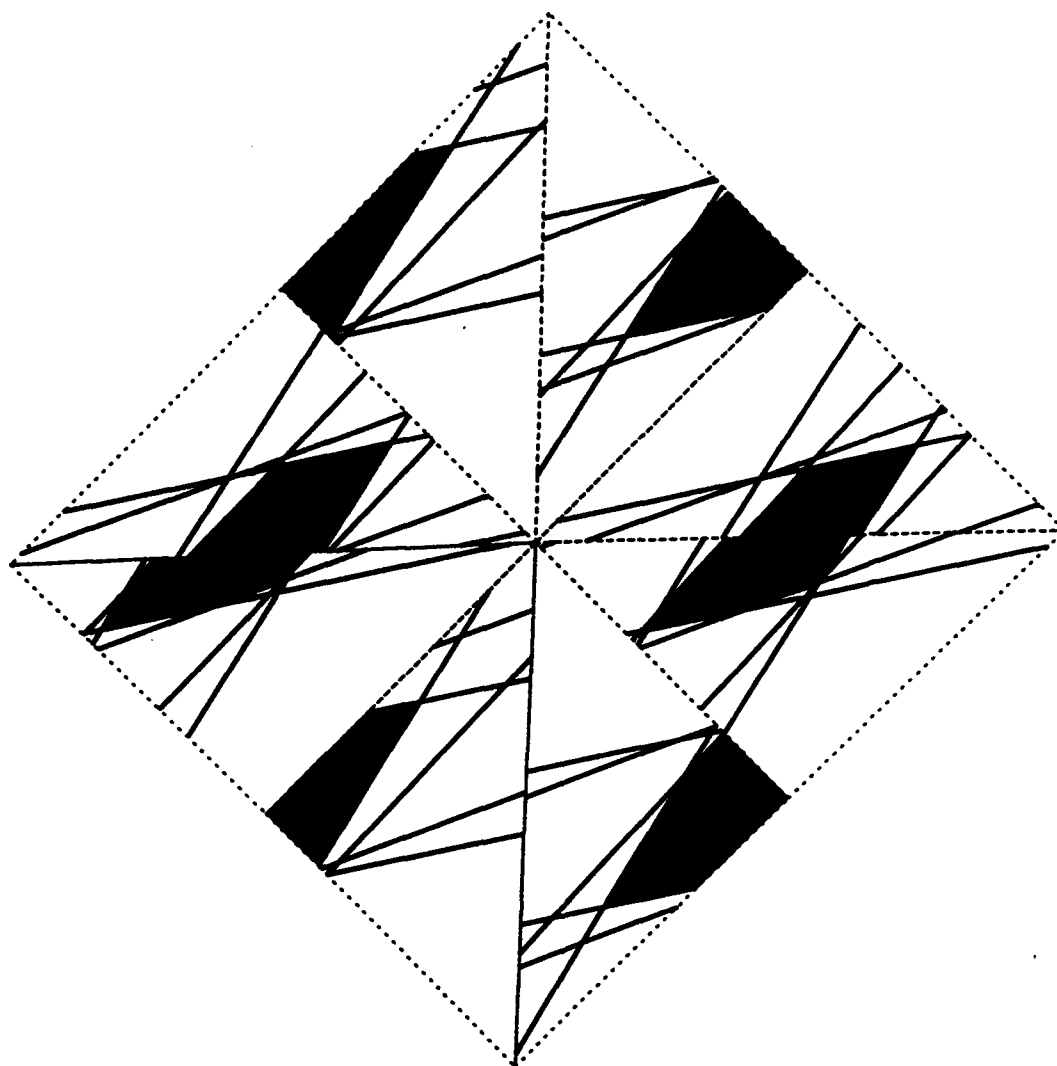


Fig. 36c

Fig. 37a

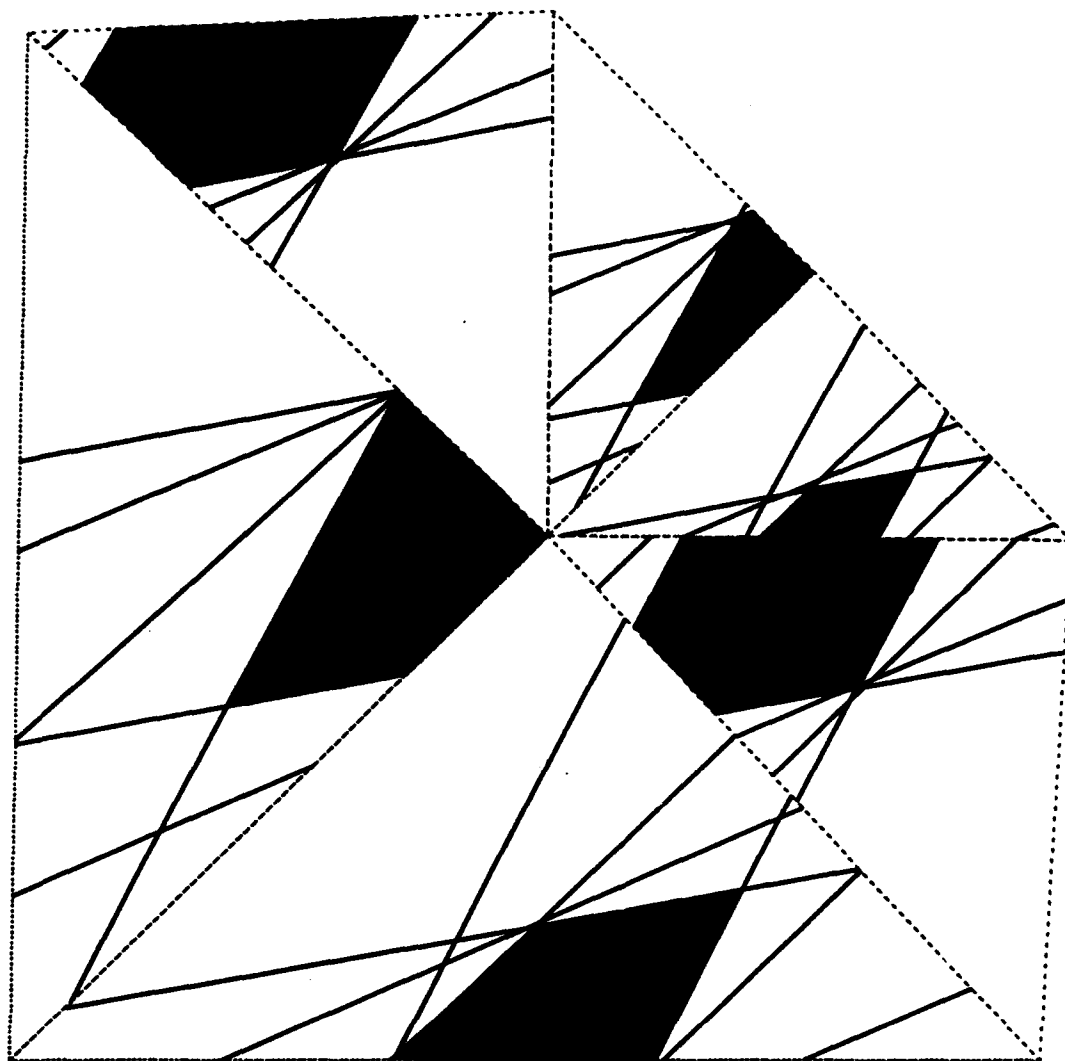


Harmonic solution

P = 1

— 25.0 % contour

Fig. 37b

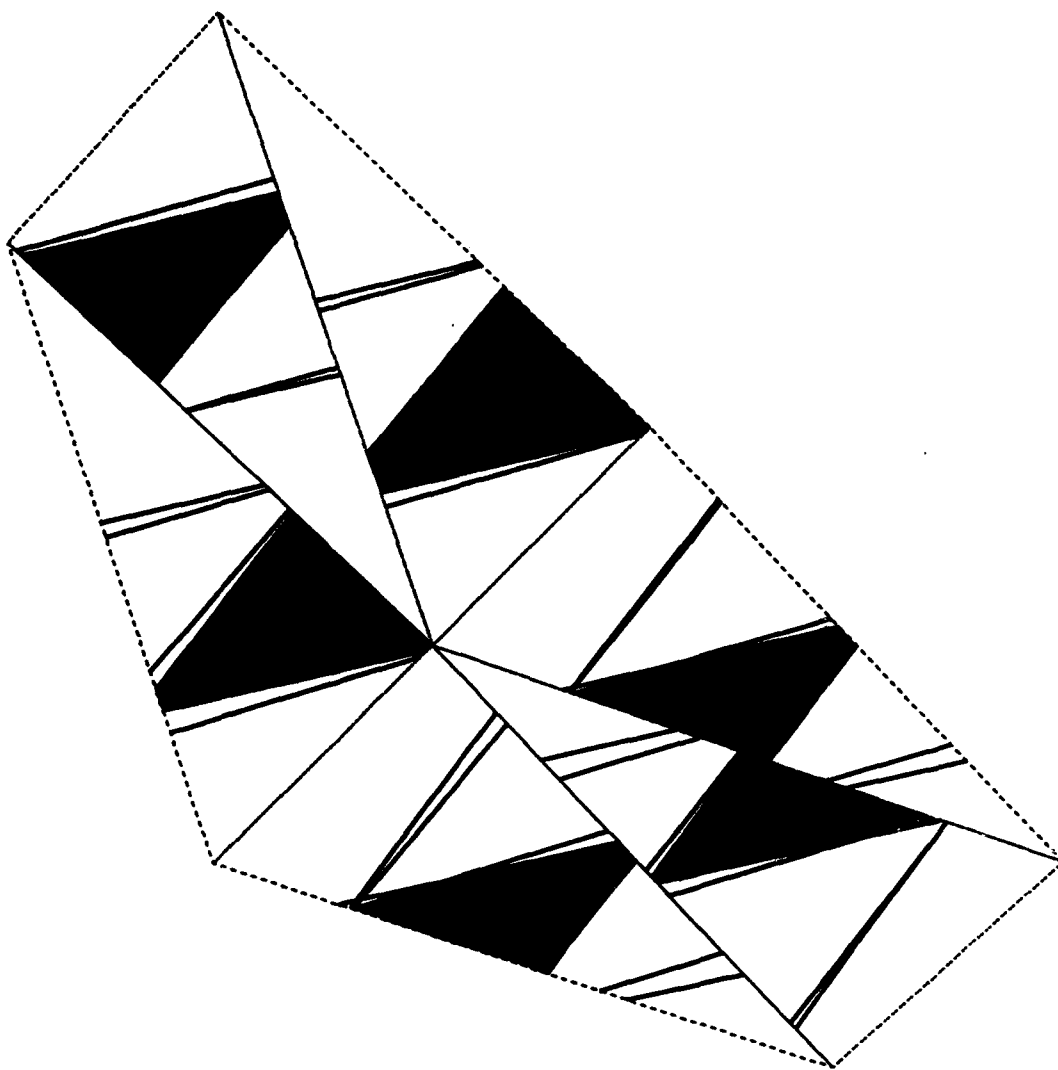


Harmonic solution

P = 1

— 25.0 % contour

Fig. 37c

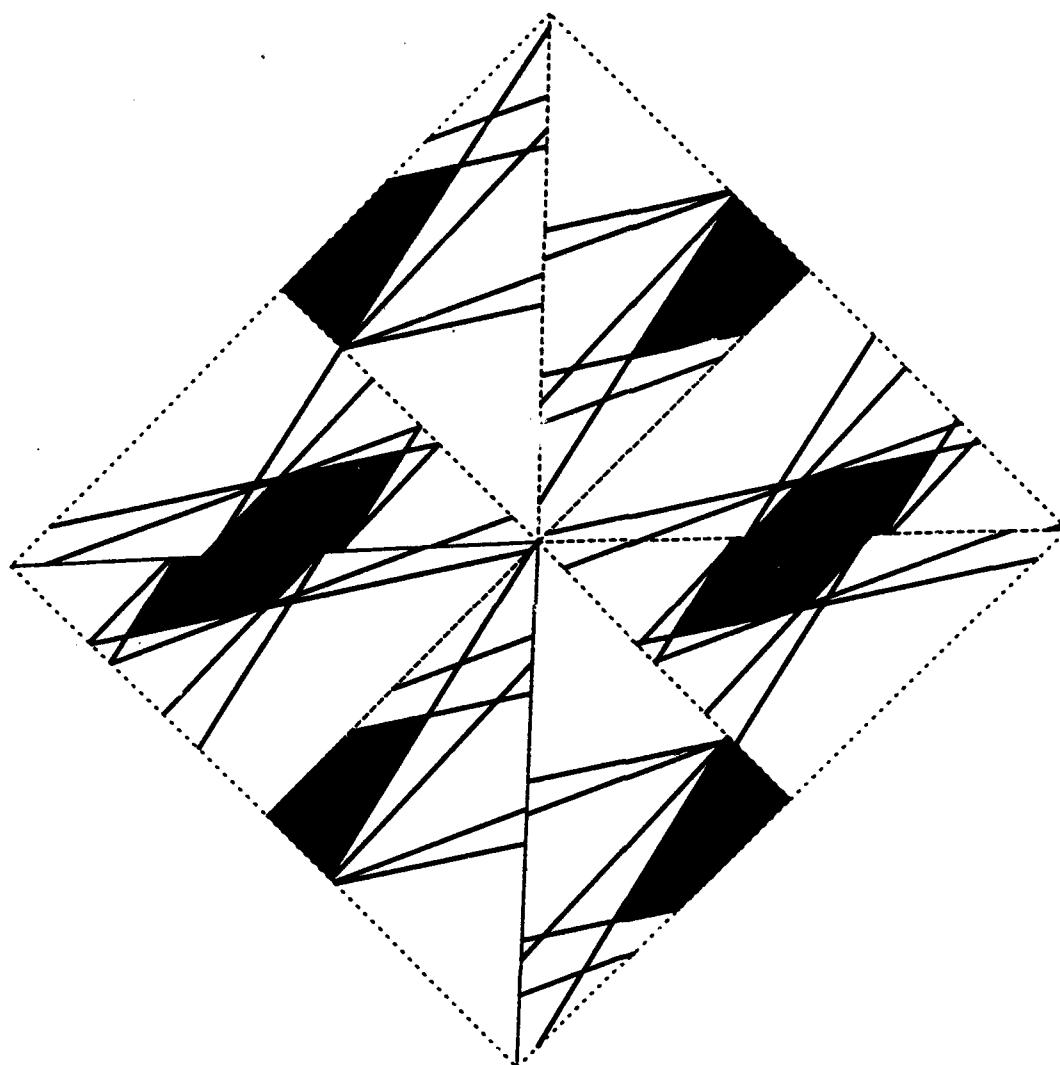


Harmonic solution

$P = 1$

— 25.0 % contour

Fig. 38a

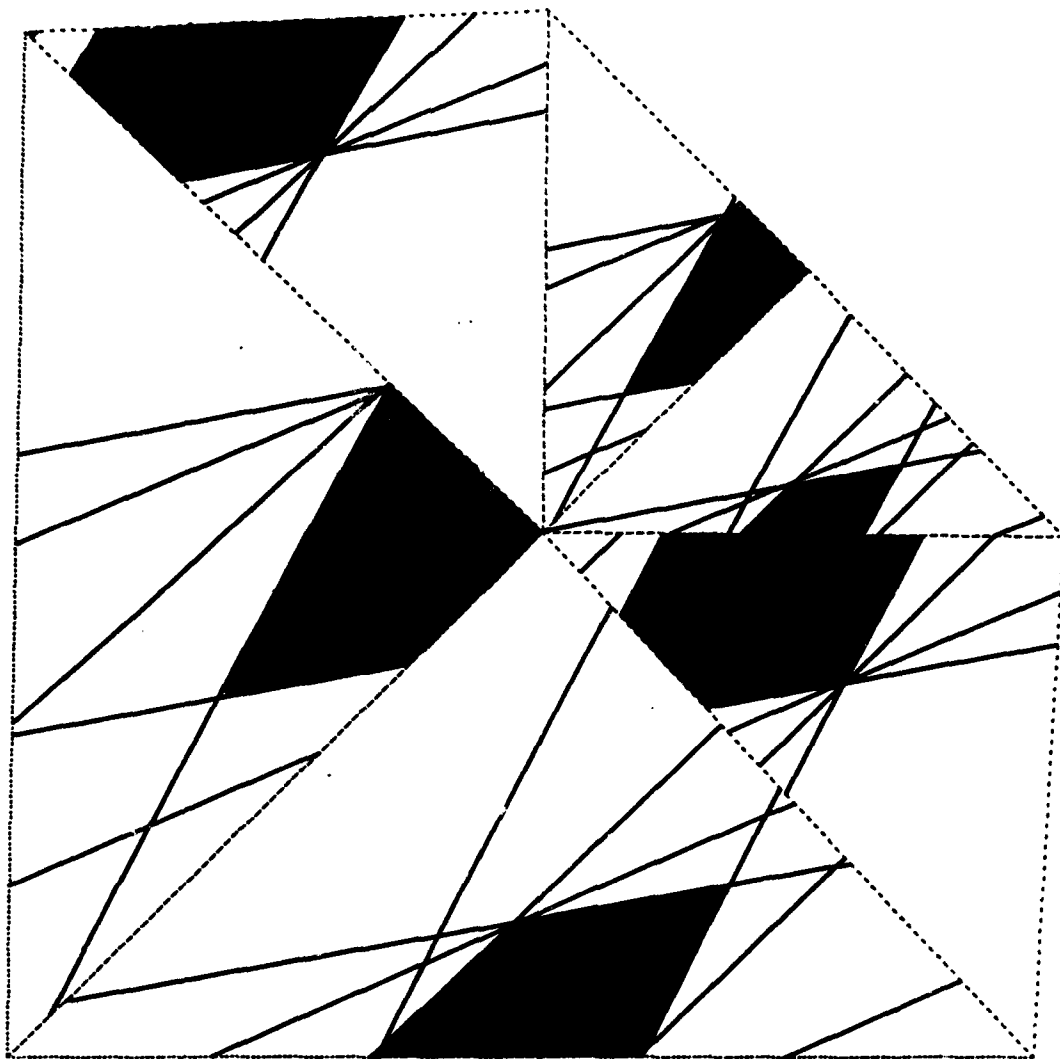


Harmonic solution

P = 1

— 25.0 % contour

Fig. 38b

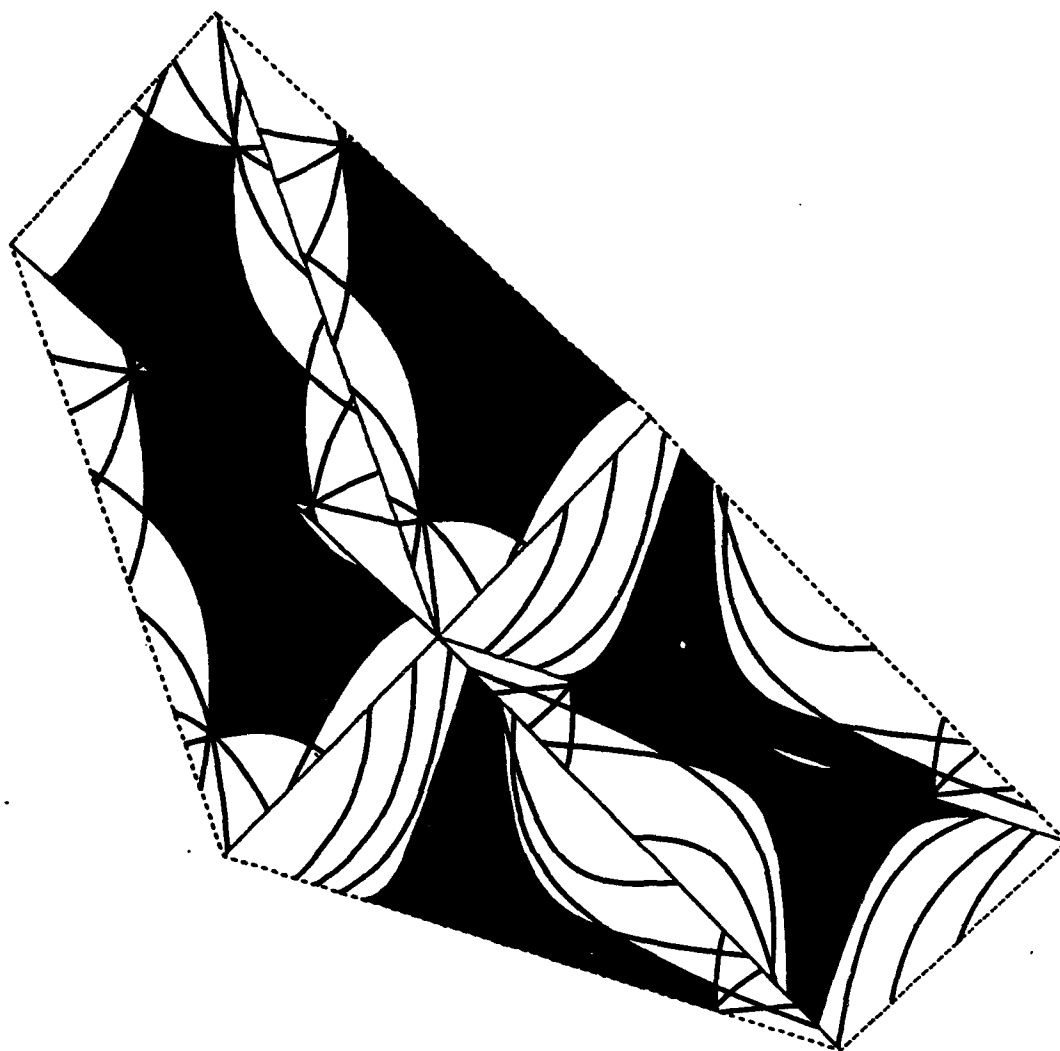


Harmonic solution

$P = 1$

— 25.0 % contour

Fig. 38c

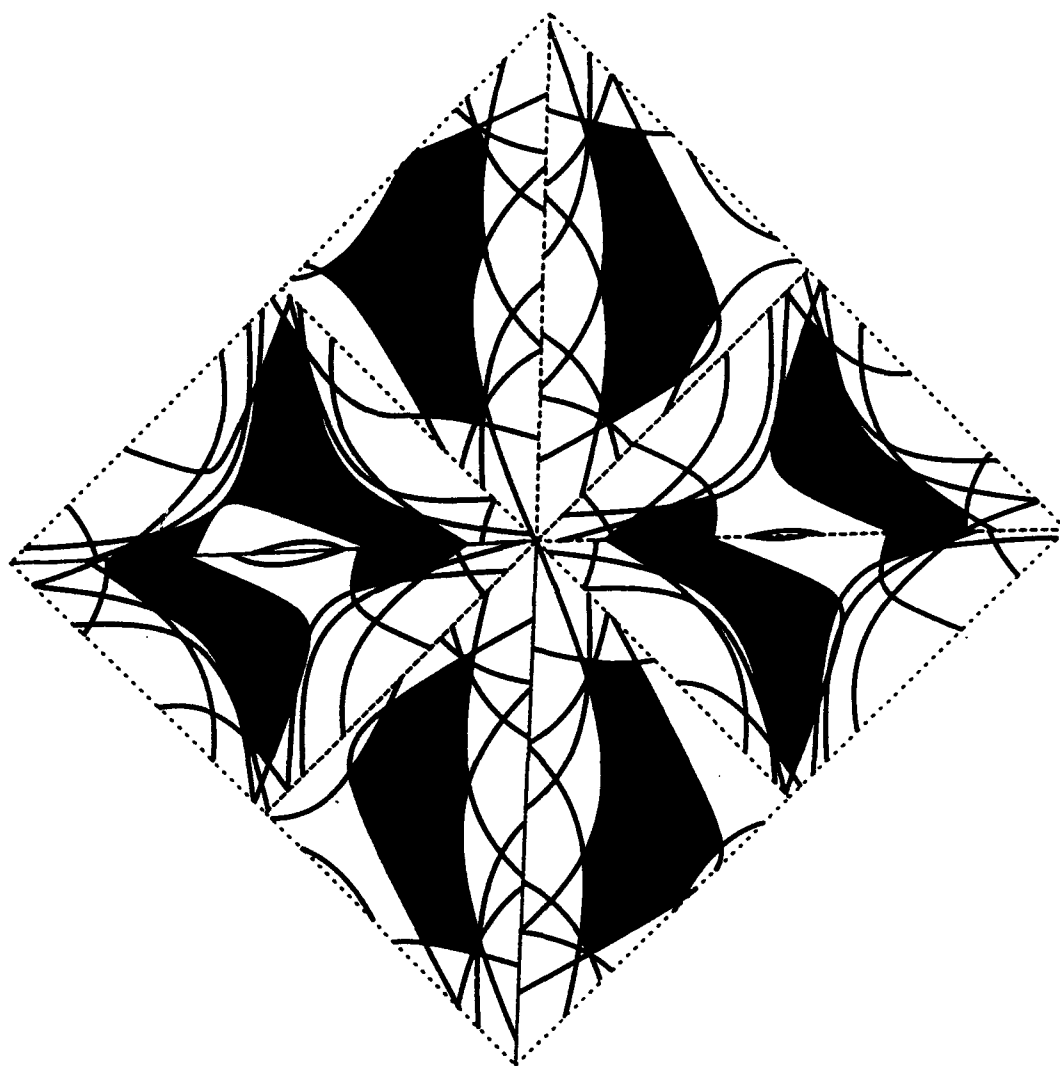


Harmonic solution

$P = 2$

— 25.0 % contour

Fig. 39a

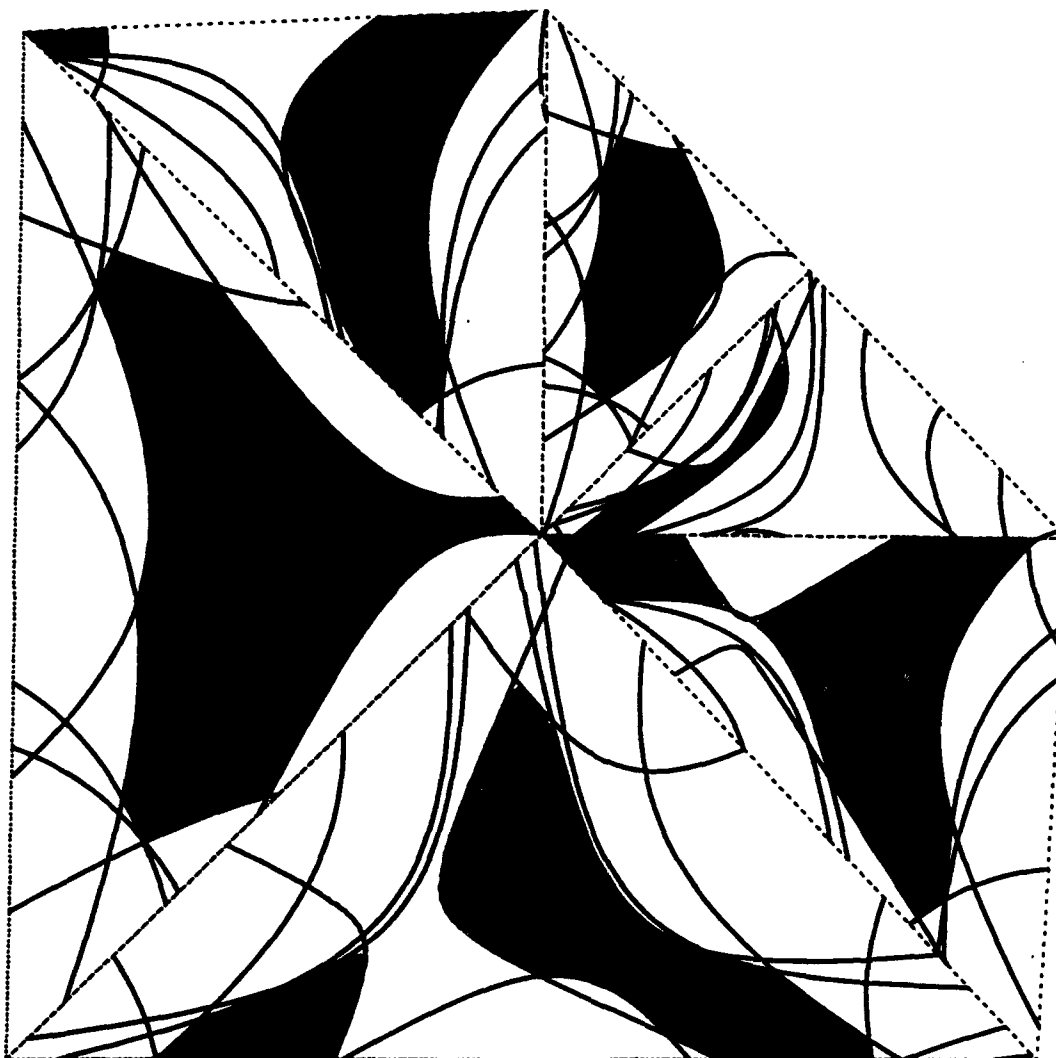


Harmonic solution

$P = 2$

— 25.0 % contour

Fig. 39b

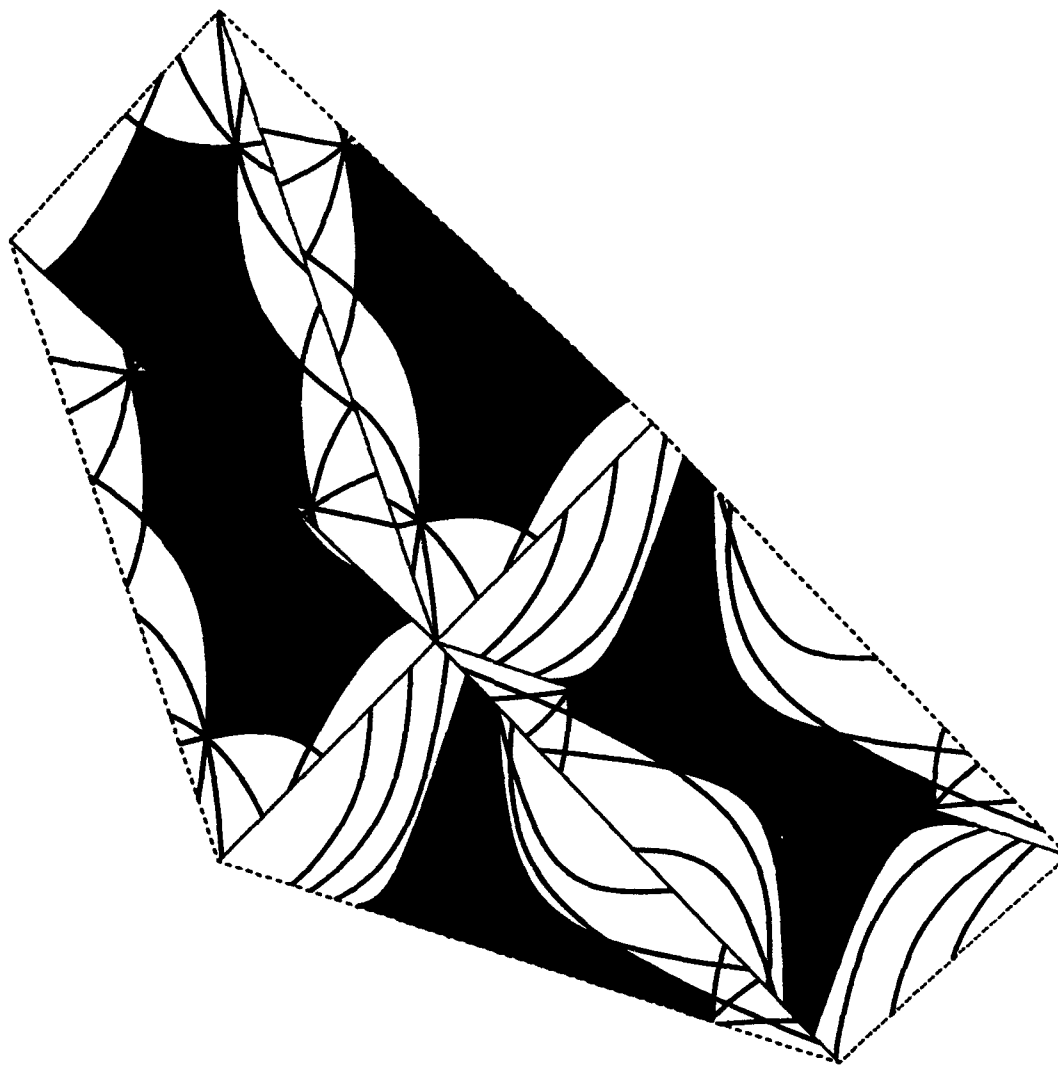


Harmonic solution

$P = 2$

— 25.0 % contour

Fig. 39c

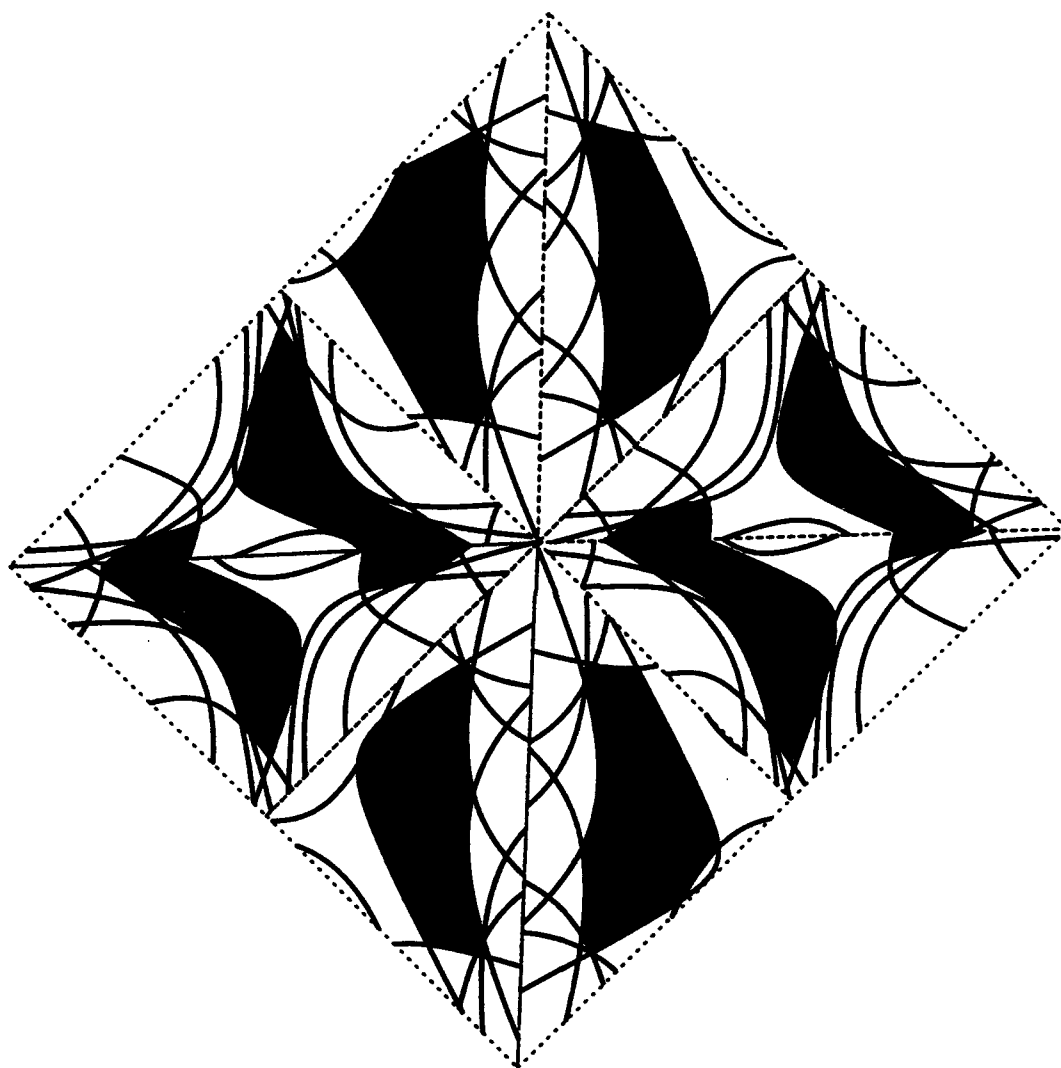


Harmonic solution

$P = 2$

— 25.0 % contour

Fig. 40a

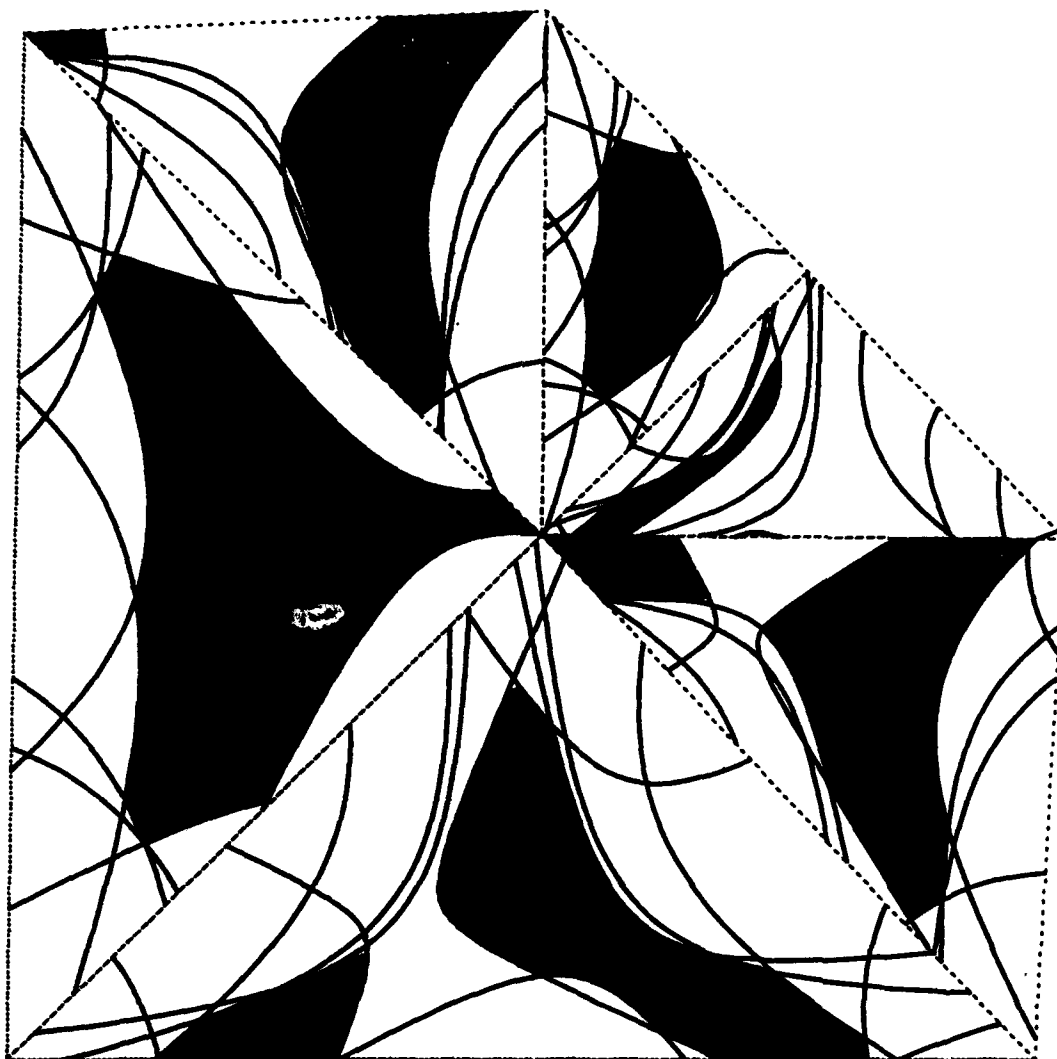


Harmonic solution

$P = 2$

— 25.0 % contour

Fig. 40b



Harmonic solution

$P = 2$

— 25.0 % contour

Fig. 40c

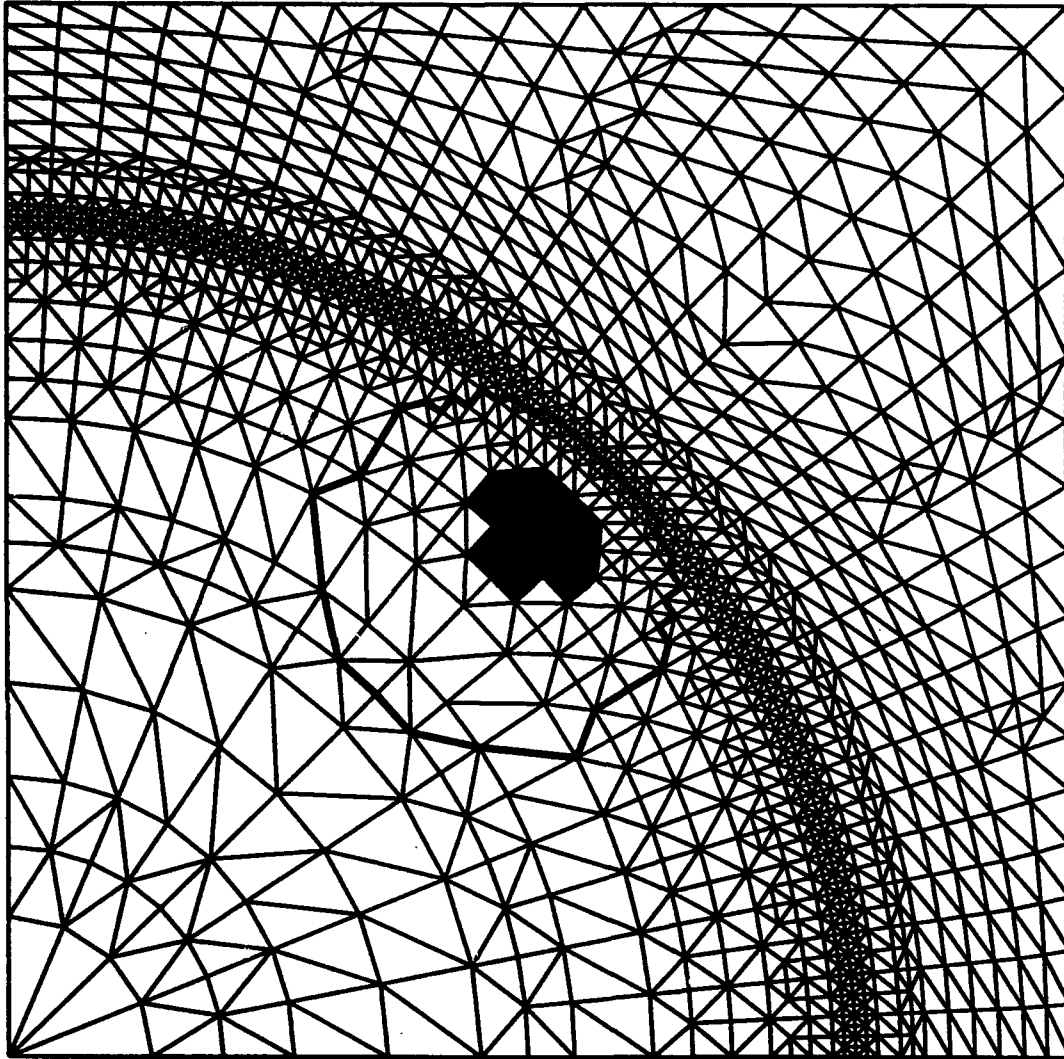
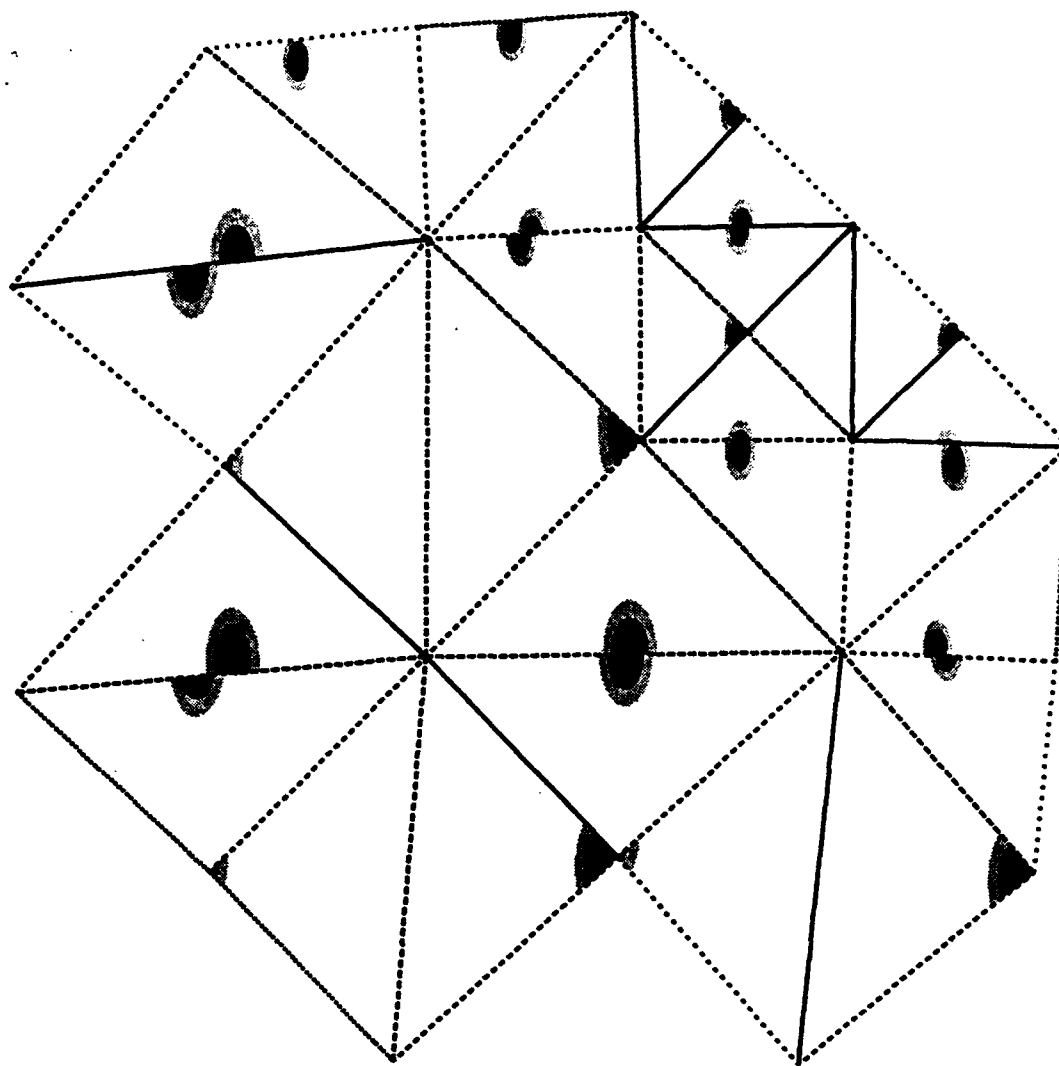


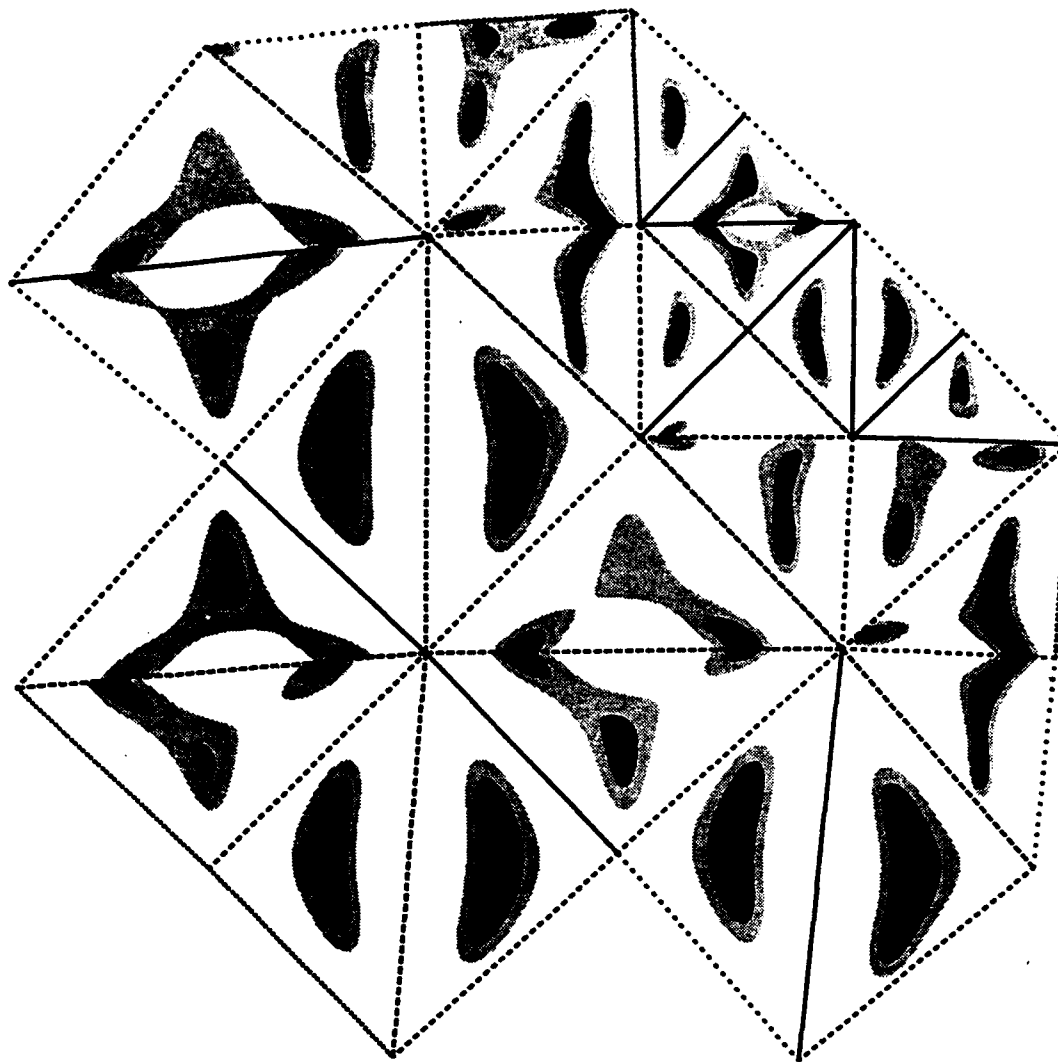
Fig. 41



Harmonic solution $P = 1$
SIMPLIFIED L2-APPROACH



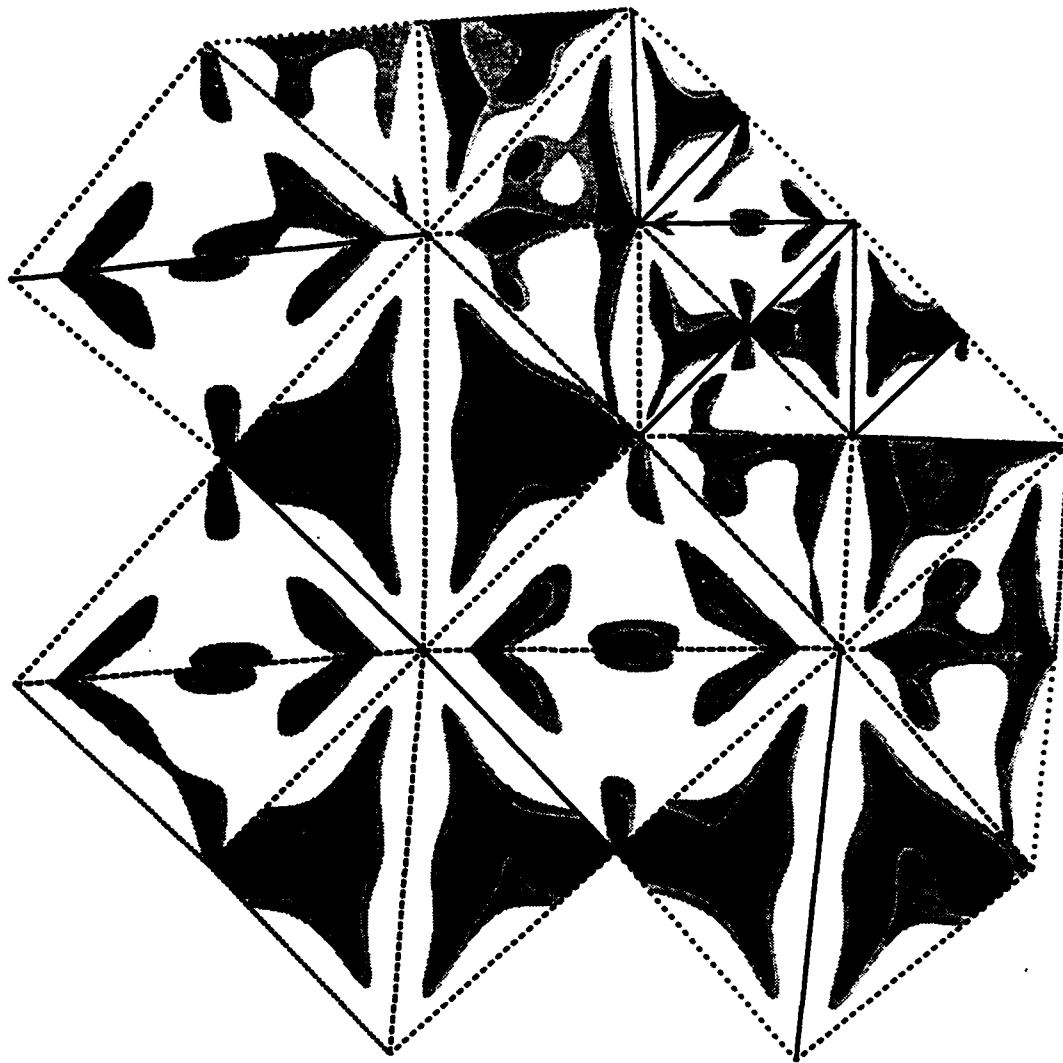
Fig. 42a



Harmonic solution $P = 2$
SIMPLIFIED L2 APPROACH



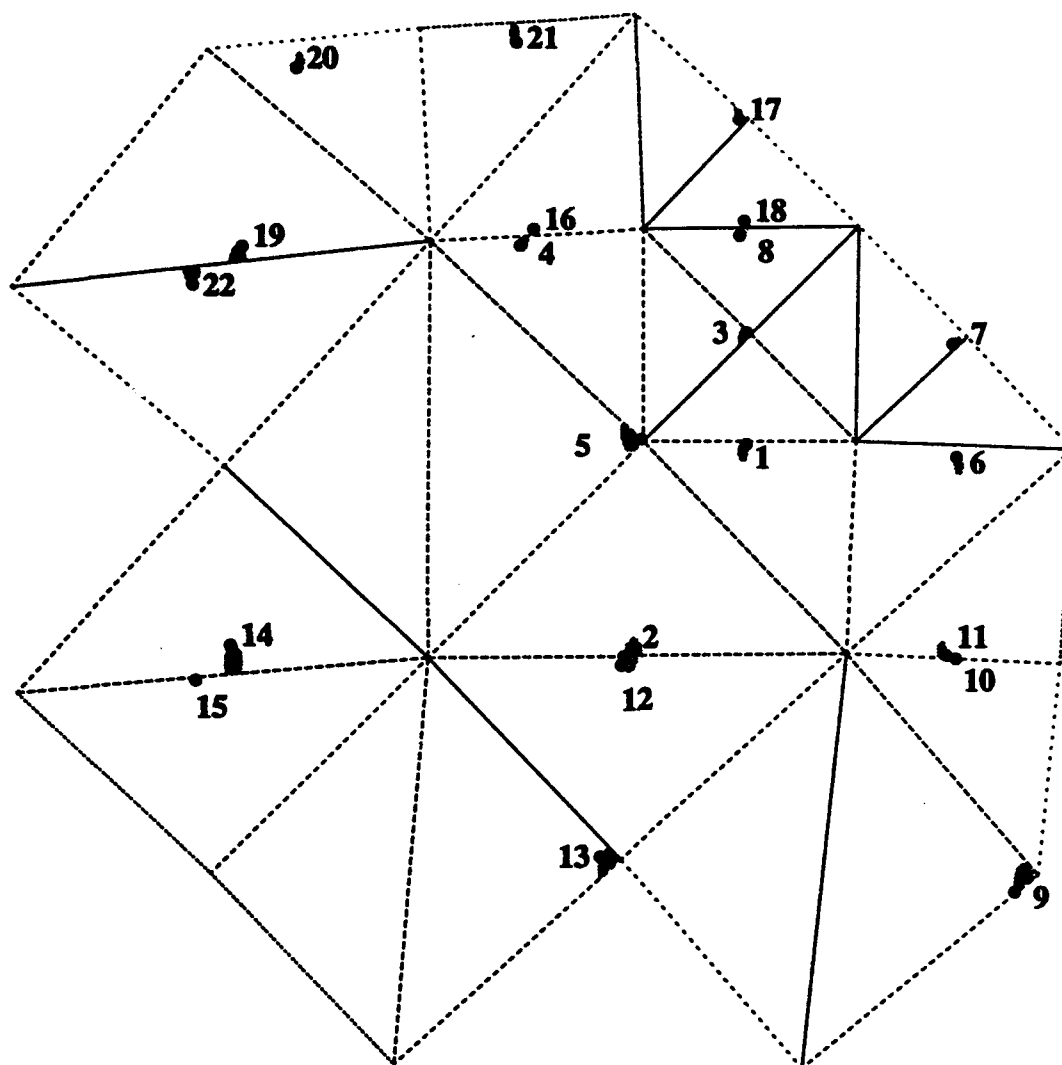
Fig. 42b



Harmonic solution $P = 3$
SIMPLIFIED L2 APPROACH



Fig. 42c

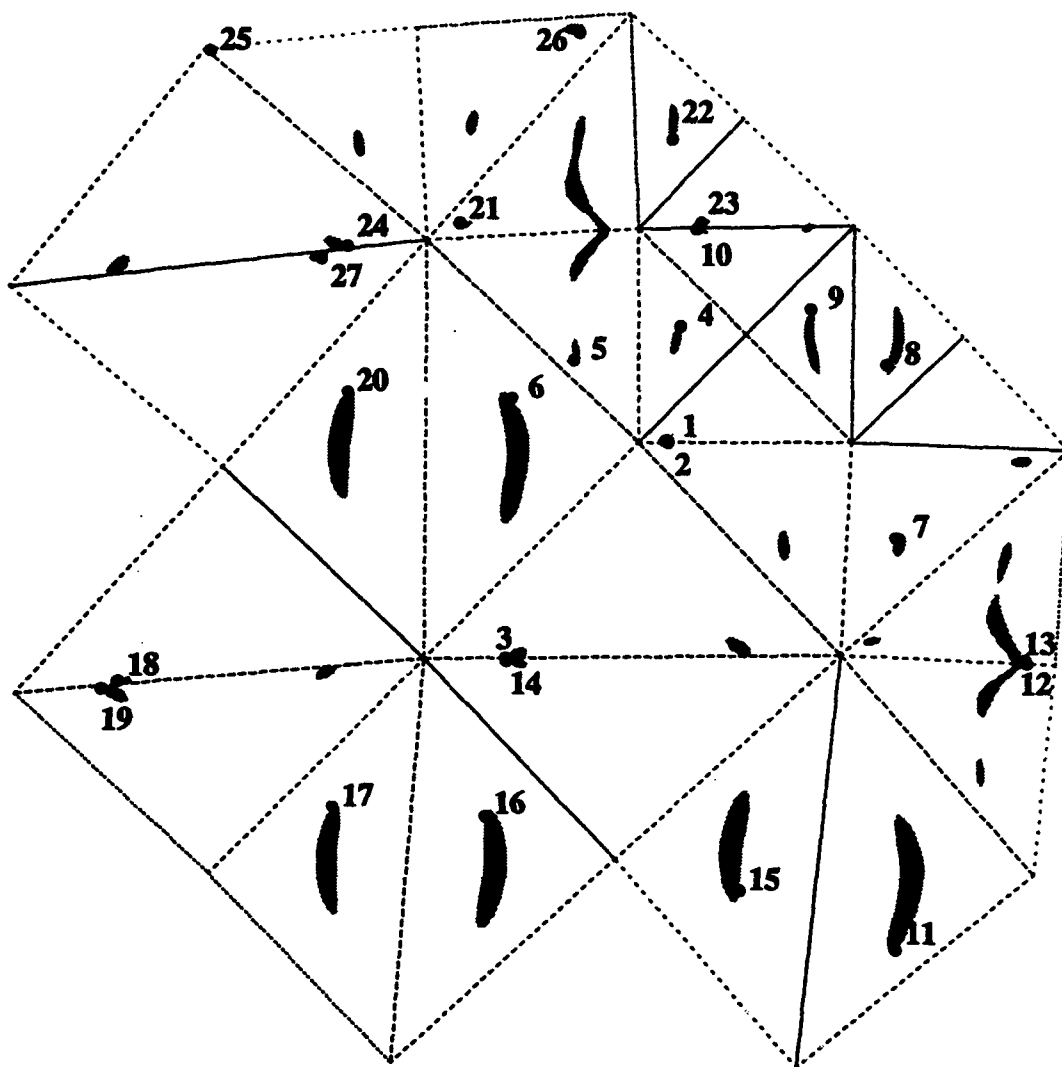


10% regions

Harmonic solution $P = 1$

SIMPLIFIED L2 APPROACH

Fig. 43a



10% regions

Harmonic solution $P = 2$

SIMPLIFIED L2 APPROACH

Fig. 43b

The Laboratory for Numerical Analysis is an integral part of the Institute for Physical Science and Technology of the University of Maryland, under the general administration of the Director, Institute for Physical Science and Technology. It has the following goals:

- To conduct research in the mathematical theory and computational implementation of numerical analysis and related topics, with emphasis on the numerical treatment of linear and nonlinear differential equations and problems in linear and nonlinear algebra.
- To help bridge gaps between computational directions in engineering, physics, etc., and those in the mathematical community.
- To provide a limited consulting service in all areas of numerical mathematics to the University as a whole, and also to government agencies and industries in the State of Maryland and the Washington Metropolitan area.
- To assist with the education of numerical analysts, especially at the postdoctoral level, in conjunction with the Interdisciplinary Applied Mathematics Program and the programs of the Mathematics and Computer Science Departments. This includes active collaboration with government agencies such as the National Institute of Standards and Technology.
- To be an international center of study and research for foreign students in numerical mathematics who are supported by foreign governments or exchange agencies (Fulbright, etc.).

Further information may be obtained from **Professor I. Babuška**, Chairman, Laboratory for Numerical Analysis, Institute for Physical Science and Technology, University of Maryland, College Park, Maryland 20742-2431.

END